CHARACTERIZATION AND MODELING OF RELATIVE LUMINESCENCE EFFICIENCY OF OPTICALLY STIMULATED LUMINESCENCE DETECTORS EXPOSED TO HEAVY CHARGED PARTICLES

By

GABRIEL OLIVEIRA SAWAKUCHI

Bachelor of Science in Physics
University of Sao Paulo
Sao Paulo, Brazil
2001

Master of Science in Physics
University of Sao Paulo
Sao Paulo, Brazil
2003

Submitted to the Faculty of the
Graduate College of
Oklahoma State University
in partial fulfillment of
the requirements for
the Degree of
DOCTOR OF PHILOSOPHY
October, 2007

CHARACTERIZATION AND MODELING OF RELATIVE LUMINESCENCE EFFICIENCY OF OPTICALLY STIMULATED LUMINESCENCE DETECTORS EXPOSED TO HEAVY CHARGED PARTICLES

Dissertation Approved:

Eduardo G. Yukihara

Dissertation Advisor

Stephen W. S. McKeever

Kaladi S. Babu

Ulrich Melcher

A. Gordon Emslie

Dean of the Graduate College

ACKNOWLEDGMENTS

I would like to thank the staff from the Department of Physics for the technical assistance. I appreciate the help of Susan Cantrell, Cindi Raymond, Stephanie Hall, Danyelle Talbot and Warren Grider. Also, many thanks to Tammy Austin, secretary of Venture I building. Tammy's assistance and attention were extremely helpful.

I gratefully thank Landauer Inc. for kindly providing the Luxel^{TM} detectors and Dr. Mark Akselrod (Landauer Inc.) for discussions and providing information about the Luxel^{TM} detectors.

Many thanks to Dr. Adan Russek and Dr. Michael Sivertz for the beam time and assistance during the irradiations at NSRL-BNL; Dr. Edward Semones and Dr. Ramona Gaza from JSC-NASA for the proton irradiations at TAMU; Dr. Michael F. Moyers for the beam time and irradiations at Loma Linda University; and Dr. Chris Soares for ^{60}Co irradiations at NIST.

I would like to thank the National Institute of Radiological Sciences, Japan, for the beam time at HIMAC. Particularly, I would like to thank Dr. Yukio Uchihori, Dr. Nakahiro Yasuda and Hisashi Kitamura for the assistance during the irradiations at HIMAC-NIRS, and for fruitful discussions regarding this project.

I appreciate the discussions and friendship from my colleagues from the Radiation Dosimetry Laboratory. Specially, I would like to thank David Klein, Dr. Regina DeWiit, Dr. Juan Mittani, Dr. Michael Blair, Dr. Ramona Gaza, and Dr. Razvan Gaza. Also, I would like to thank Dr. Jens Edmund from Risø National Laboratory, Denmark, for fruitful discussions during his stay at the Radiation Dosimetry Laboratory.

Thanks to Dr. Stephen W. S. McKeever for sharing his immeasurable knowledge on

radiation dosimetry. Dr. McKeever's suggestions and contributions were very helpful for the accomplishment of this project.

In particular, I would like to thank Dr. Eric R. Benton for sharing his beam time at HIMAC and NSRL. Also, I would like to thank Dr. Benton not only for suggestions, contributions and fruitful discussions, but also for his friendship and encouragement.

Finally and most importantly, I would like to thank my advisor and friend, Dr. Eduardo G. Yukihara, for guiding me throughout this project with his expertise in radiation dosimetry and brilliant scientific talent. Dr. Yukihara's motivation, dedication and patience in teaching and advising, and warm personality make him an example to follow.

Some of the irradiations were performed as part of the Inter-Comparison for Cosmic-rays with Heavy Ion Beams at NIRS (ICCHIBAN) project.

This work was financially supported by Dr. Eduardo G. Yukihara's startup grant from the Department of Physics at Oklahoma State University.

TABLE OF CONTENTS

Chapter Page

1 INTRODUCTION 1

2 OPTICALLY STIMULATED LUMINESCENCE 5

2.1 THE OPTICALLY STIMULATED LUMINESCENCE PHENOMENON . 5

2.2 OPTICALLY STIMULATED LUMINESCENCE PROPERTIES OF Al_2O_3:C 9

3 RESPONSE OF LUMINESCENCE DETECTORS TO HEAVY CHARGED PARTICLE RADIATION 13

3.1 EXPERIMENTAL RELATIVE LUMINESCENCE EFFICIENCY 15

3.2 TRACK STRUCTURE MODEL 17

4 ANALYTICAL MODELING OF RADIAL DOSE DISTRIBUTION 26

4.1 CHATTERJEE AND SCHAEFER MODEL 26

4.2 BUTTS AND KATZ MODEL 32

4.2.1 MODIFICATIONS OF BUTTS AND KATZ MODEL 36

4.3 KIEFER AND STRAATEN MODEL 40

4.4 GEIß *ET AL.* MODEL 46

4.5 SUMMARY OF ANALYTICAL MODELS OF RADIAL DOSE DISTRIBUTION 48

5 MONTE CARLO MODELING OF RADIAL DOSE DISTRIBUTION 51

5.1 SINGLE DIFFERENTIAL CROSS-SECTION FOR PRODUCTION OF SECONDARY ELECTRONS USED BY GEANT4 52

5.2 RADIAL DOSE DISTRIBUTION OBTAINED WITH GEANT4 55
5.2.1 MODEL DESCRIPTION 55
5.2.2 ENERGY DEPOSITED BY ELECTROMAGNETIC INTERACTION OF THE INCIDENT PARTICLE AND SECONDARY ELECTRONS 56
5.2.3 EFFECTS OF VARIOUS PARAMETERS IN THE RADIAL DOSE DISTRIBUTION 57

6 EXPERIMENTAL DETAILS 61
6.1 DETECTORS AND PREPARATION 61
6.2 HEAVY CHARGED PARTICLE IRRADIATIONS 62
6.3 CALIBRATION OF A ^{90}Sr/^{90}Y SOURCE AGAINST A ^{60}Co SOURCE . . 63
6.4 OPTICALLY STIMULATED LUMINESCENCE READOUTS 65
6.5 THERMOLUMINESCENCE READOUTS 66
6.6 CALIBRATION METHOD 68

7 OPTICALLY STIMULATED LUMINESCENCE PROPERTIES OF Al_2O_3:C EXPOSED TO DIFFERENT IONIZATION DENSITIES 72
7.1 DOSE RESPONSE 72
7.1.1 BETA RAYS DOSE RESPONSE 73
7.1.2 HEAVY CHARGED PARTICLE DOSE RESPONSE 74
7.2 DEPENDENCE ON IONIZATION DENSITY 83
7.2.1 OSL CURVES FOR DIFFERENT RADIATION QUALITIES AT LOW DOSES 83
7.2.2 OSL CURVES FOR DIFFERENT ABSORBED DOSES BUT SAME RADIATION QUALITY 85
7.3 RELATIVE LUMINESCENCE EFFICIENCY OF LUXEL™ DETECTORS 92
7.3.1 BARE BEAM DATA 93

7.3.2 BINARY FILTER DATA 95

8 PREDICTIONS OF RELATIVE LUMINESCENCE EFFICIENCY USING THE TRACK STRUCTURE MODEL 100

8.1 RELATIVE LUMINESCENCE EFFICIENCY CALCULATED IN WATER AND IN THE DETECTOR'S MATERIAL 101

8.2 TEST RADIATION TO SIMULATE THE DELTA RAY SPECTRUM . . . 103

8.3 RELATIVE LUMINESCENCE EFFICIENCY OBTAINED USING ANALYTICAL MODELS OF RADIAL DOSE DISTRIBUTION 110

8.4 IMPROVEMENT OF BUTTS AND KATZ MODEL OF RADIAL DOSE DISTRIBUTION AND DETERMINATION OF RELATIVE LUMINESCENCE EFFICIENCY 115

8.5 RELATIVE LUMINESCENCE EFFICIENCY OBTAINED USING MONTE CARLO SIMULATIONS WITH GEANT4 124

9 MEASUREMENT OF ABSORBED DOSE AND DOSE EQUIVALENT IN COMPLEX RADIATION FIELDS 128

10 CONCLUSION 133

A RELATIVE LUMINESCENCE EFFICIENCY DATA 151

B GEANT4 CODE FOR THE PHYSICS PROCESSES 157

B.1 ION PROCESSES 157

B.2 ELECTRON PROCESSES 157

LIST OF TABLES

Table Page

4.1 $L_{\infty}^{H_2O}$ determined using the Brookhaven National Laboratory (BNL) Energy vs. LET vs. Range calculator version 1.24 program and different RDD models. 39

4.2 Summary of the main parameters of different RDD models. r_c is the radius of the core region and R_{Max} is the maximum radial distance of a secondary electron. SDCS stands for single differential cross–section and $\beta = v/c$ is the speed of the incident particle with respect to the speed of light in vacuum. 50

6.1 Pre-irradiation treatments for the detectors used in this study: Luxel^{TM}, Al_2O_3:C single crystals and TLD-100. 62

6.2 Beam characteristics of the HCP irradiations. 64

6.3 Dose rate of ^{90}Sr/^{90}Y beta source calibrated against a ^{60}Co source from NIST in absorbed dose rate to water for all the detectors and readout procedures used in this work. 65

6.4 Summary of readout methods, and filter packages used for OSL and TL measurements. 70

7.1 Absorbed dose to water and fluence in which the OSL curves start to change, distance $r = d/2$, and accumulated minimum absorbed dose to water D_{min} at the distance $r = d/2$ from the center of the track for Ne 400 MeV/u and Fe 200 MeV/u beams. We calculated D_{min} using Chatterjee and Schaefer, Butts and Katz, Kiefer and Straaten, and Geiß *et al.* models of RDD (see chapter 4). 92

8.1 Conversion factor $\alpha^{H_2O}_{Al_2O_3:C}(1.25\ \mathrm{MeV}, L_\infty^{H_2O,Al_2O_3:C})$ to transform the $\eta_{HCP,\gamma}$ calculated to Al_2O_3:C to the one calculated to water or vice-versa. 104

8.2 Values of the parameters A_0, A_1, A_2 and A_3 from the fitting of the response function versus absorbed dose to Al_2O_3:C (eq. 8.19). 111

8.3 Values of the parameters A and B from eq. 8.25 to make RDD from the modified Butts and Katz model fit data for the two different filter sets. 117

8.4 Modeling of OSL $\eta_{HCP,\gamma}$ of Luxel™ detectors detecting both F-center and UV emission bands (Hoya U-340 filter). We obtained the $\eta_{HCP,\gamma}$ values through TSM using different RDD analytical models and MC simulations with GEANT4. The $\eta_{HCP,\gamma}$values are calculated in water. 122

8.5 Modeling of OSL $\eta_{HCP,\gamma}$ of Luxel™ detectors detecting only F-center emission band (Hoya U-340 and Schott WG-360 filters). We obtained the $\eta_{HCP,\gamma}$ values through TSM using different RDD analytical models and MC simulations with GEANT4. The $\eta_{HCP,\gamma}$values are calculated in water. 123

A.1 Relative luminescence efficiency of HCP in respect to gamma radiation for 24 combinations of particles and energies. The relative luminescence efficiency was calculated in water. We considered the OSL signals from Luxel™ and Al_2O_3:C single crystal detectors equal to the total area under the OSL curve, and the TL signals from Al_2O_3:C single crystal and TLD-100 detectors equal to the height of the dosimetric TL peaks. See section 6 for experimental details. 153

LIST OF FIGURES

Figure Page

2.1 Band diagram illustrating the OSL phenomenon. Full and empty circles represent electrons and holes, respectively. E_e and E_h are the activation energies of the electron trap and hole trap, respectively. 6

2.2 Examples of OSL curves obtained with three readout methods: (a) CW-OSL, (b) LM-OSL and (c) POSL. The insets represent the stimulation power as a function of time (courtesy of E. G. Yukihara). 7

2.3 Band diagram model of the main defects involved in the OSL, TL and RL in Al_2O_3:C. The numbers indicate the possible electronic transitions during the irradiation stage. MDT, DET and DHT stand for main dosimetric trap, deep electron trap and deep hole trap, respectively (Yukihara et al., 2004b; Yukihara and McKeever, 2006a; Chen et al., 2006; Pagonis et al., 2006). 10

2.4 OSL emission spectrum of Al_2O_3:C samples irradiated with 200 Gy of ^{60}Co gamma rays during short stimulation pulses of 500 ns (Yukihara and McKeever, 2006b). 12

3.1 Monte Carlo simulations with GEANT4 of He and Fe tracks in water. The number of primary particles in both simulations is the same. The blue line is the primary particle, red lines are negative charged secondary, tertiary and higher order particles, and the yellow dots are interaction points where events occurred. 14

3.2 Relative luminescence efficiency, $\eta_{HCP,\gamma}$, *versus* unrestricted linear energy transfer, L_∞, of LiF. The ordinate axis refers to the relative luminescence efficiency of HCP relative to gamma radiation (see eq. 3.3) and the abscissa axis refers to the unrestricted linear energy transfer in units of mass stopping power. The data is a compilation of different experiments performed by different groups. Horowitz (1981) provides the references listed in the figure. 16

3.3 OSL $\eta_{HCP,\gamma}$ *versus* $L_\infty^{H_2O}$ of Luxel™ detectors (Al_2O_3:C). The OSL signal was considered to be the total area under the OSL curve. The data is a compilation of all experiments performed at Oklahoma State University before this work (Gaza, 2004). 17

3.4 Illustration of the luminescence process. The material's volume V absorbs the energy E_k from the radiation k creating a concentration of low energy free charges n_k. The low energy free charges are trapped in the main dosimetric trap. The trapped charges are proportional to the luminescence signal. W_k is the average energy required to create a electron-hole pair by the radiation k. 19

3.5 (a) Dose response function $S(D)$ of a detector that has linear behavior in the "low dose" range followed by saturation. (b) Luminescence response function $f_k(D)$ for the same detector represented in (a). 21

3.6 Illustration of HCP stopping inside of a detector to show the cylindrical symmetry of RDD. R_{Max} is the maximum radial distance of the delta rays from the path of the HCP, and L is the maximum depth of penetration of the delta rays from the surface of the detector. 23

4.1 Chatterjee and Schaefer RDD in water (eq. 4.14) around the path of oxygen (23 MeV/u) and iron (1000 MeV/u). The particles have approximately the same LET. . 31

4.2 Butts and Katz RDD in water (eq. 4.33) around the path of oxygen (23 MeV/u) and iron (1000 MeV/u). The particles have approximately the same LET. The ionization potential used on the plots was $I = 10$ eV. 36

4.3 RDD in water around the path of oxygen (23 MeV/u). The full line is the Butts and Katz model, dotted line is the Waligórski *et al.* model and dashed line is the Fageeha *et al.* model. 38

4.4 Illustration of angular distributions and ranges of secondary electrons produced by HCPs (adapted from (Kiefer and Straaten, 1986)). 41

4.5 Geometrical considerations for derivation of eq. 4.49. θ is the angle between the primary HCP and the secondary electron, x_0 is the projection of the maximum distance perpendicular to the path of the primary HCP that a secondary electron of initial energy w_0 can travel, and r is the range of a secondary electron with initial energy w_0. 44

4.6 Kiefer and Straaten RDD in water (eq. 4.55) around the path of oxygen (23 MeV/u) and iron (1000 MeV/u). The particles have approximately the same LET. . 46

4.7 Geiß *et al.* RDD in water (eq. 4.56) around the path of oxygen (23 MeV/u) and iron (1000 MeV/u). The particles have approximately the same LET. 48

4.8 RDD in water around the path of iron (1000 MeV/u) for different RDD analytical models. 49

5.1 Comparison between data (Ohsawa et al., 2005b) and models of SDCS for production of secondary electrons by 6 MeV/u and 10 MeV/u He^{+2} ions in water vapor. Both graphs present the oxygen KLL Auger peak at ~ 500 eV. Dr. D. Ohsawa kindly provided the data. 54

5.2 Geometry used in the RDD simulations. The material of the detector, radius r, thickness z, and number of concentric shells can be conveniently varied. 56

5.3 Influence of maximum step size on the RDD simulations of He 144.2 MeV/u ions in Al_2O_3:C. 58

5.4 Influence of the number of particles on the RDD simulations of He 144.2 MeV/u ions in Al_2O_3:C. 58

5.5 Influence of the thickness z of the detector on the RDD simulations of He 144.2 MeV/u ions in Al_2O_3:C. 59

6.1 Transmission of a) Hoya U-340 and Schott WG-360 filters used in the OSL readouts and b) Schott BG-39 and Corning 5-58 filters used in the TL readouts. 67

6.2 Typical OSL curve from Luxel^{TM} detectors. We considered the OSL signal equal to the total area under the OSL curve subtracting the background signal. 68

6.3 Typical TL curves of a) Al_2O_3:C single crystal, and b) TLD-100 detectors. We considered the TL signal from Al_2O_3:C single crystal and TLD-100 equal to the height of their dosimetric TL peaks. 69

6.4 Example of calibration curve using the reference dose method. The full line is the fit to the three data points using a saturated exponential. The value of the fitting parameters are: $A = 7.54 \pm 1.8$, and $B = (4.02 \times 10^4 \pm 1.10 \times 10^4)$ Gy^{-1}. . . . 71

7.1 OSL dose response and luminescence response function of Luxel^{TM} detectors irradiated with beta rays from a ^{90}Sr/^{90}Y source. a) and b) OSL measured with Hoya U-340 filter (F-center and UV emission bands), and c) and d) OSL measured with combination of Schott WG-360 and Hoya U-340 filters (F-center emission band). The dashed lines in a) and c) represent the linearity, and the full lines in b) and d) represent arbitrary functions fitted to the data for better visualization. 73

7.2 OSL dose response and luminescence response function of Luxel^{TM} irradiated with H 1000 MeV beam. a) and b) OSL measured with Hoya U-340 filter (F-center and UV emission bands), and c) and d) OSL measured with combination of Schott WG-360 and Hoya U-340 filters (F-center emission band). The dashed lines in a) and c) represent the linearity, and the full lines in b) and d) are the beta rays luminescence response functions (see section 3.2). 76

7.3 OSL dose response and luminescence response function of Luxel^{TM} irradiated with He 150 MeV/u beam. a) and b) OSL measured with Hoya U-340 filter (F-center and UV emission bands), and c) and d)OSL measured with combination of Schott WG-360 and Hoya U-340 filters (F-center emission band). The dashed lines in a) and c) represent the linearity, and the full lines in b) and d) are the beta ray luminescence response functions (see section 3.2). 77

7.4 OSL dose response and luminescence response function of Luxel^{TM} detectors irradiated with Ne 400 MeV/u beam. a) and b) OSL measured with Hoya U-340 filter (F-center and UV emission bands), and c) and d)OSL measured with combination of Schott WG-360 and Hoya U-340 filters (F-center emission band). The dashed lines in a) and c) represent the linearity, and the full lines in b) and d) are the beta rays luminescence response functions (see section 3.2). 78

7.5 OSL dose response and luminescence response function of Luxel^{TM} detectors irradiated with Si 490 MeV/u beam. a) and b) OSL measured with Hoya U-340 filter (F-center and UV emission bands), and c) and d)OSL measured with combination of Schott WG-360 and Hoya U-340 filters (F-center emission band). The dashed lines in a) and c) represent the linearity, and the full lines in b) and d) are the beta rays luminescence response functions (see section 3.2). 79

7.6 OSL dose response and luminescence response function of Luxel^{TM} detectors irradiated with Fe 1000 MeV/u beam. a) and b) OSL measured with Hoya U-340 filter (F-center and UV emission bands), and c) and d)OSL measured with combination of Schott WG-360 and Hoya U-340 filters (F-center emission band). The dashed lines in a) and c) represent the linearity, and the full lines in b) and d) are the beta rays luminescence response functions (see section 3.2). 80

7.7 OSL dose response and luminescence response function of Luxel^{TM} detectors irradiated with Fe 500 MeV/u beam. a) and b) OSL measured with Hoya U-340 filter (F-center and UV emission bands), and c) and d)OSL measured with combination of Schott WG-360 and Hoya U-340 filters (F-center emission band). The dashed lines in a) and c) represent the linearity, and the full lines in b) and d) are the beta rays luminescence response functions (see section 3.2). 81

7.8 OSL dose response and luminescence response function of Luxel^{TM} detectors irradiated with Fe 200 MeV/u beam. a) and b) OSL measured with Hoya U-340 filter (F-center and UV emission bands), and c) and d)OSL measured with combination of Schott WG-360 and Hoya U-340 filters (F-center emission band). The dashed lines in a) and c) represent the linearity, and the full lines in b) and d) are the beta rays luminescence response functions (see section 3.2). 82

7.9 OSL curve shape of Luxel^{TM} detectors irradiated with gamma of ^{60}Co source, beta of a ^{90}Sr/^{90}Y, H 1000 MeV, He 150 MeV/u, Ne 400 MeV/u, Si 490 MeV/u, Fe 1000 MeV/u, Fe 500 MeV/u and Fe 200 MeV/u. For all OSL curves the same nominal dose of 100 mGy was delivered to the detector. a) OSL measured with Hoya U-340 filter detecting both F-center and UV emission bands, and b) OSL measured with combination of Schott WG-360 and Hoya U-340 filters detecting F-center emission band. 84

7.10 OSL curve shape of Luxel^{TM} detectors irradiated with H 1000 MeV, He 150 MeV/u, Ne 400 MeV/u, Fe 1000 MeV/u, Fe 500 MeV/u and Fe 200 MeV/u with approximately the same particle fluences. The particle fluences were: 2.79×10^7 cm^{-2}, 2.79×10^7 cm^{-2}, 1.99×10^7 cm^{-2}, 2.06×10^7 cm^{-2}, 3.13×10^7 cm^{-2} and 2.90×10^7 cm^{-2}, respectively. The absorbed doses in water were: 10 mGy, 100 mGy, 1 Gy, 5 Gy, 10 Gy and 20 Gy, respectively. a) OSL measured with Hoya U-340 filter detecting both F-center and UV emission bands, and b) OSL measured with combination of Schott WG-360 and Hoya U-340 filters detecting F-center emission band. 86

7.11 Normalized OSL curves of Luxel^{TM} detectors irradiated with beta rays. a) OSL measured with Hoya U-340 filter detecting both F-center and UV emission bands, and b) OSL measured with combination of Schott WG-360 and Hoya U-340 filters detecting F-center emission band. The insets represent the total area under the normalized OSL curves as a function of absorbed dose. 87

7.12 Normalized OSL curves of Luxel^{TM} detectors irradiated with Ne 400 MeV/u beam. a) OSL measured with Hoya U-340 filter detecting both F-center and UV emission bands, and b) OSL measured with combination of Schott WG-360 and Hoya U-340 filters detecting F-center emission band. The insets represent the total area under the normalized OSL curves as a function of absorbed dose. 88

7.13 Normalized OSL curves of Luxel^{TM} detectors irradiated with Fe 200 MeV/u beam. a) OSL measured with Hoya U-340 filter detecting both F-center and UV emission bands, and b) OSL measured with combination of Schott WG-360 and Hoya U-340 filters detecting F-center emission band. The insets represent the total area under the normalized OSL curves as a function of absorbed dose. 89

7.14 Illustration of overlap between HCP tracks when considering that the tracks are parallel and randomly distributed. $D(r)$ is a schematic representation of the RDD, d is the mean distance between two tracks, and $r = d/2$ is the middle point between two tracks where the accumulated radial dose $D(r)$ has its minimum value D_{min}. 90

7.15 Chatterjee and Schaefer model of RDD in Al_2O_3:C for 1 Gy, 10 Gy and 50 Gy of Fe 200 MeV/u, illustrating the effect of track overlap in the inter-track region. . . . 91

7.16 $\eta_{HCP,\gamma}$ calculated in water of Luxel^{TM} detectors exposed to 24 different combinations of particles and energies. We considered the OSL signal equal to the total area under the OSL curve. a) OSL measured with Hoya U-340 filter detecting both F-center and UV emission bands, and b) OSL measured with combination of Schott WG-360 and Hoya U-340 filters detecting F-center emission band. Red lines are arbitrary functions that fit the data for better visualization. 94

7.17 a) Luminescence response function of Luxel^{TM} detectors irradiated with beta rays. b) $\eta_{HCP,\gamma}$ *versus* L_∞ in water of Luxel^{TM} detectors exposed to different combinations of particles and energies. a) and b) the full symbols represent the OSL detected with Hoya U-340 filters, open symbols represent the OSL detected with combination of Schott WG-360 and Hoya U-340 filters, and full and dashed lines are arbitrary functions fitted to the data for better visualization. 96

7.18 $\eta_{HCP,\gamma}$ calculated in water of Luxel^{TM}detectors. The full line represents the bare beam experimental data. The full symbols represent the bare beam data of the H 40 MeV, He 150 MeV/u, Ne 400 MeV/u and Si 490 MeV/u beams. The open symbols represent data obtained by placing binary filters in front of the H 40 MeV, He 150 MeV/u, Ne 400 MeV/u and Si 490 MeV/u to stop the primary particles. a) OSL detected with Hoya U-340 filter, and b) OSL detected with combination of Schott WG-360 and Hoya U-340 filters. 97

7.19 Monte Carlo simulations with GEANT4 in Al_2O_3:C, density 3.97 g/cm^3, with a) and c) He 9.810 MeV/u (L_∞ in water of 18.76 keV/μm); and b) and d) O 385.5 MeV/u (L_∞ in water of 19.84 keV/μm). The number of particles for both beams were 50. 98

8.1 $\eta_{HCP,\gamma}$ calculated in water and Al_2O_3:C of Luxel^{TM} detectors. a) OSL measured with Hoya U-340 filter detecting both F-center and UV emission bands, and b) OSL measured with combination of Schott WG-360 and Hoya U-340 filters detecting F-center emission band. Red lines are arbitrary functions that fit the $\eta_{HCP,\gamma}$ data calculated in water for better visualization. 105

8.2 The solid line represents the ratio between the mass-energy absorption coefficients of Al_2O_3 and water, normalized to the mean energy of ^{60}Co gamma rays. Solid circles represent the relative TL of Al_2O_3:C normalized to the mean energy of ^{60}Co gamma rays. The TL data are from the literature (Akselrod et al., 1990) and mass-energy absorption coefficient data are from the NIST database (Hubbell and Seltzer, 2004). 108

8.3 Luminescence response function of Luxel^{TM} detectors for absorbed dose to Al_2O_3:C. Full circles represent the data when detecting both F-center and UV emission bands. Empty squares represent the data when detecting only F-center emission band. Full and dashed lines represent the fitting to the data when detecting both F-center and UV emission bands, and only F-center emission band, respectively. . 111

8.4 Comparison between OSL $\eta_{HCP,\gamma}$ experimental data and modeling using the RDD functions from Chatterjee and Schaefer, Butts and Katz, Waligórski *et al.* and Fageeha *et al.* models. The figures in the left side present the comparison for OSL detected with Hoya U-340 filters (F-center and UV emission bands), and the figures in the right side for OSL detected with Hoya U-340 and Schott WG-360 (F-center emission band). 113

8.5 Comparison between OSL $\eta_{HCP,\gamma}$ experimental data and modeling using the RDD functions from Kiefer and Straaten, and Geiß *et al.* models. The figures in the left side present the comparison for OSL detected with Hoya U-340 filters (F-center and UV emission bands), and the figures in the right side for OSL detected with Hoya U-340 and Schott WG-360 (F-center emission band). 114

8.6 RDD in Al_2O_3:C according to the modified version of Butts and Katz model. The RDD was plotted for two different detection windows. For comparison we included the Butts and Katz RDD. 117

8.7 Comparison between $\eta_{HCP,\gamma}$ experimental data and modeling using the RDD functions from a modified version of Butts and Katz model. The arrows indicate the data points used to find the parameters A and B for the core radius. The insets represent the percentage deviation between data and model. a) OSL from Luxel^{TM} detected with Hoya U-340 filters (F-center and UV emission bands); b) OSL from Luxel^{TM} detected with Hoya U-340 and Schott WG-360 (F-center emission band). 120

8.8 Comparison between $\eta_{HCP,\gamma}$ experimental data and modeling using the RDD functions from a modified version of Butts and Katz model. The experimental data was obtained by placing binary filters in front of the H 40 MeV, He 150 MeV/u, Ne 400 MeV/u, and Si 490 MeV/u to stop the primary particles. The full lines represent the results from the modeling, and symbols the experimental data. The insets represent the percentage deviation between data and model. a) OSL from Luxel^{TM} detected with Hoya U-340 filter (F-center and UV emission bands); b) OSL from Luxel^{TM} detected with Hoya U-340 and Schott WG-360 filters (F-center emission band). 121

8.9 Influence of the thickness z of the detector on the $\eta_{HCP,\gamma}$ calculated in water using GEANT4. The dashed lines represent the interval of the experimental data for one standard deviation of the data. 125

8.10 Relative luminescence efficiency *versus* L_∞ in water using RDD simulated with GEANT4 for different detector thicknesses z. a)-c) $\eta_{HCP,\gamma}$ when OSL from Luxel^{TM} is detected with Hoya U-340 filter (F-center emission band). e)-f) $\eta_{HCP,\gamma}$ when OSL from Luxel^{TM} is detected with Hoya U-340 and Schott WG-360 filters (F-center emission band). 126

9.1 Method to estimate the "effective" LET L_∞^{eff}, and effective relative luminescence efficiency $\eta_{HCP,\gamma}^{eff}$ of the radiation field using OSL from Luxel^{TM}. a) Characterization of the shape of the OSL curve from Luxel^{TM} to different LETs. The ordinate axis represents the "Ratio" between the OSL initial intensity and total area. b) Relative luminescence efficiency as a function of LET. The OSL was measured with Hoya U-340 filters detecting F-center and UV emission bands. The red lines are arbitrary functions fitted to the data for better visualization. 130

A.1 $\eta_{HCP,\gamma}$ calculated in water of OSL from Al_2O_3:C single crystal detectors. We considered the OSL signal equal to the total area under the OSL curve. The OSL was measured with Hoya U-340 filter detecting both F-center and UV emission bands. For comparison we include the Luxel^{TM} data (full and dashed lines). 151

A.2 $\eta_{HCP,\gamma}$ calculated in water of TL from Al_2O_3:C single crystal detectors. We considered the TL signal equal to the height of the dosimetric TL peak. The TL was measured with Corning 5-58 filter detecting both F-center emission band. For comparison we include the Luxel^{TM} data (full and dashed lines). 152

A.3 $\eta_{HCP,\gamma}$ calculated in water of TL from TLD-100 detectors. We considered the TL signal equal to the height of the dosimetric TL peak. The TL was measured with Schott BG-39 filter. For comparison we include the Luxel^{TM} data (full and dashed lines). 152

NOMENCLATURE

BNL Brookhaven National Laboratory

CW-OSL Continuous-Wave Optically Stimulated Luminescence

DDCS Double Differential Cross-Section

DET Deep Electron Trap

DHT Deep Hole Trap

FWHM Full Width at Half Maximum

HCP Heavy Charged Particle

HIMAC Heavy Ion Medical Accelerator in Chiba

ICCHIBAN Inter-Comparison for Cosmic-rays with Heavy Ion Beams at NIRS

ICRU International Commission on Radiation Units and Measurements

LED Light Emitting Diode

LET Linear Energy Transfer

LLUMC Loma Linda University Medical Center

LM-OSL Linear-Modulation Optically Stimulated Luminescence

MC Monte Carlo

MDT Main Dosimetric Trap

NIRS National Institute of Radiological Sciences

NIST National Institute of Standards and Technology

NSRL NASA Space Radiation Laboratory

OSL Optically Stimulated Luminescence

OSLD Optically Stimulated Luminescence Dosimeter/Detector

OSU Oklahoma State University

PNTD Plastic Nuclear Track Detector

POSL Pulsed Optically Stimulated Luminescence

RDD Radial Dose Distribution

SDCS Single Differential Cross-Section

TAMU Texas A & M University

TL Thermoluminescence

TLD Thermoluminescence Dosimeter/Detector

TSM Track Structure Model

UV Ultraviolet

LIST OF SYMBOLS

A	re-trapping probability of electrons
A_m	recombination probability of electrons with holes
c	speed of light in vacuum
$D(r)$	radial dose distribution
D_k	absorbed dose from a radiation field k
e	electron charge
E_k	energy imparted from a radiation field k
f_k	response function from a detector exposed to the radiation field k
I	ionization potential
I_0	optically stimulated luminescence initial intensity
I_{OSL}	optically stimulated luminescence intensity
L	maximum depth of penetration
L_∞^m	unrestricted linear energy transfer calculated in the material m
m	concentration of holes in the hole trap
m_e	electron mass
m_v	concentration of holes in the valence band
$m_e c^2$	rest energy of an electron
N_e	density of electrons
N	total concentration of electron traps
n	concentration of electron in the electron trap
n_c	concentration of electron in the conduction band

n_k	concentration of low energy charges created by the radiation field k
r	radial distance
r_c	core radius
R_{Max}	penumbra radius
S_k	luminescence signal produced by the radiation field k
t	time
V	volume
W	maximum energy of secondary electrons in a heavy charged particle collision
W_k	average energy required to create an electron-hole pair by the radiation field k
w	electron energy
Z	atomic number
Z^*	effective atomic number
α	detection efficiency of the experimental apparatus
β	relative velocity with respect to velocity of light in vacuum
η_k	luminescence efficiency to the radiation field k
η'_k	efficiency to convert low energy charges created by the radiation field k into luminescence
$\eta_{k,l}$	relative luminescence efficiency of radiation field k in respect with a reference radiation field l
ρ_m	density of the medium
σ	photoionization cross-section
τ_d	optically stimulated luminescence decay constant
Φ	fluence
Ω_p	plasma oscillation frequency

CHAPTER 1

INTRODUCTION

This work investigates the optically stimulated luminescence (OSL) response of carbon-doped aluminum oxide (Al_2O_3:C) detectors exposed to heavy charged particles (HCPs) with energies relevant to radiation protection in space, and cancer therapy. This investigation includes ground-based experiments in accelerators and theoretical studies of the detector's response. These theoretical studies are based on the track structure model (TSM) and require information of the spatial pattern of energy deposition around the HCP path – the radial dose distribution (RDD). Thus, RDDs were obtained using six analytical models, and Monte Carlo simulations with the code GEANT4. In addition, we propose a modified analytical model to improve the agreement between calculated and experimental efficiency values.

The interest in HCP[1] dosimetry is growing because of the increasing human presence in space geared toward future manned space exploration missions, and the dissemination of new facilities for proton and carbon cancer therapy. However, the dosimetry of HCPs remains a challenging problem in luminescence dosimetry, motivating the investigation of the effects of HCPs on new detectors, such as Al_2O_3:C OSL detectors (OSLDs). For appropriate use of radiation and for radiation protection, development of new dosimetric methods is important for reliable measurement of absorbed doses in HCP radiation fields.

The challenge in space dosimetry stems from the presence of different particles with a wide range of energies (McKeever, 2002; Benton and Benton, 2001). Solid state luminescence detectors exhibit decreasing efficiency with increasing ionization density of the

[1]Throughout this work the term heavy charged particle (HCP) is used for all nuclei, including proton.

radiation field (Horowitz, 1981; Olko, 2002; Yukihara et al., 2006), making the detector's response dependent upon the spectrum of the radiation field. The decreasing efficiency is due to the non-uniform distribution of physical events created by the HCP along its path, which produces doses as high as 10^6 Gy (Gy = J/kg) along the vicinity of the track, depending on the charge and speed of the particle (Butts and Katz, 1967). To complicate matters even further, the ionization density is not uniquely related to the linear energy transfer (LET), but depends on the particle atomic number Z and energy E (Horowitz, 1981).

Proton and carbon cancer therapy dosimetry is also challenging because the particle's energy varies along the Bragg curve, therefore affecting the luminescence efficiency. In addition, in proton and carbon therapy, the energy of the beam is spread using a "range shifter" to create the so-called "spread-out Bragg peak" (Ragu, 1980). Consequently, any point measurement of the dose includes contributions from particles with different energies.

OSL is a technique of growing importance in HCP dosimetry. In addition to the advantages common to solid state luminescence detectors, such as small size, no need for power or cables, and no power consumption, Al_2O_3:C OSLDs also offer high sensitivity, rapid readout, elimination of complex thermal annealing steps, possibility of re-estimation of absorbed dose, possibility of dose imaging, high precision, and accuracy (McKeever and Moscovitch, 2003; Yukihara et al., 2006). In personnel dosimetry in space, the partial solution to the HCP dosimetry problem is to combine two or more types of detectors with complementary properties, such as thermoluminescence (TL) detectors (TLDs) or OSLDs, and plastic nuclear track detectors (PNTD) (NCRP, 2002; McKeever et al., 2007). TLDs and OSLDs are efficient for low LET radiation (LET in water, $L_\infty^{H_2O} < 10$ keV/μm), whereas PNTDs are efficient for high LET radiation ($L_\infty^{H_2O} > 10$ keV/μm). Al_2O_3:C OSLDs are currently part of the NASA crew and area monitoring detector packages (Zhou et al., 2006, 2007), and are also under investigation for real-time in vivo proton therapy dosimetry (Edmund et al., 2007b,a).

The objective of this work is to evaluate the possibility of applying the TSM to predict

the response of luminescence detectors to different combinations of HCPs and energies relevant to radiation protection in space and cancer therapy. Such a model is important considering that only a limited number of accelerator facilities around the world can provide the relevant combination of HCPs and energies for characterization of the detectors. Therefore, the experimental characterization is very time consuming and expensive.

This work will be presented according to the following structure.

Chapters 2 to 5 present the theoretical background and calculations of RDDs. The basic properties and model for the OSL are presented in chapter 2, which provides the basis to understand the results of this dissertation. Chapter 3 derives a formula to predict the relative luminescence efficiency ($\eta_{HCP,\gamma}$) of detectors exposed to HCPs. The formula requires RDDs that are obtained in chapters 4 and 5 using analytical models and Monte Carlo simulations.

Chapters 6 and 7 present the experimental work on the characterization of luminescence detectors. The experimental details (type of detectors, measurement, HCP irradiations, and protocols) are presented in chapter 6, whereas experimental results on the OSL dose response, shape of the OSL curve, and $\eta_{HCP,\gamma}$ data for different types of radiation are presented in chapter 7. A complete table with $\eta_{HCP,\gamma}$ data for different detector's type (Luxel^{TM}, Al_2O_3:C single crystal and TLD-100), readout method (OSL and TL), and combinations of HCPs and energies can be found in the Appendix A.

Chapters 8 and 9 combine the theoretical background with the experimental results. The predictions of the OSL response of Luxel^{TM} detectors are compared with experimental data in chapter 8. In addition to the analytical models of RDD presented in chapter 4, we propose a modified model which predicts relative luminescence efficiency values for Luxel^{TM} detectors in agreement with experimental data within 20 %. Moreover, the relative luminescence efficiencies predicted with the Monte Carlo code GEANT4 are compared with experimental data. Additionally, chapter 9 discusses a method to measure absorbed dose and dose equivalent in space, which incorporates the results of this dissertation.

To conclude, chapter 10 summarizes the relevant results, discusses the limitations and weaknesses of our approach, and suggests improvements and future work.

CHAPTER 2

OPTICALLY STIMULATED LUMINESCENCE

Optically stimulated luminescence (OSL) is a phenomenon of light emission by an irradiated insulator or semiconductor crystal when the material is exposed to light of appropriate wavelength. Synthetic Al_2O_3:C crystal is one of the most sensitive OSL materials, being used for personnel, environmental, and medical dosimetry applications on Earth (Bøtter-Jensen et al., 2003), and for crew passive and area monitoring in space (Zhou et al., 2006, 2007). This chapter presents the basic theoretical framework of OSL and a summary of the luminescence properties and characteristics of Al_2O_3:C material that are relevant to understand the results of this dissertation.

2.1 THE OPTICALLY STIMULATED LUMINESCENCE PHENOMENON

The OSL intensity, also called OSL signal, is proportional to the energy absorbed by the detector. A band diagram containing two localized pre-existing defects between the conduction and valence bands summarizes the OSL process. Defects localized between the bottom of the conduction band and Fermi level, called electron traps, can localize free electrons moving in the conduction band. On the other hand, defects localized between the top of the valence band and Fermi level, called hole traps, can localize free holes moving in the valence band. The band diagram in Figure 2.1 summarizes the OSL process: i) the material is in the ground state; ii) ionizing radiation creates electron-hole pairs; the free electrons move in the conduction band and free holes in the valence band; pre-existing defects within the material can localize the free electrons and holes; iii) after the irradiation is over the trapped electrons and holes remain in a metastable state; iv) illumination with

an appropriate wavelength leads to electron transitions from the trap into the delocalized conduction band. Recombination of the free electrons with localized holes, (or vice-versa) results in luminescence emission (Bøtter-Jensen et al., 2003).

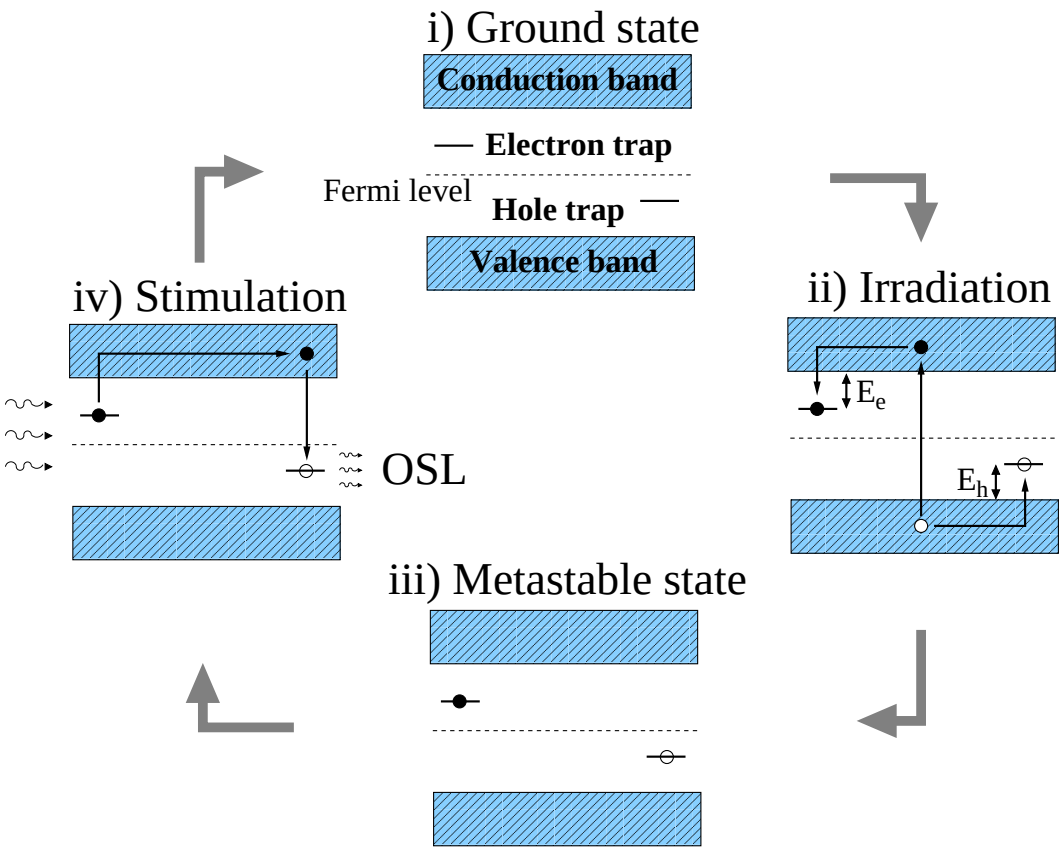

Figure 2.1: Band diagram illustrating the OSL phenomenon. Full and empty circles represent electrons and holes, respectively. E_e and E_h are the activation energies of the electron trap and hole trap, respectively.

The OSL curve is a graph of the OSL intensity versus time of stimulation. The OSL curve can be read out under different conditions including continuous-wave OSL (CW-OSL) (Figure 2.2a), linear-modulation OSL (LM-OSL) (Figure 2.2b), and pulsed OSL (POSL) (Figure 2.2c). This work uses the CW-OSL readout. The advantages of each readout mode are discussed in Bøtter-Jensen et al. (2003).

The simplest OSL model is a crystal containing only one type of electron trap and one type of hole trap participating in the luminescence process (Figure 2.1). In this case, when the stimulation light is turned on, trapped electrons are excited to the conduction band with

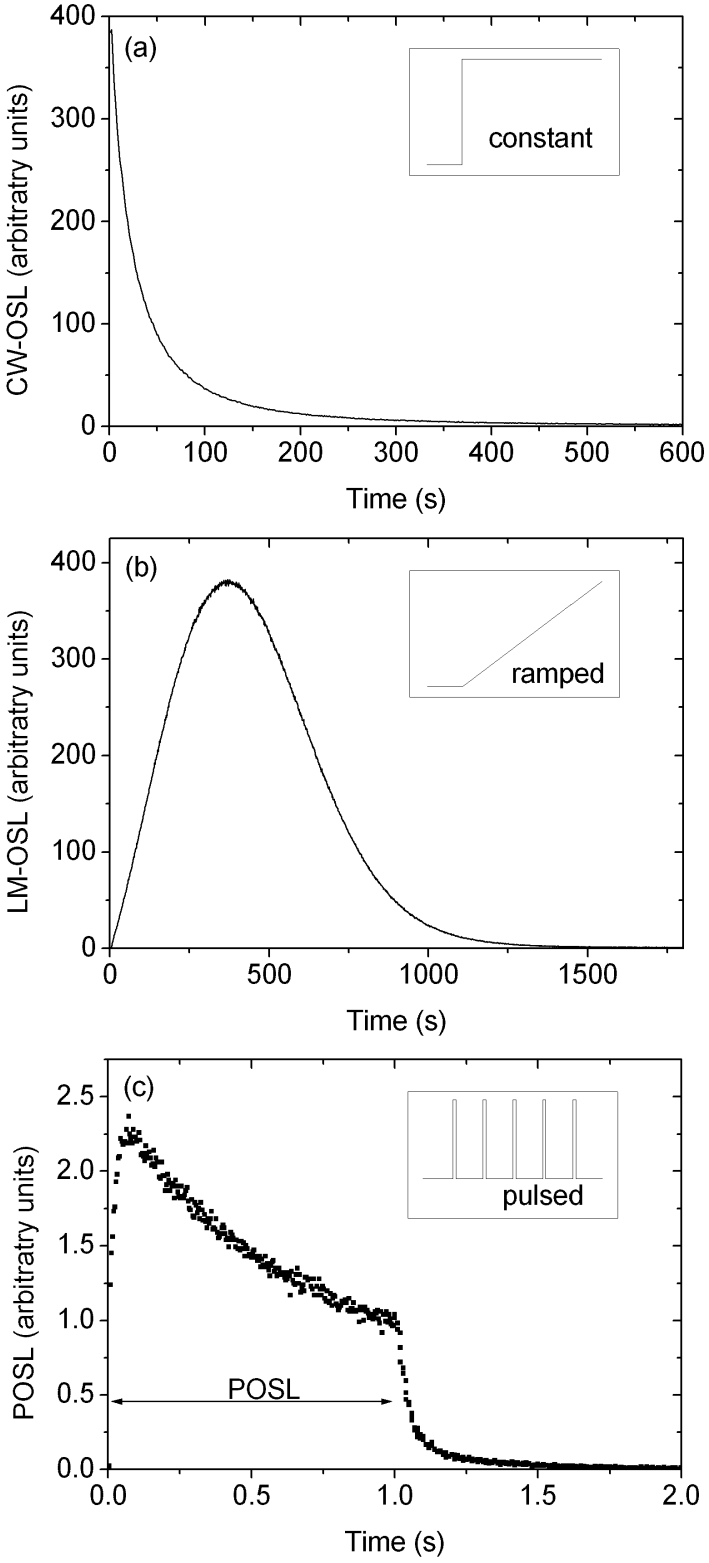

Figure 2.2: Examples of OSL curves obtained with three readout methods: (a) CW-OSL, (b) LM-OSL and (c) POSL. The insets represent the stimulation power as a function of time (courtesy of E. G. Yukihara).

probability rate p. The probability rate p is equal to the incident photon flux Φ times the photoionization cross-section σ ($p = \Phi\sigma$). The electrons in the conduction band can be re-trapped by the electron traps with probability A, or recombine with a hole in a hole trap, also called recombination center, with probability A_m. The electron-hole recombination at the recombination center follows OSL emission. Charge neutrality for this system can be written as

$$n_c + n = m_v + m \tag{2.1}$$

where n_c and n are the concentrations of electrons in the conduction band and electron traps, respectively, and m_v and m are the concentrations of holes in the valence band and hole traps, respectively.

Considering that at the beginning of the optical stimulation $n_c = m_v = 0$, then $n_0 = m_0$. The subscript 0 stands for time $t = 0$.

Assuming that optical stimulation only causes electron transitions to the conduction band, the rate of change in the concentrations can be written as

$$\frac{dn_c}{dt} = -\frac{dn}{dt} + \frac{dm}{dt} \tag{2.2}$$

where

$$\frac{dn}{dt} = -np + n_c A(N - n) \tag{2.3}$$

and

$$\frac{dm}{dt} = -n_c A_m m \tag{2.4}$$

where N is the total available concentration of electron traps. Considering that the rate of change in the concentration of electrons in the conduction band is low compared to the rate of change in the traps (the so called "quasi-equilibrium approximation"), $dn_c/dt \ll$

$dn/dt, dm/dt$ and $n_c \ll n, m$, we have from 2.2 that:

$$\frac{dm}{dt} = \frac{dn}{dt} \tag{2.5}$$

Assuming that there is slow re-trapping of electrons, $n_c A(N-n) \ll np, n_c A_m m$. Thus, the OSL intensity as a function of time can be written as

$$I_{OSL}(t) = -\frac{dm}{dt} = -\frac{dn}{dt} = np \tag{2.6}$$

in which the solution is a pure exponential decay

$$I_{OSL}(t) = n_0 p e^{-tp} = I_0 e^{-\frac{t}{\tau_d}} \tag{2.7}$$

where I_0 is the initial OSL intensity at $t = 0$ and $\tau_d = 1/p$ is the OSL decay constant. Thus, the simplest model of only one type of electron trap and one type of recombination center leads to a OSL intensity that decays exponentially as the constant stimulation light intensity is applied to the sample (Bøtter-Jensen et al., 2003).

2.2 OPTICALLY STIMULATED LUMINESCENCE PROPERTIES OF Al_2O_3:C

Al_2O_3:C, first introduced as a TLD (Akselrod et al., 1990, 1993), has been widely used as an OSLD over the last decade. The high sensitivity, fast and all-optical nature of OSL readout of Al_2O_3:C opened the possibility of developing new technologies such as: POSL (McKeever et al., 1996; McKeever and Akselrod, 1999), imaging (Akselrod et al., 2000), and remote real-time fiber dosimetry (Huston et al., 2001; Polf et al., 2002; Aznar et al., 2004). These technologies have been used in environmental (Kalchgruber and Wagner, 2006), personnel, medical (Aznar et al., 2004, 2005; Andersen et al., 2006), and space dosimetry (Goossens et al., 2006; Yukihara et al., 2006).

Figure 2.3 presents a band diagram model that summarizes the OSL process in Al_2O_3:C

(Yukihara et al., 2004b; Yukihara and McKeever, 2006a; Chen et al., 2006; Pagonis et al., 2006). Because the defects participating in the OSL, thermoluminescence (TL) and radioluminescence (RL) processes are the same, the band diagram also explains these phenomena (Bøtter-Jensen et al., 2003).

The defects relevant to the OSL process in Al_2O_3:C are the main dosimetric trap (MDT) and oxygen vacancies. The nature of the MDT is unclear (Yukihara and McKeever, 2006a), although the MDT is usually considered to be an electron trap (Bøtter-Jensen et al., 2003). Al_2O_3:C crystals are grown with a high concentration of oxygen vacancies. The oxygen vacancies with two captured electrons (F-center) and one captured electron (F^+-center) are the most important. Radiative relaxation of the F-centers is responsible for the main luminescence emission at $\sim$ 420 nm (Evans and Stapelbroek, 1978; Evans et al., 1994).

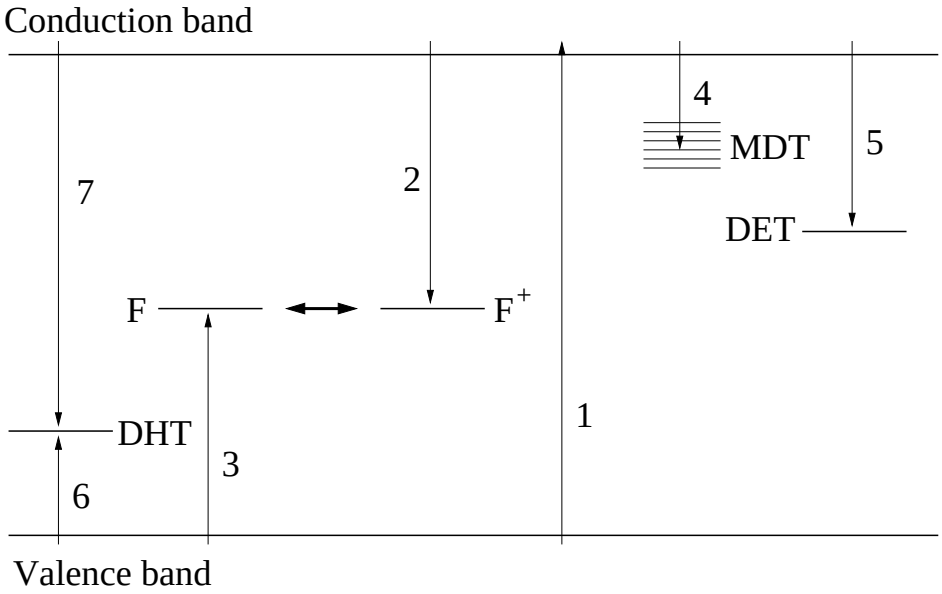

Figure 2.3: Band diagram model of the main defects involved in the OSL, TL and RL in Al_2O_3:C. The numbers indicate the possible electronic transitions during the irradiation stage. MDT, DET and DHT stand for main dosimetric trap, deep electron trap and deep hole trap, respectively (Yukihara et al., 2004b; Yukihara and McKeever, 2006a; Chen et al., 2006; Pagonis et al., 2006).

We summarize the filling of traps in Al_2O_3:C during radiation as follows: ionizing radiation creates electron-hole pairs in the conduction band and valence band of the crystal. When the electrons are in the conduction band they are free to move and they can be trapped in the MDT, deep electron traps (DET), or undergo recombination with F^+-centers.

Recombination of electrons with F^+-centers produces F-centers in the excited state

$$F^+ + e^- \longrightarrow F^* \tag{2.8}$$

Then, F-center transitions to the ground state causes luminescence emission at 420 nm

$$F^* \longrightarrow F + h\nu_{420\,\mathrm{nm}} \tag{2.9}$$

On the other hand, free holes can be trapped at deep hole traps (DHT) and F-centers. The trapping of holes in F-centers causes F-center to F^+-center conversion:

$$F + h^+ \longrightarrow F^+ \tag{2.10}$$

During the OSL or TL readout, electrons are released from the MDT and recombine with the F^+-centers resulting in luminescence emission at 420 nm (eqs. 2.8 and 2.9).

Step annealing studies of the F^+-center optical absorption band in irradiated and ultraviolet (UV) illuminated Al_2O_3:C crystals confirmed the existence of DET and DHT (Akselrod and Gorelova, 1993; Yukihara et al., 2003, 2004b). Heating irradiated crystals to (500-600) °C causes an increasing in the F^+-center optical absorption band. This increasing is due to the release of holes from deep traps unstable in this temperature range, and creation of F^+-centers (see eq. 2.10). The evidence of DET is a decrease in the F^+-center optical absorption band at $\sim$ (700-1000) °C, attributed to the releasing of electrons from deep traps and conversion of F^+-centers to F-centers (see eq. 2.8). Changes in the concentration of F^+-centers cause changes in the sensitivity of the material. Annealing to 900 °C empties the DET and DHT restoring the sensitivity of the crystal (Yukihara et al., 2004b).

The model presented in Figure 2.3 is a simplification of the OSL process in Al_2O_3:C. In fact, other defects participate in the OSL emission. For example, the model ignores the presence of an unknown defect responsible for an emission band centered at $\sim$ 334 nm

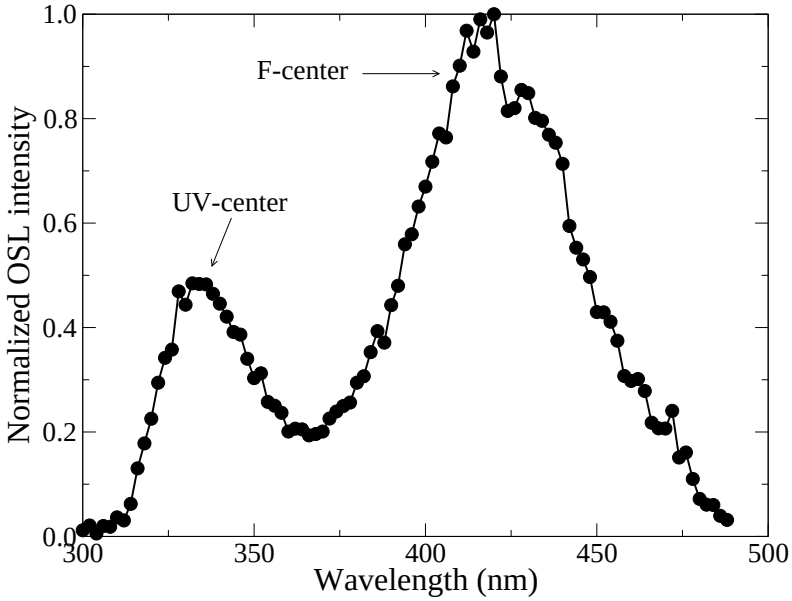

Figure 2.4: OSL emission spectrum of Al_2O_3:C samples irradiated with 200 Gy of ^{60}Co gamma rays during short stimulation pulses of 500 ns (Yukihara and McKeever, 2006b).

(Yukihara and McKeever, 2006b) (Figure 2.4). Taking advantage of the short lifetime of the UV emission band (< 6 μs) (Evans and Stapelbroek, 1978; Yukihara and McKeever, 2006b) compared to the F-center emission band (35 ms) (Lee and Crawford, 1979; Markey et al., 1995), Yukihara and McKeever (2006b) used time discrimination OSL to study the dependence of the F-center and UV emission bands to ionization density. Yukihara and McKeever (2006b) observed that the contribution of OSL from the UV emission band to the total OSL emission increases as the ionization density increases. Furthermore, the intensity of the UV emission band at room temperature increases with time elapsed since irradiation. Such observations are important when applying the Al_2O_3:C OSL to HCP radiation because HCPs create high ionization densities in the vicinity of their paths. Thus, adequate readout procedures with detection of the appropriate luminescence bands are important.

CHAPTER 3

RESPONSE OF LUMINESCENCE DETECTORS TO HEAVY CHARGED PARTICLE RADIATION

Heavy charged particles (HCPs) dissipate energy in matter mainly through electromagnetic interactions with the atoms of the material. The main product of the electromagnetic interactions are ionizations and excitations of the medium for HCPs with energies greater than $\sim$ 0.1 MeV/u (Kalef-Ezra and Horowitz, 1982; ICRU, 1993). Excitations deposit energy locally, whereas ionizations produce secondary electrons (delta rays). The secondary electrons can deposit energy at large distances from the path of the particle. Thus, the passage of HCP through matter leaves a trail of physical events characterized by the HCP's atomic number and speed. The spatial distribution of the physical events created around the HCP path, the radial dose distribution (RDD), influences the final effect produced by the radiation action (e.g. OSL, TL, mutation inductions, DNA strand breaks, etc).

Figure 3.1 illustrates this spatial distribution of the physical events created around the path of He 144.2 MeV/u and Fe 120.4 MeV/u particles in water. Figure 3.1 was created using the Monte Carlo code GEANT4 (Agostinelli et al., 2003). The number of incident particles is the same for both simulations. Figure 3.1 shows that the Fe 120.4 MeV/u particle produces higher ionization densities than the He 144.2 MeV/u particle. The distribution of secondary particles (red lines) produced by ionizations of the medium is a characteristic of the particle's atomic number and speed. In regions close to the path of the HCP the local absorbed dose reaches values as large as 10^6 Gy, depending on the HCP's charge and speed. Therefore, in regions of such high localized doses, the traps responsible for the luminescence process may become totally filled, saturating the detector. Moreover, for the energies

of HCPs relevant to this work, secondary particles that deposit energy in the material can have energies as low as a few eV, and as high as a few MeV.

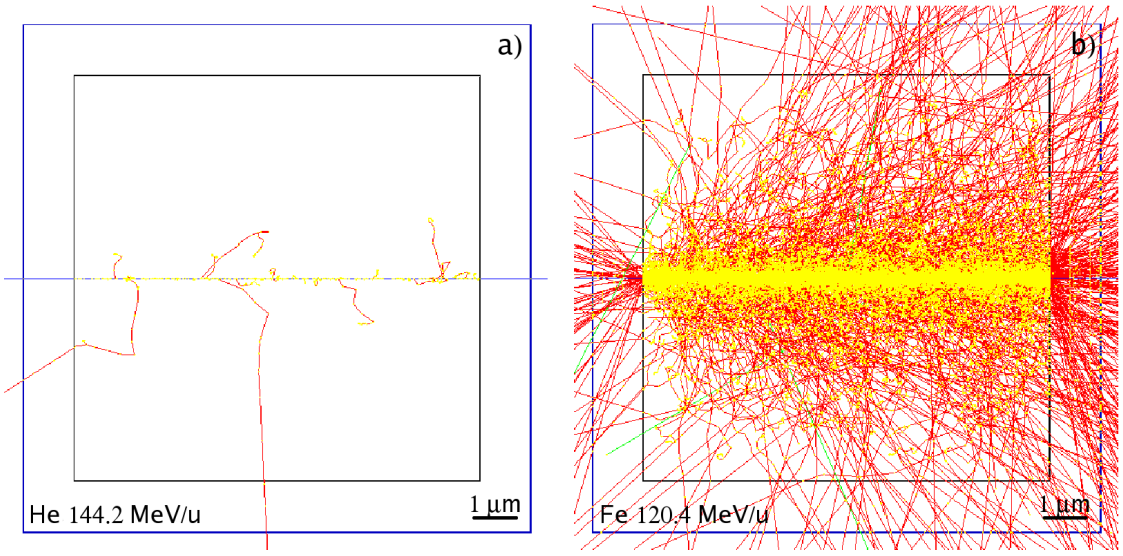

Figure 3.1: Monte Carlo simulations with GEANT4 of He and Fe tracks in water. The number of primary particles in both simulations is the same. The blue line is the primary particle, red lines are negative charged secondary, tertiary and higher order particles, and the yellow dots are interaction points where events occurred.

Due to the different ionization density profiles, we expect the response of luminescence detectors to vary for different types of HCP radiation. Indeed, the literature documents the experimental dependence of the relative luminescence efficiency to HCP ($\eta_{HCP,\gamma}$) (see section 3.1).

The definition of efficiency of a luminescence detector to a radiation field k is the ratio between the energy emitted by the detector as luminescence ϵ_k and the mean absorbed energy E_k by the detector from the radiation field k:

$$\eta_k(E_k) = \frac{\epsilon_k(E_k)}{E_k} \tag{3.1}$$

The energy emitted as luminescence ϵ_k relates to the total amount of light collected by

the experimental apparatus S_k through:

$$\epsilon_k(E_k) = \alpha^{-1} S_k(E_k) \tag{3.2}$$

where α is the detection efficiency of the experimental apparatus, which depends on experimental factors such as quantum efficiency of the light detector, and light collection efficiency.

The definition of the relative luminescence efficiency follows as the ratio of the luminescence efficiency of two radiation fields. Thus, the relative luminescence efficiency of detectors with the same mass to the radiation field k with respect to a reference radiation field l, $\eta_{k,l}$, is defined as

$$\eta_{k,l} = \frac{\eta_k(E_k)}{\eta_l(E_l)} = \frac{S_k(E_k)}{E_k} \Big/ \frac{S_l(E_l)}{E_l} \tag{3.3}$$

where E_k and E_l are the mean absorbed energy from the radiation fields k and l, respectively, and S_k and S_l are the luminescence signals of detectors with the same mass produced by the radiation fields k and l, respectively. Measuring both luminescence efficiencies with the same experimental apparatus, the detection efficiency of the experimental apparatus α cancels out.

3.1 EXPERIMENTAL RELATIVE LUMINESCENCE EFFICIENCY

Considerable investigation has been performed on the response of luminescence detectors to neutron and HCPs. Experimental results show that detectors exposed to HCP present different luminescence efficiencies compared to detectors exposed to ^{60}Co gamma radiation (Horowitz, 1981). To quantify the different responses of the detectors for intercalibration purposes, investigators established the relative luminescence efficiency, $\eta_{\mathrm{HCP},\gamma}$, *versus* unrestricted linear energy transfer (L_∞), as a parameter to characterize the response

of the detectors to different particles and energies. Horowitz (1981) presents a compilation of $\eta_{HCP,\gamma}$ *versus* L_∞ data for LiF, $Li_2B_4O_7$:Mn, and CaF_2:Mn TL materials (see Figure 3.2 for LiF). The TL data show a general trend of decreasing the $\eta_{HCP,\gamma}$ for increasing LET of the radiation field.

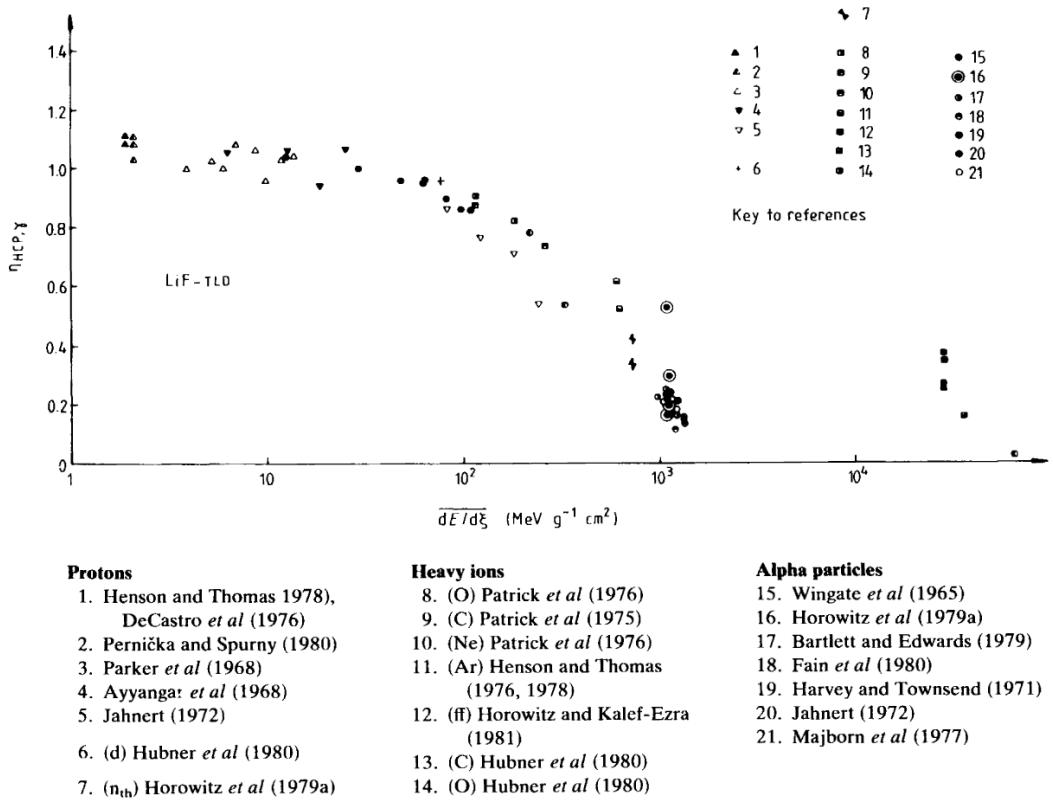

Figure 3.2: Relative luminescence efficiency, $\eta_{HCP,\gamma}$, *versus* unrestricted linear energy transfer, L_∞, of LiF. The ordinate axis refers to the relative luminescence efficiency of HCP relative to gamma radiation (see eq. 3.3) and the abscissa axis refers to the unrestricted linear energy transfer in units of mass stopping power. The data is a compilation of different experiments performed by different groups. Horowitz (1981) provides the references listed in the figure.

Data on the OSL $\eta_{HCP,\gamma}$ of Al_2O_3:C show the same general trend of decreasing the $\eta_{HCP,\gamma}$ for increasing LET of the radiation field (Figure 3.3) (Yasuda et al., 2002; Yukihara et al., 2004a; Gaza et al., 2004; Gaza, 2004).

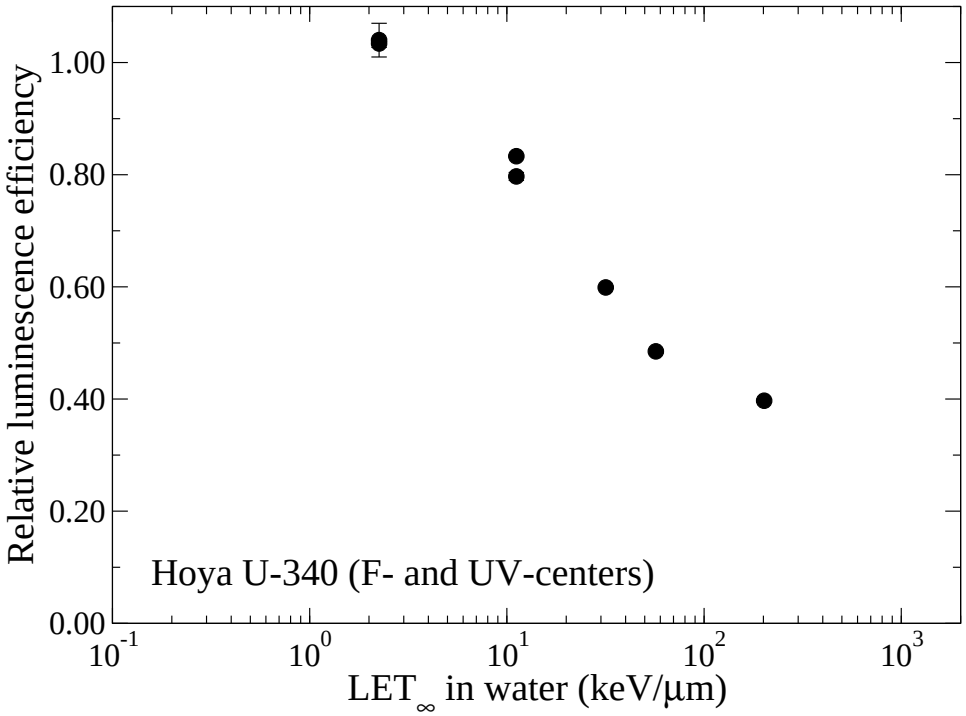

Figure 3.3: OSL $\eta_{HCP,\gamma}$ *versus* $L_{\infty}^{H_2O}$ of Luxel^{TM} detectors (Al_2O_3:C). The OSL signal was considered to be the total area under the OSL curve. The data is a compilation of all experiments performed at Oklahoma State University before this work (Gaza, 2004).

3.2 TRACK STRUCTURE MODEL

For the last 40 years semi-empirical models have been used to predict the response of different systems to HCP radiation. The track structure model (TSM) (Butts and Katz, 1967) and microdosimetric model (Rossi and Zaider, 1996) compare the biological efficiency of different HCP radiations using biological end-points relevant to radiation protection (mutation inductions, chromosome aberrations, DNA strand breaks), or radiotherapy (cell survival). The TSM and microdosimetry also provide the framework to predict the response of detectors, such as TLDs and dye films, to HCPs (Horowitz, 1981; Kalef-Ezra and Horowitz, 1982; Katz et al., 1972; Waligórski and Katz, 1980; Hansen and Olsen, 1984; Geiß et al., 1998; Olko, 2002). This section presents the fundamentals of the TSM and derives an expression to predict $\eta_{HCP,\gamma}$values from knowledge of the RDD and luminescence response of the detector to low LET radiation.

Butts and Katz (1967) introduced the TSM to explain the response of dry enzymes and viruses exposed to HCP. The model's main hypothesis is that the final effect (such as luminescence, DNA strand breaks and mutation) produced by HCP radiation can be approximated by the bulk effect created by uniform electron or photon radiation of a macroscopic volume (test radiation), so that the processes that take place in the macroscopic volume mimic as closely as possible the processes that take place in the volume element dV under HCP irradiation (Kalef-Ezra and Horowitz, 1982). If the only factor that influences the final effect in a system is the density of ionizations, the final effect can be approximately simulated using electron or photon irradiations. Then, knowledge of the RDD around the HCP path allows the calculation of the final effect of the system under HCP irradiation. Following we present an expression to calculate the $\eta_{HCP,\gamma}$ of detectors based on the TSM. We adopt the Kalef-Ezra and Horowitz (1982) formalism to derive the $\eta_{HCP,\gamma}$ expression.

In luminescence detectors the final effect produced by the HCP radiation is emission of light. Eq. 3.3 gives the relative luminescence efficiency expression. We use gamma rays from a ^{60}Co source as the reference radiation field because gamma rays from a ^{60}Co source are one of the standard calibration fields in dosimetry.

Rewriting eq. 3.3 with the appropriated notation we have

$$\eta_{HCP,\gamma} = \frac{S_{HCP}}{E_{HCP}} \Big/ \frac{S_{\gamma}}{E_{\gamma}} \tag{3.4}$$

where S_{HCP} and S_{γ} are the signals of detectors with the same mass, thickness, and volume created under HCP and gamma radiations, respectively, E_{HCP} is the mean absorbed energy from a HCP beam of fluence Φ on the detector's area A, and E_{γ} is the mean absorbed energy from gamma radiation. For equal doses delivered to the whole detector, $D_{HCP} = D_{\gamma}$. For detectors with the same mass, $E_{HCP} = E_{\gamma}$, and the relative luminescence efficiency is simply $\eta_{HCP,\gamma} = S_{HCP}/S_{\gamma}$.

Kalef-Ezra and Horowitz (1982) consider the luminescence signal as proportional to

the concentration of low energy charges n_k created by the radiation k within the lattice of the crystal. These low energy charges are trapped and converted to luminescence with efficiency η'_k. Therefore, the luminescence signal of the detector is:

$$S_k = \alpha \eta'_k n_k V \tag{3.5}$$

where the index k indicates the type of radiation, α is the detection efficiency of the experimental apparatus, η'_k is the efficiency to convert the low energy charges created by the radiation k into luminescence, and n_k is the concentration of low energy charges created by the radiation k.

Figure 3.4 illustrates the difference between the efficiency η'_k to convert the low energy charges created by the radiation k into luminescence, and the luminescence efficiency η_k (see eq. 3.1).

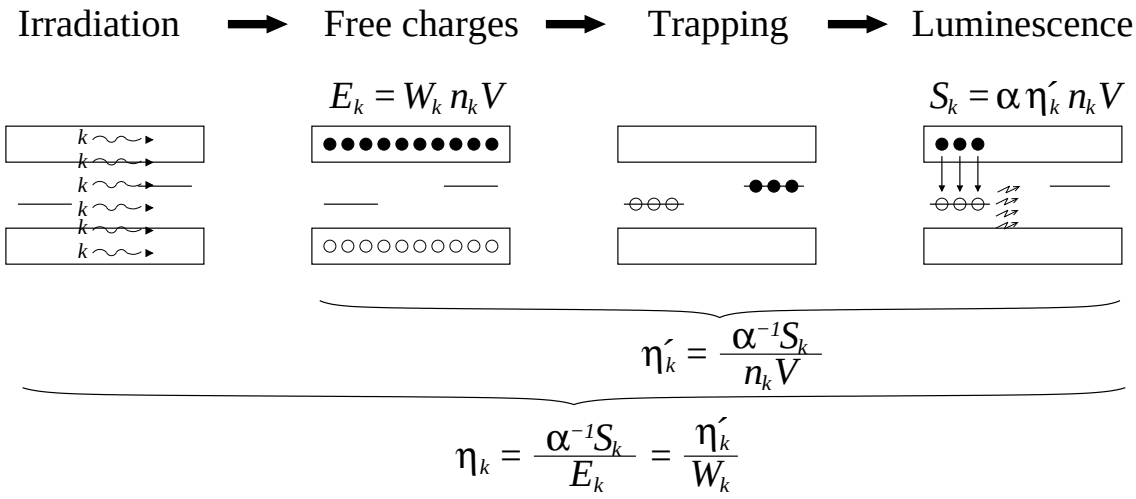

Figure 3.4: Illustration of the luminescence process. The material's volume V absorbs the energy E_k from the radiation k creating a concentration of low energy free charges n_k. The low energy free charges are trapped in the main dosimetric trap. The trapped charges are proportional to the luminescence signal. W_k is the average energy required to create a electron-hole pair by the radiation k.

The absorbed energy E_k is given by:

$$E_k = W_k n_k V \tag{3.6}$$

where W_k is the average energy required to create an electron-hole pair by the radiation k, n_k is the concentration of low energy free charges created by the radiation k, and V is the irradiated volume.

Thus, we find the relationship between η_k and η'_k substituting eq. 3.6 and eq. 3.5 in eq. 3.1:

$$\eta_k = \frac{\eta'_k}{W_k} \tag{3.7}$$

The absorbed dose D_k can be obtained as:

$$D_k = \frac{W_k n_k V}{m} = \frac{W_k n_k}{\rho_m} \tag{3.8}$$

where V, m, and ρ_m are the volume, mass, and density of the detector. Thus, the signal as a function of absorbed dose is given by

$$S_k(D_k) = \alpha \eta'_k \frac{D_k}{W_k} \rho_m V = \alpha \eta_k D_k \rho_m V \tag{3.9}$$

For convenience we define the luminescence response function or supralinearity index $f_k(D)$ of an uniformly irradiated mass of the luminescence detector to the radiation field k as:

$$f_k(D) = \frac{\eta_k(D)}{\eta_k(D_0)} \tag{3.10}$$

where $\eta_k(D)$ is the luminescence efficiency at absorbed dose D and $\eta_k(D_0)$ is the luminescence efficiency obtained at the "low dose" D_0 where the signal S_k is linear.

Figure 3.5 shows an example of the dose response and luminescence response function $f_k(D)$ for a detector that behaves linearly in the "low dose" range followed by saturation.

Thus, for gamma radiation the signal becomes

$$S_\gamma(D) = \alpha \eta_\gamma(D_0) f_\gamma(D) D_\gamma \rho_m V \tag{3.11}$$

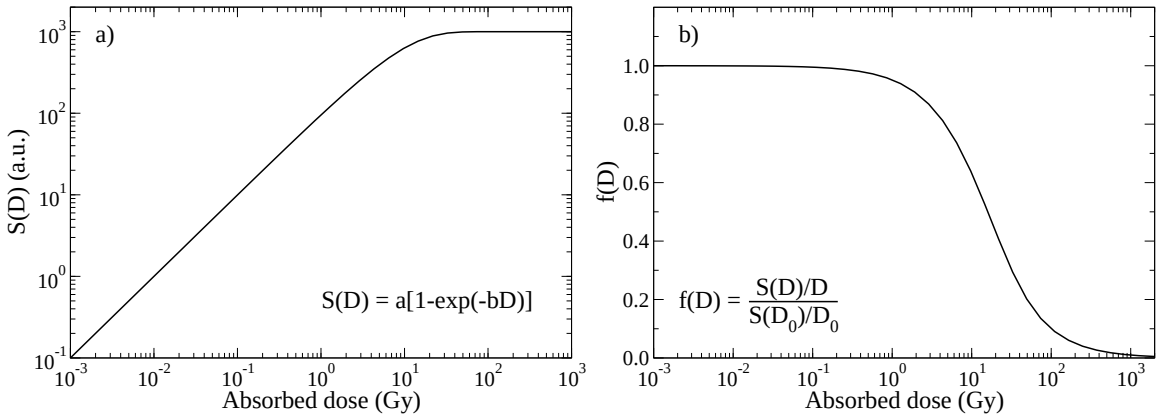

Figure 3.5: (a) Dose response function $S(D)$ of a detector that has linear behavior in the "low dose" range followed by saturation. (b) Luminescence response function $f_k(D)$ for the same detector represented in (a).

The mean absorbed energy from gamma rays is given by:

$$E_\gamma = D_\gamma \rho_m V \tag{3.12}$$

Therefore, the luminescence efficiency to the gamma radiation field is given by (eq. 3.1)

$$\eta_\gamma(D) = \frac{\alpha^{-1} S_\gamma}{E_\gamma} = \eta_\gamma(D_0) f_\gamma(D) \tag{3.13}$$

For HCPs, the signal dS_{HCP} of an element of volume dV of a detector exposed to a single HCP can be written differentiating eq. 3.9

$$dS_{HCP} = \alpha \eta'_\delta \frac{D(r,l)}{W_{HCP}} \rho_m dV = \alpha \eta_\delta D(r,l) \rho_m dV \tag{3.14}$$

where η'_δ is the efficiency to convert the low energy charges created by the HCP into luminescence, $D(r,l)$ is the RDD around the path of the incident HCP, W_{HCP} is the average energy required to create an electron-hole pair by HCP radiation, and η_δ is the luminescence efficiency to the delta ray (subscript δ) spectrum created by the HCP.

Using eq. 3.10, the signal due to HCP radiation becomes

$$dS_{HCP} = \alpha\eta_\delta(D_0) f_\delta[D(r,l)] D(r,l)\rho_m dV \tag{3.15}$$

where $\eta_\delta(D_0)$ is the luminescence efficiency to the delta ray (subscript δ) spectrum created by the HCP in the "low dose" region of the response of the detector, and $f_\delta[D(r,l)]$ is the luminescence response function of the detector to the delta rays created by the HCP. Note that $f_\delta[D(r,l)]$ is a function of the RDD.

Faïn et al. (1974) showed that the average energy required to create an ion pair in gas by HCP radiation varies as a function of the radial distance from the path of the incident HCP. Although data on the dependence of W_{HCP} as a function of radial distance in solids are unavailable, likely the W_{HCP} in solids presents the same trend. Thus, the luminescence efficiency $\eta_\delta(D_0)$ changes with radial distance from the path of the HCP. W_{HCP} data in solids are scarce and exist only for a restricted number of scintillator materials (ICRU, 1979; IAEA, 1995).

A HCP beam with fluence Φ incident in the detector area A produces the luminescence signal S_{HCP} given by:

$$S_{HCP} = A\Phi \int_0^{R_{Max}} \int_0^{L} \alpha\eta_\delta(D_0) f_\delta[D(r,l)] D(r,l)\rho_m 2\pi r dr dl \tag{3.16}$$

where R_{Max} is the maximum radial distance of the delta rays from the path of the HCP, and L is the maximum depth of penetration of the delta rays from the surface of the detector, assuming that the incident particles are normal to the surface of the detector and that the HCP fluence is low. Figure 3.6 illustrates an incident HCP stopping inside of the detector, the symmetry of the problem and the adopted coordinate system.

The RDD function $D(r,l)$ determines the mean absorbed energy from the incident HCP, E_{HCP}:

$$E_{HCP} = A\Phi \int_0^{R_{Max}} \int_0^{L} D(r,l)\rho_m 2\pi r dr dl \tag{3.17}$$

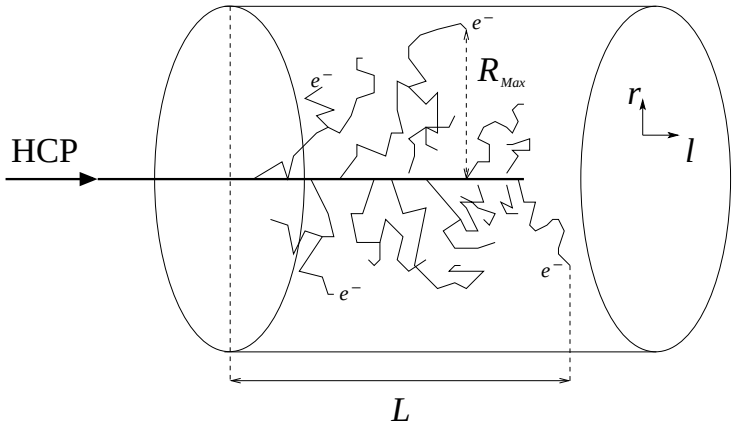

Figure 3.6: Illustration of HCP stopping inside of a detector to show the cylindrical symmetry of RDD. R_{Max} is the maximum radial distance of the delta rays from the path of the HCP, and L is the maximum depth of penetration of the delta rays from the surface of the detector.

Using eq. 3.16 and 3.17 we evaluate the efficiency to HCP as

$$\eta_{HCP}(D) = \frac{\alpha^{-1} S_{HCP}}{E_{HCP}} = \frac{\int_0^{R_{Max}} \int_0^L \eta_\delta(D_0) f_\delta[D(r,l)] D(r,l) \rho_m 2\pi r dr dl}{\int_0^{R_{Max}} \int_0^L D(r,l) \rho_m 2\pi r dr dl} \tag{3.18}$$

Dividing eq. 3.18 by eq. 3.13 we obtain the $\eta_{HCP,\gamma}$ of HCP to the reference gamma radiation:

$$\eta_{HCP,\gamma}(D) = \frac{\eta_{HCP}(D)}{\eta_\gamma(D)} = \frac{\int_0^{R_{Max}} \int_0^L \eta_{\delta,\gamma}(D_0) f_\delta[D(r,l)] D(r,l) \rho_m 2\pi r dr dl}{f_\gamma(D) \int_0^{R_{Max}} \int_0^L D(r,l) \rho_m 2\pi r dr dl} \tag{3.19}$$

For practical purposes the relative luminescence efficiency is defined in the "low dose" (linear) region of the reference gamma radiation field. In this case, $f_\gamma(D_0)$ simply equals unity and eq. 3.19 reduces to

$$\eta_{HCP,\gamma} = \frac{\int_0^{R_{Max}} \int_0^L \eta_{\delta,\gamma} f_\delta[D(r,l)] D(r,l) \rho_m 2\pi r dr dl}{\int_0^{R_{Max}} \int_0^L D(r,l) \rho_m 2\pi r dr dl} \tag{3.20}$$

where

$$\eta_{\delta,\gamma} = \eta'_{\delta,\gamma} \frac{1/W_{HCP}}{1/W_\gamma} \tag{3.21}$$

We now make the TSM assumption: the ionization density is the only factor that in-

fluences the luminescence response of the detector. Thus, an infinitesimal volume of the detector exposed to radiation responds the same way as if the whole bulk of the detector was irradiated. Therefore, the luminescence signal from a detector exposed to HCP is a linear combination of luminescence signals from detectors exposed to a test radiation X that mimics as closely as possible the energy spectrum of delta rays produced by the primary particle. The test radiation X determines the luminescence response function, $f_\delta[D(r,l)] \cong f_X[D(r,l)]$, and $\eta_{HCP,\gamma}$ becomes

$$\eta_{HCP,\gamma} = \frac{\int_0^{R_{Max}} \int_0^L \eta_{\delta,\gamma} f_X[D(r,l)] D(r,l) \rho_m 2\pi r dr dl}{\int_0^{R_{Max}} \int_0^L D(r,l) \rho_m 2\pi r dr dl} \tag{3.22}$$

Assuming that the energy of the incident HCP is large such that the change in the HCP LET is negligible when the HCP passes through the detector, as a first approximation, on average the delta rays deposit their energy uniformly through the whole depth of the detector, L. Thus, the RDD can be approximated as $D(r,l) \cong D(r)$ and the integrals in l on the numerator and denominator cancel out reducing eq. 3.22 to

$$\eta_{HCP,\gamma} = \frac{\int_0^{R_{Max}} \eta_{\delta,\gamma} f_X[D(r)] D(r) \rho_m 2\pi r dr}{\int_0^{R_{Max}} D(r) \rho_m 2\pi r dr} \tag{3.23}$$

The above approximation is invalid for particles that stop inside of the detector, or for particles with energies such that the LET change inside of the detector is significant.

The integral in the denominator of eq. 3.23 is the total energy deposited by the HCP. Assuming that the energy transfered by the HCP is mainly through excitations and ionizations, producing delta rays, and that the delta rays do not have enough energy to escape the detector's volume, the total energy deposited can be approximated as the L_∞ and the integral in the denominator is equal to the L_∞ of the incident HCP calculated in the detector's material (index m), L_∞^m.

In eq. 3.23, the function $f_X[D(r)]$ is determined experimentally through dose response measurements with the appropriate test radiation that mimics as closely as possible the

delta ray spectrum produced by the primary HCP. The factor $\eta_{\delta,\gamma}$ depends on the energy spectrum of secondary electrons and can be determined measuring the energy response to photon radiation. Chapter 8 presents discussions of the test radiation and determination of the energy dependent factor $\eta_{\delta,\gamma}$. Different models, simulation or experimental data provides the $D(r)$. Chapters 4 and 5 present different approaches in the determination of $D(r)$.

CHAPTER 4

ANALYTICAL MODELING OF RADIAL DOSE DISTRIBUTION

A variety of models describes the RDD created by the passage of HCPs through matter. This chapter presents some of the models that are relevant to this work, including the models of Chatterjee and Schaefer (Chatterjee and Holley, 1993; Chatterjee and Schaefer, 1976), Butts and Katz (Butts and Katz, 1967; Hansen and Olsen, 1984; Chunxiang et al., 1985; Zhang et al., 1994), Waligórski *et al.* (Waligórski et al., 1986), Fageeha *et al.* (Fageeha et al., 1993), Kiefer and Straaten (Kiefer and Straaten, 1986), and Geiß *et al.* (Geiß et al., 1998; Krämer, 1995).

The main differences among the models are: the Chatterjee and Schaefer model simply assumes that the RDD is proportional to r^{-2}, where r is the radial distance from the path of the incident HCP, whereas the Butts and Katz, Waligórski *et al.*, Fageeha *et al.*, and Kiefer and Straaten models use Rutherford's single differential cross-section (SDCS) (Butts and Katz, 1967) to describe the number of secondary electrons produced by the HCP. Finally, the Geiß *et al.* model is a parameterization of Monte Carlo calculations of RDDs performed by Krämer (1995).

4.1 CHATTERJEE AND SCHAEFER MODEL

HCPs transfer energy mainly through collisions with electrons of the medium. Glancing collisions transferring small amounts of energy are much more frequent than close collisions transferring large amounts of energy. Thus, the Chatterjee and Schaefer model suggests an approximate equipartition of the total energy loss between glancing and close collisions (Chatterjee and Schaefer, 1976). The core is defined by them as the central re-

gion of the track where glancing and close collisions prevail. In the core region the density of energy deposition is very high. The core of the track is surrounded by a region called penumbra where secondary electrons are the main event of energy deposition.

The equipartition of energy suggested by the Chatterjee and Schaefer model assigns half of the total energy loss to glancing collisions and the other half to close collisions. Glancing collisions are responsible for excitations and close collisions for ionizations. The two types of collisions occur in the core region. On the other hand, only ionizations occur in the penumbra region. Therefore, half or more of the energy loss by the incident particle is in the core region.

$$\begin{cases} \text{Excitation} \longrightarrow \text{core} = L_{\infty}^{m}/2 \\ \text{Ionization} \longrightarrow \text{core and penumbra} = L_{\infty}^{m}/2 \end{cases}$$

where L_{∞}^{m} is the unrestricted total linear energy transfer in the material of the detector (index m) by the incident particle.

Considering a cylindrical geometry, the total energy loss due to excitation in an infinitesimal concentric cylindrical layer can be written as

$$\frac{L_{\infty}^{m}}{2} = \rho_m \int_0^{r_c} D_{exc}(r)\ 2\pi r\ dr \tag{4.1}$$

where $D_{exc}(r)$ is the radial dose due to excitation, and ρ_m is the density of the medium. The Chatterjee and Schaefer model assumes that in the core the radial dose is constant, $D_{exc}(r) = D_{exc}^{c}$. Thus, the integral of eq. 4.1 can be solved:

$$D_{exc}^{c} = \frac{L_{\infty}^{m}/2}{\pi r_c^2 \rho_m} \tag{4.2}$$

The core and penumbra regions share the total energy loss due to ionizations. For a

charged particle traveling a distance dz

$$\frac{L_{\infty}^{m}}{2} = \rho_m \int_0^{r_c} D_{ion}(r)\ 2\pi r\ dr + \rho_m \int_{r_c}^{R_{Max}} D_{ion}(r)\ 2\pi r\ dr \tag{4.3}$$

where $D_{ion}(r)$ is the radial dose due to ionizations, and r_c and R_{Max} are the core and penumbra radius, respectively. Considering the radial dose constant in the core, $D_{ion}(r) = D_{ion}^{c}$. Chatterjee and Schaefer (1976) then assume that the radial dose in the penumbra due to ionization decreases with r^2, thus:

$$D_{ion}(r) = \begin{cases} D_{ion}^{c}, & r < r_c \\ D_{ion}^{c}\dfrac{r_c^2}{r^2}, & r_c < r < R_{Max} \end{cases} \tag{4.4}$$

So that eq. 4.3 gives:

$$\begin{aligned} \frac{L_{\infty}^{m}}{2\rho_m} &= D_{ion}^{c} \int_0^{r_c} 2\pi r\ dr + D_{ion}^{c} \int_{r_c}^{R_{Max}} \frac{r_c^2}{r^2}\ 2\pi r\ dr \\ \frac{L_{\infty}^{m}}{2\rho_m} &= \pi r_c^2\ D_{ion}^{c} + 2\pi r_c^2 D_{ion}^{c} \ln\frac{R_{Max}}{r_c} \\ D_{ion}^{c} &= \frac{L_{\infty}^{m}/2}{\pi r_c^2 \rho_m \left(1 + 2\ln\frac{R_{Max}}{r_c}\right)} \end{aligned} \tag{4.5}$$

The radial dose due to ionization can be written as:

$$D_{ion}(r) = \begin{cases} \dfrac{L_{\infty}^{m}/2}{\pi r_c^2 \rho_m \left(1 + 2\ln\frac{R_{Max}}{r_c}\right)}, & r < r_c \\ \dfrac{L_{\infty}^{m}/2}{\pi r^2 \rho_m \left(1 + 2\ln\frac{R_{Max}}{r_c}\right)}, & r_c < r < R_{Max} \end{cases} \tag{4.6}$$

Chatterjee and Schaefer (1976) determine the contribution of the radial dose in the core due to ionizations and excitations as:

$$D_c = D_{exc}^{c} + D_{ion}^{c} \tag{4.7}$$

Using eq. 4.2 and eq. 4.6 we obtain:

$$D_c = \frac{L_\infty^m/2}{\pi r_c^2 \rho_m} + \frac{L_\infty^m/2}{\pi r_c^2 \rho_m \left(1 + 2\ln\frac{R_{Max}}{r_c}\right)} \tag{4.8}$$

Chatterjee and Schaefer (1976) assign the events of energy deposition in the penumbra to ionizations only. So that

$$D_p(r) = \frac{L_\infty^m/2}{\pi r^2 \rho_m \left(1 + 2\ln\frac{R_{Max}}{r_c}\right)} \tag{4.9}$$

The next step is to present expressions for the radius of the core and penumbra regions. Chatterjee and Schaefer (1976) define the radius of the core as the region where the primary particle energy loss causes excitations of the surrounding atoms. The core radius is equal to the Bohr's adiabatic limit region where electrons of the medium create an electric field directed against the motion of the primary particle Chatterjee and Holley (1993); Bohr (1948):

$$r_c = \frac{v}{\Omega_p} \tag{4.10}$$

where v is the velocity of the incident particle and Ω_p is the plasma oscillation frequency, which is given by

$$\Omega_p = \sqrt{\frac{4\pi N_e e^2}{m_e}} = c\sqrt{4\pi N_e r_e} \tag{4.11}$$

where N_e is the density of electrons in the medium[1], and e, m_e and $r_e = 2.8179 \times 10^{-13}$ cm are the charge, mass and classical radius of the electron. The plasma oscillation frequency is the electrostatic oscillation frequency of the medium in response to a small charge displacement.

[1] In water and Al_2O_3 the density of electrons is 3.34×10^{23} electrons/cm^3 and 1.17×10^{24} electrons/cm^3, respectively.

Thus, the final expression for the core radius is:

$$r_c = 5.314 \times 10^{12} \sqrt{N_e}\, \beta \quad \text{(nm)} \tag{4.12}$$

where $\beta = v/c$ is the relative speed of the incident particle with respect to the speed of light in vacuum, and N_e is the electron density of the material given in units of electrons/cm^3.

Chatterjee and Holley (1993) define the penumbra radius by the empirical relation

$$R_{Max} = \frac{3.85 \times 10^5}{\rho_m}\, \beta^{2.7} \quad \text{(nm)} \tag{4.13}$$

where $\beta = v/c$ is the relative speed of the primary particle with respect to the speed of light c, and ρ_m is the density of the detector given in units of g/cm^{-3}. Chatterjee and Schaefer (1976) determined the empirical relation given by eq. 4.13 by fitting range of electrons obtained through scattering theory and diffusion models (Chatterjee et al., 1973; Chatterjee and Schaefer, 1976).

Eq. 4.8 and eq. 4.9 together with eq. 4.12 and eq. 4.13 are the expressions to calculate the RDD around a HCP track according to the Chatterjee and Schaefer model. We summarize them as:

$$D(r) = \frac{1.602 \times 10^5}{\rho_m} \begin{cases} \dfrac{L_\infty^m/2}{\pi r_c^2} + \dfrac{L_\infty^m/2}{\pi r_c^2 \left(1 + 2\ln \frac{R_{Max}}{r_c}\right)}, & r < r_c = 5.314 \times 10^{12} \sqrt{N_e}\, \beta \\ \dfrac{L_\infty^m/2}{\pi r^2 \left(1 + 2\ln \frac{R_{Max}}{r_c}\right)}, & r_c < r < R_{Max} = \dfrac{3.85 \times 10^5}{\rho_m}\, \beta^{2.7} \end{cases} \tag{4.14}$$

where L_∞^m, ρ_m, and N_e must be in units of keV/μm, g/cm^{-3}, and cm^{-3}, respectively, so that $D(r)$ is in Gy, and r, r_c, and R_{Max} in nm.

Figure 4.1 shows RDDs around the path of ions with different kinetic energies and atomic numbers, but with similar LET. The core radius depends on the density of electrons of the medium and on the velocity of the primary particle (eq. 4.12), and the penumbra

radius depends only on the velocity of the primary particle (eq. 4.13). Therefore, larger kinetic energies of the incident particles produce a larger core and penumbra radii. In the Chatterjee and Schaefer model, the core and penumbra radii are independent of the charge of the incident particle. The discontinuity in the interface between the core and penumbra regions was introduced for conducting the analytical process. Chatterjee and Schaefer (1976) state that there is no well defined border between the two regions.

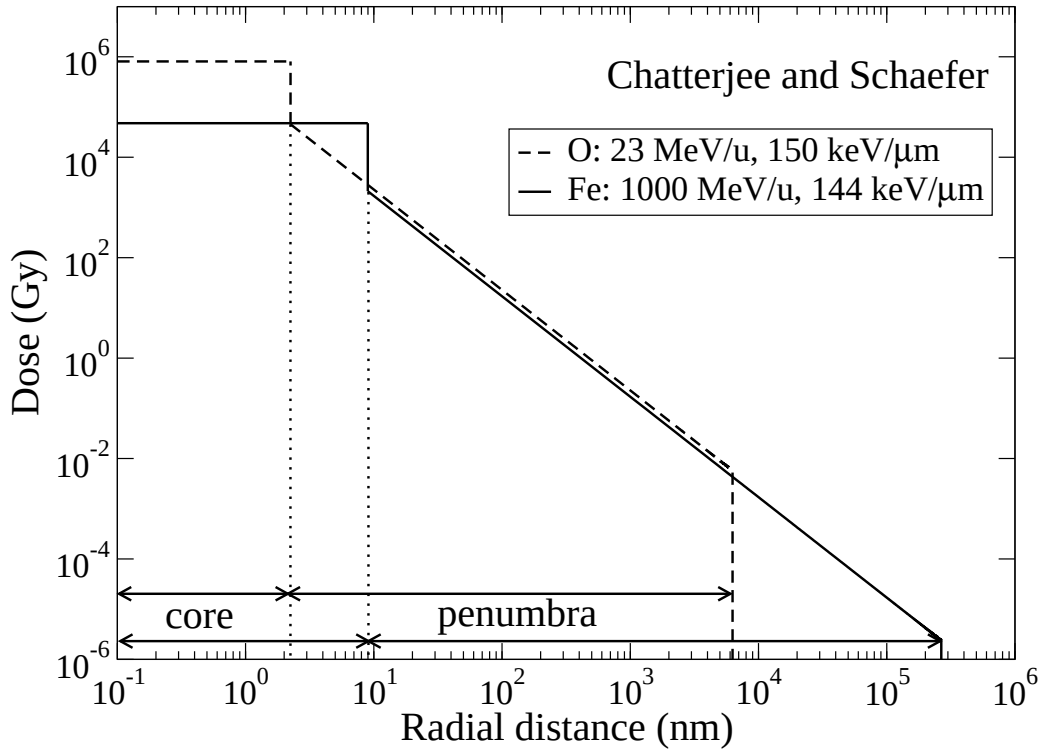

Figure 4.1: Chatterjee and Schaefer RDD in water (eq. 4.14) around the path of oxygen (23 MeV/u) and iron (1000 MeV/u). The particles have approximately the same LET.

The problem with the Chatterjee and Schaefer model is that it is based on the equipartition of energy where half of the energy is deposited through excitation and the other half through ionization. However, recent publications indicate that only (5-10) % of the energy loss produces excitations for primary particles in the range from 0.5 MeV/u up to 100 MeV/u (IAEA, 1995).

4.2 BUTTS AND KATZ MODEL

Butts and Katz model uses Rutherford's SDCS for production of secondary electrons (Mott, 1929; Bradt and Petters, 1948; ICRU, 1995). Rutherford's secondary electron distribution formula gives the number of secondary electrons per unit of path length having energies in the interval from w to $w + dw$, produced by an incident ion of effective charge[2] Z^* moving with speed βc

$$dn = \frac{2\pi N_e e^4 Z^{*2}}{m_e c^2 \beta^2} \frac{dw}{(w+I)^2} \tag{4.15}$$

where m_e and e are the electron mass and charge, N_e is the density of electrons in the material, I is the mean ionization potential of the material, c is the speed of light and $\beta = v/c$ is the speed of the incident particle with respect to the speed of light. Considering water as the target material

$$\frac{2\pi N_e e^4}{m_e c^2} = 8.5 \times 10^{-3} \ \frac{\text{keV}}{\mu\text{m}} \tag{4.16}$$

Electrons with energy w are ejected at an angle θ to the path of the incident moving ion where (Butts and Katz, 1967)

$$\cos^2\theta = \frac{w}{W} \tag{4.17}$$

Since eq. 4.15 is proportional to $1/w^2$, the majority of secondary electrons have energies much less than maximum electron energy W and therefore, have ejection angles approximately equal to 90°. Thus, to simplify the calculations Butts and Katz model assumes that all secondary electrons are ejected normally to the ion path (Butts and Katz, 1967).

Butts and Katz model uses the effective charge Z^* expression given by Barkas (1963), which is a parameterization of experimental data:

$$Z^* = Z[1 - \exp(-125\beta Z^{-2/3})] \tag{4.18}$$

[2]The nuclear charge is shielded by orbital electrons and outer electrons will see an reduced nuclear charge as the effective charge Z^* (Barkas, 1963).

where Z is the atomic number of the particle and β is the velocity of the particle relative to the speed of light in vacuum.

The Butts and Katz model range-energy relation for secondary electrons is a semi-empirical model obtained by fitting a power law relation to the experimental data (Butts and Katz, 1967; Chunxiang et al., 1985; Waligórski et al., 1986; Zhang et al., 1994). The range-energy relationship was fitted to the available experimental data of electron ranges in aluminum (Kobetich and Katz, 1968; Iskef et al., 1983; Kanter and Sternglass, 1962):

$$t = kw^{\alpha} \tag{4.19}$$

where t is the range of an electron of energy w and

$$k = 6 \times 10^{-6} \text{ g cm}^{-2} \text{ keV}^{-\alpha} \tag{4.20}$$

Two components characterizes the power law relation:

$$w < 1 \text{ keV} \Longrightarrow \alpha = 1.079$$

$$w > 1 \text{ keV} \Longrightarrow \alpha = 1.667$$

Differentiation of eq. 4.19 with respect to w leads

$$\frac{dt}{t} = \alpha \frac{dw}{w} \tag{4.21}$$

After penetrating a thickness r of material an electron of initial energy w and range t has a residual energy

$$kw_r^{\alpha} = t - r \tag{4.22}$$

Using eq. 4.19 we can write eq. 4.22 as

$$w_r = w\left(1 - \frac{r}{t}\right)^{\frac{1}{\alpha}} \tag{4.23}$$

Differentiating eq. 4.23 with respect to r, Butts and Katz model obtains the energy loss of electrons at a distance r from the path of the incident particle

$$-\frac{dw_r}{dr} = \frac{w}{\alpha t}\left(1 - \frac{r}{t}\right)^{\frac{1}{\alpha}-1} \tag{4.24}$$

An expression for the radial dose $D(r)$ deposited in a cylindrical shell of thickness dr at radius r from the path of the incident ion can be written as (Waligórski et al., 1986)

$$D(r) = \frac{1}{2\pi r dr \rho_m}\int_0^W \left(-\frac{dw_r}{dr}\right) dr \frac{dn}{dw} dw \tag{4.25}$$

where $2\pi r dr \rho_m$ is the volume of the shell, $-dw_r/dr$ is the energy loss, dn/dw is the number of electrons per path length with energy dw,

$$W = 2m_e c^2 \frac{\beta^2}{1-\beta^2} \tag{4.26}$$

is the maximum energy of a secondary electron in a head-on collision and

$$kw_0^\alpha = r; \quad kI^\alpha = r_0; \quad kW^\alpha = R_{Max}; \tag{4.27}$$

where I is the ionization potential of the material, R_{Max} is the maximum distance a delta ray can travel perpendicular to the path of the incident HCP, and r_0 is the distance perpendicular to the path of the incident HCP a delta ray of energy I can travel. Waligórski et al. (1986) considered the ionization potential I to be equal to 10 eV, so that $r_0 = 0.426/\rho_m$ nm, where ρ_m is given in units of g/cm^{-3}. Using eq. 4.15 and 4.23 the radial dose $D(r)$

can be written as

$$D(r) = \frac{N_e e^4}{\alpha m_e c^2 \rho_m} \frac{Z^{*2}}{\beta^2} \frac{1}{r} \int_{w_0}^{W} \frac{w}{t} \left(1 - \frac{r}{t}\right)^{1/\alpha - 1} \frac{dw}{(w+I)^2} \tag{4.28}$$

To solve eq. 4.28 we set the ionization potential $I = 0$. Later on, the bound electron case is artificially included. Thus, taking $I = 0$ and using equation 4.21 we get

$$D(r) = \frac{N_e e^4}{\alpha^2 m_e c^2 \rho_m} \frac{Z^{*2}}{\beta^2} \frac{1}{r} \int_{r}^{R_{Max}} \left(1 - \frac{r}{t}\right)^{1/\alpha - 1} \frac{dt}{t^2} \tag{4.29}$$

Substituting

$$y = \frac{r}{t} \quad \text{and} \quad \frac{dt}{t^2} = -\frac{dy}{r}; \tag{4.30}$$

$$\begin{aligned} D(r) &= -\frac{N_e e^4}{\alpha^2 m_e c^2 \rho_m} \frac{Z^{*2}}{\beta^2} \frac{1}{r} \int_{1}^{r/R_{Max}} (1-y)^{1/\alpha - 1} \frac{dy}{r} \\ &= \frac{N_e e^4}{m_e c^2 \rho_m} \frac{Z^{*2}}{\alpha \beta^2} \frac{1}{r} \left[\frac{\left(1 - \frac{r}{R_{Max}}\right)^{1/\alpha}}{r} \right] \end{aligned} \tag{4.31}$$

The transition from the free ($I = 0, r_0 = 0$) to the bound ($r_0 = kI^\alpha$) electron case is made by replacing r and R_{Max} within the final bracket by $r + r_0$ and $R_{Max} + r_0$, respectively. So that

$$D(r) = \frac{N_e e^4}{m_e c^2 \rho_m} \frac{Z^{*2}}{\alpha \beta^2} \frac{1}{r} \left[\frac{\left(1 - \frac{r+r_0}{R_{Max}+r_0}\right)^{1/\alpha}}{r + r_0} \right] \tag{4.32}$$

If ρ_m and N_e are given in g/cm^{-3} and cm^{-3}, respectively, $D(r)$ is given in Gy and r, r_0, and R_{Max} in nm, and eq. 4.32 becomes

$$D(r) = 6.50 \times 10^{-22} \frac{N_e}{\rho_m} \frac{Z^{*2}}{\alpha \beta^2} \frac{1}{r} \left[\frac{\left(1 - \frac{r+r_0}{R_{Max}+r_0}\right)^{1/\alpha}}{r + r_0} \right], \quad r_0 < r < R_{Max} \tag{4.33}$$

where

$$\alpha = \begin{cases} 1.079, & \text{for } r_0 = 0.426/\rho_m < r < 61.3/\rho_m \\ 1.667, & \text{for } 61.3/\rho_m < r < R_{Max} = \frac{6.24\times10^6}{\rho_m}\left(\frac{\beta^2}{1-\beta^2}\right)^{1.667} \end{cases}$$

Figure 4.2 shows the RDD in water around the path of ions with different kinetic energies and atomic numbers, but with similar LET.

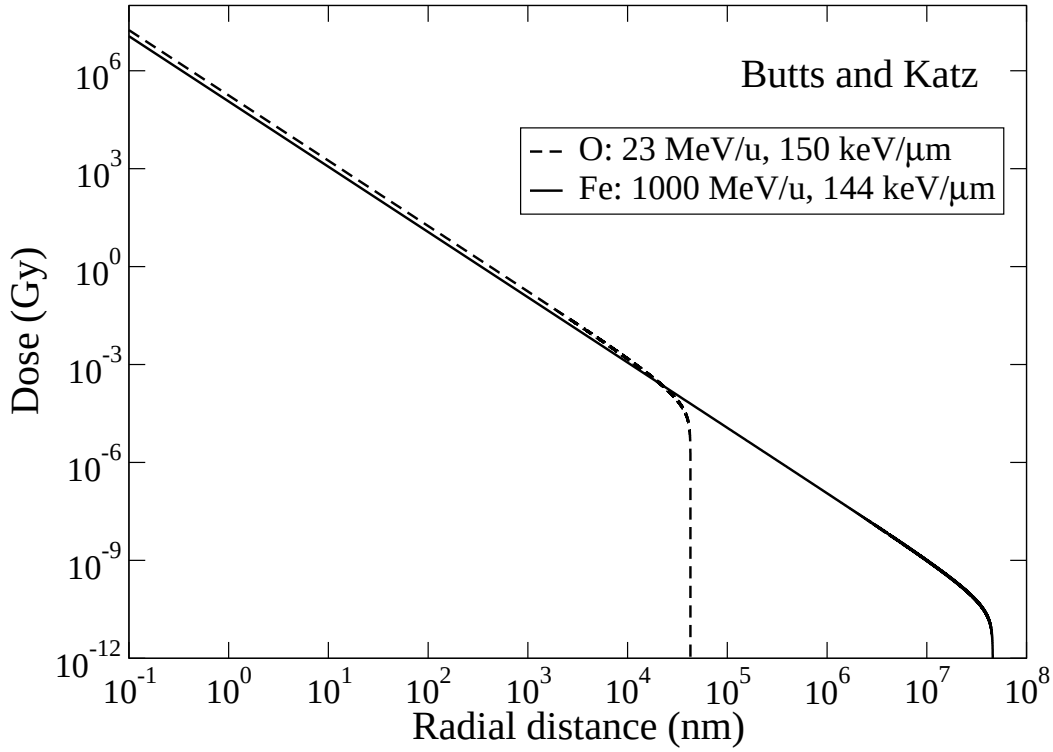

Figure 4.2: Butts and Katz RDD in water (eq. 4.33) around the path of oxygen (23 MeV/u) and iron (1000 MeV/u). The particles have approximately the same LET. The ionization potential used on the plots was $I = 10$ eV.

4.2.1 MODIFICATIONS OF BUTTS AND KATZ MODEL

Waligórski et al. (1986) and Fageeha et al. (1993) modified Butts and Katz expression (eq. 4.33) by an arbitrary function of the form:

$$D_{cor}(r) = D(r)[1 + K(r)] \tag{4.34}$$

Waligórski *et al.* and Fageeha *et al.* modifications attempted to correct the Butts and

Katz model to fit the experimental and Monte Carlo data in the region of small radius and also to correct the prediction of LET when the distribution of dose is radially integrated. This section describes the Waligórski *et al.* and the Fageeha *et al.* corrections.

WALIGÓRSKI *ET AL.* CORRECTION

Waligórski *et al.* used the following function

$$K(r) = A\left(\frac{r-B}{C}\right)\exp\left(-\frac{r-B}{C}\right) \tag{4.35}$$

where r is in nanometers and

(a) for $r > B = 0.1$ nm, $C = 1.5$ nm + 5 nm $\times\ \beta$ and

$$A = 8 \times \beta^{1/3}, \quad \text{for } \beta < 0.03$$

or

$$A = 19 \times \beta^{1/3}, \quad \text{for } \beta > 0.03$$

(b) for $r < B = 0.1$ nm

$$K(r) = 0$$

Figure 4.3 compares the RDD from Butts and Katz model with the RDD from Waligórski *et al.* model. The Waligórski *et al.* model presents a hump at small radial distances and are equal to the Butts and Katz model at larger radius. This hump is observed in the experimental data of radial dose distribution (Waligórski et al., 1986). Another important feature is that the Waligórski *et al.* model improves the prediction of incident particle $L_{\infty}^{H_2O}$.

$$L_{\infty} = \rho_m \int_{r_0}^{R_{Max}} D(r)\ 2\pi r dr \tag{4.36}$$

Table 4.1 presents the comparison of $L_{\infty}^{H_2O}$ between the results given by Energy vs.

LET vs. Range calculator version 1.24[3] (Zajic) and different RDD models. Note that the $L_{\infty}^{H_2O}$ predictions of Butts and Katz model is around 60% below the correct value. The Waligórski *et al.* model improves the difference for $L_{\infty}^{H_2O}$ around 15% below the correct value.

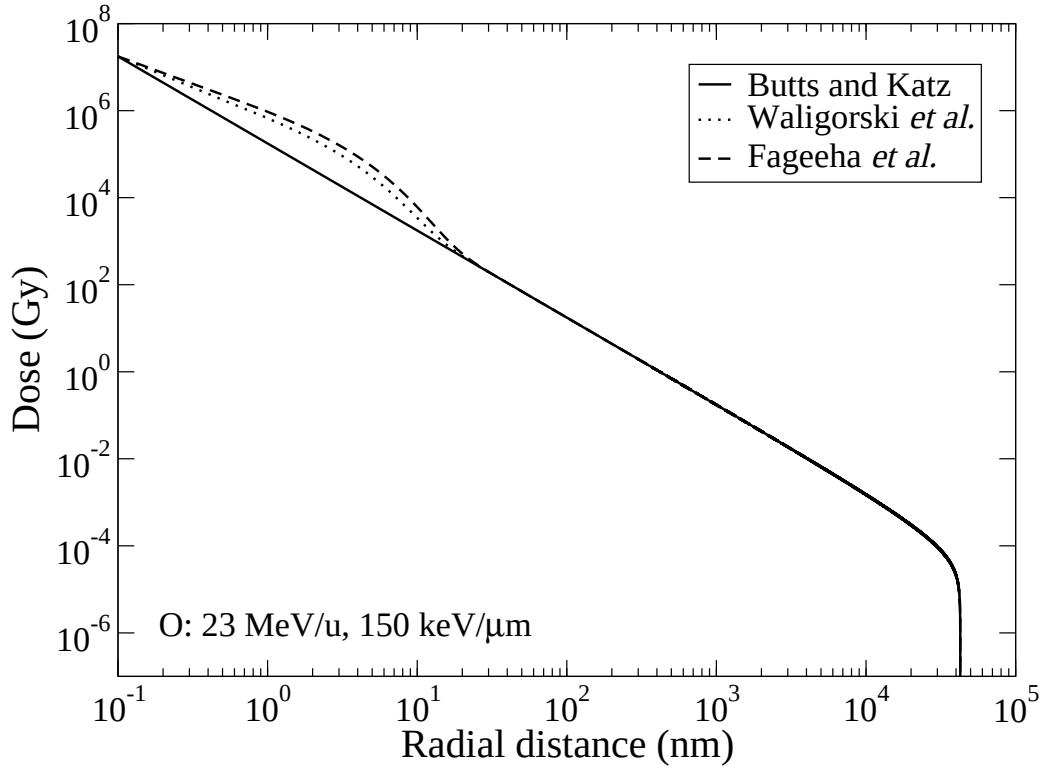

Figure 4.3: RDD in water around the path of oxygen (23 MeV/u). The full line is the Butts and Katz model, dotted line is the Waligórski *et al.* model and dashed line is the Fageeha *et al.* model.

FAGEEHA *ET AL.* **CORRECTION**

Fageeha *et al.* improved Butts and Katz model using a correction function of the form

$$K(r) = A\beta^B\,(r - 0.1)\exp\left(-\frac{r}{C}\right) \tag{4.37}$$

[3]The program provided by Brookhaven National Laboratory calculates L_{∞} and range for different materials, particles and energies.

Table 4.1: $L_{\infty}^{H_2O}$ determined using the Brookhaven National Laboratory (BNL) Energy vs. LET vs. Range calculator version 1.24 program and different RDD models.

		$L_{\infty}^{H_2O}$ (keV/μm)			
Z	Energy (MeV/u)	BNL	Butts and Katz	Waligórski *et al.*	Fageeha *et al.*
1	230	0.41	0.15	0.36	0.45
1	70	0.96	0.31	0.78	1.06
2	150	2.18	0.75	1.85	2.40
6	400	10.96	3.96	9.65	11.9
6	290	12.97	4.62	11.3	14.1
8	400	19.48	7.03	17.2	21.1
10	400	30.44	11.0	26.8	32.9
26	500	186.3	67.7	164	200
54	290	1047	371	909	1135

where r is in nanometers, $B = 0.215$, $C = 3.127 - 0.434\beta$, and

$$A = \begin{cases} 0, & \beta < 0.0081 \\ 112\beta - 0.899, & 0.0081 < \beta < 0.091 \\ 0.674\beta + 9.21, & \beta > 0.091 \end{cases}$$

Figure 4.3 compares Butts and Katz, Waligórki *et al.* and Fageeha *et al.* models. Fageeha *et al.* model presents the same hump at small radius observed in the Waligórki *et al.* model, and reduces to the Butts and Katz model at larger radius. The Fageeha *et al.* model improves the predictions of $L_{\infty}^{H_2O}$ to around 6 % above the correct value (Table 4.1).

Although the Butts and Katz model agrees with the experimental data in the intermediate region of radial distances, the limitations are:

1. only energy deposition by secondary electrons is considered
2. energy deposition by excitations is not considered
3. the model agrees with $L_{\infty}^{H_2O}$ only after artificial correction using arbitrary functions
4. the model uses empirical data to obtain the range-energy relationship for electrons in aluminum

5. the fitted range-energy relation deviates from experimental data for high energy electrons, causing a wrong prediction for primary particles with total kinetic energy higher than approximately 300 MeV/u where the maximum secondary electron energy is around 800 keV

6. the model assumes that all delta rays are ejected normal to the ion's path. This approximation underestimates the dose around the center of the track

7. the Rutherford's SDCS for production of secondary electrons underestimates the experimental values. ICRU report 55 (ICRU, 1995) and chapter 5 discuss this issue.

4.3 KIEFER AND STRAATEN MODEL

Kiefer and Straaten model (Kiefer and Straaten, 1986) is based on the same assumptions made by Butts and Katz (1967):

1. heavy-ion produces secondary electrons in the exposed medium according to classical collision dynamics

2. the energy distribution of secondary electrons is proportional to the inverse of their initial energy

3. the range of the secondary electrons relates to their kinetic energy by a power law and the secondary electrons trajectories are straight lines

The angle between the direction of the primary HCP and secondary electron, θ, is given by (Kiefer and Straaten, 1986)

$$\sin^2\theta = \frac{1 - w_0/w_{max}}{1 - w_0/2m_e c^2} \tag{4.38}$$

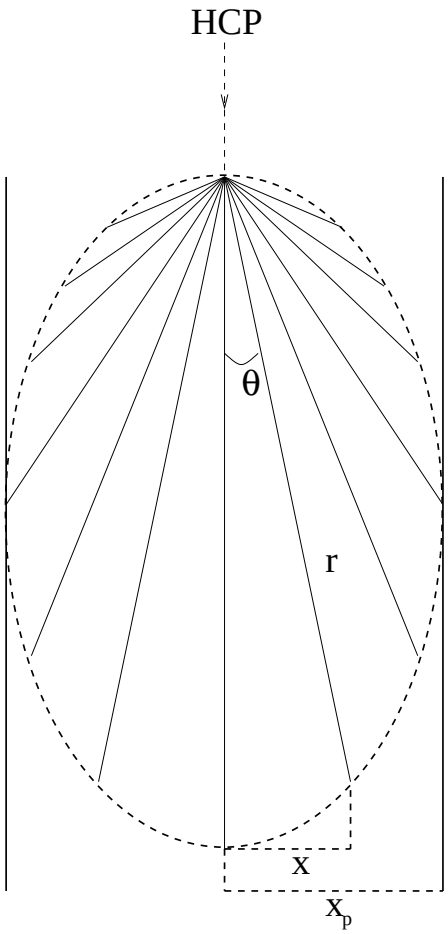

Figure 4.4: Illustration of angular distributions and ranges of secondary electrons produced by HCPs (adapted from (Kiefer and Straaten, 1986)).

where w_0 is the starting energy of the secondary electron and w_{max} is the maximum value the starting energy w_0 can take. For non-relativistic cases w_{max} is:

$$w_{max} = \frac{4AE(1 + E/2Mc^2)}{(1 + A)^2 + 2AE/Mc^2} \tag{4.39}$$

where $A = m_e/M$, E is kinetic energy of the primary particle, and m_e and M are the electron and HCP masses, respectively. For the non-relativistic case $E << Mc^2$ and since $M >> m_e$, eq. 4.39 can be approximated as

$$w_{max} = \frac{4m_e}{M}E \tag{4.40}$$

Kiefer and Straaten (1986) determine the relationship between the range r of the secondary electrons and energy by fitting range-energy data for electrons in water from ICRU report 16 (ICRU, 1970) through:

$$\rho_m r = k w^{\alpha} \tag{4.41}$$

where ρ_m is the density of the medium in g/cm^3, $k = 5.26 \times 10^{-6}$ g/cm^2 keV$^{-\alpha}$ and $\alpha = 1.70$, so that r is given in nanometers. Kiefer and Straaten (1986) recommend using the k and α values for electron energies in the interval from 200 eV up to 100 keV (Kiefer and Straaten, 1986).

The perpendicular distance from the center of the HCP path, x_0, of a secondary electron of starting energy w_0 is given by (Figure 4.4)

$$x_0 = r \sin\theta \tag{4.42}$$

Using eq. 4.38 and eq. 4.41:

$${x_0}^2 = k^2 {w_0}^{2\alpha} \frac{1 - w_0/w_{max}}{1 - w_0/2m_e c^2} \tag{4.43}$$

Differentiation of eq. 4.43 with respect to w_0 determines the penumbra radius x_p, the maximum perpendicular distance that an electron can travel from the path of the primary HCP. Kiefer and Straaten (1986) showed that the difference between x_p calculated non-relativistically (i.e., $w_{max} << 2m_e c^2$) and relativistically for particles with energies up to 1000 MeV/u is only about 5 %. Thus, Kiefer and Straaten (1986) considered the non-relativistic case and obtained:

$$x_p = k \left(\frac{2\alpha}{2\alpha + 1} \right)^{\alpha} \left(\frac{1}{2\alpha + 1} \right)^{\frac{1}{2}} w_{max}^{\alpha} \tag{4.44}$$

where the general numeric expression is

$$x_p = \frac{6.16 \times 10^1}{\rho_m} E^{1.7} \tag{4.45}$$

where x_p is given in nm, providing E and ρ_m are in MeV/u and g/cm^3, respectively.

Using geometrical considerations Kiefer and Straaten (1986) determine the residual energy at a radial distance x from the path of the primary particle (Figure 4.5):

$$\sin\theta = \frac{x_0 - x}{r'} \tag{4.46}$$

Using the range-energy relationship (eq. 4.41)

$$\frac{k w^{\alpha}}{\rho_m} \sin\theta = x_0 \left(1 - \frac{x}{x_0} \right) \tag{4.47}$$

where w is the residual energy of an secondary electron at distance x which has a range r'.

$$\begin{aligned} w^{\alpha} &= \frac{\rho_m x_0}{k \sin\theta} \left(1 - \frac{x}{x_0} \right) \\ &= \frac{\rho_m r}{k} \left(1 - \frac{x}{x_0} \right) \\ &= {w_0}^{\alpha} \left(1 - \frac{x}{x_0} \right) \end{aligned} \tag{4.48}$$

where r is the range of a secondary electron with initial energy w_0 (eq. 4.41). Finally, Kiefer and Straaten model obtains:

$$w(x, w_0) = w_0 \left(1 - \frac{x}{x_0}\right)^{\frac{1}{\alpha}} \tag{4.49}$$

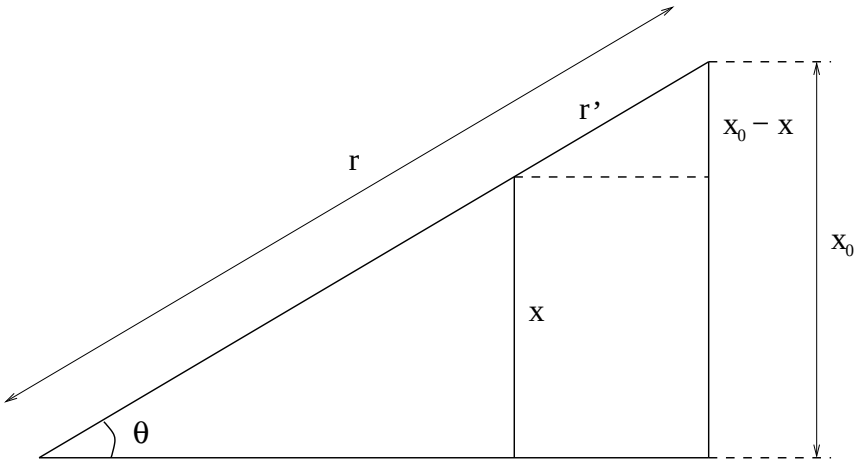

Figure 4.5: Geometrical considerations for derivation of eq. 4.49. θ is the angle between the primary HCP and the secondary electron, x_0 is the projection of the maximum distance perpendicular to the path of the primary HCP that a secondary electron of initial energy w_0 can travel, and r is the range of a secondary electron with initial energy w_0.

The total energy $w(x)$ deposited between x and x_p is determined integrating over the contributions of all electrons that have radial ranges x_0 larger than x

$$w(x) = \int_{w_{0_1}}^{w_{0_2}} w(x, w_0) f(w_0)\, dw_0 \tag{4.50}$$

where $f(w_0)\ dw_0$ is the distribution of secondary electron starting energies, assumed to have the form given by Butts and Katz (1967), which is the Rutherford's formula for production of secondary electrons as previously discussed:

$$f(w_0)\, dw_0 = \frac{2\pi N_e e^4}{m_e c^2} \frac{Z^{*2}}{\beta^2} \frac{1}{{w_0}^2}\, dw_0 \tag{4.51}$$

N_e is density of electron in the medium, e is the electron charge, $m_e c^2$ is the electron rest energy, Z^* is the effective charge of the primary particle (eq. 4.18), and $\beta = v/c$ is the

speed of the primary particle relative to the speed of light in vacuum. Therefore,

$$w(x) = \frac{2\pi N_e e^4}{m_e c^2} \frac{Z^{*2}}{\beta^2} \int_{w_{0_1}}^{w_{0_2}} \frac{1}{w_0} \left(1 - \frac{x}{x_0}\right)^{\frac{1}{\alpha}} \, dw_0 \tag{4.52}$$

Differentiating eq. 4.52 with respect to x:

$$-\frac{dw(x)}{dx} = \frac{2\pi N_e e^4}{m_e c^2} \frac{Z^{*2}}{\beta^2} \int_{w_{0_1}}^{w_{0_2}} \frac{1}{\alpha w_0 x_0} \left(1 - \frac{x}{x_0}\right)^{\frac{1}{\alpha}-1} \, dw_0 \tag{4.53}$$

The limits w_{0_1} and w_{0_2} are determined numerically as the roots of eq. 4.43 for $x_0 = x$. Therefore, the integration of eq. 4.53 can only be performed numerically.

The dose as function of radial distance is given by

$$D(x) = \frac{1}{2\pi\rho_m x} \frac{dw(x)}{dx} \tag{4.54}$$

where ρ_m is the density of the medium, and x is the radial distance from the path of the primary HCP.

Results of numerical calculations showed that the RDD follows $1/x^2$ dependence over many orders of magnitude. Thus, Kiefer and Straaten (1986) suggest that the functional dependence simply is

$$D(r) = 3.82 \times 10^{-22} \frac{N_e}{\rho_m} \frac{Z^{*2}}{\beta^2} \frac{1}{r^2}, \quad \text{for } 0.1 \text{ nm} < r < x_p = R_{Max} = \frac{6.16 \times 10^1}{\rho_m} E^{1.7} \tag{4.55}$$

where we changed the notation x to r, and $D(r)$ is in Gy and r in nm, providing the input parameters are in the following units: ρ_m in g/cm^3, N_e in cm^{-3}, and E in MeV/u.

Figure 4.6 shows the RDD in water around the path of ions with different kinetic energies and atomic numbers, but with similar LET. The differences between the two RDDs are in the maximum range of secondary electrons and in the magnitudes of the dose – the doses for the O 23 MeV/u beam are higher than the doses for the Fe 1000 MeV/u beam.

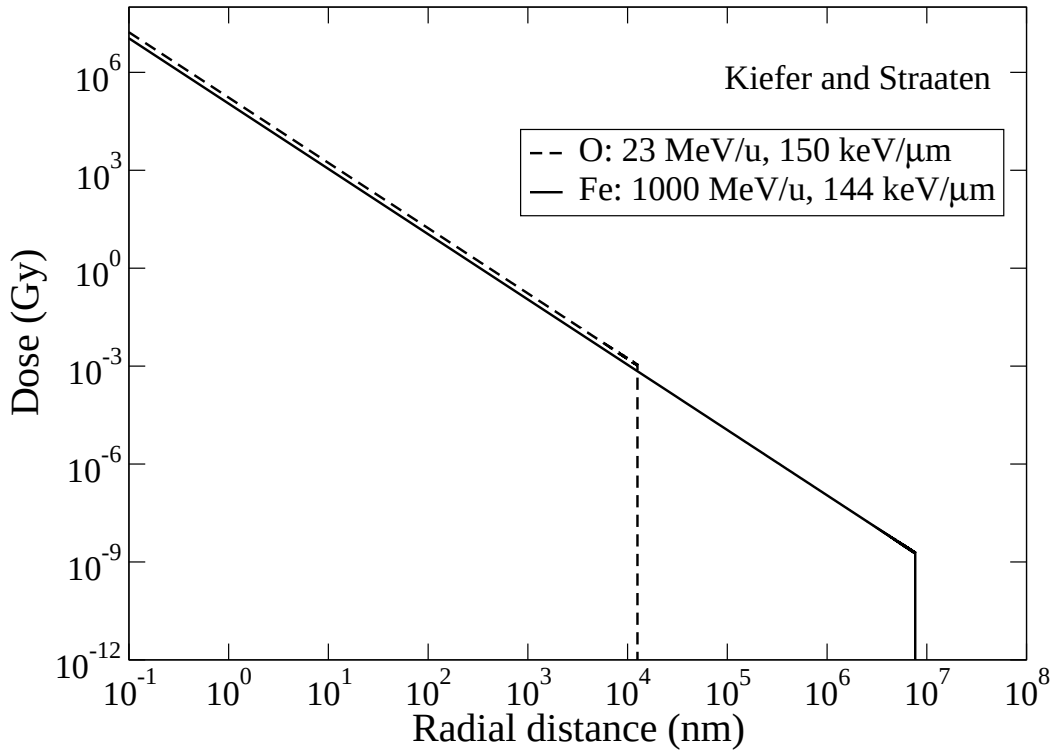

Figure 4.6: Kiefer and Straaten RDD in water (eq. 4.55) around the path of oxygen (23 MeV/u) and iron (1000 MeV/u). The particles have approximately the same LET.

The Kiefer and Straaten model is based on the Rutherford's SDCS for production of delta rays as in the Butts and Katz model. As discussed before, the Rutherford's formula considers only the energy loss by ionizations. The energy loss through excitations are not treated by the formalism. This influences the predictions of stopping powers. Other points that are not discussed by Kiefer and Straaten (1986) are the minimum radius of the track and how the deposited energy is shared between ionizations and excitations.

4.4 GEIß *ET AL.* MODEL

The Geiß *et al.* model (Geiß et al., 1998) is a parameterization of track structure calculations performed by Krämer (1995). Geiß et al. (1998), as did Chatterjee and Schaefer (1976), present both core and penumbra regions. The Monte Carlo calculations were pa-

rameterized as:

$$D(r) = \begin{cases} k, & r < r_c = 0.1 \text{ nm} \\ k\left(\frac{r_c}{r}\right)^2, & r_c < r < R_{Max} \end{cases} \tag{4.56}$$

where r_c is the core radius, R_{Max} is the maximum distance of delta rays, and k is a constant determined through the normalization of the RDD to the total energy loss per path length

$$2\pi \int_0^{R_{Max}} D(r) r dr = \frac{1}{\rho}\frac{dE}{dx} \tag{4.57}$$

The determination of R_{Max} is based on Monte Carlo calculations and is parameterized as:

$$\rho_m R_{Max} = 4 \times 10^{-5} W^{\frac{3}{2}} \tag{4.58}$$

where ρ_m is the density of the material, and W is the maximum energy of the delta ray given by eq. 4.26.

A final expression for Geiß *et al.* model is given by

$$D(r) = \frac{1.602 \times 10^5}{\rho_m} \begin{cases} \dfrac{L_\infty^m}{\pi r_c^2 \left(1 + 2\ln\frac{R_{Max}}{r_c}\right)}, & r < r_c = 0.1 \text{ nm} \\ \dfrac{L_\infty^m}{\pi r^2 \left(1 + 2\ln\frac{R_{Max}}{r_c}\right)}, & r_c < r < R_{Max} = \dfrac{1.31 \times 10^7}{\rho_m}\left(\dfrac{\beta^2}{1-\beta^2}\right)^{\frac{3}{2}} \end{cases} \tag{4.59}$$

where ρ_m and L_∞^m are in g/cm^{-3} and keV/μm, respectively, so that $D(r)$ is in Gy, and r and R_{Max} in nm.

Figure 4.7 shows the RDD in water around the path of ions with different kinetic energies and atomic numbers, but with similar LET. The differences between the two RDDs are in the maximum range of secondary electrons and in the magnitudes of the dose – the doses for the O 23 MeV/u beam are higher compared to the doses for the Fe 1000 MeV/u beam.

Geiß *et al.* model is a simplified parameterization of Monte Carlo RDD calculations.

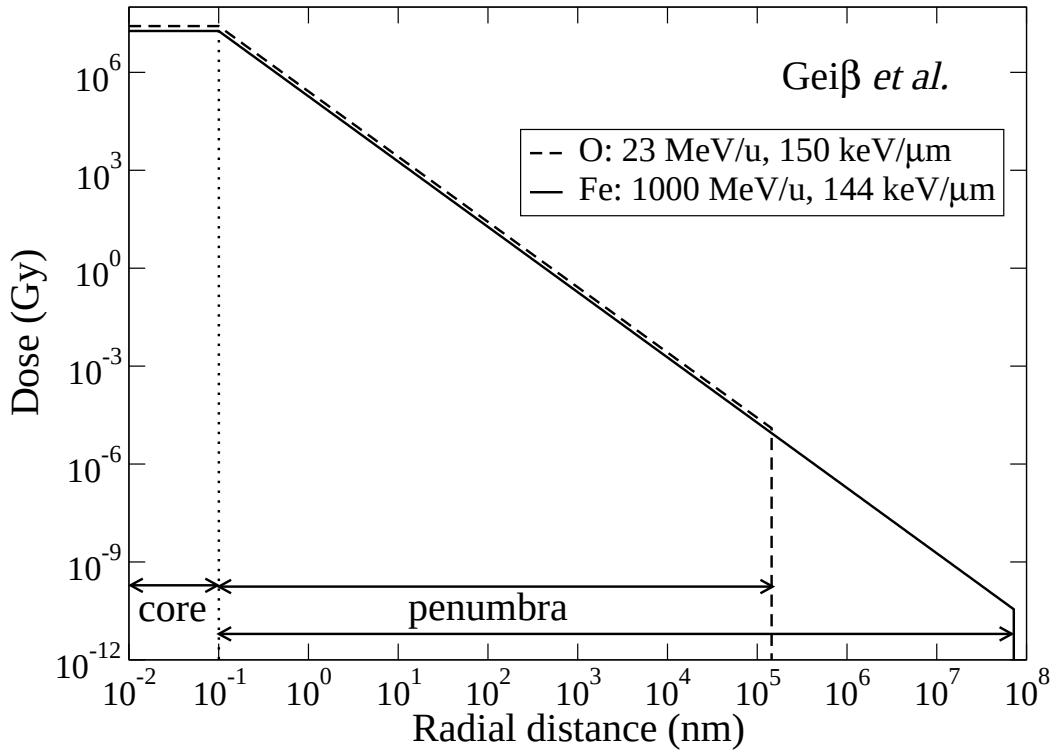

Figure 4.7: Geiß *et al.* RDD in water (eq. 4.56) around the path of oxygen (23 MeV/u) and iron (1000 MeV/u). The particles have approximately the same LET.

The size of the core is assumed to be constant and is independent on particle type and energy. Geiß *et al.* model arbitrarily chooses the core size equal to 0.1 nm.

4.5 SUMMARY OF ANALYTICAL MODELS OF RADIAL DOSE DISTRIBUTION

A common trend in the analytical models of RDD presented in this chapter is the approximated proportionality to r^{-2} in the region of intermediate radial distances from the path of the incident particle. For intermediate radial distances all the models agree with each other (Figure 4.8), and with the experimental data (Wingate and Baum, 1976).

On the other hand, for small radial distances of about a few nanometers the RDDs drastically differ from model to model (Figure 4.8). Lack of RDD data in such small distances makes impossible the verification of the model that best describes the data.

Another difference presented among the models is in the maximum radial distance a

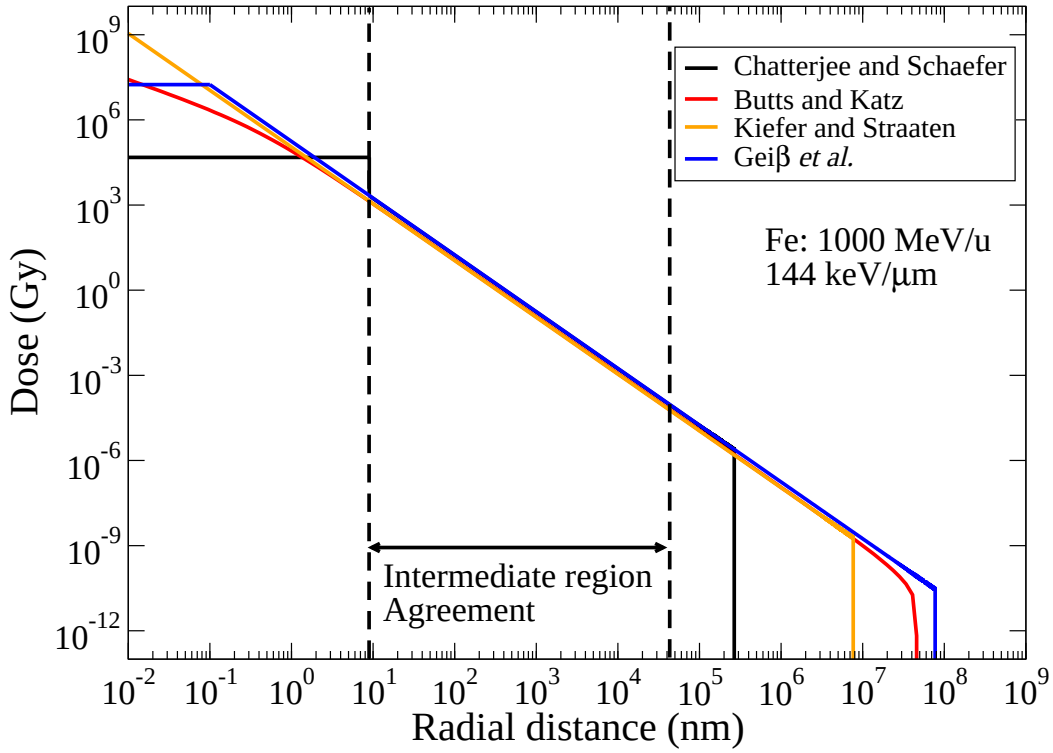

Figure 4.8: RDD in water around the path of iron (1000 MeV/u) for different RDD analytical models.

secondary electron can travel from the path of the incident particle (R_{Max}). For the same type of particle and energy, Chatterjee and Schaefer model gives the lowest R_{Max} and Geiß *et al.* model the largest R_{Max} (Figure 4.8).

Table 4.2 shows a summary of the main features of each model presented in this chapter. The Butts and Katz, Waligórski *et al.*, Fageeha *et al.*, and Kiefer and Straaten models assume Rutherford's SDCS for production of secondary electrons to derive the RDD formulas. The Chatterjee and Schaefer and Geiß *et al.* models assume the existence of the core region, where the RDD is constant; and the penumbra region, where the RDD is proportional to r^{-2}. In the Chatterjee and Schaefer model the core radius r_c is proportional to the speed of the incident particle in respect to the speed of light ($\beta = v/c$). On the other hand, with the Geiß *et al.* model the core radius is constant and equal to 0.1 nm for all types of particles and energies.

Chatterjee and Schaefer, Butts and Katz, Waligórski *et al.*, Fageeha *et al.*, and Kiefer

Table 4.2: Summary of the main parameters of different RDD models. r_c is the radius of the core region and R_{Max} is the maximum radial distance of a secondary electron. SDCS stands for single differential cross–section and $\beta = v/c$ is the speed of the incident particle with respect to the speed of light in vacuum.

Model	Assumption	r_c	R_{Max} (nm)
Chatterjee and Schaefer	$D(r) \propto \begin{cases} k, \ r \leqslant r_c \\ r^{-2}, \ r_c < r < r_p \end{cases}$	$\propto \beta$	$\propto \beta^{2.7}$
Butts and Katz	Rutherford's SDCS	–	$\propto \left(\frac{\beta^2}{1-\beta^2}\right)^{1.667}$
Waligórski *et al.*	Rutherford's SDCS	–	$\propto \left(\frac{\beta^2}{1-\beta^2}\right)^{1.667}$
Fageeha *et al.*	Rutherford's SDCS	–	$\propto \left(\frac{\beta^2}{1-\beta^2}\right)^{1.667}$
Kiefer and Straaten	Rutherford's SDCS	–	$\propto \left(\frac{1}{\sqrt{1-\beta^2}} - 1\right)^{1.7}$
Geiß *et al.*	$D(r) \propto \begin{cases} k, \ r \leqslant r_c \\ r^{-2}, \ r_c < r < r_p \end{cases}$	0.1 nm	$\propto \left(\frac{\beta^2}{1-\beta^2}\right)^{\frac{3}{2}}$

and Straaten models use empirical relations to calculate the maximum radial distance R_{Max} a secondary electron can travel from the path of the incident particle. On the other hand, Geiß *et al.* model uses parameterization of Monte Carlo calculations. Table 4.2 shows the dependence of R_{Max} with respect to $\beta = v/c$ for the models presented in this chapter.

It is important to mention that the RDD models presented in the previous sections are only a small sample of the available models in the literature. We choose to present Chatterjee and Schaefer, Butts and Katz, Waligórski *et al.*, Fageeha *et al.*, Kiefer and Straaten, and Geiß *et al.* models mainly because these models are common in the literature related to luminescence detectors, their expressions are compact and simple, and they agree with available experimental data.

CHAPTER 5

MONTE CARLO MODELING OF RADIAL DOSE DISTRIBUTION

Monte Carlo (MC) is a numerical stochastic[1] method used to find solutions of mathematical or physical problems. Specifically, for ionizing radiation interacting with matter, the method assumes that all probabilities (cross-sections) for elementary events in the life history of a particle are known. The MC method consists in following the primary particle and its secondaries throughout their life history. The elementary probabilities are used in each stage of the life history to determine the consecutive "state" of the particles until their energy is totally dissipated (Cashwell and Everett, 1959).

Among the multipurpose radiation MC codes, the most well known ones include GEANT4 (Agostinelli et al., 2003), FLUKA (Fassò et al., 2003, 2005), and MCNP/MCNPX (Boggs et al., 2005). This work uses GEANT4 version 8.1. We choose GEANT4 mainly because of its flexibility for experimental designing and the easy access to its physics documentation (Geant4-Collaboration, 2007b).

The interaction cross-sections with the medium dictate the stages of the life history of a particle interacting with matter. Thus, MC requires cross-section data and adequate physics models. This chapter presents GEANT4's relevant cross-sections and physics models used to determine the RDDs. Also, the results of the RDDs obtained using GEANT4 are presented and compared with the analytical models.

[1] Stochastic quantities are quantities which are subjected to random fluctuations.

5.1 SINGLE DIFFERENTIAL CROSS-SECTION FOR PRODUCTION OF SECONDARY ELECTRONS USED BY GEANT4

GEANT4 uses Bhabha (Bhabha, 1938), Massey and Corben (Rossi, 1952), and Oppenheimer *et al.* (Oppenheimer et al., 1940) single differential cross-sections (SDCS) for production of secondary electrons with energy in the interval T and $T + dT$ by hadrons (Geant4-Collaboration, 2007b):

$$\begin{aligned}
&\text{for spin 0} \quad \frac{d\sigma}{dT} = KZ\frac{Z^{*2}}{\beta^2 T^2}\left[1 - \beta^2\frac{T}{T_{max}}\right] \\
&\text{for spin 1/2} \quad \frac{d\sigma}{dT} = KZ\frac{Z^{*2}}{\beta^2 T^2}\left[1 - \beta^2\frac{T}{T_{max}} + \frac{T^2}{2E^2}\right] \\
&\text{for spin 1} \quad \frac{d\sigma}{dT} = KZ\frac{Z^{*2}}{\beta^2 T^2}\left[\left(1 - \beta^2\frac{T}{T_{max}}\right)\left(1 + \frac{T}{3Q_c}\right) + \frac{T^2}{3E^2}\left(1 + \frac{T}{2Q_c}\right)\right]
\end{aligned} \tag{5.1}$$

where Z is the atomic number of the medium, Z^* is the effective charge of the incident particle, β is the relativistic velocity of the incident particle, and Q_c and K are factors expressed as

$$Q_c = \frac{(Mc^2)^2}{m_e c^2}, \quad K = 2\pi r_e^2 m_e c^2$$

where M is the mass of the incident particle, m_e is the electron mass, r_e is the classical electron radius, and c is the speed of light in vacuum.

In eq. 5.1, T_{max}, the maximum energy transferable to free electrons, is calculated using classical collision theory for a head-on collision and is given by (Geant4-Collaboration, 2007b)

$$T_{max} = \frac{2m_e c^2(\gamma^2 - 1)}{1 + 2\gamma(m_e/M) + (m_e/M)^2} \tag{5.2}$$

where $\gamma = (1 - \beta^2)^{-\frac{1}{2}}$ is the relativistic factor. Eq. 5.2 does not consider effects of a mechanism know as Fermi-shuttle acceleration, which produces secondary electrons with energies higher than those obtained from two-body collision theory (Ohsawa et al., 2005b).

Note that when T is very small compared with the maximum transferable energy T_{max},

and with the factor Q_c, eq. 5.1 reduces to the classical expression known as the Rutherford's formula:

$$\frac{d\sigma}{dT} = KZ\frac{Z^{*2}}{\beta^2 T^2} \tag{5.3}$$

Thus, for small secondary electron energy compared to the energy of the incident particle, the SDCSs of different kinds of particles become identical and depend only on the energy T of the secondary electron, and on β of the primary particle (Rossi, 1952).

Ohsawa et. al (Ohsawa et al., 2005a,b; Sato et al., 2005) built an apparatus that allows measurements of the energy and angular distribution of secondary electrons with energies as low as 7 eV and as high as 10 keV. Such a device was used to measure double differential cross-sections (DDCS) for production of secondary electrons by 6 MeV/u and 10 MeV/u He^{+2} ions in water vapor. The author kindly provided his raw data, which we compare in Figure 5.1 with two SDCS models: (i) Rutherford's SDCS (eq. 5.3); and (ii) semi-empirical model by Rudd (ICRU, 1995; Rudd et al., 1992). Rudd's SDCS is only applicable for ten materials, including water vapor. Rudd et al. (1992) and ICRU report 55 (ICRU, 1995) present a detailed description of Rudd's and Rutherford's SDCSs. The SDCS experimental data present the oxygen KLL Auger peak at ~ 500 eV. The large SDCS for high energy electrons is attributed a mechanism known as Fermi-shuttle acceleration (Ohsawa et al., 2005b).

Figure 5.1 shows that Rutherford's SDCS underestimates the data. In fact, the disagreement between Rutherford's SDCS and data emphasizes the limitations of Rutherford's SDCS. Most of the multipurpose MC codes, including GEANT4, as well as Butts and Katz, Waligórski *et al.*, Fageeha *et al.*, and Kiefer and Straaten models of RDD, uses Rutherford's SDCS. The disagreement can be quantitatively presented through the calculation of the primary particle energy loss to medium by ionization, which is simply the integral of the single differential cross-section. The data give values of 0.193 MeV cm^2/mg, and 0.112 MeV cm^2/mg for the 6 MeV/u, and 10 MeV/u He^{+2} ions, respectively. Rutherford's SDCS gives 0.132 MeV cm^2/mg and 0.080 MeV cm^2/mg, respectively. A disagreement of about

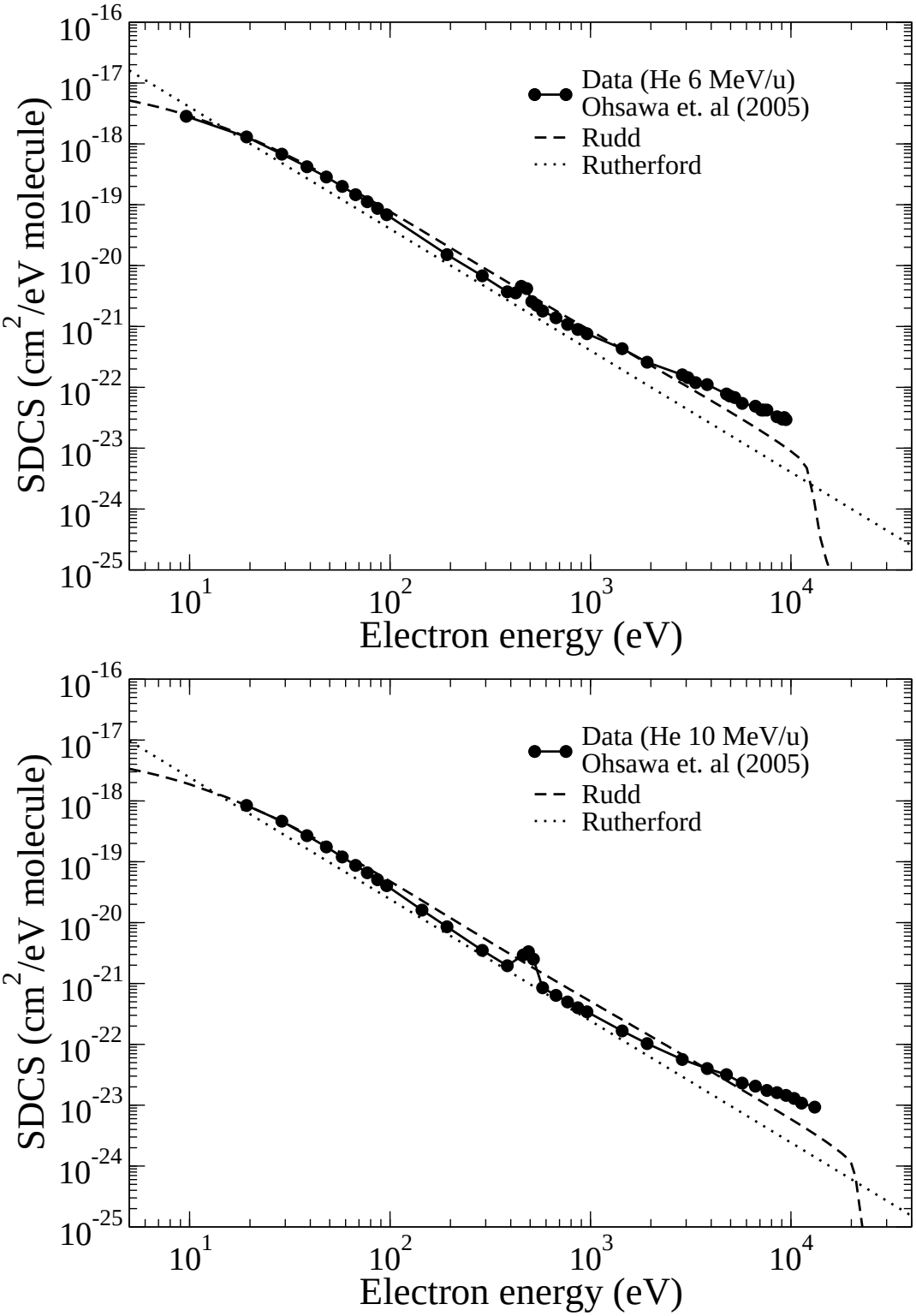

Figure 5.1: Comparison between data (Ohsawa et al., 2005b) and models of SDCS for production of secondary electrons by 6 MeV/u and 10 MeV/u He^{+2} ions in water vapor. Both graphs present the oxygen KLL Auger peak at ~ 500 eV. Dr. D. Ohsawa kindly provided the data.

30 % is verified between data and the Rutherford's SDCS for the primary particle energy loss to medium by ionization. When comparing to the total energy loss by the HCP to the medium by ionization and excitations, the total stopping power, the disagreement between data and Rutherford's model is about 20 %. Thus, calculations of RDDs using Rutherford's SDCS underestimate the results. Unfortunately, no universal method is available that yields accurate cross-sections for production of secondary electrons by HCPs for all primary and secondary energies and all target materials. Furthermore, the published SDCS experimental data is only for ten different media and primary particle energies below 10 MeV/u (Rudd et al., 1992; ICRU, 1995). These restrictions leave us with no other choices when dealing with general problems.

5.2 RADIAL DOSE DISTRIBUTION OBTAINED WITH GEANT4

MC provides a flexible approach to simulate RDDs. Physical parameters such as detector geometry and physics models can be conveniently modified. This section presents the description of the MC geometry and physics models used throughout this work and the influence of various physical parameters on the RDDs.

5.2.1 MODEL DESCRIPTION

The pattern of energy deposition by HCP exhibits radial symmetry. Thus, the natural geometry to use is cylindrical. In this work we use a cylinder divided into many concentric shells spaced from each other in logarithmic scale. Figure 5.2 illustrates the geometry utilized throughout this dissertation. The blue line represents the incident HCP, red lines the delta rays and yellow dots a MC step.

The number of concentric shells, radius r and thickness z of the cylinder, and material are input parameters and therefore can be conveniently varied.

To obtain the RDD, first we determined the energy deposited in each shell. The energy deposit in each shell was divided by the mass of the respective shell, and then normalized to

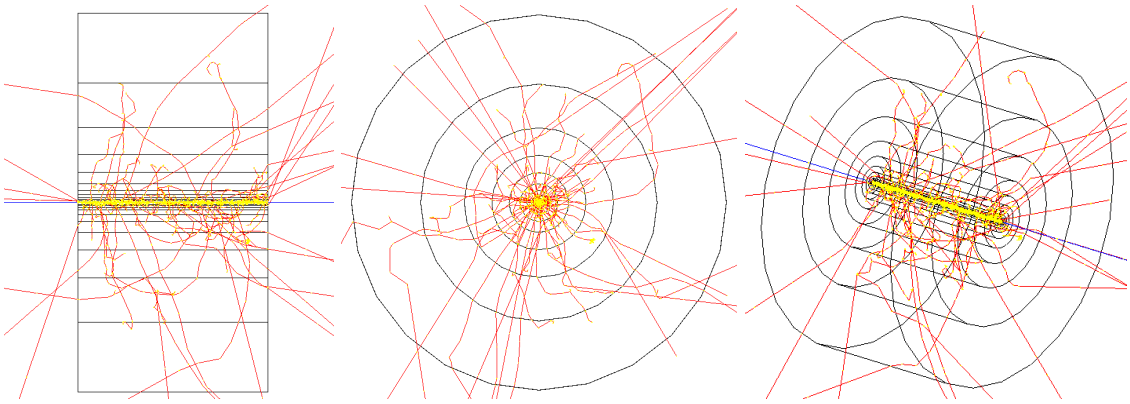

Figure 5.2: Geometry used in the RDD simulations. The material of the detector, radius r, thickness z, and number of concentric shells can be conveniently varied.

the number of particles used in the simulation. The number of particles varied for particles with different LETs. For low LET we used 1000 particles, and for high LET we used 100 particles. Thus, the RDD plots presented in this work are the average dose in each shell produced by one particle. We considered the radial distance from the path of the incident particle equal to the distance from the center of the cylinder to the center of each shell.

5.2.2 ENERGY DEPOSITED BY ELECTROMAGNETIC INTERACTION OF THE INCIDENT PARTICLE AND SECONDARY ELECTRONS

The RDD analytical models consider only the deposition of energy by the incident particle, secondary electrons, and highest order electrons (see chapter 4). Secondary photons, target and projectile fragments and other particles such as pions are disregarded in the RDD analytical models used in this work. Thus, to compare the MC simulations with the analytical models, we consider only the energy deposited by the incident particle and secondary electrons.

We use the class[2] G4hLowEnergyIonisation (Geant4-Collaboration, 2007b) to calculate the energy loss due to ionization and production of secondary electrons by the incident HCP, and the class G4LowEnergyIonisation (Geant4-Collaboration, 2007b) to calculate the

[2]In object-oriented programing, classes are independent logical units which can be developed in parallel to each other when creating large software systems such as GEANT4 (Geant4-Collaboration, 2007a).

energy loss due to ionization and production of highest order electrons by the secondary electrons produced by the incident HCP (Geant4-Collaboration, 2007b). Section 5.1 describes the cross-section for production of secondary electrons by the incident HCP. For the energy loss by the incident HCP, we use a parameterization model based on ICRU report 49 (ICRU, 1993) data. The transport of electrons was described by the Evaluated Electron Data Library (EEDL). Throughout this work we use a threshold of 250 eV for production of secondary electrons. The GEANT4 Physics Reference Manual (Geant4-Collaboration, 2007b) provides details about the physics models and parameterizations used by the classes G4hLowEnergyIonisation and G4LowEnergyIonisation. Appendix B presents the code relevant to the physics models used for the RDD simulations.

5.2.3 EFFECTS OF VARIOUS PARAMETERS IN THE RADIAL DOSE DISTRIBUTION

This subsection investigates the role of various parameters in the RDD MC simulations, including the maximum step size, number of particles, number of shells, and size of detector.

The maximum step size defines the precision of the MC calculations. At the beginning of a MC step, the code calls all active physics processes. Each process returns a step length. The code chooses the minimum step length. If the minimum step length is larger than the maximum step size defined by the user, the code uses the latter as the size of the MC step. Therefore, the maximum step size influences the computation time and affects the precision of the calculations; a smaller value produces a smoother RDD (Figure 5.3), however, the computation time increases.

As previously discussed, the values of the radial dose obtained are average values of dose per particle. Thus, as expected, Figure 5.4 shows that the RDD remains the same if the number of particles in the simulation increases. However, as the number of particle increases, the computation time also increases.

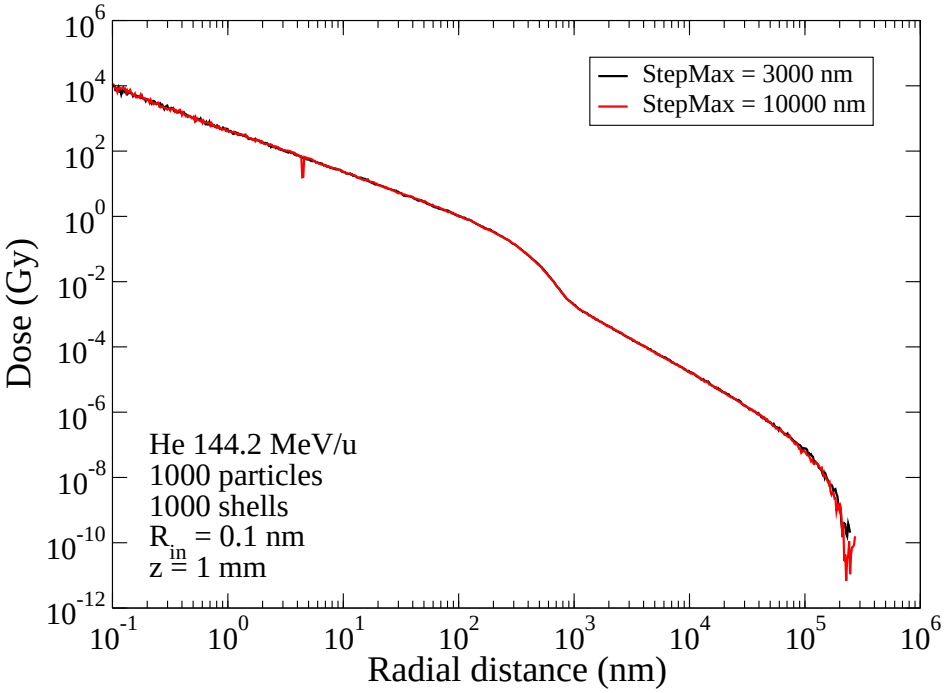

Figure 5.3: Influence of maximum step size on the RDD simulations of He 144.2 MeV/u ions in Al_2O_3:C.

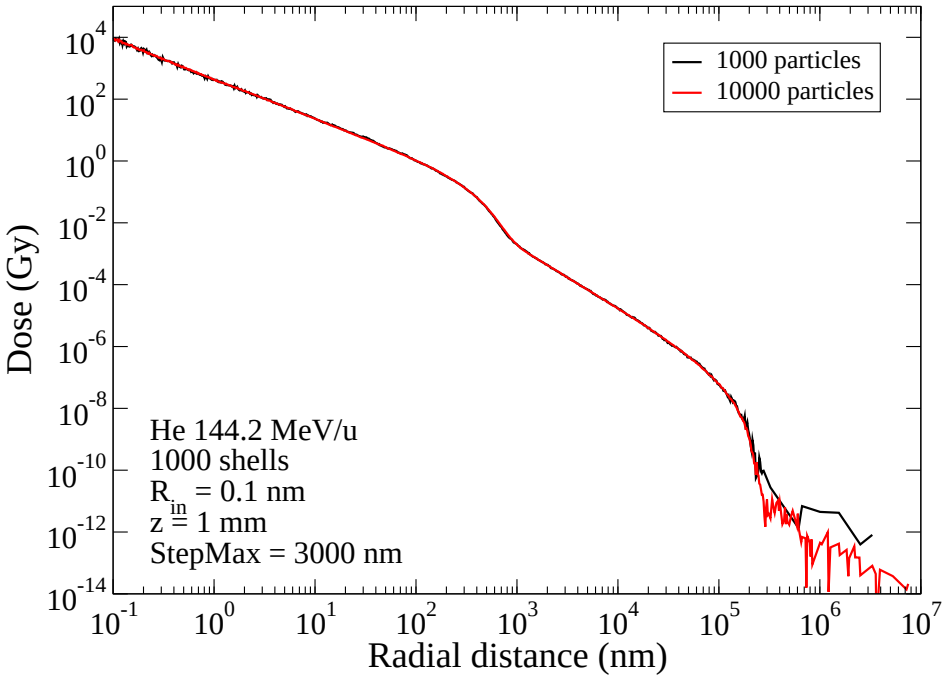

Figure 5.4: Influence of the number of particles on the RDD simulations of He 144.2 MeV/u ions in Al_2O_3:C.

Figure 5.5 shows RDDs when changing the thickness z of the detector. Note that the RDDs present a hump and are drastically changed by varying z. The hump moves to larger radial distances by increasing z. This hump is also observed in the Waligórki *et al.* and Fageeha *et al.* models of RDD (Figure 4.3), as well as experimental data (Waligórski et al., 1986).

GEANT4 determines the angular dependence of the ejected secondary electrons using conservation of momentum and energy (Geant4-Collaboration, 2007b). In Figure 5.2, the illustration on the left side shows the angular dependence of secondary electrons produced by the incident HCP. Note that secondary electrons with large energies ejected with small angles from the path of the incident particle also contribute to the dose. Thus, we expect to observe an angular dependence in the radial dose as the thickness z of the absorber increases. Therefore, we attribute the hump to the angular dependence of the ejected secondary electrons with small angles.

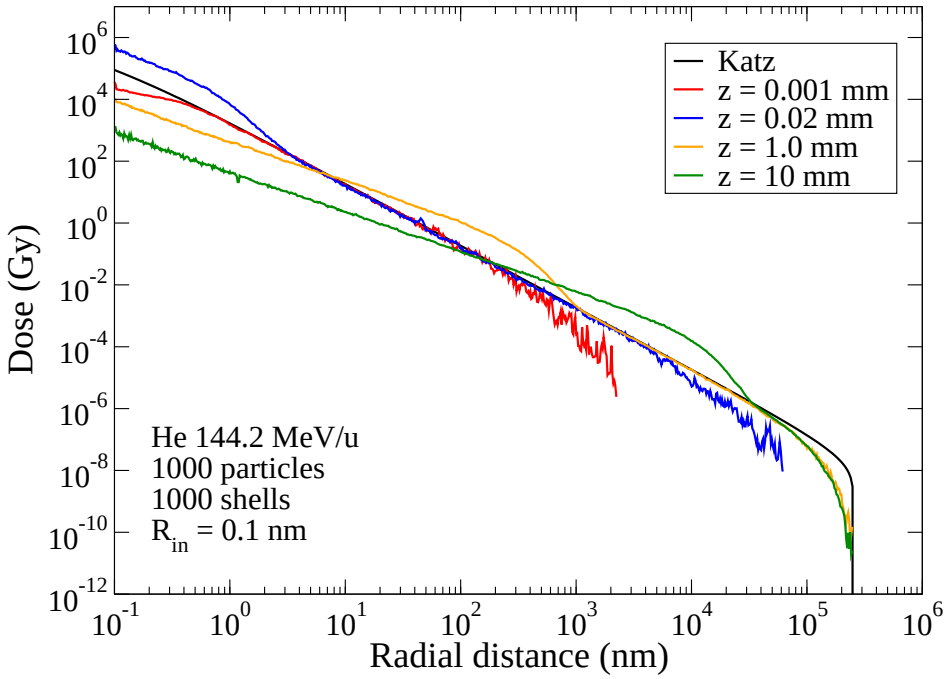

Figure 5.5: Influence of the thickness z of the detector on the RDD simulations of He 144.2 MeV/u ions in Al_2O_3:C.

For very small values of z, most of the secondary electrons that contribute to the dose

are ejected perpendicular to the trajectory of the incident particle and the RDD agrees with the Butts and Katz model (Figure 5.5).

We observed a disagreement between the MC simulation and Butts and Katz model for radial distances smaller than the radial distance where the hump is located. For small radius, the MC simulations deviate from the $D \propto r^{-2}$ dependence. Also, as z increases, the radial dose for small radius decreases. We performed various tests with different geometries, maximum step sizes, and when studying different interactions (scattering, bremsstrahlung, and energy threshold for production of secondary electrons) to understand the disagreement in the small radius, but we were unable to explain this dependence. Also, independent simulations using the FLUKA MC code performed by another group showed the same behavior of decreasing radial doses for small radius with increasing z values (Mark et al., 2007).

The dependence on the thickness z is an important point since the shape of the RDD influences on the predictions of $\eta_{HCP,\gamma}$. Chapter 8 emphasizes this dependence.

CHAPTER 6

EXPERIMENTAL DETAILS

As part of this dissertation, we performed irradiations in accelerators to characterize the response of OSL and TL detectors. This chapter describes the experimental details including preparation and types of detectors, facilities, irradiations, and readout methods.

6.1 DETECTORS AND PREPARATION

To study the difference in the $\eta_{HCP,\gamma}$ of different materials, we use three types of detectors: Al_2O_3:C single crystals, Al_2O_3:C Luxel^{TM}, and LiF:Mg,Ti. Al_2O_3:C single crystals were grown at Urals Polytechnic Institute (Russia) and have an approximate diameter of 5.0 mm and a thickness of 0.9 mm. Luxel^{TM} detectors (Landauer Inc.) are thin strips with dimensions 2.0 cm $\times$ 1.7 cm $\times$ 0.3 mm containing powdered Al_2O_3:C. From each as-received Luxel^{TM} strip we cut 16 square pieces ($\sim$ 3 mm $\times$ 3 mm), or 5 punched circular pieces ($\sim$ 7 mm diameter). LiF:Mg,Ti detectors (TLD-100, Harshaw Research Group^{TM}) are in the form of hot pressed chips with natural isotopic abundance of Li. Each TLD-100 chip has the dimensions 3.2 mm $\times$ 3.2 mm $\times$ 0.9 mm.

We used two types of detector packages for the irradiations: (i) detectors packed with black electrical tape to protect the optically stimulated luminescence detectors (OSLDs) from light, and mounted in polycarbonate (Lexan^{TM}) holders of dimensions 7.0 cm $\times$ 3.5 cm $\times$ 0.7 cm, or (ii) detectors simply packed with black electrical tape. For the detectors mounted in polycarbonate holders, the HCP beam traversed a polycarbonate thickness of 2.0 mm before reaching the detectors. Tests performed with both types of packaging showed that the holder has no influence on the results. For particles with small range, we

Table 6.1: Pre-irradiation treatments for the detectors used in this study: Luxel^{TM}, Al_2O_3:C single crystals and TLD-100.

Detector	Readout	Thickness	Annealing/bleaching
Luxel^{TM}	OSL	0.3 mm	Yellow light overnight
Al_2O_3:C	OSL/TL	0.9 mm	900 °C/15 min
TLD-100	TL	0.9 mm	400 °C/1 h + 100 °C/2 h

used the packing with black electrical tape only.

To eliminate any background signal accumulated during storage of the detectors before irradiation, the detectors were bleached or annealed. Luxel^{TM} detectors were illuminated overnight with yellow light from a halogen lamp filtered by a yellow glass filter Kopp 3-69 (Bøtter-Jensen et al., 2003). Al_2O_3:C single crystal detectors were annealed at 900 °C for 15 min (McKeever et al., 1995). TLD-100 detectors were annealed at 400 °C for 1 h following 100 °C for 2 h (McKeever et al., 1995). After bleaching or annealing, the detectors presented a background signal lower than the dark counts of the photomultiplier.

Table 6.1 shows the type of detectors, thickness and reset treatment procedures. After the reset treatments the Luxel^{TM} and Al_2O_3:C single crystal were enclosed in black plastic or black electrical tape to avoid exposure to light.

6.2 HEAVY CHARGED PARTICLE IRRADIATIONS

We performed irradiations with 24 combinations of particles and energies at four different facilities: Heavy Ion Medical Accelerator in Chiba (HIMAC) at National Institute of Radiological Sciences (NIRS), Japan; NASA Space Radiation Laboratory (NSRL) at Brookhaven National Laboratory (BNL), USA; Loma Linda University Medical Center (LLUMC), USA; and Texas A & M University (TAMU), USA. Some of the irradiations were performed during the ICCHIBAN project (Inter-Comparison for Cosmic-rays with Heavy Ion Beams at NIRS), and as part of investigations carried out by other groups (courtesy of E. R. Benton, Eril Research Inc; and E. Semones and R. Gaza, Space Radiation

Analysis Group, JSC-NASA).

The HCPs used in this study covered atomic numbers from 1 (proton) to 54 (xenon), and energies from 14 MeV/u to 1000 MeV/u, corresponding to L_∞ in water from 0.223 keV/μm to 1368 keV/μm, L_∞ in LiF:Mg,Ti (density of 2.64 g/cm^3) from 0.474 keV/μm to 2899 keV/μm, and L_∞ in Al_2O_3:C (density of 3.97 g/cm^3) from 0.734 keV/μm to 4462 keV/μm.

For most of the irradiations, the accelerator facility's staff provided us measurements of the range of the HCP in water. The ranges were measured using material with thickness equivalent to that of a slab of water (water equivalent binary filters). We use the Energy vs. LET vs. Range calculator version 1.24 build by Vladimir Zajic at Brookhaven National Laboratory (Zajic) to calculate the L_∞ values, and range in other materials (Al_2O_3:C and LiF:Mg,Ti).

Table 6.2 summarizes the beams and experiments, nominal and actual energies, L_∞ and range in water, LiF:Mg,Ti and Al_2O_3:C for all the HCP irradiations we have performed so far.

The delivered doses to the detectors were determined at the facility with plastic scintillation counters and ion chambers calibrated against gamma rays from a ^{60}Co to absorbed dose to water.

Throughout this work we use the nominal energy of the HCP to label the irradiations. For instance, a helium ion with nominal energy of 150 MeV/u and actual energy of 144.2 MeV/u is referred in the text as He 150 MeV/u. All the LET values presented here, however, are from the actual energy of the beams.

6.3 CALIBRATION OF A ^{90}Sr/^{90}Y SOURCE AGAINST A ^{60}Co SOURCE

In addition to the HCP irradiations, we also performed irradiations with a ^{90}Sr/^{90}Y source for studies of dose response and calibration purposes. The ^{90}Sr/^{90}Y beta source is build into the Risø TL/OSL-DA-15 reader (Bøtter-Jensen et al., 2000). The dose rate de-

Table 6.2: Beam characteristics of the HCP irradiations.

Beam	Energy (MeV/u)	L_∞ in H_2O (keV/μm)	Range in H_2O (cm)	L_∞ in LiF:Mg,Ti (keV/μm)	Range in LiF:Mg,Ti (cm)	L_∞ in Al_2O_3:C (keV/μm)	Range in Al_2O_3:C (cm)
Proton 1000 MeV	1000[a]	0.223	327	0.474	154	0.734	99.4
H 230 MeV	230[a]	0.413	33.1	0.875	15.7	1.35	10.2
H 70 MeV	70[a]	0.960	4.09	2.02	1.95	3.10	1.28
H 40 MeV	40[a]	1.50	1.49	3.14	0.714	4.79	0.470
H 30 MeV	30[a]	1.90	0.888	3.95	0.426	6.02	0.281
He 150 MeV/u	144.2	2.24	14.7	4.75	6.95	7.31	4.54
H 24 MeV	24[a]	2.27	0.593	4.73	0.285	7.19	0.189
H 20 MeV	20[a]	2.64	0.427	5.48	0.206	8.31	0.136
H 17 MeV	17[a]	3.01	0.319	6.24	0.154	9.45	0.102
H 14 MeV	14[a]	3.52	0.225	7.29	0.109	11.02	0.072
C 400 MeV/u	386.9	11.14	25.9	23.71	12.2	36.52	7.93
C 290 MeV/u	277.2	13.30	15.0	28.22	7.07	43.51	4.60
O 1000 MeV/u	1000[a]	14.24	80.9	30.33	38.1	46.97	24.6
O 400 MeV/u	385.5	19.84	19.2	42.11	9.10	65.03	5.91
C 135 MeV/u	111.2	24.41	3.08	51.62	1.46	79.28	0.956
Ne 400 MeV/u	371.9	31.55	14.6	66.98	6.87	103.4	4.46
Si 490 MeV/u	444.8	56.80	13.8	120.7	6.54	186.4	4.24
Ar 500 MeV/u	450.7	93.34	12.2	198.3	5.77	306.4	3.74
Ti 1000 MeV/u	977.6	108.2	31.1	230.4	14.7	356.9	9.48
Fe 1000 MeV/u	967.0	151.4	25.6	322.5	12.1	499.4	7.80
Fe 500 MeV/u	423.7	200.3	7.45	425.3	3.43	657.0	2.28
Fe 200 MeV/u	120.4	431.8	0.905	912.8	0.430	1403	0.281
Kr 400 MeV/u	313.1	447.2	6.38	948.9	1.70	1464	1.11
Xe 290 MeV/u	185.5	1368	11.0	2899	0.520	4462	0.339

[a]Nominal energy of the beam.

Table 6.3: Dose rate of $^{90}Sr/^{90}Y$ beta source calibrated against a ^{60}Co source from NIST in absorbed dose rate to water for all the detectors and readout procedures used in this work.

Detector	Readout procedure	Filter	Emission band	Dose rate (mGy/s)	Date
Luxel^{TM}	OSL	U-340 + WG-360	F-center	95.0	August 28, 2005
Luxel^{TM}	OSL	U-340	F-center + UV	82.0	August 28, 2005
Al_2O_3:C	OSL	U-340	F-center + UV	52.4	April 18, 2006
Al_2O_3:C	TL	5-58	F-center	52.4	April 18, 2006
TLD-100	TL	BG-39	Peak 5	69.4	May 8, 2004

livered by the source was obtained through calibration of the source against a ^{60}Co gamma source from National Institute of Standards and Technology (NIST), courtesy of Dr. C. Soares. An independent calibration was performed against the NIST standards for each combination of material (Luxel^{TM}, Al_2O_3:C single crystal, TLD-100), signal (OSL total area, TL peak height) and optical filter (Hoya U-340, Schott WG-360, Corning 5-58, Schott BG-39) (Table 6.3).

Luxel^{TM} detectors give different dose rates when OSL is measured with different procedures. This difference is due to the luminescence from the UV emission band, which increases with time elapsed since irradiation (Yukihara and McKeever, 2006b).

Throughout this dissertation we report the absorbed doses as ^{60}Co gamma rays absorbed doses to water, unless explicitly specified.

6.4 OPTICALLY STIMULATED LUMINESCENCE READOUTS

A Risø TL/OSL-DA-15 reader (Bøtter-Jensen et al., 2000) was used for continuous wave OSL readouts. The OSL readouts consisted of stimulation for 300 s of the detectors with green light from light emitting diodes (LEDs), with emission centered at 525 nm and power of approximately 10 mW/cm^2 at the detector's surface.

For the OSL measurements we use two different sets of filter packages to: i) discriminate the stimulation light from the luminescence light; and ii) select appropriate detection windows to measure luminescence from the F-center and UV emission bands, or F-center

emission band only in Al_2O_3:C. One of the sets, labeled set 1, is composed of Hoya U-340 filters (transmission centered at 340 nm, FWHM = 80 nm) with a thickness of 7.5 mm (Figure 6.1a) and allows detection of both F-center and UV emission bands of Al_2O_3:C (Yukihara and McKeever, 2006b). The other filter package, labeled set 2, is composed of 2 mm thick long-pass Schott WG-360 (cutoff at 360 nm) and 7.5 mm thick Hoya U-340 filter (Figure 6.1a), allowing detection only of the main emission band of Al_2O_3:C (F-center centered at 420 nm).

Throughout this work we consider the OSL signal equal to the total area under the OSL curve. The background signal of the OSL curve was considered to be the average of the last ten points in the OSL curve. We subtracted the background signal for all the analysis (Figure 6.2). Table 6.4 summarizes the stimulation power and wavelength, type of filters and detection window and analysis of the OSL signal.

All the OSL data presented in this work are the average of three OSL measurements and the error bars are one standard deviation of the data.

6.5 THERMOLUMINESCENCE READOUTS

A Risø TL/OSL-DA-15 reader with a linear heating rate and in N_2 atmosphere was used for the TL readouts.

The TL from Al_2O_3:C single crystal detectors was measured with linear heating rate of 1 °C/s and a 4 mm thick Corning 5-58 filter (transmission centered at 410 nm, FWHM = 80 nm) to select the main emission band (F-center) of Al_2O_3:C at 420 nm (Figure 6.1b).

The TL from TLD-100 was measured with linear heating rates of 1 °C/s and 5 °C/s and 6 mm thick Schott BG-39 filter (transmission centered at 475 nm, FWHM = 250 nm) (Figure 6.1b).

We considered the TL signal from Al_2O_3:C single crystal detectors equal to the height of the TL peak (Figure 6.3a), and the TL signal from TLD-100 equal to the height of the main TL peak (peak 5) (Figure 6.3b).

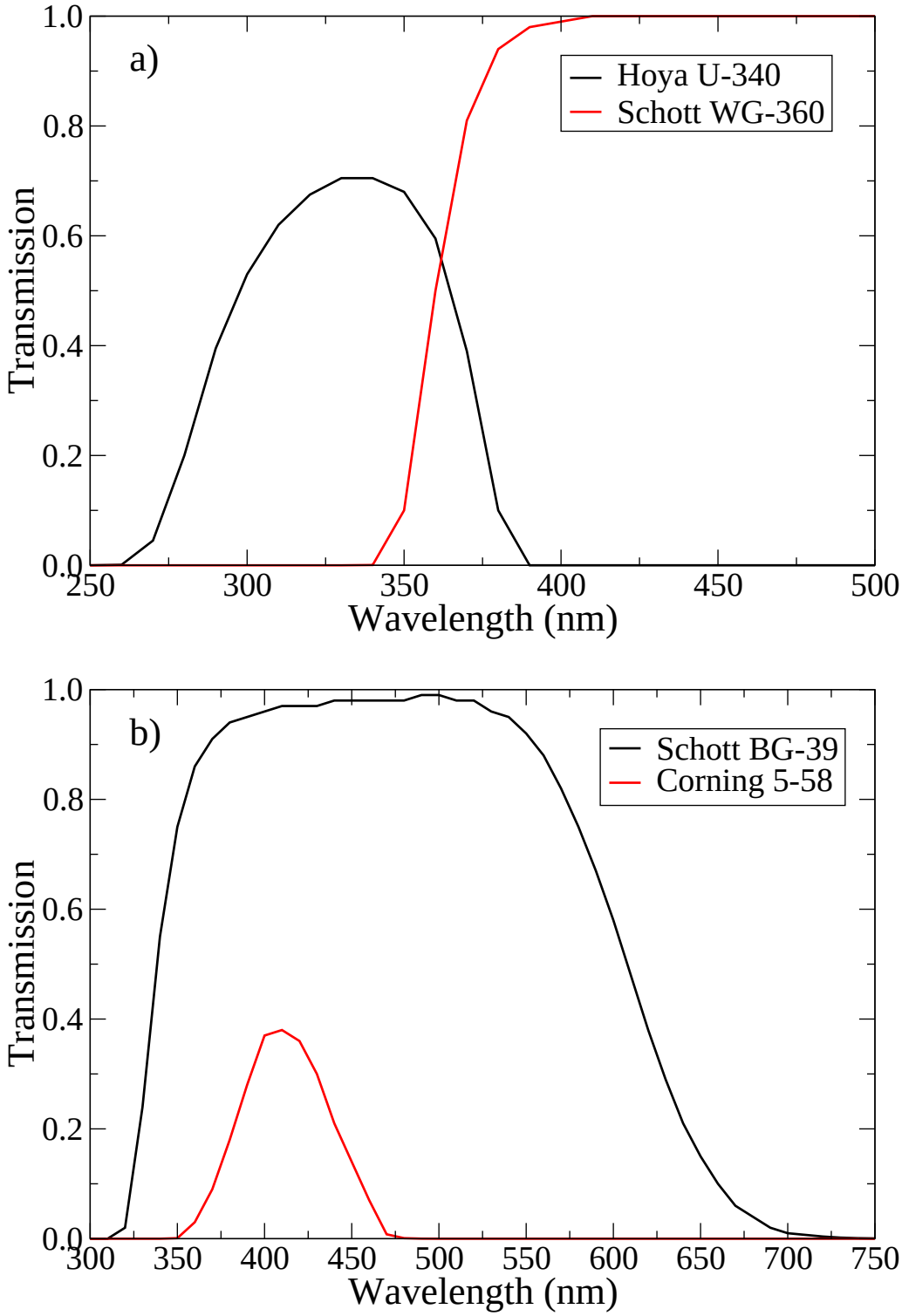

Figure 6.1: Transmission of a) Hoya U-340 and Schott WG-360 filters used in the OSL readouts and b) Schott BG-39 and Corning 5-58 filters used in the TL readouts.

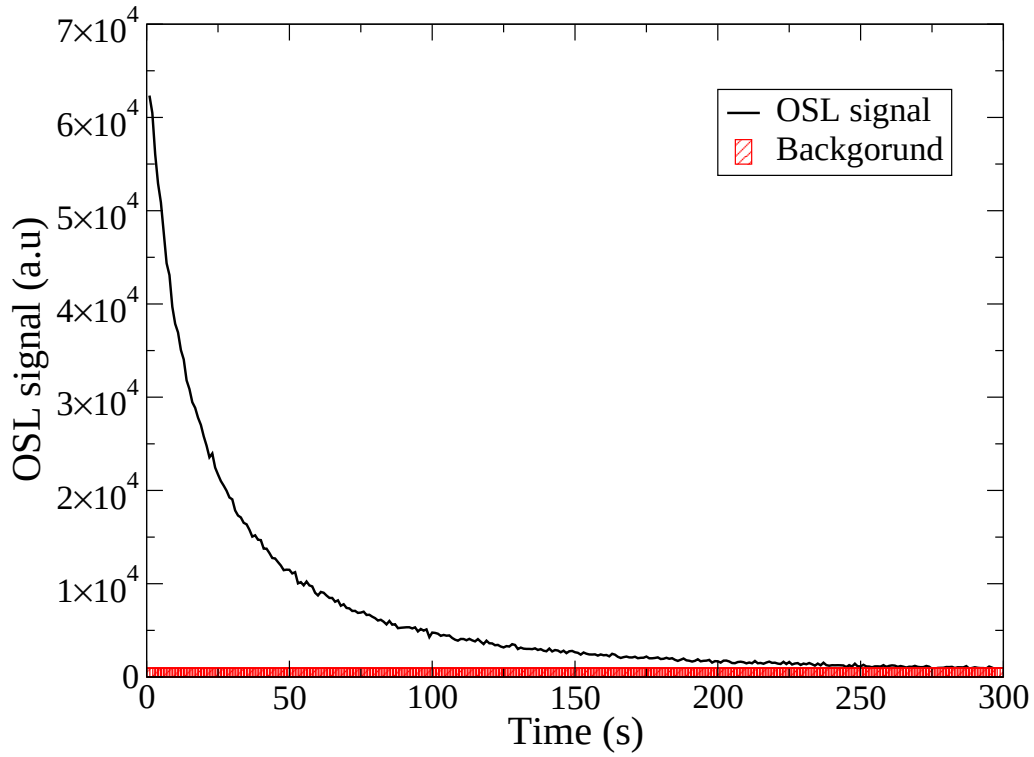

Figure 6.2: Typical OSL curve from Luxel^{TM} detectors. We considered the OSL signal equal to the total area under the OSL curve subtracting the background signal.

Table 6.4 summarizes the parameters of the OSL and TL measurements.

All the TL data presented in this work are the average of three TL measurements and the error bars are one standard deviation of the data.

6.6 CALIBRATION METHOD

A calibration curve was determined for each type of detector using irradiations with known doses. The methodology uses a second irradiation with a fixed reference dose to account for the sensitivity of each detector. In Luxel^{TM} detectors this method allows measurements of doses with uncertainties lower than 0.7 % for a single measurement (Yukihara et al., 2005).

The calibration curve is constructed using the ratio S/S_R, where S is the signal of the detector irradiated with a known dose D, and S_R is the signal of the detector irradiated with a reference dose D_R. The calibration curve is fitted using a saturating exponential (Figure

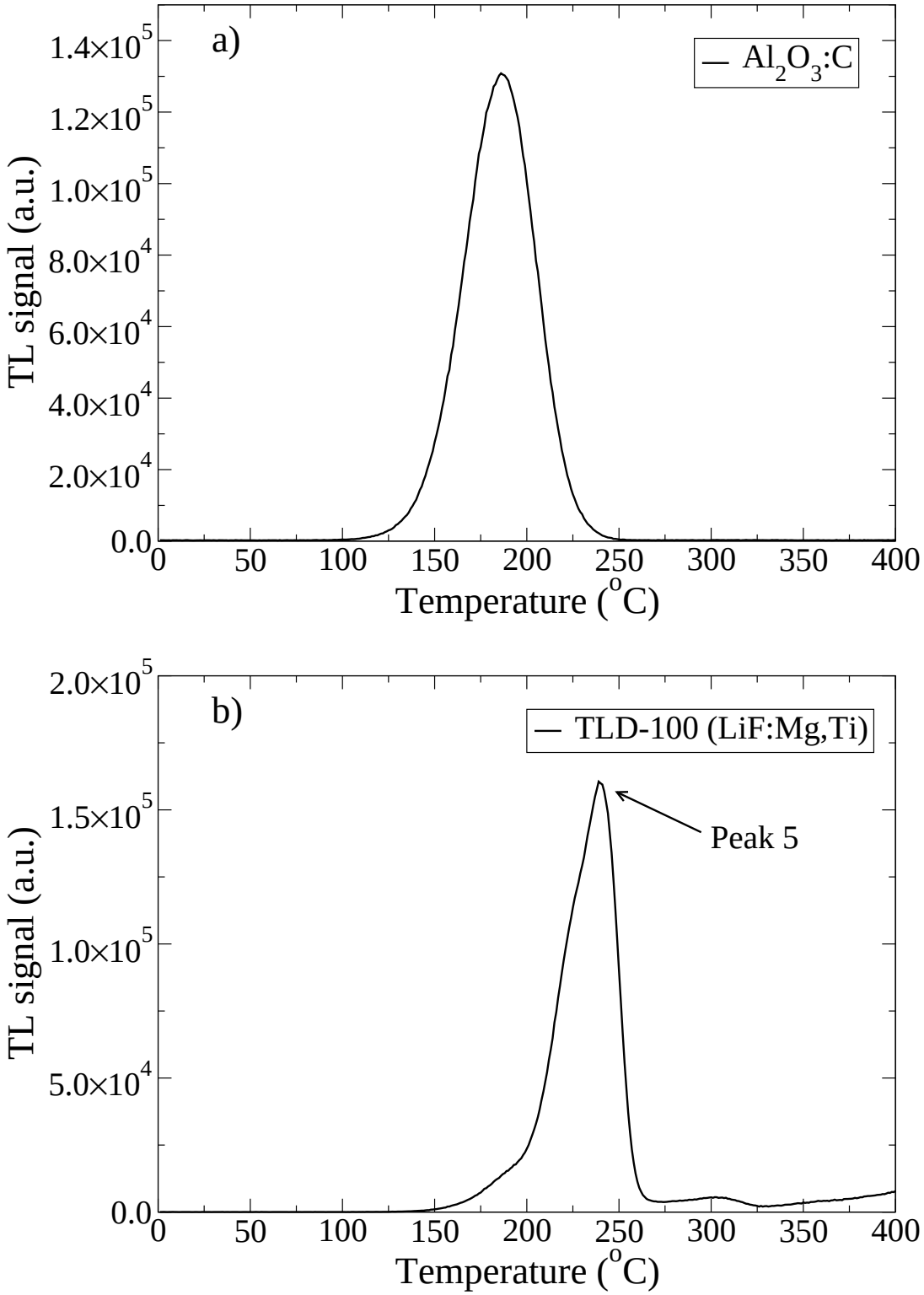

Figure 6.3: Typical TL curves of a) Al_2O_3:C single crystal, and b) TLD-100 detectors. We considered the TL signal from Al_2O_3:C single crystal and TLD-100 equal to the height of their dosimetric TL peaks.

Table 6.4: Summary of readout methods, and filter packages used for OSL and TL measurements.

Detector	Method	Heating rate	Stimulation	Detection (filters)	Signal
Luxel™	OSL	none	10 mW/cm^2 at 525 nm (green LEDs)	Set 1: Hoya U-340 (centered at 340 nm, FWHM = 80 nm)	Area (integrated over 300 s or 600 s) (F-center and UV)
Luxel™	OSL	none	10 mW/cm^2 at 525 nm (green LEDs)	Set 2: Schott WG-360 (long-pass 360 nm) and Hoya U-340	Area (integrated over 300 s or 600 s) (F-center and UV)
Al_2O_3:C single crystal	OSL	none	10 mW/cm^2 at 525 nm (green LEDs)	Set 1: Hoya U-340 (centered at 340 nm, FWHM = 80 nm)	Area (integrated over 300 s or 600 s) (F-center and UV)
Al_2O_3:C single crystal	TL	1 °C/s	none	Corning 5-58 (centered at 410 nm, FWHM = 80 nm)	Peak height (F-center)
TLD-100	TL	1 °C/s or 5 °C/s	none	Schott BG-39 (centered at 475 nm, FWHM = 250 nm)	Peak height (peak 5)

6.4). To determine an unknown HCP dose, first we measure the OSL signal S using the same setup (type of detector, filters and equipment), and then we give the same reference dose D_R adopted in the calibration curve to determine S_R. Next we calculate the ratio S/S_R and using the calibration curve we determine the dose D (Figure 6.4).

This calibration method considers that HCP, gamma, and beta radiations produce the same sensitivity changes in the detectors. Doses received during transportation and storage were carefully subtracted from the HCP doses delivered at the facilities through evaluation of control detector packages, transported and stored together with the irradiated detectors.

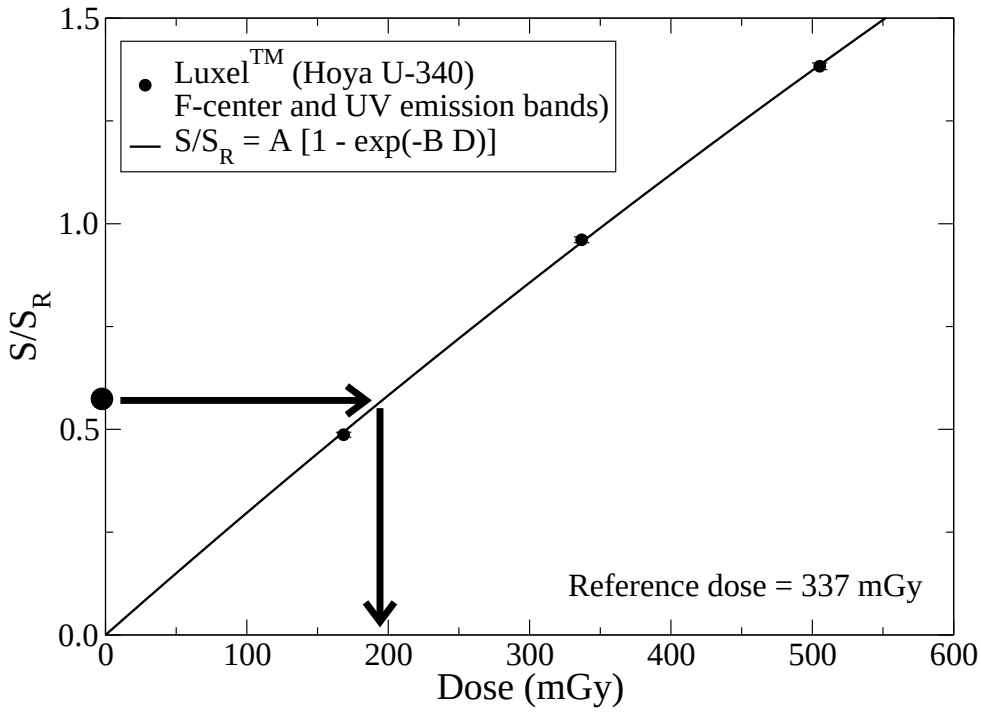

Figure 6.4: Example of calibration curve using the reference dose method. The full line is the fit to the three data points using a saturated exponential. The value of the fitting parameters are: $A = 7.54 \pm 1.8$, and $B = (4.02 \times 10^4 \pm 1.10 \times 10^4)$ Gy^{-1}.

CHAPTER 7

OPTICALLY STIMULATED LUMINESCENCE PROPERTIES OF Al_2O_3:C EXPOSED TO DIFFERENT IONIZATION DENSITIES

The OSL curves from Al_2O_3:C depend on the ionization density of the radiation. Therefore, characterization of the differences in the response of the detector to various ionization densities is important. This chapter presents OSL data from Luxel^{TM} detectors exposed to a combination of 24 particles and energies. First, we present the dose response and analysis of the shape of the OSL curve for Luxel^{TM} detectors irradiated with nine radiation qualities: gamma ray from a ^{60}Co source, beta ray from a ^{90}Sr/^{90}Y source, H 1000 MeV, He 150 MeV/u, Ne 400 MeV/u, Si 490 MeV/u, Fe 1000 MeV/u, Fe 500 MeV/u and Fe 200 MeV/u. Then, we present $\eta_{HCP,\gamma}$ *versus* L_∞ in water. Appendix A presents a complete table with TL and OSL $\eta_{HCP,\gamma}$ values for Al_2O_3:C single crystal and TLD-100 detectors.

7.1 DOSE RESPONSE

We irradiated Luxel^{TM} detectors in the interval of absorbed dose from 1 mGy to 10 kGy with: beta particles from a ^{90}Sr/^{90}Y source, exposed at Oklahoma State University (OSU) in the Risø TL/OSL-DA-15 reader; He 150 MeV/u, Ne 400 MeV/u, Si 490 MeV/u, Fe 500 MeV/u and Fe 200 MeV/u, exposed at HIMAC by OSU in 2006; and H 1000 MeV and Fe 1000 MeV/u, exposed at NSRL by Eril Research Inc. in 2006. Table 6.2 presents the parameters of the beams such as actual energy, and LET.

Dose response curves and luminescence response functions $f(D)$ were plotted to analyze the linearity of the detector to different radiation qualities. To study the role of the UV

emission band in the OSL of Luxel^{TM} detectors, the measurements were performed using different filters to measure either a combination of F-center and UV emission bands, or the F-center emission band alone.

7.1.1 BETA RAYS DOSE RESPONSE

Figures 7.1a and 7.1b present the dose response and luminescence response function when measuring F-center and UV emission bands simultaneously (Hoya U-340 filter), and Figures 7.1c and Figure 7.1d present the dose response and luminescence response function when measuring only the F-center emission band (Hoya U-340 and Schott WG-360 filters).

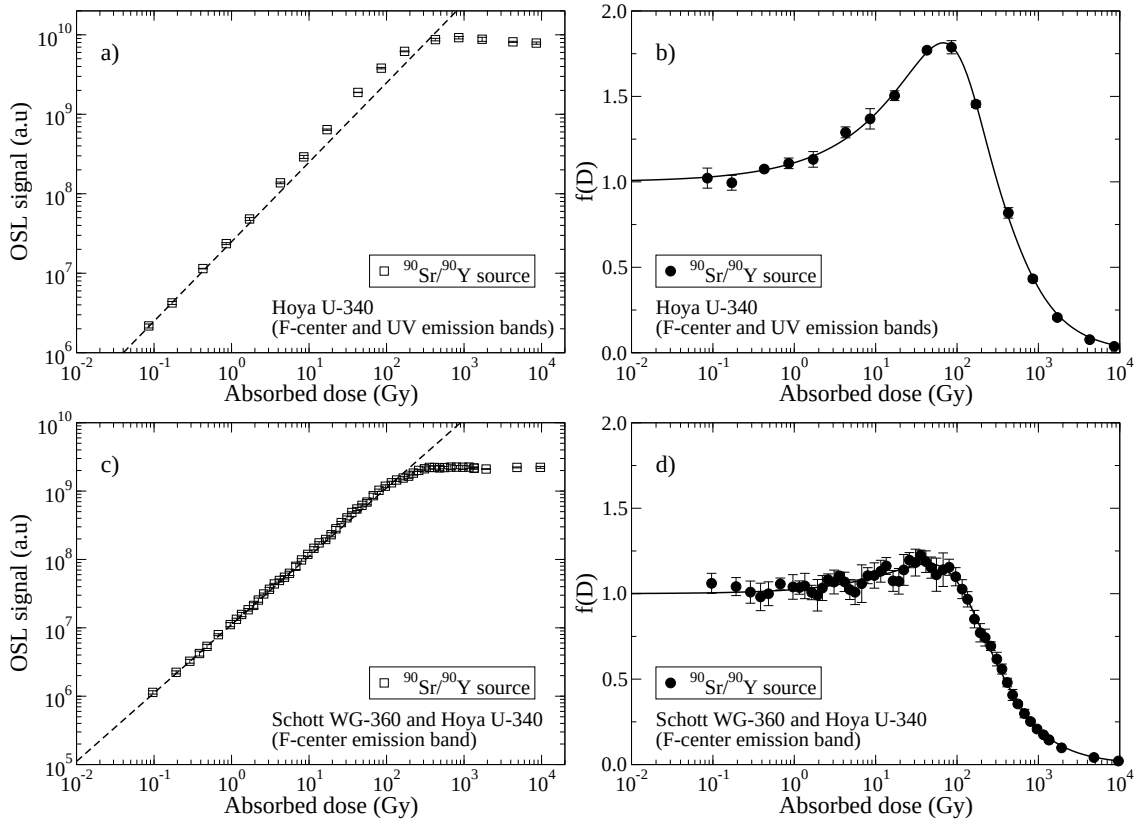

Figure 7.1: OSL dose response and luminescence response function of Luxel^{TM} detectors irradiated with beta rays from a ^{90}Sr/^{90}Y source. a) and b) OSL measured with Hoya U-340 filter (F-center and UV emission bands), and c) and d) OSL measured with combination of Schott WG-360 and Hoya U-340 filters (F-center emission band). The dashed lines in a) and c) represent the linearity, and the full lines in b) and d) represent arbitrary functions fitted to the data for better visualization.

Note that the dose response curve, and therefore, the luminescence response function of

Luxel^{TM} detectors depends drastically on the detection filter. The luminescence response function (eq. 3.10), which describes how the signal deviates from linearity, presents a maximum supralinearity equal to 1.8 at 85 Gy when F-center and UV emission bands are detected, and $\sim$ 1.2 at 45 Gy when only F-center emission band is detected. For both detection filters, the saturation starts to occur above approximately 100 Gy. These results agree with previous results (Yukihara and McKeever, 2006b; Edmund et al., 2007b).

Yukihara et al. (2004b) explained the supralinearity of the F-center emission band by a competing mechanism of filling of deep electron and hole traps and correlated changes in the concentration of recombination centers (F^+-centers) and OSL sensitivity. In the case of the Al_2O_3:C samples used in this study (Luxel^{TM}), the supralinearity is due to an unknown recombination center responsible for the UV emission band, whereas the OSL signal corresponding to F-center emission band presents a small supralinearity. In this case, the model proposed by Yukihara et al. (2004b) does not explain the supralinearity of the UV emission band, and the explanation requires a better understanding of the nature of the defects responsible for the UV emission band and their role in the OSL process.

7.1.2 HEAVY CHARGED PARTICLE DOSE RESPONSE

As in the study of the luminescence response to beta rays (see subsection 7.1.1), the dose response curves and luminescence response functions $f(D)$ were plotted to analyze the linearity of the detector to different radiation qualities. The measurements were performed using different filters to select either a combination of the F-center and UV emission bands, or only the F-center emission band. Next we discuss the dose response and $f(D)$ for seven different HCP beams (Figure 7.2 through Figure 7.8).

For H 1000 MeV irradiation a small supralinearity starts to appear for doses above 2 Gy (Figure 7.2). For the OSL detected with Hoya U-340 filter we observe a much higher degree of supralinearity (Figure 7.2a) than for OSL detected with combination of Hoya U-340 and Schott WG-360 filters (Figure 7.2c). The data for H 1000 MeV goes only up to

10 Gy due to beam time limitations.

Note that the OSL response to beta rays and H 1000 MeV is similar, regardless of the detection filter (Figure 7.2). The similarity is an indication that the pattern of energy deposition for both types of radiation is similar. Thus, the high energy H 1000 MeV beam deposit most of the energy through high-energy secondary electrons, while the local dose close to the particle tracks is not high enough to reach the saturation level of the detector.

Yukihara and McKeever (2006b) showed that the UV emission band is responsible for the supralinearity in the OSL dose response of Luxel^{TM} detectors. This work extends this observation for the H 1000 MeV beam, and shows that we can avoid the supralinearity of the dose response to H 1000 MeV using a filter combination that blocks the UV emission band of Al_2O_3:C.

For heavier particles, from He to Fe, the OSL response was linear over the investigated dose range. In the case of Fe 200 MeV/u ion, the dose response was linear up to saturation (Figure 7.8). In addition, the dose response is unaffected by the choice of detection filters.

For high-LET radiation the OSL signal can be attributed to individual tracks characterized by similar spatial pattern of energy deposition. Therefore, the ionization density pattern is unchanged by the increase in dose, i.e. particle fluence. Consequently, the OSL signal is linear. As the fluence increases the average distance between adjacent tracks decreases. For larger fluences, interaction between tracks starts to occur. Consequently, the OSL signal saturates. Thus, the luminescence saturation occurs when the particle fluence or dose is high enough for the tracks to start interacting, in the case of the Fe 200 MeV/u beam at around (50-100) Gy (Sawakuchi et al., 2007a). In contrast, ionizing radiation creates luminescence recombination centers in LiF, and HCP track interaction causes supralinearity in the TL response (Horowitz et al., 2001).

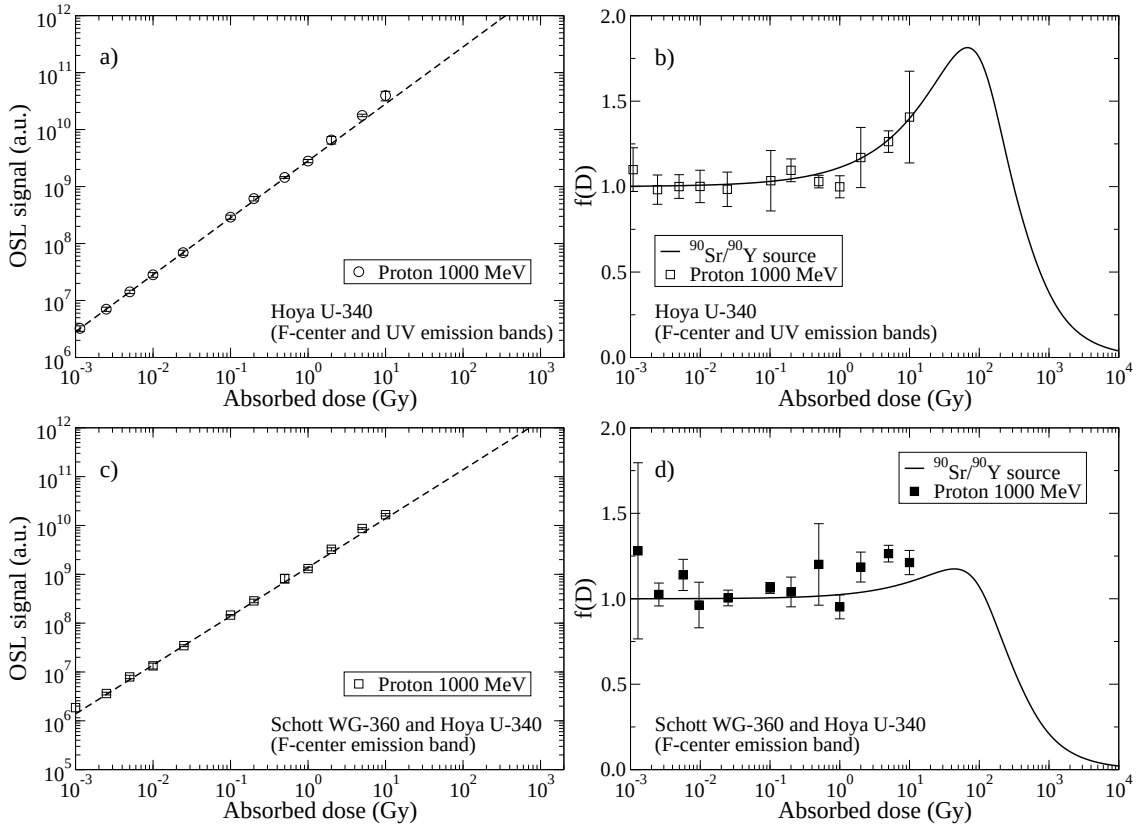

Figure 7.2: OSL dose response and luminescence response function of Luxel^{TM} irradiated with H 1000 MeV beam. a) and b) OSL measured with Hoya U-340 filter (F-center and UV emission bands), and c) and d) OSL measured with combination of Schott WG-360 and Hoya U-340 filters (F-center emission band). The dashed lines in a) and c) represent the linearity, and the full lines in b) and d) are the beta rays luminescence response functions (see section 3.2).

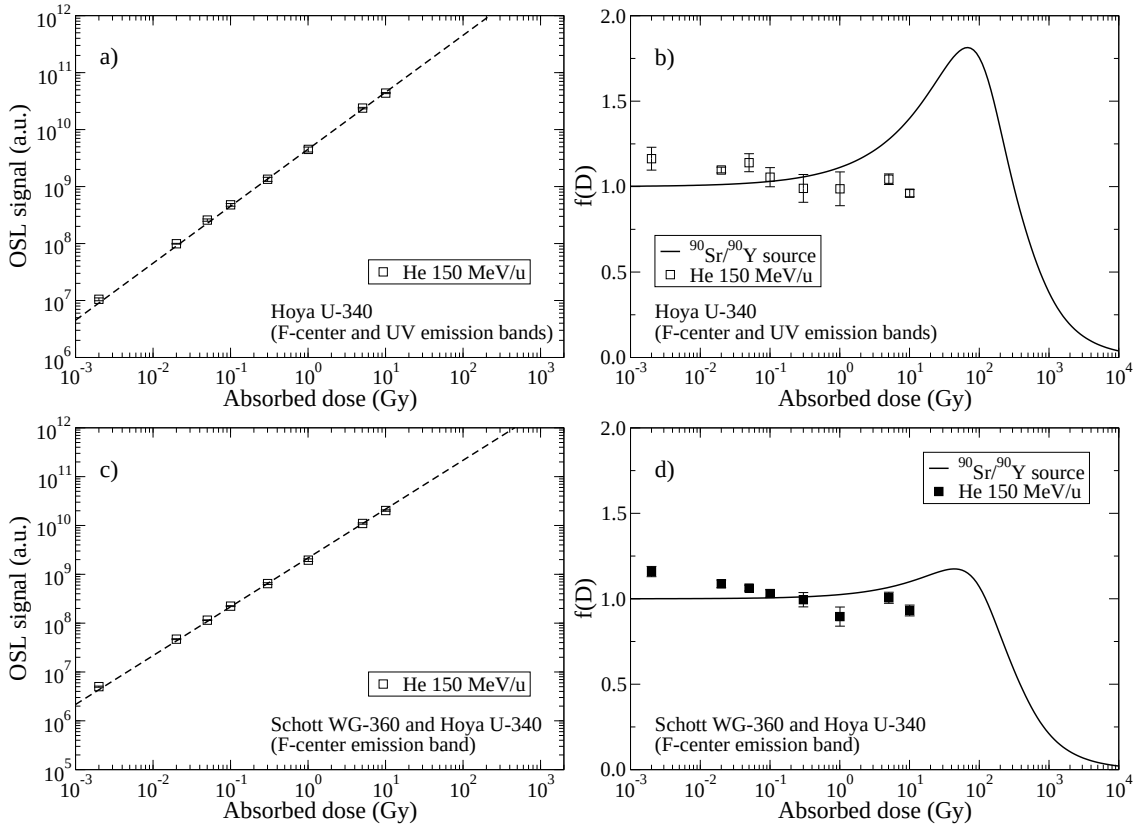

Figure 7.3: OSL dose response and luminescence response function of Luxel^{TM} irradiated with He 150 MeV/u beam. a) and b) OSL measured with Hoya U-340 filter (F-center and UV emission bands), and c) and d)OSL measured with combination of Schott WG-360 and Hoya U-340 filters (F-center emission band). The dashed lines in a) and c) represent the linearity, and the full lines in b) and d) are the beta ray luminescence response functions (see section 3.2).

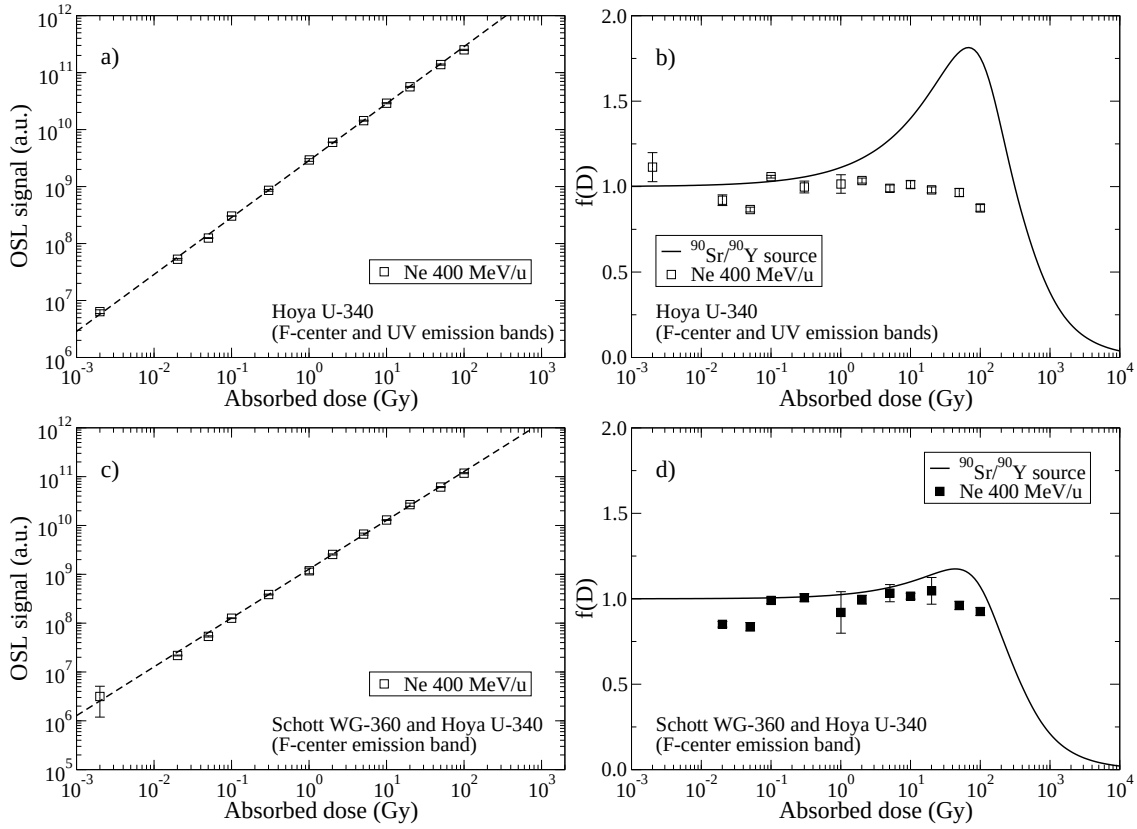

Figure 7.4: OSL dose response and luminescence response function of Luxel^{TM} detectors irradiated with Ne 400 MeV/u beam. a) and b) OSL measured with Hoya U-340 filter (F-center and UV emission bands), and c) and d)OSL measured with combination of Schott WG-360 and Hoya U-340 filters (F-center emission band). The dashed lines in a) and c) represent the linearity, and the full lines in b) and d) are the beta rays luminescence response functions (see section 3.2).

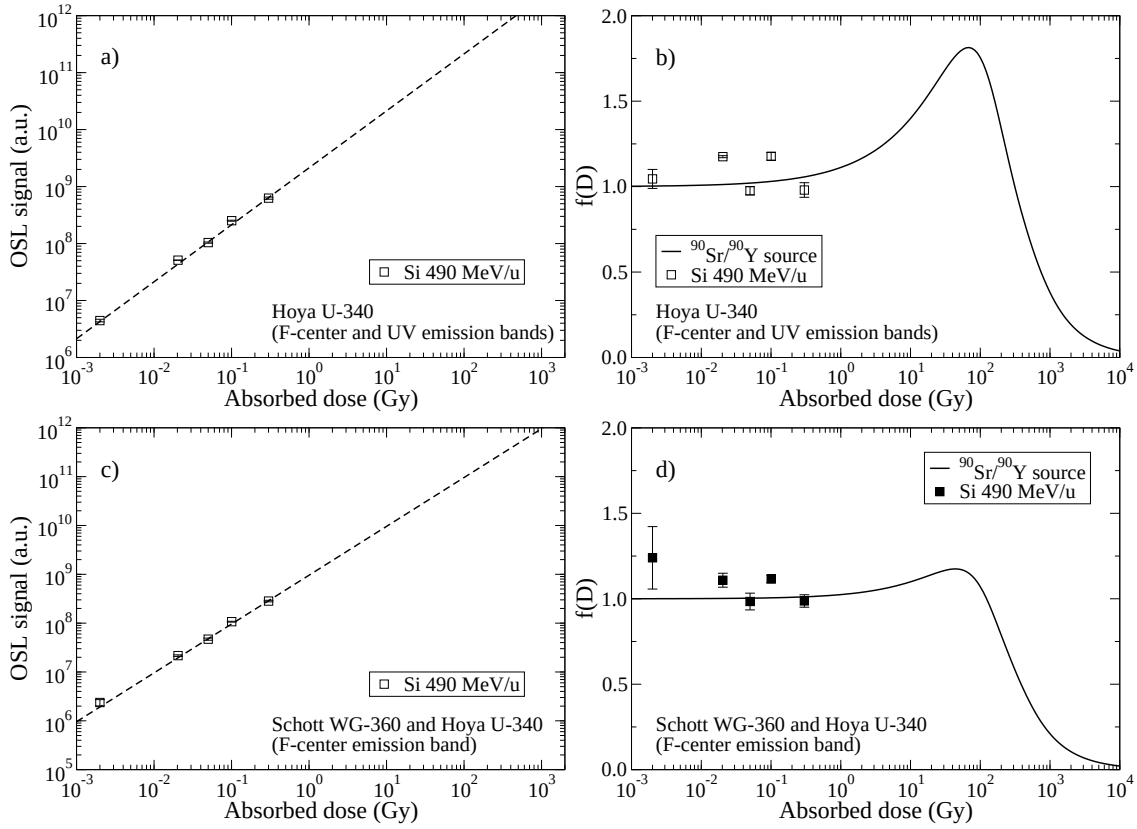

Figure 7.5: OSL dose response and luminescence response function of Luxel^{TM} detectors irradiated with Si 490 MeV/u beam. a) and b) OSL measured with Hoya U-340 filter (F-center and UV emission bands), and c) and d)OSL measured with combination of Schott WG-360 and Hoya U-340 filters (F-center emission band). The dashed lines in a) and c) represent the linearity, and the full lines in b) and d) are the beta rays luminescence response functions (see section 3.2).

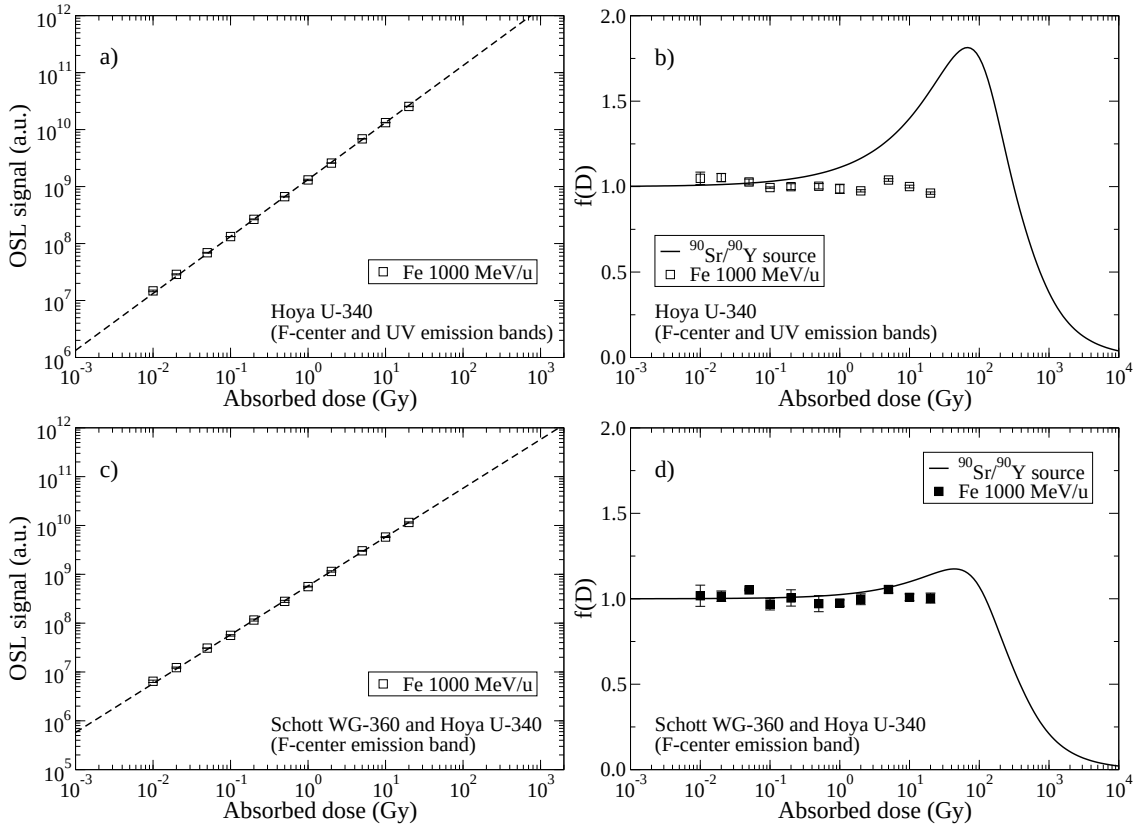

Figure 7.6: OSL dose response and luminescence response function of Luxel^{TM} detectors irradiated with Fe 1000 MeV/u beam. a) and b) OSL measured with Hoya U-340 filter (F-center and UV emission bands), and c) and d)OSL measured with combination of Schott WG-360 and Hoya U-340 filters (F-center emission band). The dashed lines in a) and c) represent the linearity, and the full lines in b) and d) are the beta rays luminescence response functions (see section 3.2).

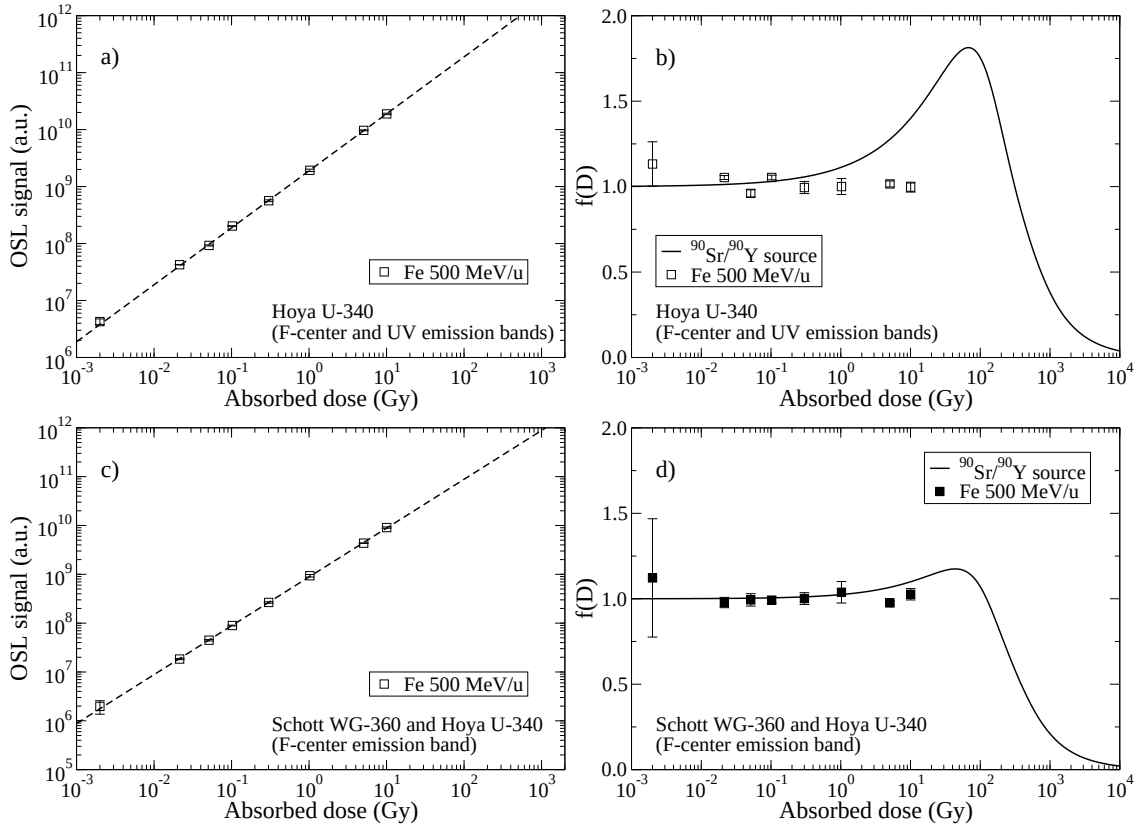

Figure 7.7: OSL dose response and luminescence response function of Luxel^{TM} detectors irradiated with Fe 500 MeV/u beam. a) and b) OSL measured with Hoya U-340 filter (F-center and UV emission bands), and c) and d)OSL measured with combination of Schott WG-360 and Hoya U-340 filters (F-center emission band). The dashed lines in a) and c) represent the linearity, and the full lines in b) and d) are the beta rays luminescence response functions (see section 3.2).

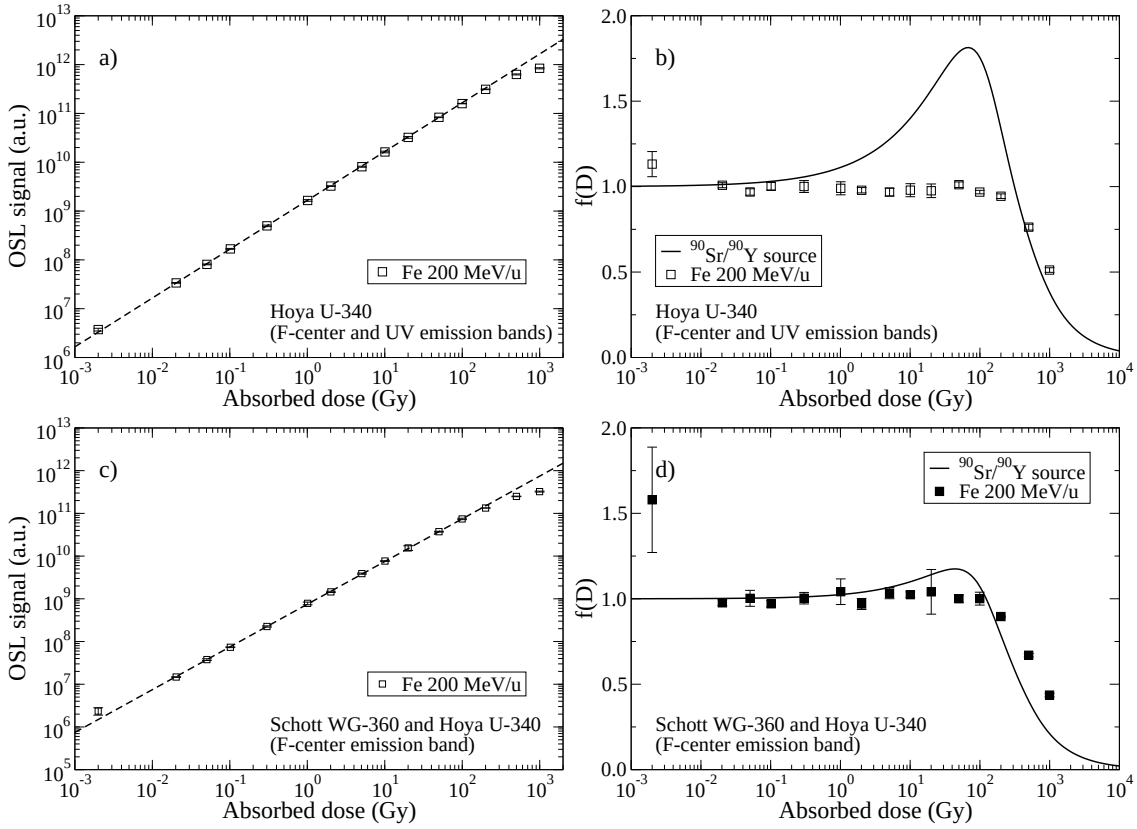

Figure 7.8: OSL dose response and luminescence response function of Luxel^{TM} detectors irradiated with Fe 200 MeV/u beam. a) and b) OSL measured with Hoya U-340 filter (F-center and UV emission bands), and c) and d)OSL measured with combination of Schott WG-360 and Hoya U-340 filters (F-center emission band). The dashed lines in a) and c) represent the linearity, and the full lines in b) and d) are the beta rays luminescence response functions (see section 3.2).

7.2 DEPENDENCE ON IONIZATION DENSITY

The shape of the OSL curve from Al_2O_3:C depends on ionization density (Yasuda et al., 2002; Yukihara et al., 2004a,b; Gaza et al., 2004, 2006b,a). This section presents a detailed study of the OSL curve shape dependence for nine radiation fields (gamma ray from a ^{60}Co source, beta ray from a ^{90}Sr/^{90}Y source, H 1000 MeV, He 150 MeV/u, Ne 400 MeV/u, Si 490 MeV/u, Fe 1000 MeV/u, Fe 500 MeV/u and Fe 200 MeV/u).

To improve the comparison between OSL curve shapes, three OSL curves were averaged, the background signal (averaged OSL curves as the average of the last ten points in the OSL curve) was subtracted, and the OSL intensity was divided by its initial intensity.

7.2.1 OSL CURVES FOR DIFFERENT RADIATION QUALITIES AT LOW DOSES

Figures 7.9a and 7.9b show the shape of the OSL curves of Luxel^{TM} detectors when detecting a combination of F-center and UV emission bands, or only F-center emission band for nine different radiation qualities, but the same dose of 100 mGy. The shape of the OSL curves is identical for gamma, beta and H 1000 MeV low LET radiations. As the LET increases the OSL curve becomes faster. Except for the He 150 MeV/u beam, all the other OSL curves have similar shape.

We considered the HCP absorbed dose delivered to the detectors to be equal to:

$$D_{HCP} = \frac{\Phi L_{\infty}^{m}}{\rho_m} \tag{7.1}$$

Note that when delivering the same absorbed dose with HCPs that have different LETs, the fluences of the HCPs are different. For example, the LET of the H 1000 MeV beam is three orders of magnitude lower than the LET of the Fe 200 MeV/ beam. Thus, to deliver the same absorbed dose of H 1000 MeV and Fe 200 MeV/u, the fluence of the H 1000 MeV beam needs to be three orders of magnitude larger than the fluence of the Fe 200 MeV/u beam. Therefore, it is also relevant to study the effect of the different radiation qualities

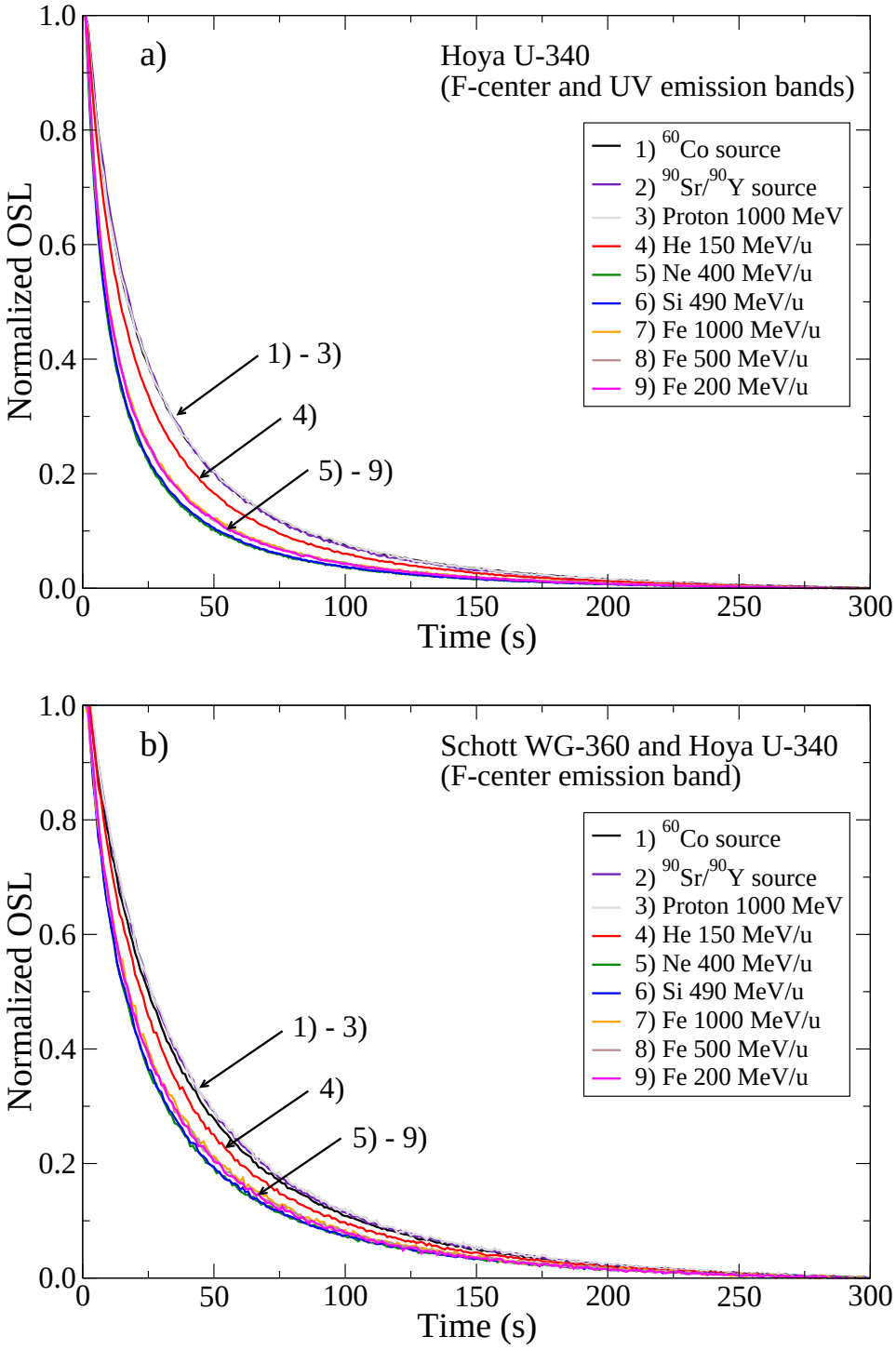

Figure 7.9: OSL curve shape of Luxel™ detectors irradiated with gamma of ^{60}Co source, beta of a ^{90}Sr/^{90}Y, H 1000 MeV, He 150 MeV/u, Ne 400 MeV/u, Si 490 MeV/u, Fe 1000 MeV/u, Fe 500 MeV/u and Fe 200 MeV/u. For all OSL curves the same nominal dose of 100 mGy was delivered to the detector. a) OSL measured with Hoya U-340 filter detecting both F-center and UV emission bands, and b) OSL measured with combination of Schott WG-360 and Hoya U-340 filters detecting F-center emission band.

when the same low fluence of HCP is delivered.

Figure 7.10 shows the normalized OSL curves of Luxel^{TM} detectors irradiated with approximately the same low fluence, but different particles and energies. The fluences and corresponding absorbed doses are given in the caption of Figure 7.10. The shape of the OSL curves is similar to the detectors irradiated with the same dose (Figure 7.9). This result is expected because, for low fluences, the HCP tracks are independent from each other.

7.2.2 OSL CURVES FOR DIFFERENT ABSORBED DOSES BUT SAME RADIATION QUALITY

We irradiated the detectors with different absorbed doses from the same radiation quality to determine the role of track overlap in the OSL curves.

Figure 7.11 presents normalized OSL curves of Luxel^{TM} detectors exposed to beta ray radiation. For absorbed doses larger than about 10 Gy, the OSL curves decay faster; the higher the dose, the faster the decay. For absorbed doses above 900 Gy the OSL curves present the same shape.

For the Ne 400 MeV/u and Fe 200 MeV/u beams the OSL curves are constant up to a dose of about 50 Gy, starting to decay faster for higher doses until the maximum dose investigated (Figures 7.12 and 7.13). In addition, for the same dose, the OSL curves after HCP irradiation decay faster than the beta irradiated OSL curve, as indicated by the smaller area under the normalized OSL curves (see insets in Figures 7.11, 7.12 and 7.13).

Further changes in the OSL curve occur for a higher value of HCP absorbed dose (50 Gy) compared to beta radiation (10 Gy, see Figure 7.11). We attribute this effect to the fact that, in this case, changes in the OSL curve start only when track overlap becomes important.

We use analytical models of RDD to show that track overlap plays an important role on the changes of the OSL curve of Luxel^{TM} detectors irradiated with HCP. Considering that

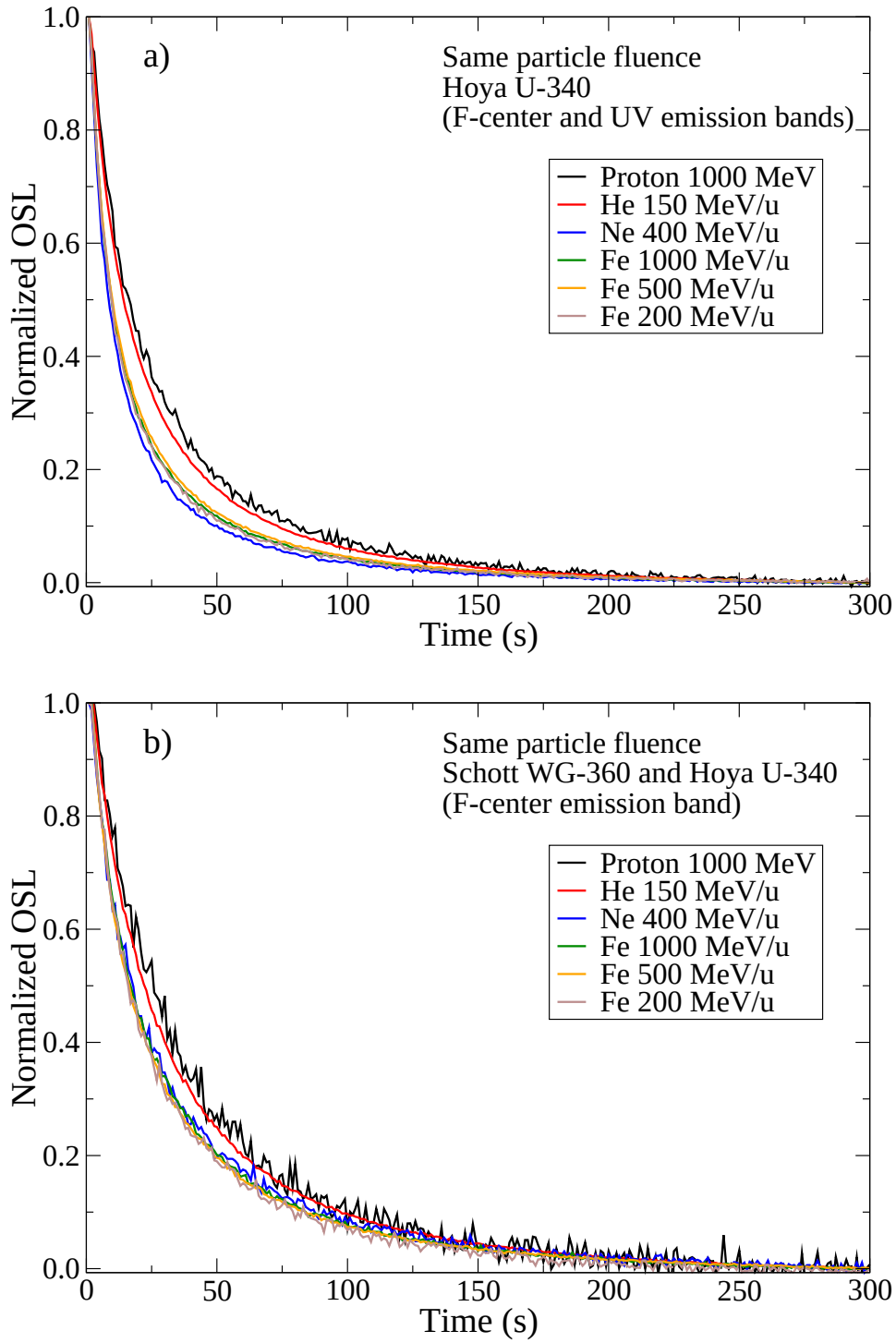

Figure 7.10: OSL curve shape of Luxel^{TM} detectors irradiated with H 1000 MeV, He 150 MeV/u, Ne 400 MeV/u, Fe 1000 MeV/u, Fe 500 MeV/u and Fe 200 MeV/u with approximately the same particle fluences. The particle fluences were: 2.79×10^7 cm^{-2}, 2.79×10^7 cm^{-2}, 1.99×10^7 cm^{-2}, 2.06×10^7 cm^{-2}, 3.13×10^7 cm^{-2} and 2.90×10^7 cm^{-2}, respectively. The absorbed doses in water were: 10 mGy, 100 mGy, 1 Gy, 5 Gy, 10 Gy and 20 Gy, respectively. a) OSL measured with Hoya U-340 filter detecting both F-center and UV emission bands, and b) OSL measured with combination of Schott WG-360 and Hoya U-340 filters detecting F-center emission band.

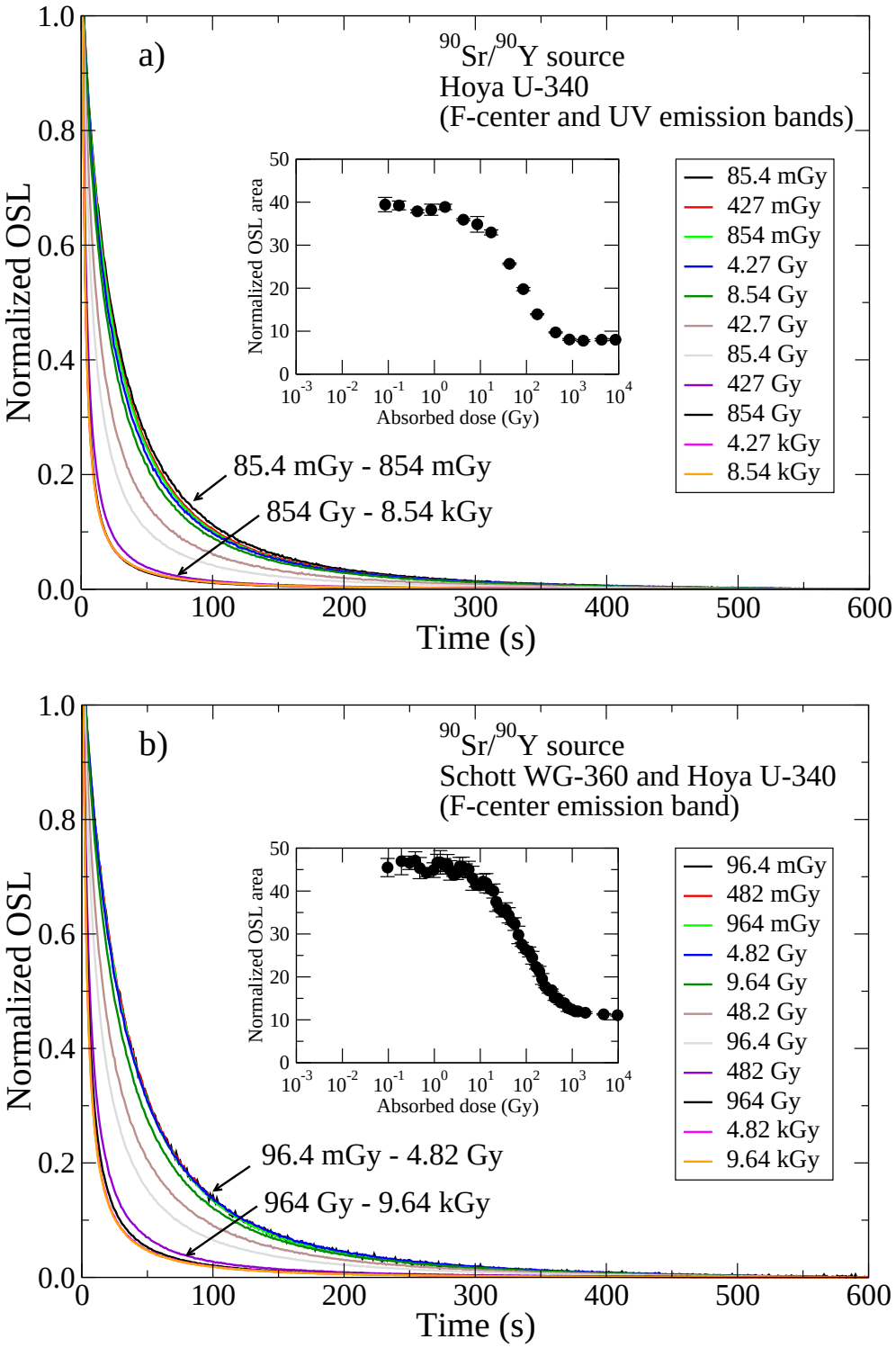

Figure 7.11: Normalized OSL curves of Luxel^{TM} detectors irradiated with beta rays. a) OSL measured with Hoya U-340 filter detecting both F-center and UV emission bands, and b) OSL measured with combination of Schott WG-360 and Hoya U-340 filters detecting F-center emission band. The insets represent the total area under the normalized OSL curves as a function of absorbed dose.

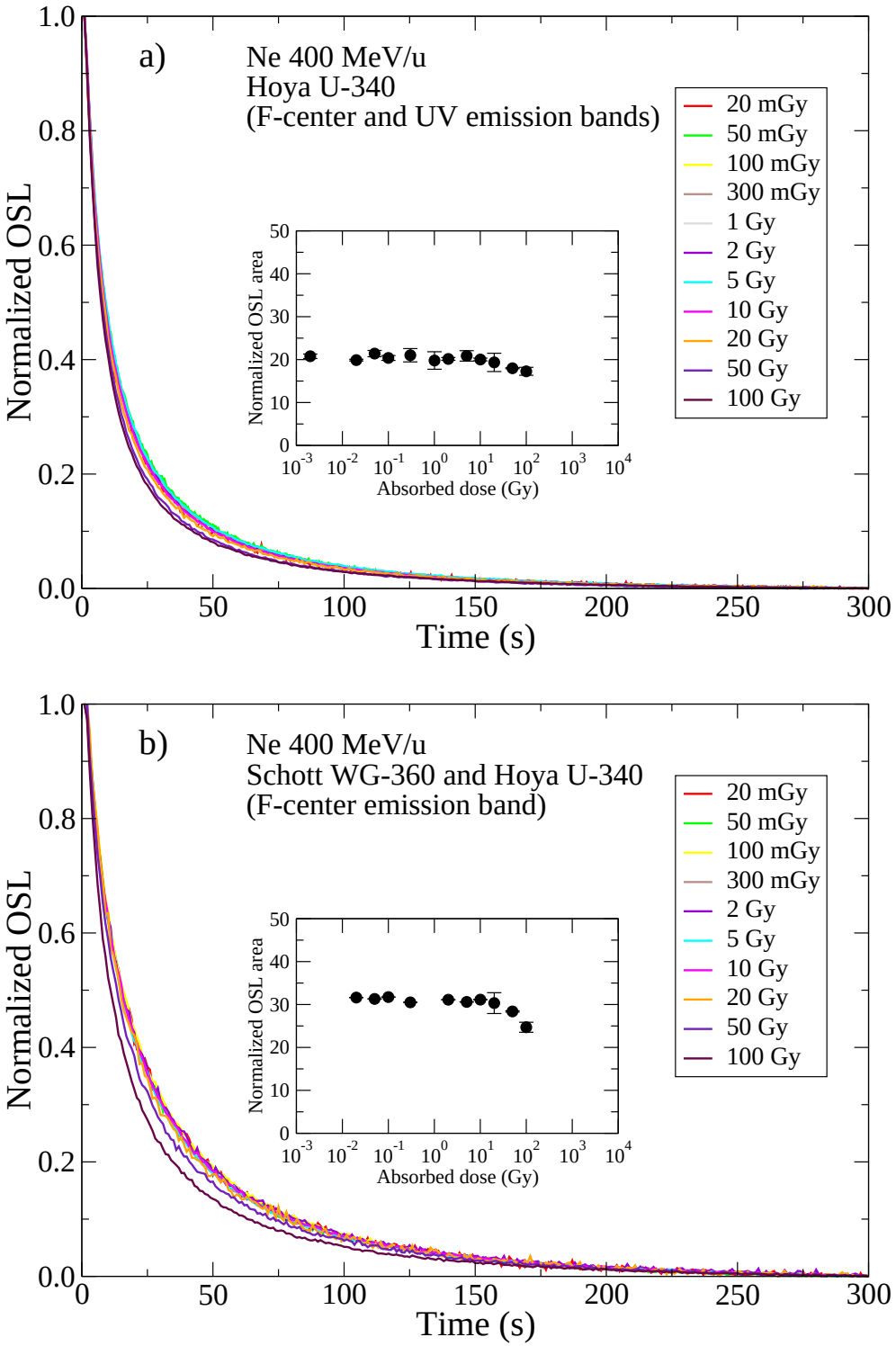

Figure 7.12: Normalized OSL curves of Luxel^{TM} detectors irradiated with Ne 400 MeV/u beam. a) OSL measured with Hoya U-340 filter detecting both F-center and UV emission bands, and b) OSL measured with combination of Schott WG-360 and Hoya U-340 filters detecting F-center emission band. The insets represent the total area under the normalized OSL curves as a function of absorbed dose.

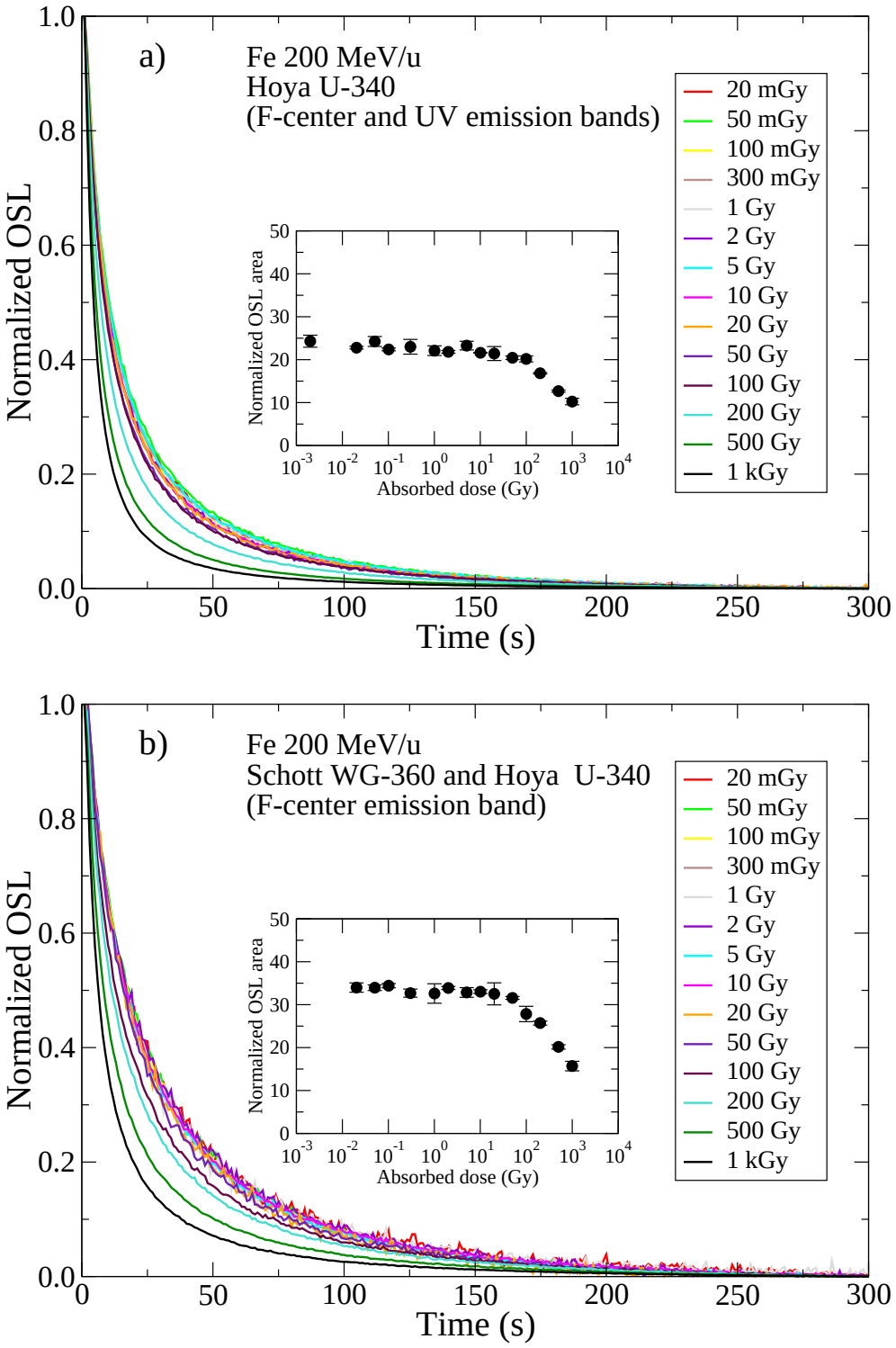

Figure 7.13: Normalized OSL curves of Luxel^{TM} detectors irradiated with Fe 200 MeV/u beam. a) OSL measured with Hoya U-340 filter detecting both F-center and UV emission bands, and b) OSL measured with combination of Schott WG-360 and Hoya U-340 filters detecting F-center emission band. The insets represent the total area under the normalized OSL curves as a function of absorbed dose.

the HCP beam is randomly distributed over the surface of the detector, the average distance d between the center of two adjacent tracks can be estimated as

$$d = 2\sqrt{\frac{1}{\pi\Phi}} \tag{7.2}$$

where Φ is the particle fluence. If $D(r)$ is the RDD around the center of the track, and if there is track overlap, the distance $r = d/2$ is the point where the radial dose $D(r)$ has its smallest value D_{min} (Figure 7.14).

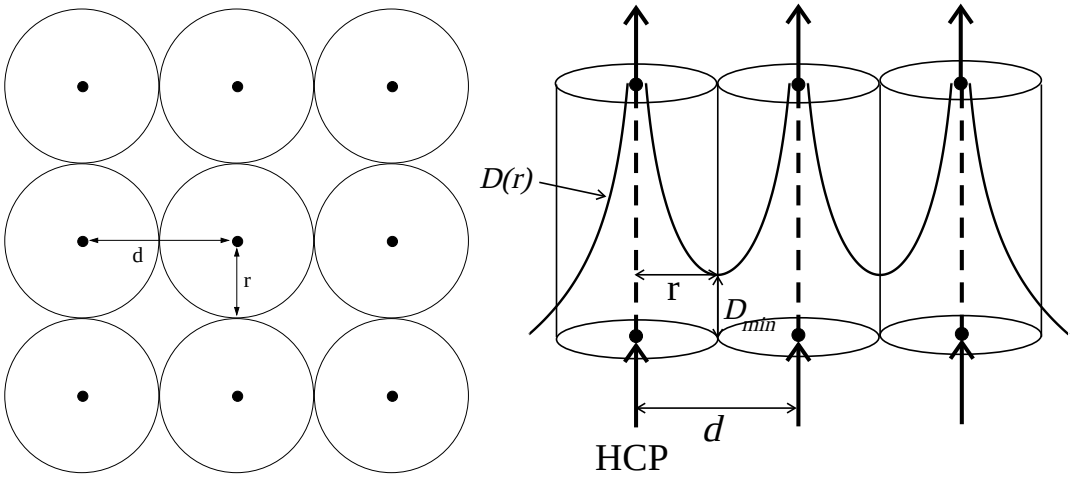

Figure 7.14: Illustration of overlap between HCP tracks when considering that the tracks are parallel and randomly distributed. $D(r)$ is a schematic representation of the RDD, d is the mean distance between two tracks, and $r = d/2$ is the middle point between two tracks where the accumulated radial dose $D(r)$ has its minimum value D_{min}.

Figure 7.15 shows Fe 200 MeV/u RDDs for 1 Gy, 10 Gy and 50 Gy in Al_2O_3:C to illustrate the effect of track overlap in the inter-track regions. At low fluences the tracks are far away from each other and the dose level in the inter-track region is very low. As the fluence increases the average distance between adjacent tracks decreases and the dose level in the inter-track region increases.

Considering 50 Gy the HCP dose in which track overlap starts to affect the shape of the OSL curves, we estimated the mean distances d between two tracks using eq. 7.2. Using different RDD models (chapter 4) we then, estimated the absorbed dose to water D_{min} at $r = d/2$, the middle distance between two tracks (Figure 7.14). Table 7.1 summarizes the

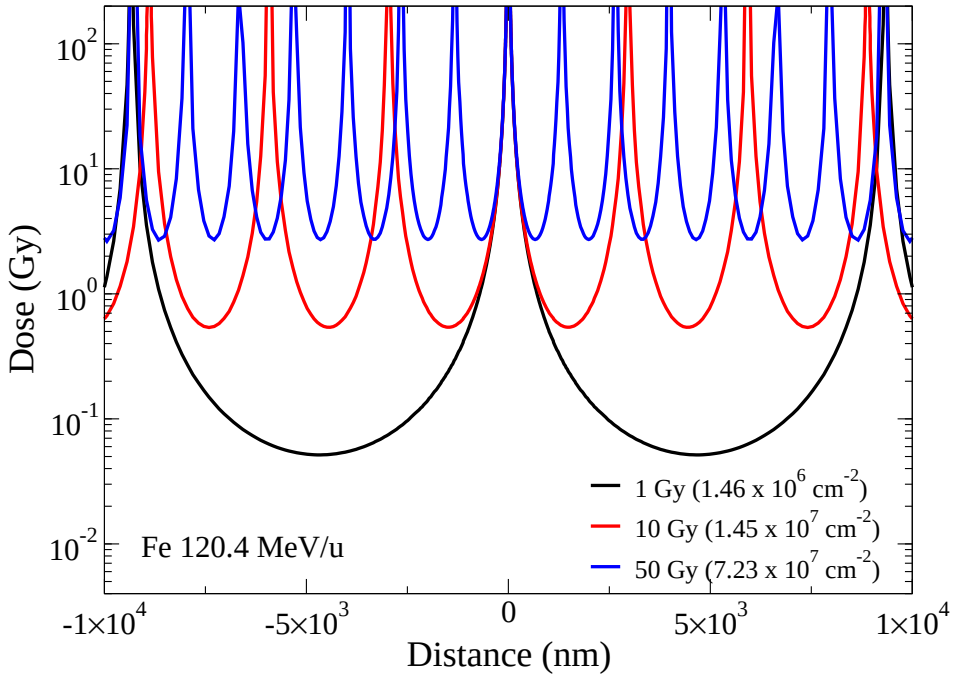

Figure 7.15: Chatterjee and Schaefer model of RDD in Al_2O_3:C for 1 Gy, 10 Gy and 50 Gy of Fe 200 MeV/u, illustrating the effect of track overlap in the inter-track region.

obtained values of D_{min}. The doses D_{min} (Table 7.1) are an underestimation because the model is one-dimensional.

Table 7.1 shows that the doses D_{min} obtained with various models are comparable to the experimental beta dose of about (1-10) Gy above which the OSL curve starts to decay faster. The dose level in the inter-track region where there is overlap of the delta rays dictates the behavior of the OSL curves: as the HCP dose increases above 50 Gy, the local dose in the region between the tracks rises above the (1-10) Gy level, and the OSL curve shape presents further changes. Therefore, the order of magnitude agreement between the inter-track dose D_{min} and the beta rays dose in which the OSL curve changes is an indication that the macroscopic effect represented by the onset of further changes in the OSL curves for HCP irradiation is due to track overlap (Sawakuchi et al., 2007b).

Table 7.1: Absorbed dose to water and fluence in which the OSL curves start to change, distance $r = d/2$, and accumulated minimum absorbed dose to water D_{min} at the distance $r = d/2$ from the center of the track for Ne 400 MeV/u and Fe 200 MeV/u beams. We calculated D_{min} using Chatterjee and Schaefer, Butts and Katz, Kiefer and Straaten, and Geiß *et al.* models of RDD (see chapter 4).

	Ne 400 MeV/u	Fe 200 MeV/u
OSL curve change	$\sim$ 50 Gy	$\sim$ 50 Gy
Fluence (ϕ)	9.90×10^8 cm^{-2}	7.23×10^7 cm^{-2}
$r = d/2$	179 nm	663 nm
Chatterjee and Schaefer	D_{min} = 2.3 Gy	D_{min} = 2.4 Gy
Butts and Katz	D_{min} = 1.6 Gy	D_{min} = 1.8 Gy
Kiefer and Straaten	D_{min} = 2.7 Gy	D_{min} = 3.0 Gy
Geiß *et al.*	D_{min} = 2.5 Gy	D_{min} = 2.8 Gy

7.3 RELATIVE LUMINESCENCE EFFICIENCY OF LUXEL™ DETECTORS

This section presents the values of $\eta_{HCP,\gamma}$ from Luxel™ detectors irradiated with the beams presented in Table 6.2. Appendix A presents a complete table with all $\eta_{HCP,\gamma}$ data that includes different types of detectors and readout methods.

The procedure used to calculate the $\eta_{HCP,\gamma}$ consisted of: (i) readout of the luminescence signal S from a detector irradiated with the HCP nominal absorbed dose to water D_{HCP}, measured at the irradiation facility; (ii) using the calibration method described in section 6.3 we determined the detector response D correspondent to the signal S. D is the gamma dose that produces the same signal of a detector irradiated with D_{HCP}. Thus, eq. 3.4 takes the form

$$\eta_{HCP,\gamma} = \frac{(S/S_\gamma)D_\gamma}{D_{HCP}} = \frac{D}{D_{HCP}} \tag{7.3}$$

(iii) we subtracted the absorbed dose D_c received during transportation and storage of the detectors after the HCP irradiations, which was obtained by control detectors, from the response D to obtain the response due to the HCP irradiations only

$$\eta_{HCP,\gamma} = \frac{D - D_c}{D_{HCP}} \tag{7.4}$$

For convenience, the doses are absorbed doses to water.

7.3.1 BARE BEAM DATA

We determined the experimental $\eta_{HCP,\gamma}$ values (eq. 7.4) in the linear range of the dose response curve, typically the HCP doses were in the interval from 50 mGy to 300 mGy. The only exception was the $\eta_{HCP,\gamma}$ for the Ti 1000 MeV/u irradiation, determined for a nominal absorbed dose of 5 Gy. Although, we did not have dose response curves for the Ti 1000 MeV/u beam, for the dose of 5 Gy we calculated the accumulated minimum inter-track absorbed dose to water D_{min}, as performed for the Fe 200 MeV/u and Ne 400 MeV/u beams (see Table 7.1), and concluded that it is only $D_{min} = 0.24$ Gy. Furthermore, we showed that the response of Luxel™ detectors is linear up to 50 Gy for high LET particles (Figure 7.8). Thus, we assumed that the Ti 1000 MeV/u dose response is linear at 5 Gy.

Figure 7.16 shows the $\eta_{HCP,\gamma}$ of Luxel™ detectors for OSL measured with Hoya U-340 filter (Figure 7.16a), and a combination of Schott WG-360 and Hoya U-340 filters (Figure 7.16b). The $\eta_{HCP,\gamma}$ values are constant for particles with low-LET, present a region of decreasing $\eta_{HCP,\gamma}$ values as a function of LET, and stabilize for $L_{\infty}^{H_2O}$ higher than around 200 keV/μm. The decreasing $\eta_{HCP,\gamma}$ values as a function of LET is a common trend also observed in other TLD materials such as Al_2O_3:C single crystals, TLD-100 (see Table A.1) and CaF_2:Tm (TLD-300) (Horowitz, 1981).

Appendix A presents a table with the $\eta_{HCP,\gamma}$ data from Luxel™ detectors. Each datum is the average of three measurements and the error represents one experimental standard deviation. In addition, we also present OSL and TL data from Al_2O_3:C single crystals and TLD-100.

Previous observations showed that the $\eta_{HCP,\gamma}$ from Luxel™ detectors depends on the readout technique and detection filters (Yukihara et al., 2006). Table A.1 and Figure 7.16 show that the use of different detection windows when measuring the OSL from Luxel™ detectors yields different values of $\eta_{HCP,\gamma}$. Thus, our results support previous observations

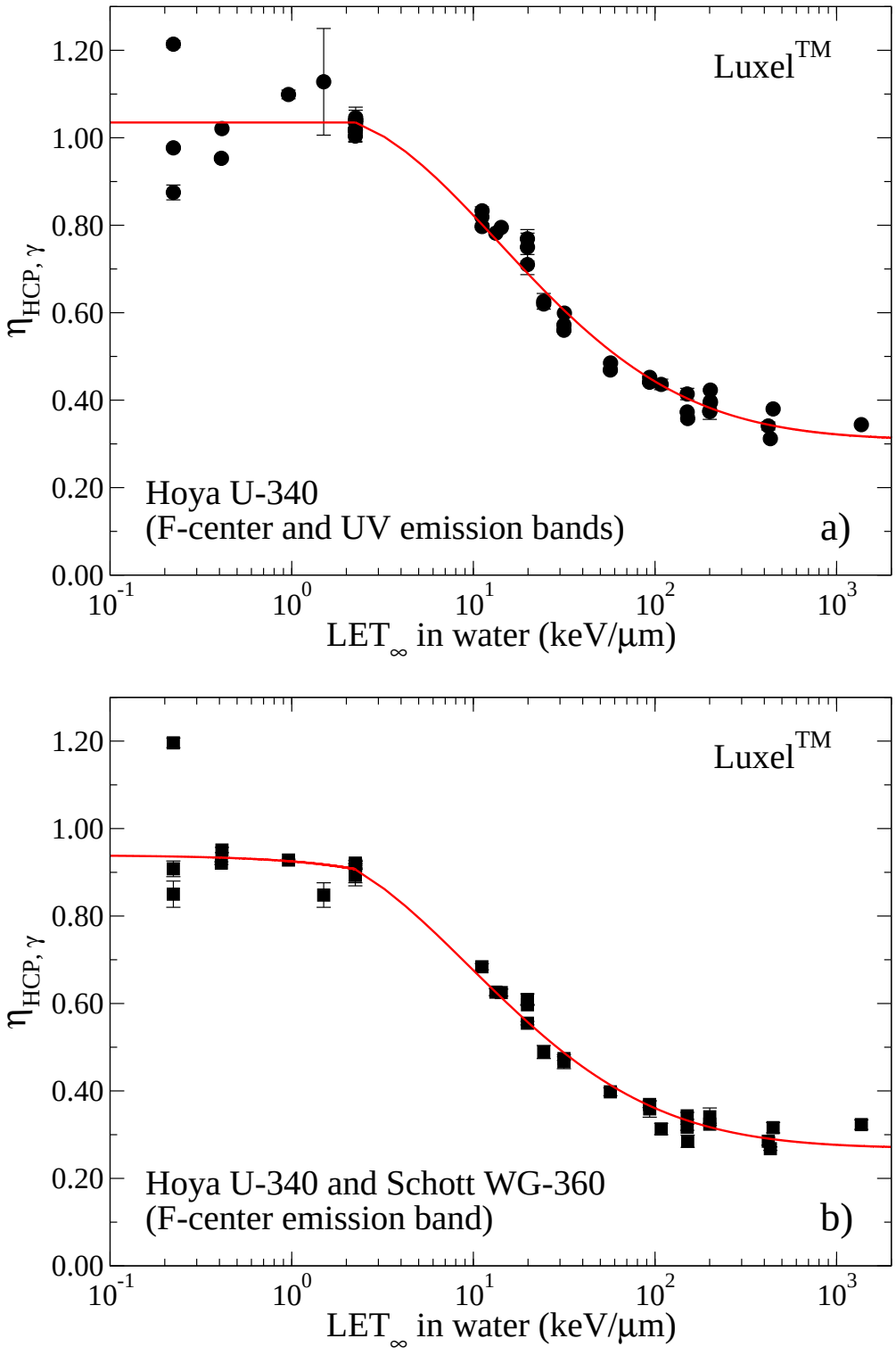

Figure 7.16: $\eta_{HCP,\gamma}$ calculated in water of Luxel™ detectors exposed to 24 different combinations of particles and energies. We considered the OSL signal equal to the total area under the OSL curve. a) OSL measured with Hoya U-340 filter detecting both F-center and UV emission bands, and b) OSL measured with combination of Schott WG-360 and Hoya U-340 filters detecting F-center emission band. Red lines are arbitrary functions that fit the data for better visualization.

that the $\eta_{HCP,\gamma}$ in Al_2O_3:C is ultimately characterized by the behavior of the point defects responsible for the detected luminescence signal (Yukihara et al., 2004a).

Figure 7.17 shows the luminescence response function $f(D)$ to low LET beta radiation (Figure 7.17a), and $\eta_{HCP,\gamma}$ *versus* L_∞ in water (Figure 7.17b). We observe larger supralinearity and larger values of $\eta_{HCP,\gamma}$ for OSL measured with Hoya U-340 filter compared to the supralinearity and $\eta_{HCP,\gamma}$ values for OSL measured with combination of Hoya U-340 and Schott WG-360 filters. Thus, for OSL measured with Hoya U-340 filter the larger $\eta_{HCP,\gamma}$ values correlate with the larger supralinearity in the dose response function compared to the OSL measured with combination of Hoya U-340 and Schott WG-360 filters.

7.3.2 BINARY FILTER DATA

We placed binary filters of known thicknesses and materials between the primary beam and the detectors to decrease the energy of the following primary beams: H 40 MeV, He 150 MeV/u, Ne 400 MeV/u and Si 490 MeV/u.

Figure 7.18 presents the $\eta_{HCP,\gamma}$ of Luxel™ detectors obtained using this approach. The data in Figure 7.18 shows that the $\eta_{HCP,\gamma}$ decreases much faster as a function of LET when compared to the data for bare beams showed in Figure 7.16. Also, we note that the $\eta_{HCP,\gamma}$ versus LET does not obey a single curve.

The HCP creates a pattern of energy deposition around its track that is characteristic of the HCP charge and energy. Thus, particles with the same LET, but different charges and energies create different patterns of energy deposition. As an example, we performed Monte Carlo simulations with the code GEANT4 in Al_2O_3:C, density 3.97 g/cm^3, with He 9.810 MeV/u (L_∞ in water of 18.76 keV/μm), and O 385.5 MeV/u (L_∞ in water of 19.84 keV/μm) which present approximately the same LET, but different charges and energies. Although the total energy transferred per path length is approximately the same for both particles (same LET), Figure 7.19 shows that the pattern the energy is distributed around the path of the HCPs is completely different.

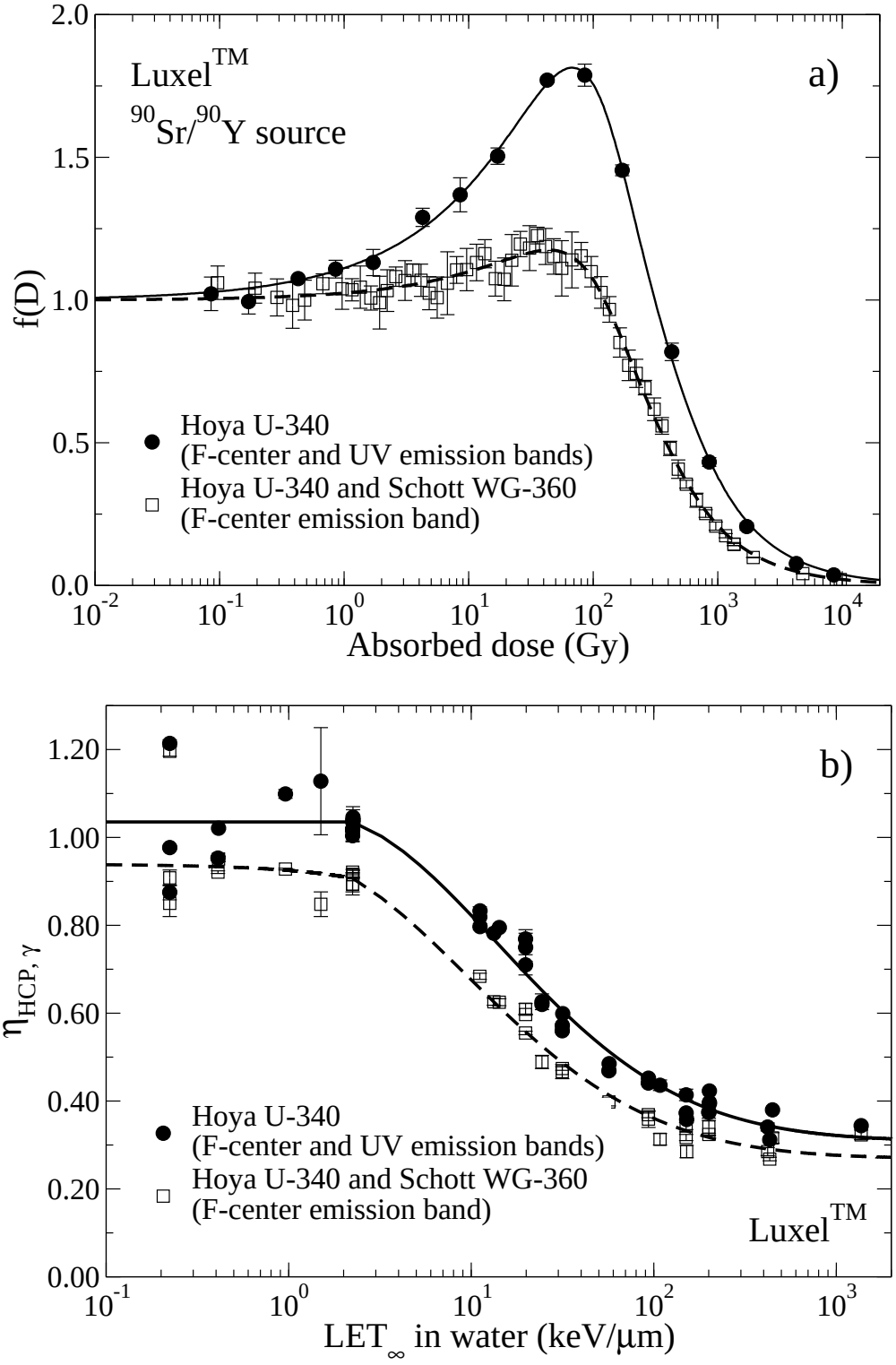

Figure 7.17: a) Luminescence response function of Luxel™ detectors irradiated with beta rays. b) $\eta_{HCP,\gamma}$ *versus* L_∞ in water of Luxel™ detectors exposed to different combinations of particles and energies. a) and b) the full symbols represent the OSL detected with Hoya U-340 filters, open symbols represent the OSL detected with combination of Schott WG-360 and Hoya U-340 filters, and full and dashed lines are arbitrary functions fitted to the data for better visualization.

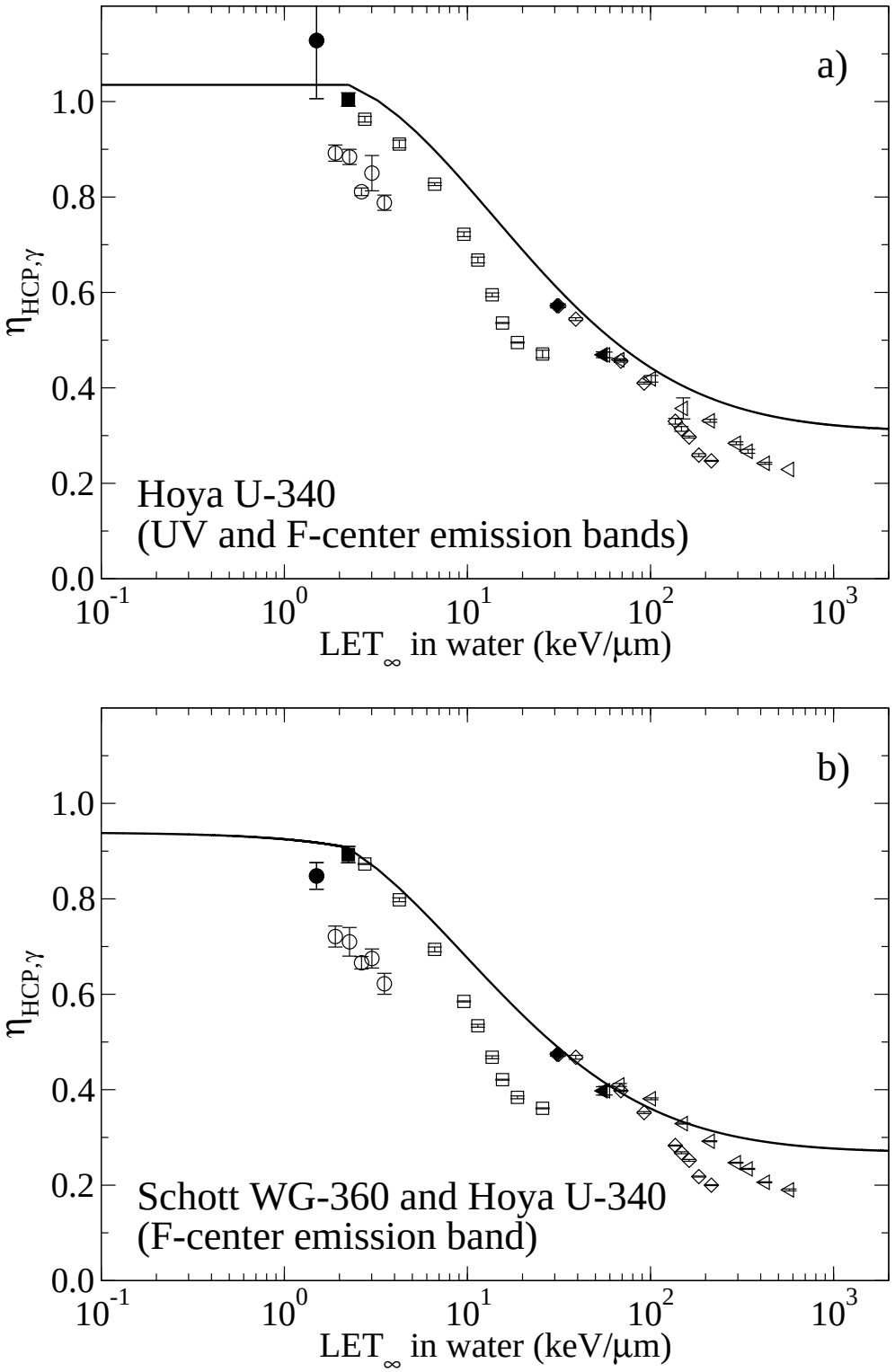

Figure 7.18: $\eta_{HCP,\gamma}$ calculated in water of Luxel^{TM}detectors. The full line represents the bare beam experimental data. The full symbols represent the bare beam data of the H 40 MeV, He 150 MeV/u, Ne 400 MeV/u and Si 490 MeV/u beams. The open symbols represent data obtained by placing binary filters in front of the H 40 MeV, He 150 MeV/u, Ne 400 MeV/u and Si 490 MeV/u to stop the primary particles. a) OSL detected with Hoya U-340 filter, and b) OSL detected with combination of Schott WG-360 and Hoya U-340 filters.

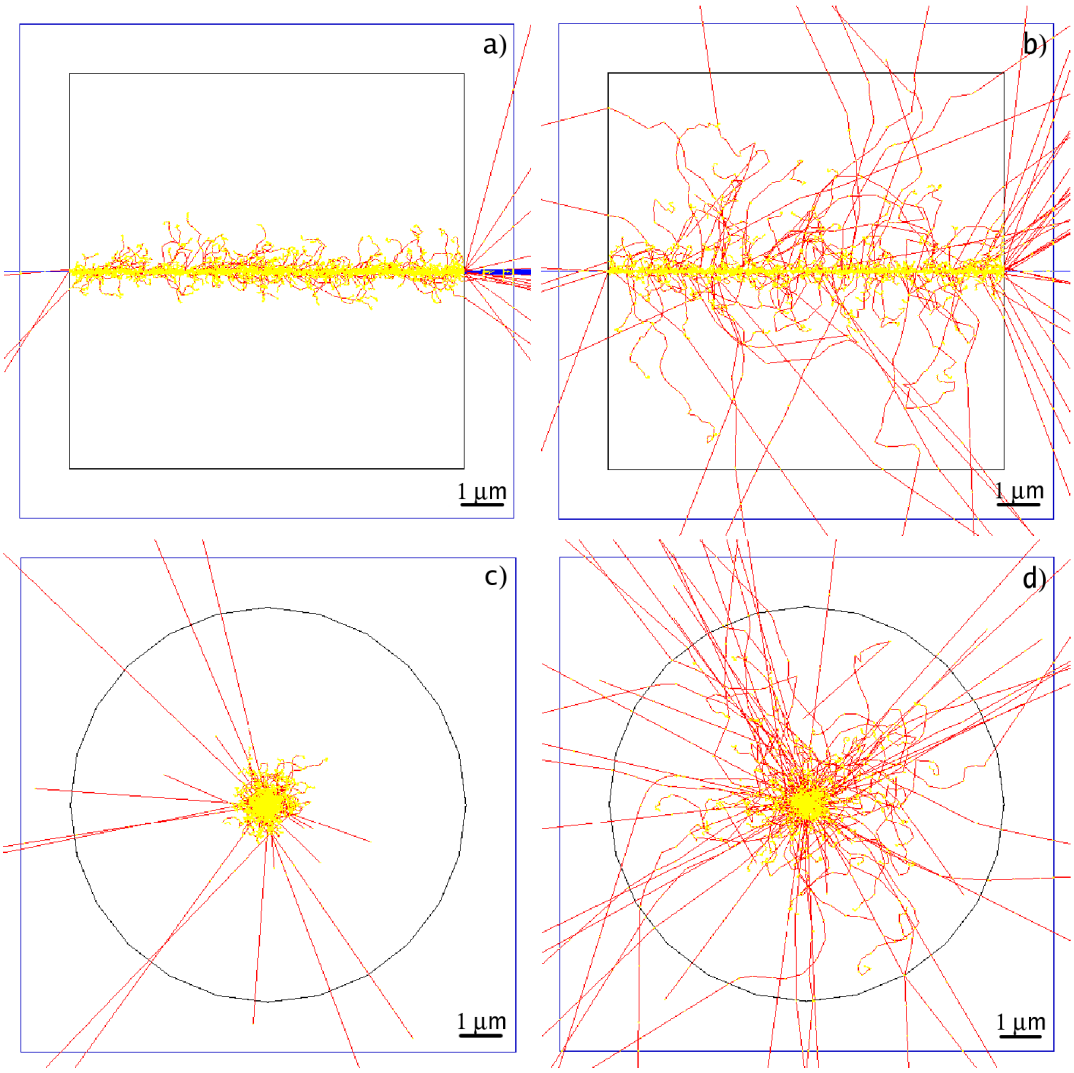

Figure 7.19: Monte Carlo simulations with GEANT4 in Al_2O_3:C, density 3.97 g/cm^3, with a) and c) He 9.810 MeV/u (L_∞ in water of 18.76 keV/μm); and b) and d) O 385.5 MeV/u (L_∞ in water of 19.84 keV/μm). The number of particles for both beams were 50.

The luminescence of the detectors is intrinsically related to the events of energy deposition. Therefore, different patterns of energy deposition causes different luminescence yields. Figure 7.18 shows that for particles with similar LETs, the particles with lower charge and energy presents lower $\eta_{HCP,\gamma}$. The lower $\eta_{HCP,\gamma}$ is due to a more concentrated spatial pattern of energy deposition.

In summary, this chapter added a significant amount of information on the OSL response of Al_2O_3:C detectors exposed to HCP, including: i) $\eta_{HCP,\gamma}$ data for 19 new combi-

nations of particles and energies; ii) $\eta_{HCP,\gamma}$ data for various energies of the same particle (H 40 MeV, He 150 MeV/u, Ne 400 MeV/u and Si 490 MeV/u); iii) $\eta_{HCP,\gamma}$ data for different detection windows to study the role of the UV emission band; and iv) detailed study of the luminescence response to different ionization densities and large range of doses and fluences.

CHAPTER 8

PREDICTIONS OF RELATIVE LUMINESCENCE EFFICIENCY USING THE TRACK STRUCTURE MODEL

This chapter tests the track structure model (TSM) presented in chapter 3 for different RDD analytical models (chapter 4) and simulation (chapter 5). Additionally, we propose a modified version of Butts and Katz model.

As previously discussed, the $\eta_{HCP,\gamma}$ experimental data is usually calculated using values referenced in absorbed dose to water. On the other hand, the TSM leads to $\eta_{HCP,\gamma}$ values based on the absorbed dose in the material. Thus, appropriate comparison between model and experimental data is only possible if we know the conversion factors that transform the $\eta_{HCP,\gamma}$ calculated in the detector's material to water. Section 8.1 presents a discussion on the definition of the $\eta_{HCP,\gamma}$ and determines the appropriate conversion factors to transform the $\eta_{HCP,\gamma}$ calculated in the detector's material to $\eta_{HCP,\gamma}$ calculated in water.

Moreover, evaluation of the $\eta_{HCP,\gamma}$ expression obtained through TSM is only possible if we determine the test radiation that reproduces as close as possible the delta ray energy spectrum created by the incident particle. Section 8.2 presents a discussion on the choice of the test radiation for Luxel^{TM} detectors.

Finally, we calculate the $\eta_{HCP,\gamma}$ through the RDD analytical models presented in chapter 4 and simulations presented in chapter 5. Additionally, we introduce a modification of the Butts and Katz model, which improves the predictions of $\eta_{HCP,\gamma}$.

8.1 RELATIVE LUMINESCENCE EFFICIENCY CALCULATED IN WATER AND IN THE DETECTOR'S MATERIAL

Defining the $\eta_{HCP,\gamma}$ of HCP relative to gamma radiation in terms of the absorbed dose (chapter 3, eq. 3.3), we have:

$$\eta_{HCP,\gamma} = \frac{S_{HCP}(D_{HCP})}{D_{HCP}} \Big/ \frac{S_{\gamma}(D_{\gamma})}{D_{\gamma}} \tag{8.1}$$

where D_{HCP} and D_{γ} are absorbed doses in the region where the luminescence signals S_{HCP} and S_{γ} of the detector behave linearly. In principle, if no saturation occurs, if $W_{HCP} = W_{\gamma}$, and $\eta_{\delta,\gamma} = 1$, the $\eta_{HCP,\gamma}$ value is unity. This is strictly true only if the absorbed doses D_{HCP} and D_{γ} in eq. 8.1 are defined in the material and the dose response is linear. However, the $\eta_{HCP,\gamma}$ is defined in terms of absorbed dose to water, since this quantity is readily available

$$\eta^{H_2O}_{\mathrm{HCP},\gamma} = \frac{S_{HCP}/D^{H_2O}_{HCP}}{S_{\gamma}/D^{H_2O}_{\gamma}} \tag{8.2}$$

The ratio between the relative luminescence efficiencies defined in water and detector's material is given by

$$\frac{\eta^{H_2O}_{\mathrm{HCP},\gamma}}{\eta^{m}_{\mathrm{HCP},\gamma}} = \frac{D^{H_2O}_{\gamma}}{D^{m}_{\gamma}} \times \frac{1/D^{H_2O}_{HCP}}{1/D^{m}_{HCP}} \tag{8.3}$$

The ratio between gamma absorbed doses in different materials is given by the ratio between the mass-energy absorption coefficients $(\mu_{en}/\rho)^m_{\gamma}$ of the materials:

$$\frac{D^{H_2O}_{\gamma}}{D^{m}_{\gamma}} = \frac{(\mu_{en}/\rho)^{H_2O}_{\gamma}}{(\mu_{en}/\rho)^{m}_{\gamma}} \tag{8.4}$$

On the other hand, the ratio between HCP absorbed doses in different materials is given by the ratio between the material's density and LET:

$$\frac{1/D^{H_2O}_{HCP}}{1/D^{m}_{HCP}} = \frac{\rho_{H_2O}/L^{H_2O}_{\infty}}{\rho_m/L^{m}_{\infty}} \tag{8.5}$$

Thus, the relationship between $\eta_{HCP,\gamma}$ for absorbed dose to water and absorbed dose to the detector's material is given by

$$\frac{\eta_{HCP,\gamma}^{H_2O}}{\eta_{HCP,\gamma}^{m}} = \frac{(\mu_{en}/\rho)_{\gamma}^{H_2O}}{(\mu_{en}/\rho)_{\gamma}^{m}} \times \frac{\rho_{H_2O}/L_{\infty}^{H_2O}}{\rho_m/L_{\infty}^{m}} = \alpha_m^{H_2O}(E, L_{\infty}^{H_2O,m}) \tag{8.6}$$

where $(\mu_{en}/\rho)_{\gamma}^{H_2O}$ and $(\mu_{en}/\rho)_{\gamma}^{m}$ are the mass-energy absorption coefficients in water and in the material of the detector for gamma rays from a ^{60}Co source, respectively. The ratio between $\eta_{HCP,\gamma}$ calculated in water and in detector's material is a constant for a given type of particle and energy, and fixed reference radiation field. We call this constant the conversion factor $\alpha_m^{H_2O}(E, L_{\infty}^{H_2O,m})$, where E is the energy of the photon from the reference radiation field. This relationship shows that the $\eta_{HCP,\gamma}$ defined in eq. 8.2 for a "perfect" detector is different from unity (for low-LET radiation in which the luminescence does not saturate in regions close to the path of the incident particle), but depends on the detector's material. Assuming a ^{60}Co reference source (mean photon energy of 1.25 MeV) and Al_2O_3:C as the detector's material, the ratio between the mass-energy absorption coefficients can be evaluated and the conversion factor $\alpha_{Al_2O_3:C}^{H_2O}(1.25\ \mathrm{MeV}, L_{\infty}^{H_2O,Al_2O_3:C})$ become

$$\alpha_{Al_2O_3:C}^{H_2O}(1.25\ \mathrm{MeV}, L_{\infty}^{H_2O,Al_2O_3:C}) = 1.134 \times \frac{\rho_{H_2O}/L_{\infty}^{H_2O}}{\rho_{Al_2O_3:C}/L_{\infty}^{Al_2O_3:C}} \tag{8.7}$$

The mass-energy absorption coefficient data were taken from the NIST database (Hubbell and Seltzer, 2004). There are no available mass-energy absorption coefficient data of Al_2O_3. Thus, we used the data from aluminum and oxygen weighted by the mass fraction of this elements in Al_2O_3 (Johns and Cunningham, 1983). Table 8.1 shows the conversion factor $\alpha_{Al_2O_3:C}^{H_2O}(1.25\ \mathrm{MeV}, L_{\infty}^{H_2O,Al_2O_3:C})$ for Al_2O_3:C detectors and for the particles and energies used in this work, and Figure 8.1 shows the comparison between the $\eta_{HCP,\gamma}$ values calculated in water and Al_2O_3:C. As an example we consider the H 230 MeV beam in

which

$$\eta_{HCP,\gamma}^{H_2O} = 0.934 \times \eta_{HCP,\gamma}^{Al_2O_3:C} \tag{8.8}$$

The dose response function to beta radiation of the F-center emission band in Al_2O_3:C presents only a small supralinearity (Figure 7.1). Thus, we expect $\eta_{HCP,\gamma}^{Al_2O_3:C}$ values close to unity for low-LET HCP beams, i.e. beams that do not saturate the luminescence of the detector in regions close to the HCP path, such as H 230 MeV. Assuming the OSL $\eta_{HCP,\gamma}^{Al_2O_3:C}$ equals to unity for low-LET HCP particles, the result of eq. 8.8 for the H 230 MeV beam shows good agreement with the experimental OSL $\eta_{HCP,\gamma}$ calculated in water of 0.951 ± 0.006 (Table A.1).

The values of OSL $\eta_{HCP,\gamma}$ larger than unity for Luxel™ detectors calculated in water when detecting both F-center and UV emission bands (Table A.1) are due to the large supralinearity observed in the response function of the detector irradiated with beta radiation (Figure 7.1).

8.2 TEST RADIATION TO SIMULATE THE DELTA RAY SPECTRUM

Under conditions of electronic equilibrium, the absorbed dose D_m in the material m is (Johns and Cunningham, 1983):

$$D^m = \Phi \bar{E}_{ab} (\mu_{en}/\rho)^m \tag{8.9}$$

where Φ is the fluence of photons, $\bar{E}_{ab}$ is the part of the average kinetic energy transferred to electrons that contribute to ionizations, and $(\mu_{en}/\rho)^m$ is the mass-energy absorption coefficient of the material.

For the same type of radiation k and same photon fluence Φ, the ratio between the absorbed dose in two different materials is:

$$\frac{D_k^{m_1}}{D_k^{m_2}} = \frac{(\mu_{en}/\rho)_k^{m_1}}{(\mu_{en}/\rho)_k^{m_2}} \tag{8.10}$$

Table 8.1: Conversion factor $\alpha^{H_2O}_{Al_2O_3:C}(1.25\ \mathrm{MeV}, L_\infty^{H_2O,Al_2O_3:C})$ to transform the $\eta_{HCP,\gamma}$ calculated to Al_2O_3:C to the one calculated to water or vice-versa.

Beam	Energy (MeV/u)	L_∞ in H_2O (keV/μm)	L_∞ in Al_2O_3:C (keV/μm)	$\alpha^{H_2O}_{Al_2O_3:C}$
H 1000 MeV	1000	0.223	0.734	0.943
H 230 MeV	230	0.413	1.35	0.934
H 70 MeV	70	0.960	3.10	0.923
H 40 MeV	40	1.50	4.79	0.910
H 30 MeV	30	1.90	6.02	0.906
He 150 MeV/u	144.2	2.24	7.31	0.930
H 24 MeV	24	2.27	7.19	0.903
H 20 MeV	20	2.64	8.31	0.900
H 17 MeV	17	3.01	9.45	0.897
H 14 MeV	14	3.52	11.02	0.894
C 400 MeV/u	386.9	11.14	36.52	0.936
C 290 MeV/u	277.2	13.30	43.51	0.935
O 1000 MeV/u	1000	14.24	46.97	0.942
O 400 MeV/u	385.5	19.84	65.03	0.936
C 135 MeV/u	111.2	24.41	79.28	0.928
Ne 400 MeV/u	371.9	31.55	103.4	0.937
Si 490 MeV/u	444.8	56.80	186.4	0.938
Ar 500 MeV/u	450.7	93.34	306.4	0.938
Ti 1000 MeV/u	977.6	108.2	356.9	0.942
Fe 1000 MeV/u	967.0	151.4	499.4	0.949
Fe 500 MeV/u	423.7	200.3	657.0	0.938
Fe 200 MeV/u	120.4	431.8	1403	0.928
Kr 400 MeV/u	313.1	447.2	1464	0.935
Xe 290 MeV/u	185.5	1368	4462	0.932

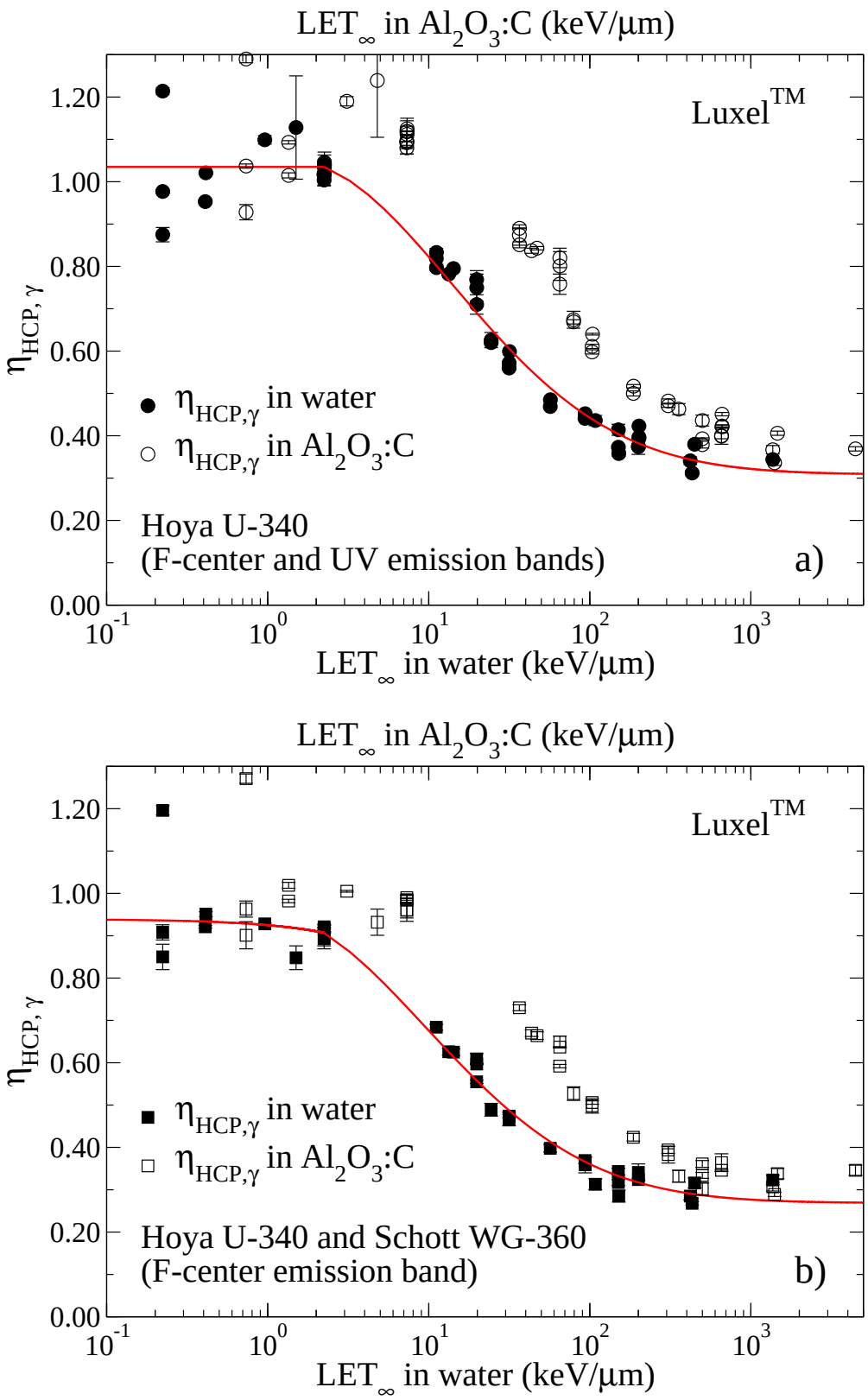

Figure 8.1: $\eta_{HCP,\gamma}$ calculated in water and Al_2O_3:C of Luxel™ detectors. a) OSL measured with Hoya U-340 filter detecting both F-center and UV emission bands, and b) OSL measured with combination of Schott WG-360 and Hoya U-340 filters detecting F-center emission band. Red lines are arbitrary functions that fit the $\eta_{HCP,\gamma}$ data calculated in water for better visualization.

In medical dosimetry it is common to calibrate the detector against a ^{60}Co source in absorbed dose to water. Thus,

$$\frac{(D^{m_1}/D^{H_2O})_k}{(D^{m_1}/D^{H_2O})_\gamma} = \frac{[(\mu_{en}/\rho)^{m_1}/(\mu_{en}/\rho)^{H_2O}]_k}{[(\mu_{en}/\rho)^{m_1}/(\mu_{en}/\rho)^{H_2O}]_\gamma} \tag{8.11}$$

For the same type of radiation and material, the luminescence signal is proportional to the absorbed dose. However, for different radiation types and materials, the partition of absorbed energy through excitations and ionizations varies. Ionizations create free electrons which are trapped in the main dosimetric trap and are responsible for the luminescence. Thus, in luminescence dosimetry the luminescence signal is ultimately proportional to the trapped number of secondary electrons produced by the primary radiation. The luminescence signal S from a detector made of material m exposed to the radiation field k is given by (see eq. 3.11):

$$S_k^m = \alpha\eta_k(D_0)f_k^m(D)D_k^m\rho_m V \tag{8.12}$$

where α is the efficiency of the experimental apparatus, η_k is the luminescence efficiency to the radiation field k for low doses D_0, $f_k^m(D)$ is the luminescence response function, D_k^m is the absorbed dose to the material m, ρ_m is the density of the material, and V is the irradiated volume.

Usually, the literature compares the luminescence response for different types of radiation relative to the response of a ^{60}Co source calibrated in absorbed dose to water:

$$\frac{(S/D^{H_2O})_k}{(S/D^{H_2O})_\gamma} = \eta_{k,\gamma}\frac{(D^m/D^{H_2O})_k}{(D^m/D^{H_2O})_\gamma} \tag{8.13}$$

where $\eta_{k,\gamma}$ is the relative luminescence efficiency between the radiation k and gamma. We assume that the dose is in the linear range of the detector's response, thus, $f(D) = 1$.

Substituting eq. 8.11 in eq. 8.13 we have:

$$\frac{(S/D^{H_2O})_k}{(S/D^{H_2O})_\gamma} = \eta_{k,\gamma}\frac{[(\mu_{en}/\rho)^m/(\mu_{en}/\rho)^{H_2O}]_k}{[(\mu_{en}/\rho)^m/(\mu_{en}/\rho)^{H_2O}]_\gamma} \tag{8.14}$$

The detector presents an "anomalous" energy response if the relative response of the detector deviates from the ratio between the mass energy absorption coefficients (eq. 8.14), indicating that the factor $\eta_{k,\gamma}$ changes with energy and differs from unity. This anomaly was partially explained using the microdosimetric approach (Olko, 2002) as being caused by the ionization density created by different photon energies.

For gases, the average energy required to create an electron pair W_k strongly increases for electron energies lower than around 1 keV (ICRU, 1979; IAEA, 1995). This increase in W_k is related to the increase in the energy absorbed through excitations in the partition of absorbed energy through excitations and ionizations (ICRU, 1979; IAEA, 1995). Thus, for low electron energies, the number of secondary electrons created by ionization events is smaller when compared to the high energy case. Indeed, the response of detectors is anomalous only for low energy photons where the contribution of low energy electrons is important to the events of absorption of energy. The luminescence signal is ultimately proportional to the trapped number of secondary electrons produced by the primary radiation. Thus, we suggest that the so-called anomalous response of luminescence detectors is also related to the increasing in the average energy required to create an electron-hole pair, which is implicitly incorporated into $\eta_{k,\gamma}$ (see eq. 3.21), for low electron energies and consequently decrease in the efficiency in which the primary radiation creates secondary electrons. Unfortunately, the lack of W_k data for TLD and OSLD materials makes impossible testing our suggestion.

Figure 8.2 presents the ratio of mass-energy absorption coefficients between Al_2O_3 and water, normalized to the mean energy of ^{60}Co gamma rays (1.25 MeV). The data are from the NIST database (Hubbell and Seltzer, 2004). We also plot in Figure 8.2 TL

data for different photon energies from Al_2O_3:C (Akselrod et al., 1990). The TL data was normalized to the mean energy of ^{60}Co gamma rays.

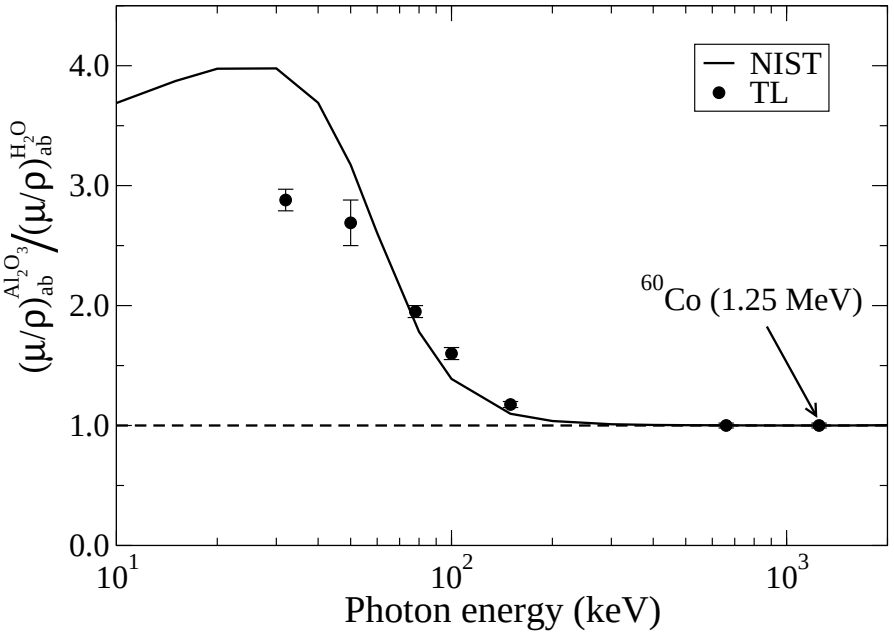

Figure 8.2: The solid line represents the ratio between the mass-energy absorption coefficients of Al_2O_3 and water, normalized to the mean energy of ^{60}Co gamma rays. Solid circles represent the relative TL of Al_2O_3:C normalized to the mean energy of ^{60}Co gamma rays. The TL data are from the literature (Akselrod et al., 1990) and mass-energy absorption coefficient data are from the NIST database (Hubbell and Seltzer, 2004).

Figure 8.2 shows that the TL yield of Al_2O_3:C follows its mass-energy absorption coefficient for photons with energy larger than 80 keV. Thus, down to 80 keV photons $\eta_{k,\gamma}$ is approximately equal to unity. For energies lower than 80 keV the TL data is lower than the mass-energy absorption coefficient, indicating that $\eta_{k,\gamma} < 1$. Data from Olko et al. (2006) and unpublished OSL[1] results show the same behavior.

We now discuss the influences of the TL and OSL anomalous energy dependence on the relative luminescence efficiency formula derived using TSM.

For completeness we rewrite the equation derived in chapter 3 that calculates the $\eta_{HCP,\gamma}$ using TSM.

$$\eta_{HCP,\gamma} = \frac{\int_0^{R_{Max}} \eta_{\delta,\gamma} f_X[D(r)] \rho_m D(r) 2\pi r dr}{\int_0^{R_{Max}} \rho_m D(r) 2\pi r dr} \tag{8.15}$$

[1]Dr. M. Akselrod personal communication, Landauer, Inc.

where

$$\eta_{\delta,\gamma} = \eta'_{\delta,\gamma} \frac{1/W_{HCP}}{1/W_{\gamma}} \tag{8.16}$$

$\eta_{HCP,\gamma}$ is the relative luminescence efficiency from the HCP field in respect to gamma radiation from a ^{60}Co source calculated in the linear range of the dose response curve; $\eta_{\delta,\gamma}$ is the relative luminescence efficiency between secondary electrons and gamma radiation; $\eta'_{\delta,\gamma}$ is the ratio between the efficiency to convert the low energy charges created by the HCP and gamma rays into luminescence; R_{Max} is the maximum radial distance a delta ray can travel; f_X is the response function of the detector to the test radiation field X obtained for doses in the detector's material; $D(r)$ is the RDD function calculated in the detector's material; ρ_m is the density of the detector; and r is the radial distance.

The factor $\eta_{\delta,\gamma}$ in eq. 8.15 can be determined from the luminescence response to different photon energies (see eq. 8.14). HCP produces secondary electrons with energies ranging from 0 eV to up to a few MeV, depending on the energy of the HCP. Thus, for accurate determination of $\eta_{HCP,\gamma}$, we must provide $\eta_{\delta,\gamma}$ data for the entire energy spectrum. Indeed, the RDD models show that low energy secondary electrons are responsible for a large part of the dose. Using Butts and Katz model we determined that for a 1000 MeV/u particle about 90 % of the secondary electrons have energies lower than 80 keV. Thus, for HCP energies lower than 1000 MeV/u most of the secondary electrons have energies lower than 80 keV, indicating that the Luxel^{TM} detectors are in the anomalous energy response region for all the particles used in this study.

We have only accurate dose response data for beta rays from a ^{90}Sr/^{90}Y source. Thus, we used beta rays as the test radiation. Moreover, to simplify the $\eta_{HCP,\gamma}$ calculations we approximate $\eta_{\delta,\gamma} = 1$ for the entire energy spectrum of the secondary electrons produced by the HCP. We encourage further investigations to determine the best compromise test radiation and the factor $\eta_{\delta,\gamma}$. We consider the use of beta rays as the test and the approximation $\eta_{\delta,\gamma} = 1$ limitations in our approach.

Thus, considering ^{90}Sr/^{90}Y source (calibrated against a ^{60}Co source) as the test radiation

X, and $\eta_{\delta,\gamma}(D_0) = 1$, eq. 8.15 can be written as

$$\eta_{HCP,\gamma}^{Al_2O_3:C} = \frac{\int_0^{R_{Max}} f_\beta^{Al_2O_3:C}[D(r)]\rho_{Al_2O_3:C}D(r)2\pi r dr}{\int_0^{R_{Max}} \rho_{Al_2O_3:C}D(r)2\pi r dr} \tag{8.17}$$

We explicitly wrote the index Al_2O_3:C to emphasize that the $\eta_{HCP,\gamma}$ is calculated in the detector's material. Eq. 8.6 and Table 8.1 provide the ingredients to transform $\eta_{HCP,\gamma}$ calculated in the detector's material to $\eta_{HCP,\gamma}$ calculated in water. Throughout this chapter all $\eta_{HCP,\gamma}$ values are properly converted into $\eta_{HCP,\gamma}$ values calculated in water.

8.3 RELATIVE LUMINESCENCE EFFICIENCY OBTAINED USING ANALYTICAL MODELS OF RADIAL DOSE DISTRIBUTION

We used the RDD analytical models presented in chapter 4 together with eq. 8.17 to calculate $\eta_{HCP,\gamma}$. To evaluate eq. 8.17 we first converted the OSL dose response *versus* absorbed dose to water (Figure 7.1) to the OSL dose response *versus* absorbed dose to Al_2O_3:C using the ratio between the mass-energy absorption coefficients in water and Al_2O_3 for the mean photon energy of 1.25 MeV for a ^{60}Co source:

$$\frac{D_{Al_2O_3}}{D_{H_2O}} = \frac{(\mu/\rho)_{ab}^{Al_2O_3}}{(\mu/\rho)_{ab}^{H_2O}} = 0.882 \tag{8.18}$$

The response functions from Luxel™ detectors for absorbed dose to Al_2O_3:C when detecting F-center and UV emission bands (Hoya U-340 filter), and when detecting F-center emission band only (Hoya U-340 and Schott WG-360 filters) were parameterized with the following expression:

$$f_\beta^{Al_2O_3:C}(D) = \frac{(1 - e^{-A_0 D})}{(A_0 D)} + \frac{A_1(1 - e^{-A_2 D^{A_3}})}{(A_0 D)} \tag{8.19}$$

Table 8.2 gives the parameters A_0, A_1, A_2 and A_3 for each detection window and Figure 8.3 shows the experimental data and the fitted functions.

Table 8.2: Values of the parameters A_0, A_1, A_2 and A_3 from the fitting of the response function versus absorbed dose to Al_2O_3:C (eq. 8.19).

	Luxel^{TM} detector	
	U-340 (F-center and UV emission)	WG-360 and U-340 (F-center)
A_0 (Gy^{-1})	$4.52 \times 10^{-3} \pm 0.39 \times 10^{-3}$	$6.65 \times 10^{-3} \pm 0.46 \times 10^{-3}$
A_1	$5.35 \times 10^{-1} \pm 0.75 \times 10^{-1}$	$2.34 \times 10^{-1} \pm 0.46 \times 10^{-1}$
A_2 (Gy$^{-A_3}$)	$1.04 \times 10^{-3} \pm 0.08 \times 10^{-3}$	$8.47 \times 10^{-4} \pm 1.40 \times 10^{-3}$
A_3	1.57 ± 0.02	1.68 ± 0.05

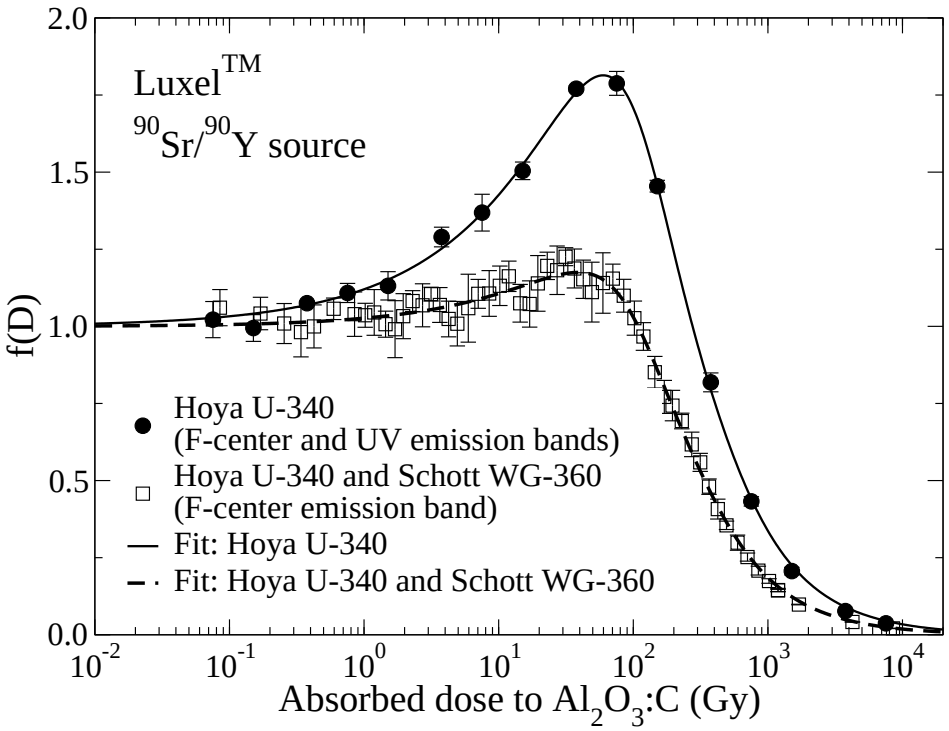

Figure 8.3: Luminescence response function of Luxel^{TM} detectors for absorbed dose to Al_2O_3:C. Full circles represent the data when detecting both F-center and UV emission bands. Empty squares represent the data when detecting only F-center emission band. Full and dashed lines represent the fitting to the data when detecting both F-center and UV emission bands, and only F-center emission band, respectively.

Substituting eq. 8.19 in eq. 8.17 we obtain the final expression used to calculate the $\eta_{HCP,\gamma}$:

$$\eta_{HCP,\gamma}^{Al_2O_3:C} = \frac{2\pi\rho_{Al_2O_3:C}}{A_0 L_\infty^{Al_2O_3:C}} \int_0^{R_{Max}} \left[(1 - e^{-A_0 D(r)}) + A_1(1 - e^{-A_2 D(r)^{A_3}})\right] r dr \qquad (8.20)$$

where $D(r)$ is the RDD model, and the integral was numerically evaluated using Maple 10 (Maplesoft™, 2005). Finally, we converted $\eta_{HCP,\gamma}^{Al_2O_3:C}$ calculated in Al_2O_3:C by eq. 8.20 to $\eta_{HCP,\gamma}$ calculated in water.

We represented the comparison between the $\eta_{HCP,\gamma}$ data and the modeling in terms of the percentage deviation:

$$\% = \left[1 - \frac{\eta_{HCP,\gamma}(Exp.)}{\eta_{HCP,\gamma}(Model)}\right] \times 100 \qquad (8.21)$$

Figures 8.4 and 8.5 present the comparison between $\eta_{HCP,\gamma}$ experimental data and modeling according to eq. 8.21. We included in Figures 8.4 and 8.5 only particles with range in Al_2O_3:C about three times larger than the thickness of the detector so that the approximation of constant LET is valid. Note that none of the models agree with experimental data in the whole range of LET. Different RDD analytical models leads to different predictions of $\eta_{HCP,\gamma}$. For $L_\infty^{H_2O}$ lower than around 100 keV/μm, the Chatterjee and Schaefer, Waligórski *et al.* and Fageeha *et al.* models overestimate the experimental data to about 50 %. For $L_\infty^{H_2O}$ lager than around 10 keV/μm, Butts and Katz, Kiefer and Straaten, and Geiß *et al.* models underestimate the experimental data to about 80 %.

From the calculations of OSL $\eta_{HCP,\gamma}$ using the RDDs of Chatterjee and Schaefer, Butts and Katz, Waligóski *et al.*, Fageeha *et al.*, Kiefer and Straaten, and Geiß *et al.* models we conclude that improvements needed to be done since the predictions present up to 80 % disagreement from data for the particles and energies of interest.

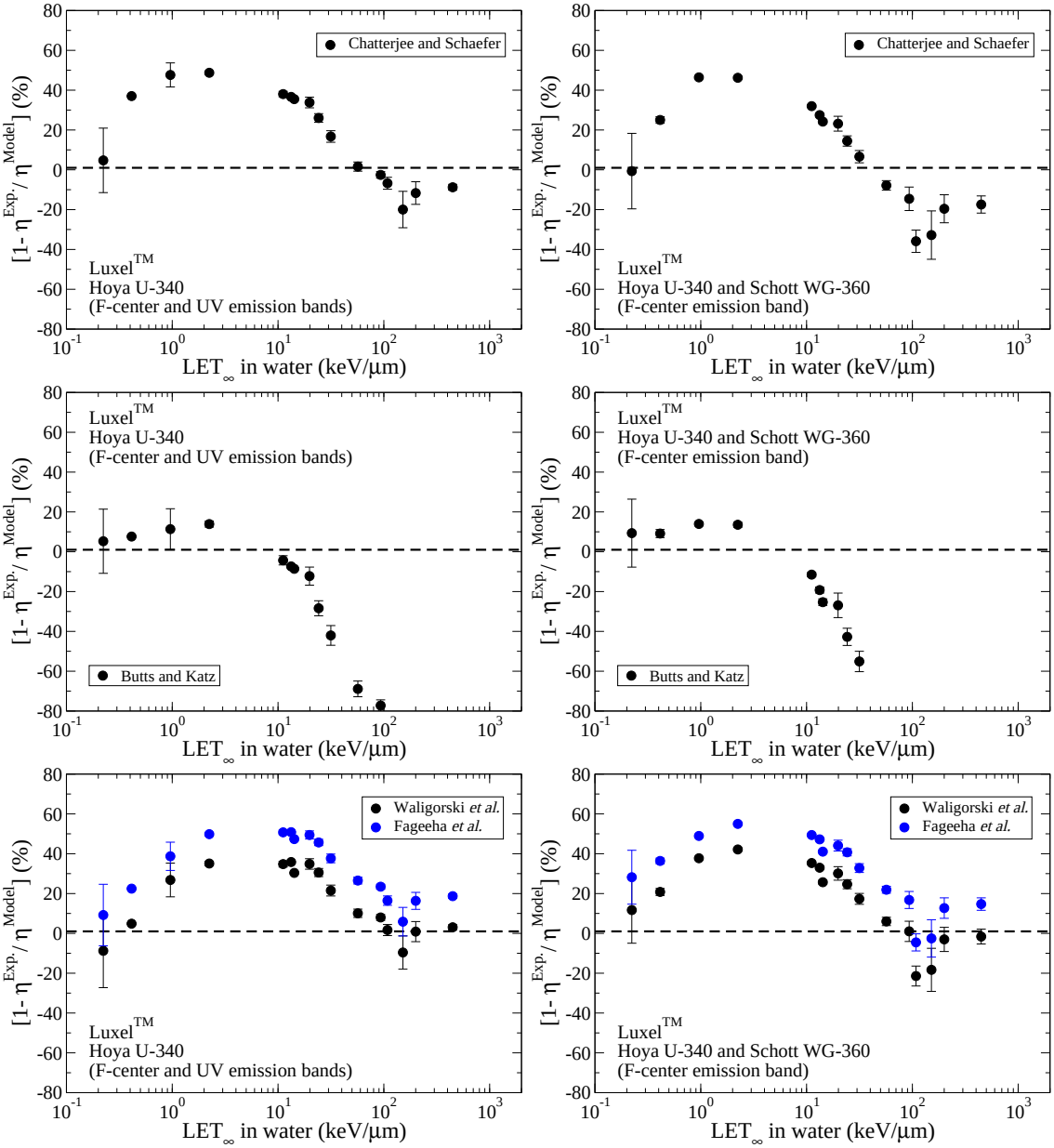

Figure 8.4: Comparison between OSL $\eta_{HCP,\gamma}$ experimental data and modeling using the RDD functions from Chatterjee and Schaefer, Butts and Katz, Waligórski *et al.* and Fageeha *et al.* models. The figures in the left side present the comparison for OSL detected with Hoya U-340 filters (F-center and UV emission bands), and the figures in the right side for OSL detected with Hoya U-340 and Schott WG-360 (F-center emission band).

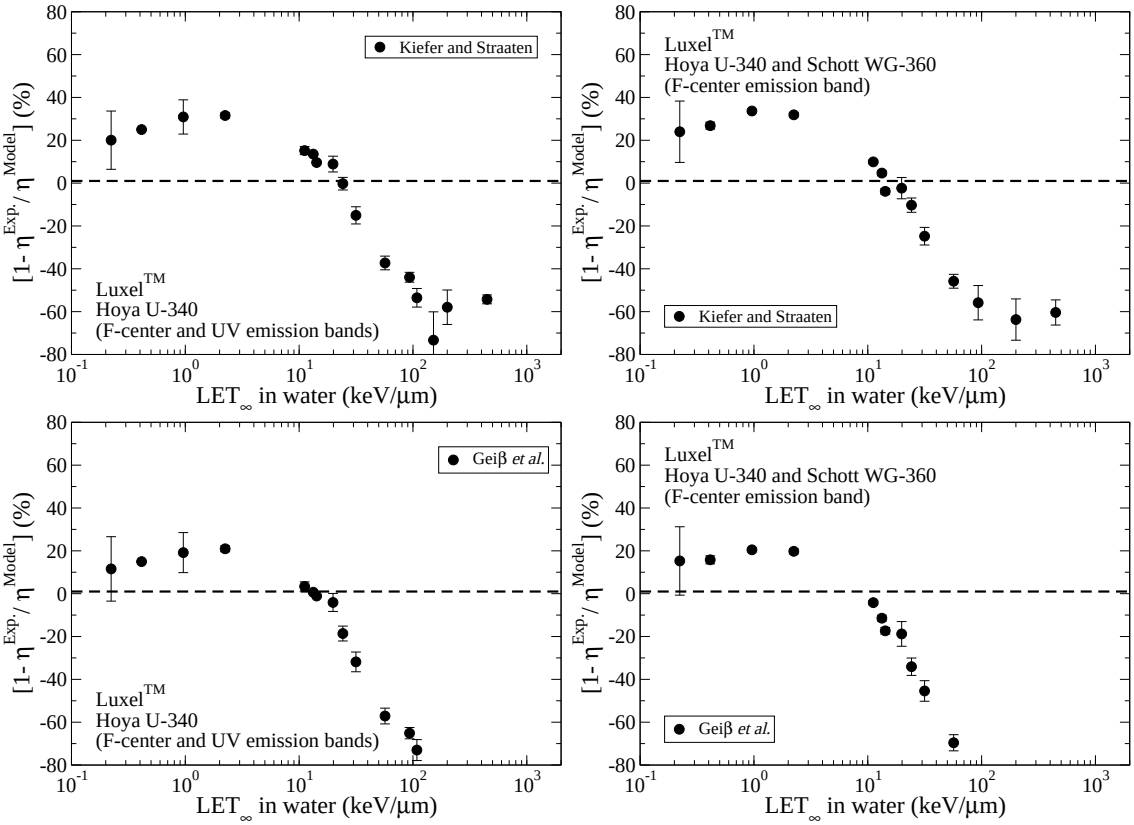

Figure 8.5: Comparison between OSL $\eta_{HCP,\gamma}$ experimental data and modeling using the RDD functions from Kiefer and Straaten, and Geiß *et al.* models. The figures in the left side present the comparison for OSL detected with Hoya U-340 filters (F-center and UV emission bands), and the figures in the right side for OSL detected with Hoya U-340 and Schott WG-360 (F-center emission band).

8.4 IMPROVEMENT OF BUTTS AND KATZ MODEL OF RADIAL DOSE DISTRIBUTION AND DETERMINATION OF RELATIVE LUMINESCENCE EFFICIENCY

Butts and Katz model of RDD uses the Rutherford's SDCS for production of secondary electrons. As discussed in section 4.2, Rutherford's formula considers only the ionization energy, excluding excitation energy. Therefore, estimation of the total energy transferred per path length (LET) leads to incorrect values.

Waligórski et al. (1986) and Fageeha et al. (1993) improved the estimation of LET by multiplying the RDD function derived in the Butts and Katz model by an arbitrary function, as discussed in section 4.2.

This section presents a modified version of the Butts and Katz model. We introduce a constant region of energy deposition for small radial distances. This constant region is similar to the definition of core in the Chatterjee and Schaefer, and Geiß *et al.* models. We determine the core region normalizing the total energy loss per path length to the LET of the particle. Hansen and Olsen (1984) used similar approach.

We modify Butts and Katz model adding a constant term representing the energy transferred by excitation and ionization. The final equation then becomes:

$$D(r) = \begin{cases} k, & 0 < r < r_c \\ \dfrac{N_e e^4}{m_e c^2} \dfrac{Z^{*2}}{\alpha \beta^2} \dfrac{1}{r} \left[\dfrac{\left(1 - \frac{r+r_0}{R_{Max}+r_0}\right)^{1/\alpha}}{r + r_0} \right], & r_c < r < R_{Max} \end{cases} \tag{8.22}$$

where r_0 is given by eq. 4.27, R_{Max} is parameterized as

$$R_{Max} = \frac{6.24 \times 10^6}{\rho_m} \left(\frac{\beta^2}{\kappa - \beta^2} \right)^{1.667} \tag{8.23}$$

where $\kappa = 1.5$ was determined by adjusting the relative luminescence efficiency values to

the experimental data.

The constant k is determined by normalizing the total energy loss per path length to the LET of the particle:

$$2\pi \int_0^{R_{Max}} rD(r)\, dr = \frac{L_\infty^m}{\rho_m} \tag{8.24}$$

We parameterize the radius of the core r_c using a function of the form:

$$r_c = A(1 - e^{-B\frac{Z^*}{\beta}}) \tag{8.25}$$

where we determine the constants A and B adjusting their values to fit three values of $\eta_{HCP,\gamma}$ data from Luxel™ detectors when F-center emission band is detected (Table A.1) – one value for low LET particle, one value in the intermediate range of LET and one value for high LET particle. Thus, we determine $A = 47.3$ nm, and $B = 0.145$.

To choose the form of the function 8.25, we consider that the core can be approximated by a region that depends not only on the properties of the detector, but also on the strength with which an incident particle can interact with the detector, represented by the saturated exponential term. Thus, the term between parentheses is an intrinsic property of the incident particle, such as charge and speed. The constant B has the same numerical value for all types of detectors. On the other hand, the constant A has dimension of length, relating to physical distances inside of the detector.

We also determined the constant A for the OSL from F-center and UV emission bands. A was determined fixing the value of $B = 0.145$ and adjusting the constant A such that the $\eta_{HCP,\gamma}$ fits three data points located: one in the low-LET region, one in the intermediate-LET region, and one in the high-LET region. A value of $A = 38.0$ nm was determined. Table 8.3 summarizes the values of the constant A and B for both detection windows.

Figure 8.6 shows RDD in Al_2O_3:C according to the modified version of Butts and Katz model. Note that the core radius depends on the properties of the defects related to the luminescence process. For comparison we also include in Figure 8.6 the Butts and Katz

Table 8.3: Values of the parameters A and B from eq. 8.25 to make RDD from the modified Butts and Katz model fit data for the two different filter sets.

	Luxel^{TM}detector	
	F-center and UV emissions	F-center emission
A	38.0 nm	47.3 nm
B	0.145	0.145

RDD.

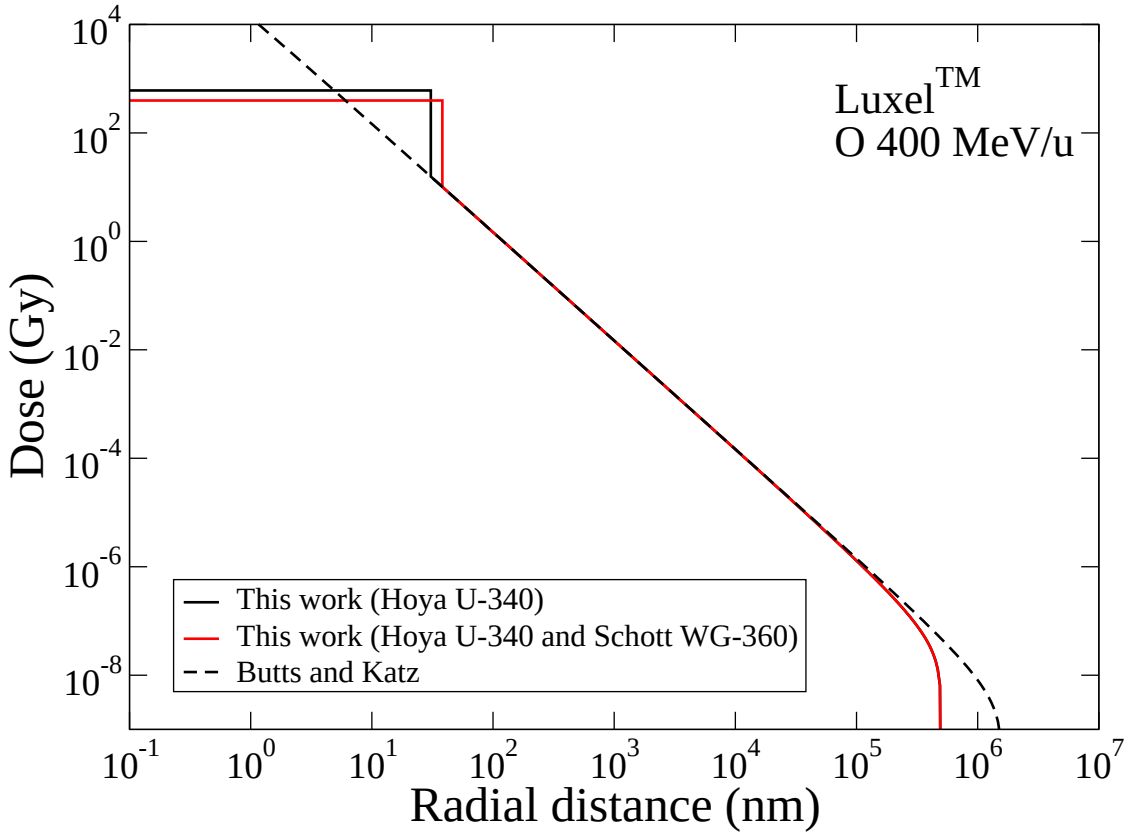

Figure 8.6: RDD in Al_2O_3:C according to the modified version of Butts and Katz model. The RDD was plotted for two different detection windows. For comparison we included the Butts and Katz RDD.

A physical interpretation of the constant A leads to a physical interpretation of the core region. Matter in such small regions can not be consider "continuous" and the definition of dose breaks down. Thus, the RDD core region as defined in our model is not the physical absorbed dose, but is related to the luminescence properties of the detector. It is not the

scope of this work to give a definitive interpretation of such region, but we would like to make comparisons between the determined A values in Luxel™ detectors and distances between the luminescence centers that take place in the OSL process in Al_2O_3:C.

Luxel™ detectors are made of Al_2O_3:C crystals in powder form. The luminescence centers responsible for the OSL process in Al_2O_3:C are the F-center and F^+-center, plus an unknown center with emission centered at 334 nm (see chapter 2). The concentration of F^+-centers in non-irradiated Al_2O_3:C crystals used to make the Luxel™ detectors is in the interval between[2] 0.5×10^{15} cm^{-3} and 2.0×10^{15} cm^{-3}. The concentration of F-centers is about one order of magnitude higher than the concentration of F^+-centers (Akselrod et al., 1993). By the concentration of centers, we estimate the average distance between defects to be in the range between 79 nm and 126 nm for F^+-centers, and in the range between 37 nm and 58 nm for F-centers.

The value of $A = 47.3$ nm obtained when detecting only F-center emission band is within the calculated (37-58) nm interval of the average distance between F-centers in Luxel™ detectors. Furthermore, for the OSL when detecting F-center and UV emission bands, in addition to the F-center, another unknown defect participates in the OSL process. In this case, the total concentration of defects participating in the OSL process is higher and the average distance between defects that participate in the OSL process is smaller than the case when detecting only the F-center emission band. Indeed, a lower value of $A = 38.0$ nm is obtained when detecting F-center and UV emission bands, correlating to the larger concentration of defects participating in the OSL process.

Although we observe a correlation between the maximum size of the core radius and the average distance between F-centers in Al_2O_3:C, we do not claim that this is a definitive physical interpretation. The definition of the core region presented in this subsection was with the purpose of finding a parameter that can be adjusted to improve the prediction of $\eta_{HCP,\gamma}$ in Luxel™ detectors.

[2] M. Akselrod, personal communication, Landauer Inc.

Figure 8.7 shows the comparison between the $\eta_{HCP,\gamma}$ calculated using the RDD from the modified version of the Butts and Katz model and experimental data for the bare beam irradiations. In Figure 8.7 the arrows indicate the data points used to find the parameters A and B for the core radius, and the insets represent the difference between experimental data and modeling according to eq. 8.21. Agreement within 15 % is observed when F-center and UV emission bands are detected and within 20 % when F-center emission band is detected.

For the irradiations placing binary filters in front of the bare beam, the agreement between the experimental data and modeling is within 35 % when F-center and UV emission bands are detected and within 35 % when F-center emission band is detected (Figure 8.8). Note that the predictions are inaccurate for the proton beam and also for the last points of each beam. This deviation is because these particles have low energies and they can not be considered to have a constant LET inside of the detector. To accurately apply the calculations of $\eta_{HCP,\gamma}$ using the model presented in this work the $\eta_{HCP,\gamma}$ expression needs to be modified to include the LET variation for particles that stop inside of the detector.

Table 8.4 and Table 8.5 show the experimental data and the calculated $\eta_{HCP,\gamma}$ determined in water for all the RDD models. Table 8.4 presents the $\eta_{HCP,\gamma}$ values of Luxel^{TM} detectors measuring both F-center and UV emission bands (Hoya U-340 filter), and Table 8.5 presents the $\eta_{HCP,\gamma}$ values measuring only F-center emission band (Hoya U-340 and Schott WG-360 filters). In Table 8.4 and Table 8.5 we also included the calculated values of $\eta_{HCP,\gamma}$ for particles and energies in which the approximation of constant LET of the particle is invalid.

In summary, the modeling shows results in agreement within 20 % of experimental data for particles that have constant LET when passing through the detector, and with charges up to 54 and L_∞ in water up to 1368 keV/μm.

The model presented in this section has the radius of the core as a free parameter, which is determined by fitting the constant A in eq. 8.25 to the $\eta_{HCP,\gamma}$ data – at least three points

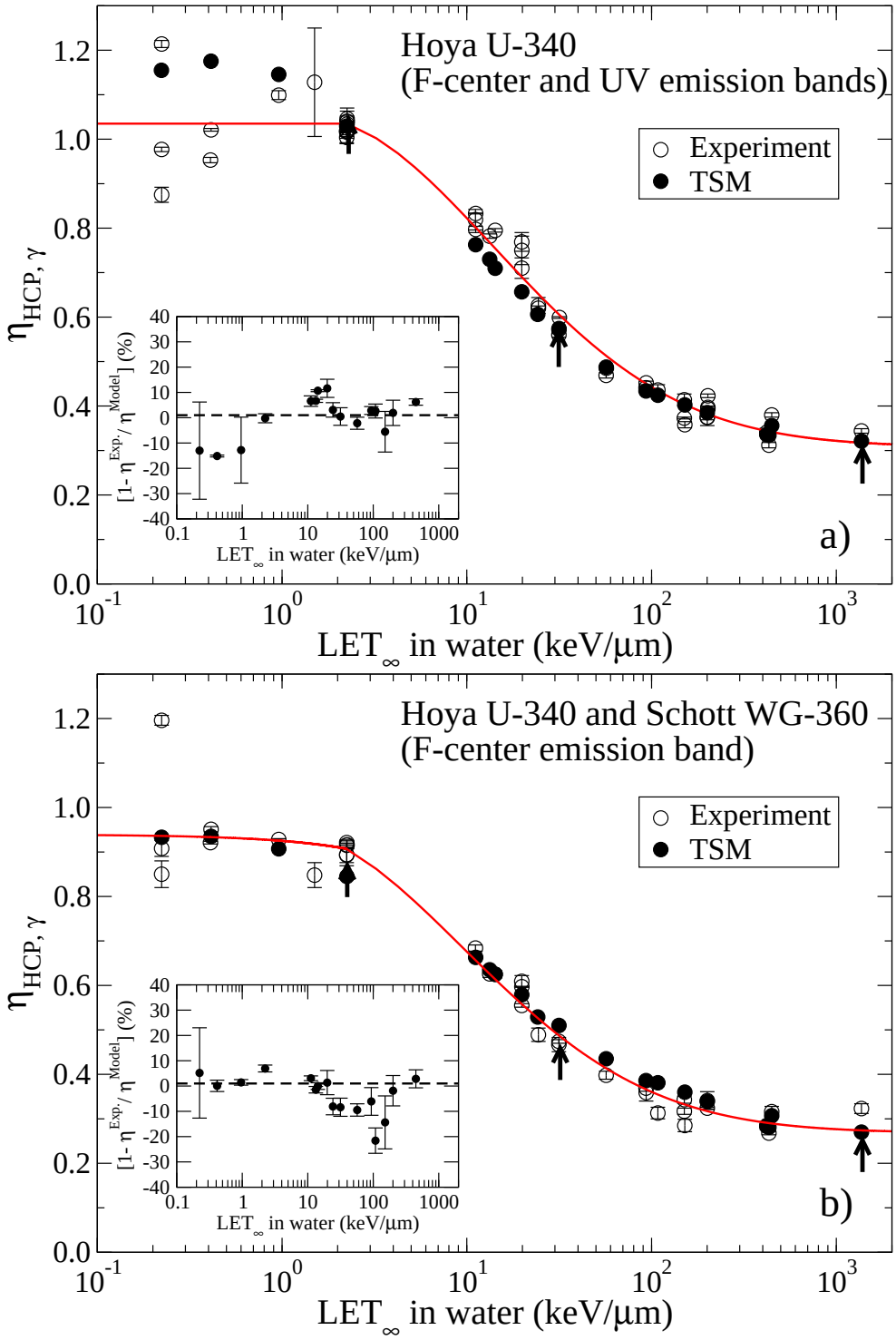

Figure 8.7: Comparison between $\eta_{HCP,\gamma}$ experimental data and modeling using the RDD functions from a modified version of Butts and Katz model. The arrows indicate the data points used to find the parameters A and B for the core radius. The insets represent the percentage deviation between data and model. a) OSL from Luxel^{TM} detected with Hoya U-340 filters (F-center and UV emission bands); b) OSL from Luxel^{TM} detected with Hoya U-340 and Schott WG-360 (F-center emission band).

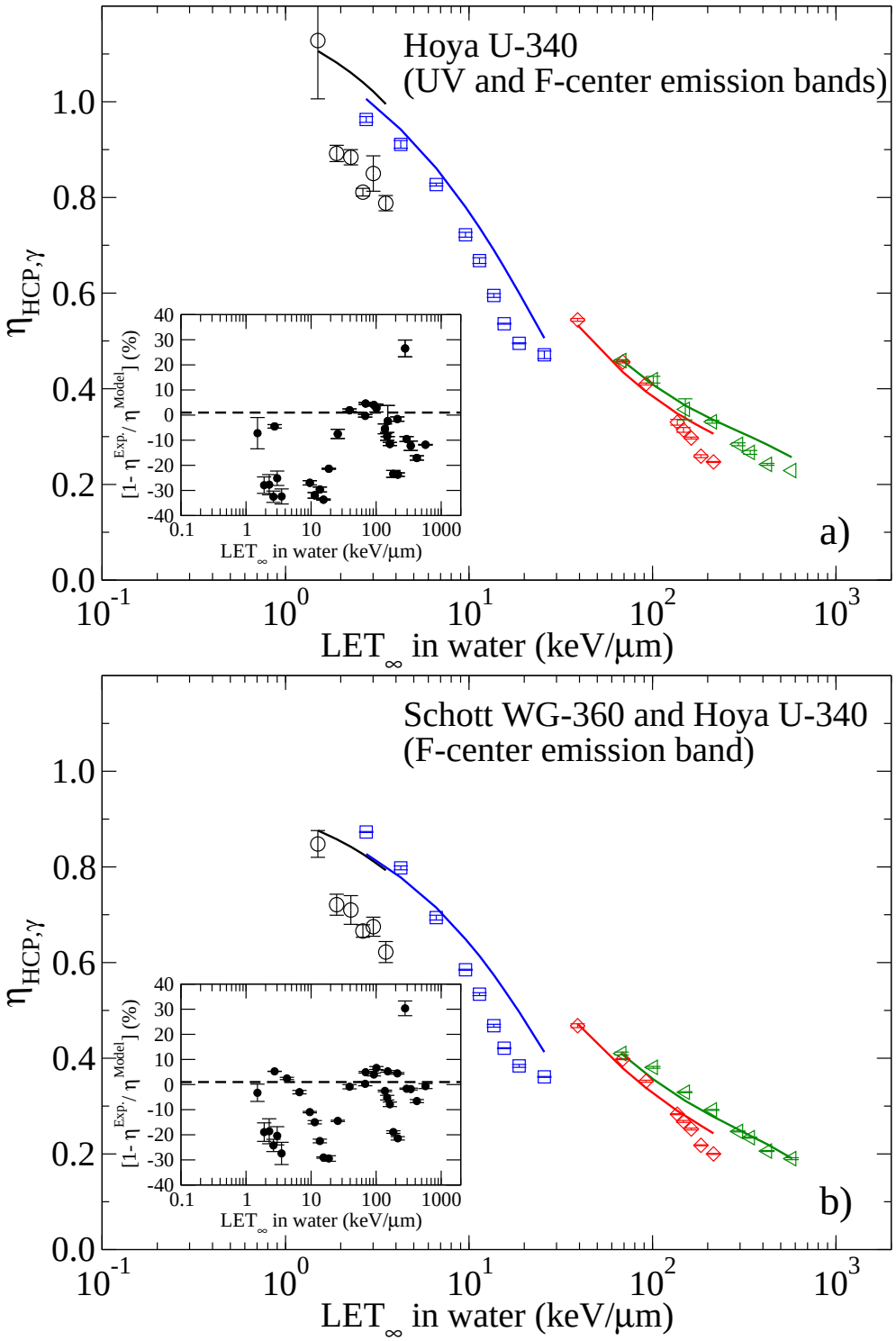

Figure 8.8: Comparison between $\eta_{HCP,\gamma}$ experimental data and modeling using the RDD functions from a modified version of Butts and Katz model. The experimental data was obtained by placing binary filters in front of the H 40 MeV, He 150 MeV/u, Ne 400 MeV/u, and Si 490 MeV/u to stop the primary particles. The full lines represent the results from the modeling, and symbols the experimental data. The insets represent the percentage deviation between data and model. a) OSL from Luxel^{TM} detected with Hoya U-340 filter (F-center and UV emission bands); b) OSL from Luxel^{TM} detected with Hoya U-340 and Schott WG-360 filters (F-center emission band).

Table 8.4: Modeling of OSL $\eta_{HCP,\gamma}$ of Luxel^{TM} detectors detecting both F-center and UV emission bands (Hoya U-340 filter). We obtained the $\eta_{HCP,\gamma}$ values through TSM using different RDD analytical models and MC simulations with GEANT4. The $\eta_{HCP,\gamma}$values are calculated in water.

			Luxel^{TM} OSL (Hoya U-340): F-center and UV emission bands								
Beam	Energy (MeV/u)	$L_{\infty}^{H_2O}$ (keV/μm)	Experimental data	Chatterjee	Katz	Waligórski	Fageeha	Geiß	Kiefer	Katz-Core (This work)	GEANT4 (This work)
H 1000 MeV	1000	0.223	1.022 $\pm$ 0.174	0.973	0.968	0.1.111	0.928	0.904	0.859	1.155	1.119
H 230 MeV	230	0.413	1.021 $\pm$ 0.003	0.643	0.943	0.971	0.791	0.868	0.799	1.175	1.097
H 70 MeV	70	0.960	1.016 $\pm$ 0.117	0.532	0.900	0.743	0.622	0.821	0.736	1.146	1.055
H 40 MeV	40	1.50	1.032 $\pm$ 0.060	0.499	0.866	0.634	0.537	0.788	0.699	1.106	1.054
H 30 MeV	30	1.90	0.846 $\pm$ 0.022	0.483	0.849	0.585	0.497	0.771	0.680	1.082	1.047
He 150 MeV/u	144.2	2.24	1.027 $\pm$ 0.018	0.527	0.884	0.667	0.515	0.812	0.734	1.030	1.150
H 24 MeV	24	2.27	0.831 $\pm$ 0.026	0.470	0.835	0.552	0.467	0.758	0.665	1.061	1.045
H 20 MeV	20	2.64	0.785 $\pm$ 0.013	0.459	0.823	0.526	0.443	0.747	0.653	1.041	1.038
H 17 MeV	17	3.01	0.816 $\pm$ 0.019	0.449	0.811	0.504	0.423	0.737	0.642	1.022	1.038
H 14 MeV	14	3.52	0.752 $\pm$ 0.017	0.436	0.796	0.480	0.399	0.724	0.627	0.995	1.030
C 400 MeV/u	384.9	11.17	0.816 $\pm$ 0.018	0.506	0.851	0.532	0.402	0.789	0.726	0.763	0.778
C 290 MeV/u	277.2	13.30	0.782 $\pm$ 0.005	0.496	0.840	0.502	0.385	0.777	0.707	0.730	0.814
O 1000 MeV/u	1000	14.24	0.795 $\pm$ 0.004	0.513	0.863	0.553	0.418	0.803	0.755	0.710	0.511
O 400 MeV/u	385.5	19.84	0.743 $\pm$ 0.030	0.492	0.834	0.484	0.376	0.773	0.710	0.657	0.666
C 135 MeV/u	111.2	24.21	0.626 $\pm$ 0.018	0.463	0.803	0.434	0.340	0.742	0.653	0.606	0.995
Ne 400 MeV/u	371.9	31.55	0.577 $\pm$ 0.020	0.480	0.819	0.453	0.360	0.761	0.696	0.574	0.610
Si 490 MeV/u	444.8	56.80	0.477 $\pm$ 0.011	0.469	0.806	0.429	0.350	0.750	0.687	0.488	0.463
Ar 500 MeV/u	450.7	93.34	0.447 $\pm$ 0.007	0.458	0.791	0.411	0.342	0.737	0.674	0.434	0.411
Ti 1000 MeV/u	977.6	108.2	0.436 $\pm$ 0.012	0.465	0.807	0.429	0.364	0.754	0.703	0.424	0.354
Fe 1000 MeV/u	967	151.4	0.381 $\pm$ 0.029	0.457	0.798	0.418	0.359	0.746	0.695	0.403	0.346
Fe 500 MeV/u	423.7	200.3	0.393 $\pm$ 0.020	0.438	0.766	0.389	0.329	0.715	0.651	0.385	0.370
Fe 200 MeV/u	120.4	431.8	0.312 $\pm$ 0.006	0.387	0.697	0.353	0.282	0.654	0.562	0.334	0.447
Kr 400 MeV/u	313.1	447.2	0.380 $\pm$ 0.005	0.413	0.732	0.368	0.309	0.685	0.613	0.356	0.345
Xe 290 MeV/u	185.5	1368	0.344 $\pm$ 0.005	0.372	0.675	0.340	0.278	0.637	0.549	0.321	0.329

Table 8.5: Modeling of OSL $\eta_{HCP,\gamma}$ of Luxel^{TM} detectors detecting only F-center emission band (Hoya U-340 and Schott WG-360 filters). We obtained the $\eta_{HCP,\gamma}$ values through TSM using different RDD analytical models and MC simulations with GEANT4. The $\eta_{HCP,\gamma}$values are calculated in water.

			Luxel^{TM} OSL (Hoya U-340 and Schott WG-360): F-center emission band								
Beam	Energy (MeV/u)	$L_{\infty}^{H_2O}$ (keV/μm)	Experimental data	Chatterjee	Katz	Waligórski	Fageeha	Geiß	Kiefer	Katz-Core (This work)	GEANT4 (This work)
H 1000 MeV	1000	0.223	0.984 ± 0.185	0.991	0.892	0.869	0.707	0.834	0.786	0.933	0.897
H 230 MeV	230	0.413	0.936 ± 0.021	0.702	0.851	0.741	0.596	0.788	0.715	0.935	0.943
H 70 MeV	70	0.960	0.920 ± 0.010	0.493	0.792	0.573	0.470	0.732	0.640	0.907	0.944
H 40 MeV	40	1.50	0.848 ± 0.028	0.452	0.749	0.495	0.407	0.694	0.597	0.876	0.954
H 30 MeV	30	1.90	0.721 ± 0.022	0.434	0.727	0.460	0.377	0.675	0.574	0.858	0.954
He 150 MeV/u	144.2	2.24	0.908 ± 0.013	0.488	0.785	0.525	0.409	0.728	0.645	0.845	0.894
H 24 MeV	24	2.27	0.710 ± 0.030	0.420	0.709	0.435	0.355	0.660	0.555	0.842	0.955
H 20 MeV	20	2.64	0.666 ± 0.013	0.408	0.693	0.415	0.337	0.647	0.540	0.827	0.954
H 17 MeV	17	3.01	0.675 ± 0.020	0.397	0.678	0.398	0.321	0.636	0.525	0.812	0.955
H 14 MeV	14	3.52	0.622 ± 0.022	0.383	0.659	0.379	0.302	0.621	0.507	0.793	0.955
C 400 MeV/u	384.9	11.17	0.684 ± 0.007	0.465	0.762	0.442	0.346	0.712	0.646	0.663	0.575
C 290 MeV/u	277.2	13.30	0.626 ± 0.008	0.454	0.747	0.420	0.331	0.698	0.624	0.635	0.598
O 1000 MeV/u	1000	14.24	0.625 ± 0.008	0.474	0.784	0.465	0.369	0.734	0.682	0.625	0.407
O 400 MeV/u	385.5	19.84	0.587 ± 0.029	0.451	0.745	0.410	0.328	0.697	0.630	0.579	0.499
C 135 MeV/u	111.2	24.21	0.489 ± 0.015	0.418	0.698	0.368	0.290	0.656	0.562	0.529	0.715
Ne 400 MeV/u	371.9	31.55	0.470 ± 0.016	0.439	0.730	0.389	0.316	0.684	0.615	0.510	0.463
Si 490 MeV/u	444.8	56.80	0.398 ± 0.009	0.429	0.718	0.374	0.310	0.674	0.608	0.435	0.371
Ar 500 MeV/u	450.7	93.34	0.364 ± 0.019	0.417	0.704	0.360	0.303	0.662	0.596	0.386	0.337
Ti 1000 MeV/u	977.6	108.2	0.313 ± 0.013	0.426	0.728	0.380	0.327	0.684	0.631	0.381	0.306
Fe 1000 MeV/u	967	151.4	0.315 ± 0.029	0.418	0.718	0.372	0.323	0.676	0.622	0.360	0.299
Fe 500 MeV/u	423.7	200.3	0.333 ± 0.020	0.398	0.678	0.343	0.290	0.640	0.571	0.339	0.309
Fe 200 MeV/u	120.4	431.8	0.268 ± 0.004	0.343	0.593	0.300	0.240	0.569	0.472	0.281	0.344
Kr 400 MeV/u	313.1	447.2	0.316 ± 0.012	0.372	0.640	0.322	0.270	0.607	0.531	0.307	0.289
Xe 290 MeV/u	185.5	1368	0.323 ± 0.011	0.329	0.577	0.291	0.238	0.555	0.463	0.270	0.273

in a large range of LET must be considered. Thus, the model and methodology presented in this section present a way to estimate $\eta_{HCP,\gamma}$ values for the particles and energies that can not be experimentally obtained.

8.5 RELATIVE LUMINESCENCE EFFICIENCY OBTAINED USING MONTE CARLO SIMULATIONS WITH GEANT4

This section discusses the methodology and presents the results of predictions of $\eta_{HCP,\gamma}$ using the MC code GEANT4 to calculate the RDDs (chapter 5).

To calculate the $\eta_{HCP,\gamma}$ values , eq. 8.17 was written in terms of the energy deposited. We changed the integral by a sum,

$$\eta_{HCP,\gamma}^{Al_2O_3:C}(D_0) = \frac{\sum_i f_\beta^{Al_2O_3:C}(D_i)E_i}{E_{Tot}} \tag{8.26}$$

where $f_\beta^{Al_2O_3:C}$ is the response function (eq. 8.19), D_i and E_i are the dose and energy deposited in the i^{th} shell (see chapter 5), and $E_{Tot} = \sum_i E_i$ is the total energy deposited. We converted the $\eta_{HCP,\gamma}$ calculated in Al_2O_3:C obtained with GEANT4 to $\eta_{HCP,\gamma}$ calculated in water using Table 8.1. We present all the $\eta_{HCP,\gamma}$ results calculated in water.

The shape of RDD changes with the thickness z of the detector. Part of this dependence we attributed to the angular dependence in the production of secondary electrons by the incident HCP. However, other factors that we could not explain are also responsible for the change in the shape of the RDD (see chapter 5). Thus, the thickness z of the detectors influences the $\eta_{HCP,\gamma}$ predictions because $\eta_{HCP,\gamma}$ depends on the shape the RDD. Figure 8.9 shows the $\eta_{HCP,\gamma}$ *versus* z. For comparison, we also represent in Figure 8.9 the experimental values of the $\eta_{HCP,\gamma}$ by the dashed lines ($\pm$ one standard deviation of the data).

Figure 8.10 shows the relative luminescence efficiency calculated using RDDs simu-

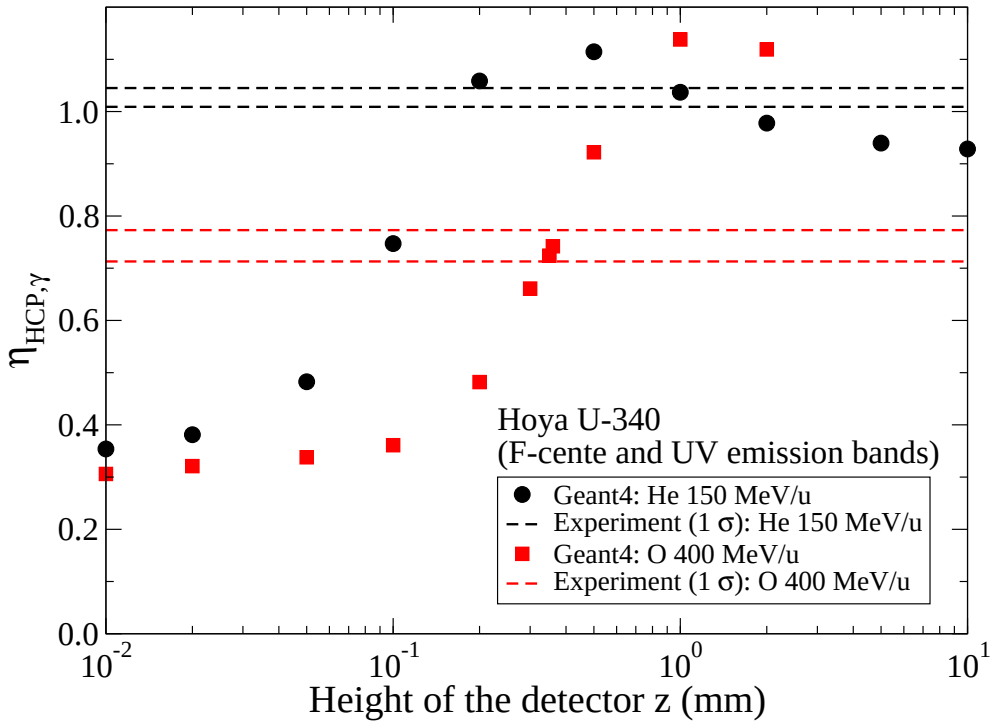

Figure 8.9: Influence of the thickness z of the detector on the $\eta_{HCP,\gamma}$ calculated in water using GEANT4. The dashed lines represent the interval of the experimental data for one standard deviation of the data.

lated with GEANT4 for three different detector's thickness z. For $z = 0.01$ mm the $\eta_{HCP,\gamma}$ predictions are very poor, showing differences larger than 100 % from the experimental data (Figures 8.10a and 8.10d) . For $z = 1$ mm, the predictions for low LET particles are in good agreement with experimental data (within 28 %), but strongly deviate from experimental data for high-LET particles (Figures 8.10c and 8.10f).

For $z = 0.3$ mm, which corresponds to the physical thickness of Luxel^{TM} detectors, the predictions using GEANT4 are in overall agreement with the experimental data. Except for two beams (O 1000 MeV/u and C 135 MeV/u), the agreement between predictions and experimental data are within 35 % (Figures 8.10b and 8.10e).

Avila et al. (1996) developed a Monte Carlo code exclusive to calculate RDDs in luminescence materials. They used TSM with the RDD obtained by their code to estimate TL $\eta_{HCP,\gamma}$ of LiF for a variety of particles and energies (Avila et al., 1999; Massillon-JL et al., 2006). Although their TSM results describe the general features of $\eta_{HCP,\gamma}$ data, their ab-

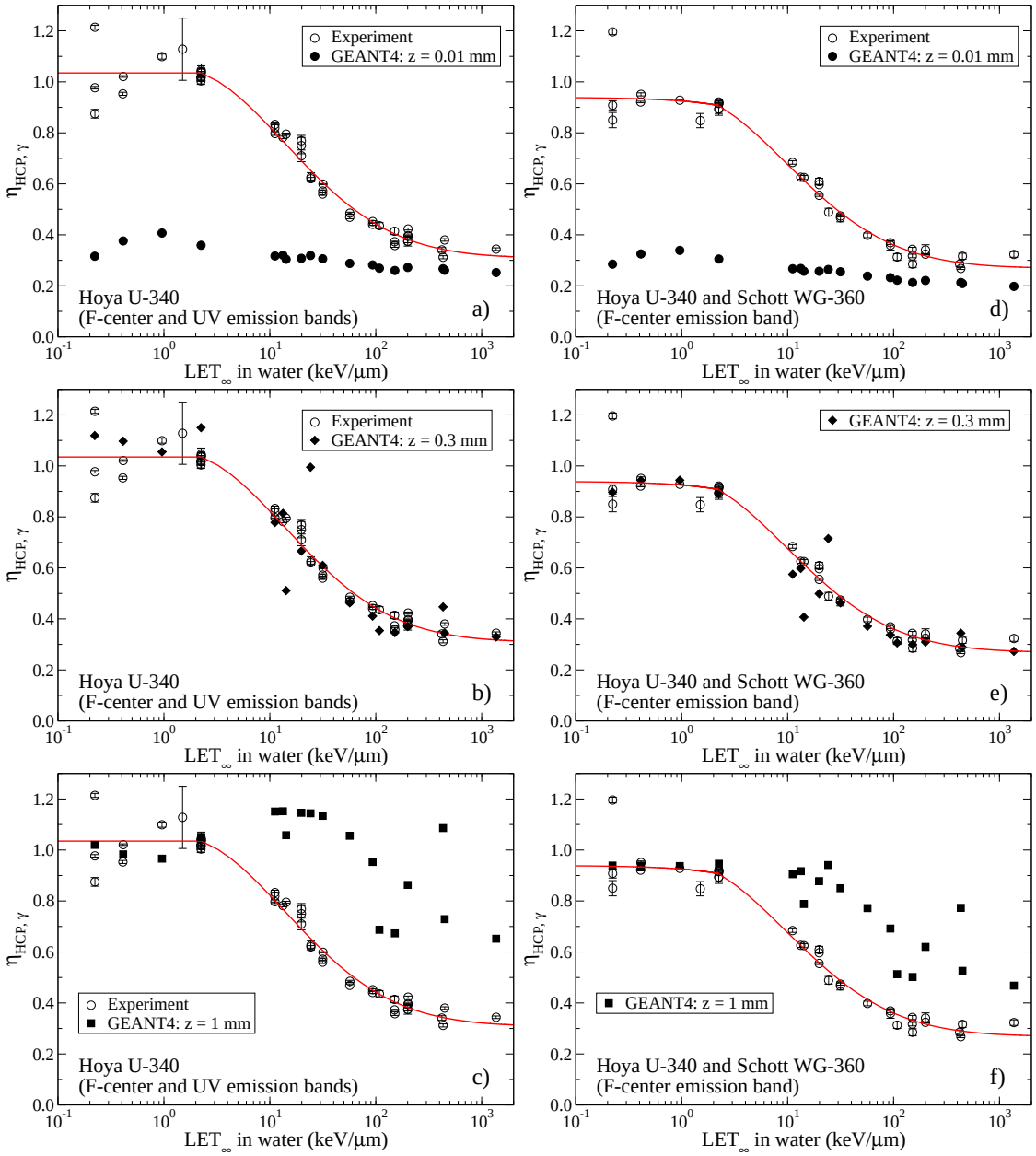

Figure 8.10: Relative luminescence efficiency *versus* L_∞ in water using RDD simulated with GEANT4 for different detector thicknesses z. a)-c) $\eta_{HCP,\gamma}$ when OSL from Luxel^{TM} is detected with Hoya U-340 filter (F-center emission band). e)-f) $\eta_{HCP,\gamma}$ when OSL from Luxel^{TM} is detected with Hoya U-340 and Schott WG-360 filters (F-center emission band).

solute values disagree for particles with $L_{\infty}^{H_2O}$ larger than 10 keV/μm (Massillon-JL et al., 2006). The disagreement reaches one order of magnitude for the predictions of $\eta_{HCP,\gamma}$ from peak 5 in LiF for a carbon beam with $L_{\infty}^{H_2O}$ of about 500 keV/μm.

Thus, we conclude that the verified agreement of about 35 % between the relative luminescence efficiency determined using GEANT4 and experimental data are an improvement compared to the results reported in the literature (Avila et al., 1996; Massillon-JL et al., 2006). Not only, did the calculations include a much wider range of particles and energies, but also the overall agreement between simulations and data are much better.

The change in shape of the RDD with the thickness z of the detector, which is responsible for the variation in the $\eta_{HCP,\gamma}$ needs to be further investigated. The same behavior was also observed with the FLUKA code (Mark et al., 2007).

In summary, GEANT4 demonstrated to be an useful tool for the estimation of OSL $\eta_{HCP,\gamma}$ of Luxel^{TM} detectors. However, for more accurate $\eta_{HCP,\gamma}$ estimates, GEANT4 needs to improve the cross-section models relevant to microdosimetry, such as the SDCS for production of secondary electrons (see section 5.1). Although there are a variety of MC track structure codes that utilize more fundamental and detailed physics relevant to microdosimetry and radiobiology, all of these codes are only for calculations in water (Nikjoo et al., 2006).

CHAPTER 9

MEASUREMENT OF ABSORBED DOSE AND DOSE EQUIVALENT IN COMPLEX RADIATION FIELDS

In personnel dosimetry in space, the partial solution to the HCP dosimetry problem is to combine two or more types of detectors with complementary properties, such as TLDs and OSLDs, and plastic nuclear track detectors (PNTD) (NCRP, 2002; McKeever et al., 2007). TLDs and OSLDs are efficient for low-LET radiation ($L_{\infty}^{H_2O} < 10$ keV/μm), whereas PNTDs are efficient for high-LET radiation ($L_{\infty}^{H_2O} > 10$ keV/μm). Thus, the total absorbed dose can be estimated as:

$$D = D_{<10\ keV/\mu m}^{TLD/OSLD} + D_{>10\ keV/\mu m}^{PNTD} \tag{9.1}$$

where $D_{<10\ keV/\mu m}^{TLD/OSLD}$ is the TLD/OSLD absorbed dose for particles with $L_{\infty}^{H_2O} < 10$ keV/μm, and $D_{>10\ keV/\mu m}^{PNTD}$ is the PNTD absorbed for particles with $L_{\infty}^{H_2O} > 10$ keV/μm.

As discussed in this dissertation, the relative luminescence efficiency depends on the ionization density. The absorbed dose as-measured by TLDs/OSLDs contains contribution not only from particles with $L_{\infty}^{H_2O}$ lower than 10 keV/μm, but also for all the other particles that constitute the radiation field.

Fortunately, PNTD provides some information about the LET spectrum of the radiation field. Thus, knowing the $\eta_{HCP,\gamma}$ *versus* L_{∞}, we can use the LET spectrum provided by PNTD to subtract the $L_{\infty}^{H_2O} > 10$ keV/μm contribution from the TLD/OSLD total absorbed

dose $D^{TLD/OSLD}$ (Benton et al., 2002):

$$D^{TLD/OSLD}_{<10\ keV/\mu m} = D^{TLD/OSLD} - \sum_{L_i=10\ keV/\mu m}^{1500\ keV/\mu m} \eta^i_{HCP,\gamma} D^{PNTD}_i \tag{9.2}$$

where $\eta^i_{HCP,\gamma}$ and D^{PNTD}_i are the relative luminescence efficiency, and PNTD absorbed dose from particles with LET i, respectively. Thus, the total absorbed dose is estimated as:

$$D = D^{TLD/OSLD}_{<10\ keV/\mu m} + \sum_{L_i=10\ keV/\mu m}^{1500\ keV/\mu m} D^{PNTD}_i \tag{9.3}$$

Radiation protection requires not only the estimation of absorbed dose, but also the estimation of dose equivalent H. Using the LET spectrum provided by PNTD, H is estimated as:

$$H = D^{TLD/OSLD}_{<10\ keV/\mu m} + \sum_{L_i=10\ keV/\mu m}^{1500\ keV/\mu m} Q^i D^{PNTD}_i \tag{9.4}$$

where Q_i is the quality factor for a particle with LET i (ICRP, 1990), and the numerical value of $D^{TLD/OSLD}_{<10\ keV/\mu m}$ (in Gy) is equal to the numerical value of $H^{TLD/OSLD}_{<10\ keV/\mu m}$ (in Sv).

For Al_2O_3:C, TLD-100 and TLD-300, the relative luminescence efficiency is different from unity even for particles with $L^{H_2O}_\infty$ lower than 10 keV/μm. Thus, for reliable estimation of the absorbed dose, correction of $D^{TLD/OSLD}_{<10\ keV/\mu m}$ must be performed. PNTD does not provide reliable information for $L^{H_2O}_\infty$ lower than 10 keV/μm. Thus, methods to estimate an "effective" LET (L^{eff}_∞) of the radiation field based on the analysis of the TL or OSL curves were developed (Yukihara and McKeever, 2006a; Yukihara et al., 2006; Gaza et al., 2006a; Berger et al., 2006; Hajek et al., 2006). For OSL from Luxel™, L^{eff}_∞ is extracted analyzing the ratio between the OSL initial intensity and total area, providing that the shape of the OSL curve is characterized for different LETs. Using the $\eta_{HCP,\gamma}$ *versus* L_∞ curve, the L^{eff}_∞ is translated into an effective relative luminescence efficiency $\eta^{eff}_{HCP,\gamma}$ of the detector. Then,

$\eta^{eff}_{HCP,\gamma}$ is used to correct the TLD/OSLD absorbed dose:

$$D^{eff}_{cor} = \frac{D^{TLD/OSLD}_{<10\ keV/\mu m}}{\eta^{eff}_{HCP,\gamma}} \tag{9.5}$$

Figure 9.1 illustrates the determination of the L^{eff}_{∞} and $\eta^{eff}_{HCP,\gamma}$. This method works only for radiation fields dominated by low-LET particles.

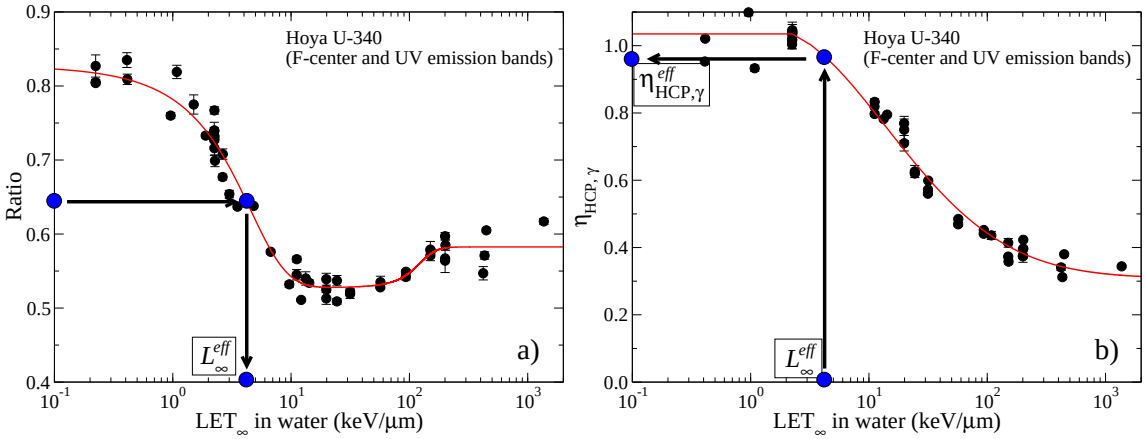

Figure 9.1: Method to estimate the "effective" LET L^{eff}_{∞}, and effective relative luminescence efficiency $\eta^{eff}_{HCP,\gamma}$ of the radiation field using OSL from Luxel^{TM}. a) Characterization of the shape of the OSL curve from Luxel^{TM} to different LETs. The ordinate axis represents the "Ratio" between the OSL initial intensity and total area. b) Relative luminescence efficiency as a function of LET. The OSL was measured with Hoya U-340 filters detecting F-center and UV emission bands. The red lines are arbitrary functions fitted to the data for better visualization.

Alternatively, if the particles and energies of the HCP radiation field are known, a corrected absorbed dose D^{eq}_{cor} measured by the luminescence detector is obtained by:

$$D^{eq}_{cor} = \frac{D^{TLD/OSLD}_{<10\ keV/\mu m}}{\eta^{eq}_{HCP,\gamma}} \tag{9.6}$$

where $\eta^{eq}_{HCP,\gamma}$ is the equivalent relative luminescence efficiency of the detector to the radiation field the detector was exposed. $\eta^{eq}_{HCP,\gamma}$ depends on the spectrum of charges and

energies of the particles that constitute the radiation field:

$$\eta^{eq}_{HCP,\gamma} = \sum_{Z_i,E_i} \frac{\eta^{i}_{HCP,\gamma}(Z_i,E_i)}{\Gamma^{i}(Z_i,E_i)} \tag{9.7}$$

where $\eta^{i}_{HCP,\gamma}(Z_i,E_i)$ is the relative luminescence efficiency for a particle with the charge Z_i and energy E_i, and $\Gamma^{i}(Z_i,E_i)$ is the fraction of dose per particle with charge Z_i and energy E_i that constitutes the radiation field. If the spectrum of charges and energies is known, we can determine $\eta^{i}_{HCP,\gamma}(Z_i,E_i)$ using the TSM presented in this dissertation, or experimental data, if available. Thus, we can estimate $\eta^{eq}_{HCP,\gamma}$ and correct the absorbed dose.

The two methods presented above, $\eta^{eff}_{HCP,\gamma}$ and $\eta^{eq}_{HCP,\gamma}$, to correct the response of the detector present advantages and disadvantages. The method based on the determination of $\eta^{eff}_{HCP,\gamma}$ requires characterization of the luminescence response of the detectors as a function of LET. Thus, this method is very time consuming and expensive because HCPs relevant to radiation protection in space can be obtained only in a few accelerators located in different places worldwide. In addition, the correction factor $\eta^{eff}_{HCP,\gamma}$ presents systematic errors which are introduced when determining the "effective" LET of the radiation field.

The method based on the determination of the $\eta^{eq}_{HCP,\gamma}$ requires knowledge of the spectrum of charges and energies of the radiation field, which is complicated to accurately measure, or simulate using transport codes. In addition, inside of the ISS the spectrum of particles and energies varies with location because of different shielding composition and thickness (Benton and Benton, 2001; Benton et al., 2002). Thus, although the correction factor $\eta^{eq}_{HCP,\gamma}$ can be used to estimate the true value of the absorbed dose, the accuracy of the method depends on the accuracy of the determination of the radiation field.

We mentioned in the introduction of this dissertation that NASA is currently using Luxel^{TM} detectors inside of the ISS to measure absorbed dose and dose equivalent (Zhou et al., 2006, 2007). However, NASA does not apply any correction to the $\eta_{HCP,\gamma}$ of the

detectors on the doses estimated by Luxel^{TM} detectors. Thus, the results and methodology presented in this dissertation can be used to estimate the Luxel^{TM} $\eta^{eq}_{HCP,\gamma}$ in different locations inside the ISS where the spectrum of charges and energies is known. Independently, the dose estimations should also be performed with the correction factor $\eta^{eff}_{HCP,\gamma}$ for cross-check and reliability. A reliable measurement of absorbed dose and dose equivalent is extremely important for the radiation protection program in space.

CHAPTER 10

CONCLUSION

This work investigated the optically stimulated luminescence (OSL) response of Luxel^{TM} detectors exposed to 24 combinations of heavy charged particles (HCPs) and energies relevant to radiation protection in space and cancer therapy. We used the track structure model (TSM) combined with different radial dose distribution (RDD) analytical models and Monte Carlo (MC) simulations to predict relative luminescence efficiencies, $\eta_{HCP,\gamma}$. Below we summarize the results of the experimental characterization and TSM predictions.

The OSL dose response of Luxel^{TM} detectors exposed to HCP beams was investigated using two different filter sets. Regardless of the filter set, we observed that beta rays and H 1000 MeV produced similar responses in the detectors, which indicated that the pattern of energy deposition by H 1000 MeV and beta rays is similar. Using Hoya U-340 filter, which detects the F-center and UV emission bands, we observed that the beta rays and H 1000 MeV caused a strong supralinearity of $f(D) = 1.8$ in the dose response curve. On the other hand, the supralinearity index for beta rays and H 1000 MeV when using a combination of Hoya U-340 and Schott WG-360 filters, which detects the F-center emission band only, was less than 1.2. Thus, we concluded that the UV emission band is responsible for most of the supralinearity in the OSL dose response of Luxel^{TM} detectors irradiated with beta rays and H 1000 MeV. For heavier ions from He to Fe no supralinearity was observed in the investigated range of doses for both filter sets. In the case of the Fe 200 MeV/u beam we attributed the linear-saturation behavior to the fact that high-LET particles such as Fe 200 MeV/u ions produce a pattern of energy deposition that is concentrated in regions close to the track of the particle. Thus, the luminescence saturation occurs only when the particle

fluence is high enough for the tracks to start interacting (Sawakuchi et al., 2007a).

We studied the change in shape of the OSL curves from Luxel^{TM} detectors for different radiation qualities and absorbed doses and observed that the important parameter that causes changes in the OSL curve is the ionization density. Beta doses of about (1-10) Gy are needed to cause changes in the OSL curves. On the other hand, for Ne 400 MeV/u and Fe 200 MeV/u radiations, the OSL curve presents further changes only for absorbed doses larger than 50 Gy. Based on the fluence corresponding to the absorbed dose of 50 Gy and analytical models of RDD, we estimated that the dose level in the inter-track region is comparable to the beta dose in which the OSL curve starts to change. This is an indication that track overlap is responsible for further changes in shape of the OSL curves of Luxel^{TM} detectors as the HCP fluence increases (Sawakuchi et al., 2007b).

Relative luminescence efficiency values $\eta_{HCP,\gamma}$ of Luxel^{TM} detectors were determined for different detection filters to discriminate the F-center and UV emission bands. Data on OSL and TL $\eta_{HCP,\gamma}$ of Al_2O_3:C single crystals and TLD-100 was also obtained for comparison. A common trend of decreasing $\eta_{HCP,\gamma}$ as increasing the LET of the radiation field was observed for all the detectors. For Luxel^{TM} detectors the $\eta_{HCP,\gamma}$ is close to unit for particles with $L_{\infty}^{H_2O}$ lower than 3 keV/μm. Then, the $\eta_{HCP,\gamma}$ decreases and stabilizes at 200 keV/μm. The $\eta_{HCP,\gamma}$ of Luxel^{TM} detectors presented different values when using different detection windows to measure the OSL. We used TSM to show that this difference correlates with the luminescence response functions of the detector. These results support previous observations that the $\eta_{HCP,\gamma}$ is ultimately characterized by the behavior of the point defects responsible for the detected luminescence signal (Yukihara et al., 2006). Using MC simulations with GEANT4, we qualitatively explained that the different values of $\eta_{HCP,\gamma}$ for particles with the same LET, but different charges and energies are due to the different spatial pattern of energy deposition around the track of the incident particle.

The definition of $\eta_{HCP,\gamma}$ was studied and we showed that $\eta_{HCP,\gamma}$ has the value of unity for low LET radiation only if $\eta_{HCP,\gamma}$ is calculated in the material of the detector and

the detector presents a “perfect” luminescence dose response (linear-saturation behavior) (Sawakuchi et al., 2007c).

We derived an expression to calculate the $\eta_{HCP,\gamma}$ based on TSM. This expression depends on the RDD and luminescence response function of the detector to low LET test radiation that mimics as closely as possible the energy spectrum of delta rays produced by the incident HCP. To calculate the $\eta_{HCP,\gamma}$, we used the following RDDs: Chatterjee and Schaefer, Butts and Katz, Waligórski *et al.*, Fageeha *et al.*, Kiefer and Straaten, Geiß *et al.* models, and MC simulations with GEANT4. In general, the analytical models failed to provide agreement better than 40 %. On the other hand, the MC simulations provided agreement with experimental data within 35 %.

To improve the agreement between the predicted $\eta_{HCP,\gamma}$ values and experimental data, we proposed a modified model based on Butts and Katz model, which introduces a constant region of energy deposition for small radial distances. This constant region is similar to the definition of core by Chatterjee and Schaefer, and Geiß *et al.* models. We determined the core region normalizing the total energy loss by path length to the LET of the particle. We proposed that the radius of the core region, which is critical when predicting $\eta_{HCP,\gamma}$, depends on properties of the incident HCP and detector. With these modifications, agreements within 15 % and 20 % were observed between $\eta_{HCP,\gamma}$ experimental data and modeling for the two different detection windows, respectively. This is the first time that such agreement is achieved for a wide range of particles and energies and when using a single RDD model. The model shows 20 % agreement with experimental data for particles that have constant LET when passing through the detector, and with charges up to 54 and $L_{\infty}^{H_2O}$ up to 1368 keV/μm.

The $\eta_{HCP,\gamma}$ obtained with MC simulation presented a strong dependence on the thickness z of the detector. Although we performed tests using different MC geometries, step sizes and physics models, we were unable to understand the causes of the $\eta_{HCP,\gamma}$ dependence on the thickness of the detector. Nevertheless, we verified agreement within 35 %

between $\eta_{HCP,\gamma}$ experimental data and simulations if an appropriate thickness is used.

We suggested a correction method, based on the calculation of $\eta_{HCP,\gamma}$ using the TSM presented in this dissertation, to measure more reliable absorbed doses when using luminescence detectors in complex radiation fields.

To conclude this dissertation, we comment on the limitations and weakness of our model to predict the relative luminescence efficiency, suggest further improvements, and future work.

We performed two approximations in the relative luminescence efficiency formula used in the predictions. The approximations were as follows: i) we considered the factor $\eta_{\delta,\gamma}$ independent on the energy of the secondary electrons created by the incident HCP and we assumed $\eta_{\delta,\gamma}$ equal to unity; and ii) we used beta rays from a ^{90}Sr/^{90}Y source as the test radiation. We consider these two approximations the main limitations of our approach. Thus, we encourage further investigations to accurately determine the energy response of Luxel^{TM} detectors, which provides adequate inclusion of the energy dependent factor $\eta_{\delta,\gamma}$ in the predictions, and determination of the test radiation that best suits the energy spectrum of secondary electrons produced by the incident HCP.

The proposed RDD model, based on the introduction of a core region in the Butts and Katz RDD model, presents two free parameters. These parameters are determined fitting three values of $\eta_{HCP,\gamma}$ experimental data in a wide range of LET. Although we found a correlation between one of the free parameters with the distance between the defects responsible for the luminescence process, a definite physical meaning is still missing.

The $\eta_{HCP,\gamma}$ model presented in this dissertation is only accurate for high energy particles in which the change in LET is negligible when the particle transverses the detector. Therefore, we suggest an implementation of a numerical routine that accounts for LET changes of the particle, which is of large importance for cancer therapy dosimetry, where doses are measured in the Bragg peak.

The shape of RDDs calculated with GEANT4 depends on the detector's thickness. We

attributed part of the dependence to the angular distribution of secondary electrons produced by the primary particle. Moreover, other factors that we could not explain cause the RDD changes. Further investigations need to be performed to better understand the RDD dependence on the detector's thickness.

MC codes provide flexible design capabilities to reproduce experimental conditions. Therefore, we suggest testing other MC geometry setups. For example, the detector could be divided in micro voxels where the dose in each voxel is translated to signal through the luminescence response function. In this way, we can simulate the absolute luminescence dose response of the detector exposed to a HCP fluence Φ. Preliminary results showed that this method reproduces the dose response of Luxel^{TM} detectors for Fe 200 MeV/u, and also improves the agreement between $\eta_{HCP,\gamma}$ predictions and data to within 15 % for particles with $Z > 2$.

BIBLIOGRAPHY

Agostinelli, S., J. Allison, K. Amako, J. Apostolakis, H. Araujo, P. Arce, M. Asai, D. Axen, S. Banerjee, G. Barrand, F. Behner, L. Bellagamba, J. Boudreau, L. Broglia, A. Brunengo, H. Burkhardt, S. Chauvie, J. Chuma, R. Chytracek, G. Cooperman, G. Cosmo, P. Degtyarenko, A. Dell'Acqua, G. Depaola, D. Dietrich, R. Enami, A. Feliciello, C. Ferguson, H. Fesefeldt, G. Folger, F. Foppiano, A. Forti, S. Garelli, S. Giani, R. Giannitrapani, D. Gibin, J. J. G. Cadenas, I. González, G. G. Abril, G. Greeniaus, W. Greiner, V. Grichine, A. Grossheim, S. Guatelli, P. Gumplinger, R. Hamatsu, K. Hashimoto, H. Hasui, A. Heikkinen, A. Howard, V. Ivanchenko, A. Johnson, F. W. Jones, J. Kallenbach, N. Kanaya, M. Kawabata, Y. Kawabata, M. Kawaguti, S. Kelner, P. Kent, A. Kimura, T. Kodama, R. Kokoulin, M. Kossov, H. Kurashige, E. Lamanna, T. Lampén, V. Lara, V. Lefebure, F. Lei, M. Liendl, W. Lockman, F. Longo, S. Magni, M. Maire, E. Medernach, K. Minamimoto, P. M. de Freitas, Y. Morita, K. Murakami, M. Nagamatu, R. Nartallo, P. Nieminen, T. Nishimura, K. Ohtsubo, M. Okamura, S. O'Neale, Y. Oohata, K. Paech, J. Perl, A. Pfeiffer, M. G. Pia, F. Ranjard, A. Rybin, S. Sadilov, E. D. Salvo, G. Santin, T. Sasaki, N. Savvas, Y. Sawada, S. Scherer, S. Sei, V. Sirotenko, D. Smith, N. Starkov, H. Stoecker, J. Sulkimo, M. Takahata, S. Tanaka, E. Tcherniaev, E. S. Tehrani, M. Tropeano, P. Truscott, H. Uno, L. Urban, P. Urban, M. Verderi, A. Walkden, W. Wander, H. Weber, J. P. Wellisch, T. Wenaus, D. C. Williams, D. Wright, T. Yamada, H. Yoshida, and D. Zschiesche. Geant4 - A simulation toolkit. *Nucl. Instr. Meth. Res. A* **506**, 250–303, 2003.

Akselrod, M. S., and E. A. Gorelova. Deep traps in highly sensitive α-Al_2O_3:C TLD crystals. *Nucl. Tracks Radiat. Meas.* **21**, 143–146, 1993.

Akselrod, M. S., V. S. Kortov, and E. A. Gorelova. Preparation and properties of α-Al_2O_3:C. *Radiat. Prot. Dosim.* **47**, 159–164, 1993.

Akselrod, M. S., V. S. Kortov, D. J. Kravetsky, and V. I. Gotlib. Highly sensitive thermoluminescent anion-defect α-Al_2O_3:C single crystal detectors. *Radiat. Prot. Dosim.* **33**, 119–122, 1990.

Akselrod, M. S., N. A. Larsen, and S. W. S. McKeever. A procedure for the distinction between static and dynamic radiation exposures of personal radiation badges using pulsed optically stimulated luminescence. *Radiat. Meas.* **32**, 215–225, 2000.

Andersen, C. E., C. J. Marckmann, M. C. Aznar, L. Bøtter-Jensen, F. Kjær-Kristoffersen, and J. Medin. An algorithm for real-time dosimetry in intensity-modulated radiation therapy using the radioluminescence signal from Al_2O_3:C. *Radiat. Prot. Dosim.* **120**, 7–13, 2006.

Avila, O., M. E. Brandan, F. Salvat, and J. M. Fernandez-Varea. Radial energy distributions in LiF by alpha particle irradiation using Monte Carlo simulation. *Radiat. Prot. Dosim.* **65**, 37–40, 1996.

Avila, O., I. Gamboa-deBuen, and M. E. Brandan. Study of the energy deposition in LiF by heavy charged particle irradiation and its relation to the thermoluminescent efficiency of the material. *J. Phys. D: Appl. Phys.* **32**, 1175–1181, 1999.

Aznar, M. C., C. E. Andersen, L. Bøtter-Jensen, S. A. J. Bäck, S. Mattsson, F. Kjær-Kristoffersen, and J. Medin. Real-time optical-fibre luminescence dosimetry for radiotherapy: physical characteristics and applications in photon beams. *Phys. Med. Biol.* **49**, 1655–1669, 2004.

Aznar, M. C., B. Hemdal, J. Medin, C. J. Marckmann, C. E. Andersen, L. Bøtter-Jensen, I. Andersson, and S. Mattsson. *In vivo* absorbed dose measurements in mammography using a new real-time luminescence technique. *Br. J. Radiol.* **78**, 328–334, 2005.

Barkas, W. H. *Nuclear Research Emulsions: I. Techniques and Theory*. Academic Press, USA, 1963.

Benton, E. R., and E. V. Benton. Space radiation dosimetry in low-Earth orbit and beyond. *Nucl. Instr. Meth. Res. B* **184**, 255–294, 2001.

Benton, E. R., E. V. Benton, and A. L. Frank. Passive dosimetry aboard the Mir Orbital Station: internal measurements. *Radiat. Meas.* **35**, 439–455, 2002.

Berger, T., M. Hajek, M. Fugger, and N. Vana. Efficiency-corrected dose verification with thermoluminescence dosemeters in heavy-ion beams. *Radiat. Prot. Dosim.* **120**, 361–364, 2006.

Bhabha, H. J. On the penetrating component of cosmic radiation. *Proc. R. Soc. London A* **164**, 257–294, 1938.

Boggs, M., T. Goorley, C. Royer, T. E. Booth, H. G. Hughes, A. Sood, F. B. Brown, S. Mashnick, J. E. Sweezy, J. S. Bull, S. Pollack, A. Zukaitis, R. A. Forster, R. E. Prael, S. C. Frankle, R. C. Little, and M. C. White. *MCNP-A General Monte Carlo N-Particle Transport Code Version 5*. Los Alamos National Laboratory, Los Alamos, 5 edition, 2005.

Bohr, N. The penetration of atomic particles through matter. *Mathemtisk-fysiske Meddelelser* **18**, 1–144, 1948.

Bøtter-Jensen, L., E. Bulur, G. A. T. Duller, and A. S. Murray. Advances in luminescence instrument systems. *Radiat. Meas.* **32**, 523–528, 2000.

Bøtter-Jensen, L., S. W. S. McKeever, and A. G. Wintle. *Optically stimulated luminescence dosimetry*. Elsevier, The Netherlands, 2003.

Bradt, H. L., and B. Petters. Investigation of the primary cosmic radiation with nuclear photographic emulsions. *Phys. Rev.* **74**, 1828–1837, 1948.

Butts, J. J., and R. Katz. Theory of RBE for heavy ion bombardment of dry enzymes and viruses. *Radiat. Res.* **30**, 855–871, 1967.

Cashwell, E. D., and C. J. Everett. *A practical manual on the Monte Carlo method for random walk problems*, volume 1 of *Computer science and technology and their application*. Pergamon Press, UK, 1959.

Chatterjee, A., and W. R. Holley. Computer simulation of initial events in the biochemical mechanisms of DNA damage. *Adv. Radiat. Biol.* **17**, 181–226, 1993.

Chatterjee, A., H. D. Maccabee, and C. A. Tobias. Radial cutoff LET and radial cutoff dose calculations for heavy charged particles in water. *Radiat. Res.* **54**, 479–494, 1973.

Chatterjee, A., and H. J. Schaefer. Microdosimetric structure of heavy ion tracks in tissue. *Radiat. Environ. Biophys.* **13**, 215–227, 1976.

Chen, R., V. Pagonis, and J. L. Lawless. The nonmonotonic dose dependence of optically stimulated luminescence in Al_2O_3:C: Analytical and numerical simulation results. *J. Appl. Phys.* **99**, 033511, 2006.

Chunxiang, Z., D. E. Dunn, and R. Katz. Radial distribution of dose and cross-sections for the inactivation of dry enzymes and viruses. *Radiat. Prot. Dosim.* **13**, 215–218, 1985.

Edmund, J. M., C. E. Andersen, and S. Greilich. A track structure model of optically stimulated luminescence from Al_2O_3:C irradiated with 10-60 MeV protons. *Nucl. Instrum. Meth. Phys. Res. B* **262**, 261–275, 2007a.

Edmund, J. M., C. E. Andersen, S. Greilich, G. O. Sawakuchi, E. G. Yukihara, M. Jain, W. Hajdas, and S. Mattsson. Optically stimulated luminescence from Al_2O_3:C irradiated with 10-60 MeV protons. *Nucl. Instrum. Meth. Phys. Res. A* **580**, 210–213, 2007b.

Evans, B. D., G. J. Pogatshnik, and Y. Chen. Optical properties of lattice defects in α-Al_2O_3. *Nucl. Instr. Meth. Res. B* **91**, 258–262, 1994.

Evans, B. D., and M. Stapelbroek. Optical properties of the F^+ center in crystalline Al_2O_3. *Phys. Rev. B* **18**, 7089–7098, 1978.

Fageeha, O., J. Howard, and R. C. Block. Distribution of radial energy deposition around the track of energetic charged particles in silicon. *J. Appl. Phys.* **75**, 2317–2321, 1993.

Faïn, J., M. Monnin, and M. Montret. Spatial energy distribution around heavy-ion path. *Radiat. Res.* **57**, 379–389, 1974.

Fassò, A., A. Ferrari, J. Ranft, , and P. Sala. FLUKA: a multi-particle transport code. CERN 2005-10, 2005.

Fassò, A., A. Ferrari, S. Roesler, P. Sala, G. Battistoni, F. Cerutti, E. Gadioli, M. Garzelli, F. Ballarini, A. Ottolenghi, A. Empl, and J. Ranft. The physics models of FLUKA: status and recent developments. In *Computing in High Energy and Nuclear Physics 2003 Conference (CHEP2003)*, La Jolla, CA, USA, March 24-28 2003. (paper MOMT005) eConf C0303241 (2003), arXiv:hep-ph/0306267.

Gaza, R. *Space radiation dosimetry: an optically stimulated luminescence radiation detector for low-Earth orbit*. Ph.D. dissertation, Oklahoma State University, Stillwater, OK, USA, 2004.

Gaza, R., E. G. Yukihara, and S. W. S. McKeever. The response of thermally and optically stimulated luminescence from Al_2O_3:C to high-energy heavy charged particles. *Radiat. Meas.* **38**, 417–420, 2004.

Gaza, R., E. G. Yukihara, and S. W. S. McKeever. The use of optically stimulated luminescence from Al_2O_3:C in the dosimetry of high-energy heavy charged particle fields. *Radiat. Prot. Dosim.* **120**, 354–357, 2006a.

Gaza, R., E. G. Yukihara, S. W. McKeever, O. Ávila, A. Buenfil, I. Gamboa-deBuen, M. Rodríguez-Villafuerte, C. Ruiz-Trejo, and M. Brandan. Ionisation density depen-

dence of the optically stimulated luminescence dose-response of Al_2O_3:C to low-energy charged. *Radiat. Prot. Dosim.* **119**, 375–379, 2006b.

Geant4-Collaboration. *Geant4 user's guide for application developers*. Gean4 collaboration, http://geant4.web.cern.ch/geant4/support/userdocuments.shtml, 8.3 edition, 2007a.

Geant4-Collaboration. *Physics reference manual*. Gean4 collaboration, http://geant4.web.cern.ch/geant4/support/userdocuments.shtml, 8.3 edition, 2007b.

Geiß, O. B., M. Krämer, and G. Kraft. Efficiency of thermoluminescent detectors to heavy charged particles. *Nucl. Instr. Meth. Res. B* **142**, 592–598, 1998.

Goossens, O., F. Vanhavere, N. Leys, P. D. Boever, D. O'Sullivan, D. Zhou, F. Spurny, E. G. Yukihara, R. Gaza, and S. W. S. McKeever. Radiation dosimetry for microbial experiments in the International Space Station using different etched track and luminescent detectors. *Radiat. Prot. Dosim.* **120**, 433–437, 2006.

Hajek, M., T. Berger, M. Fugger, M. Fürstner, N. Vana, Y. Akatov, V. Shurshakov, and V. Arkhangelsky. Dose distribution in the russian segment of the international space station. *Radiat. Prot. Dosim.* **120**, 446–449, 2006.

Hansen, J. W., and K. J. Olsen. Experimental and calculated response of a radiochromic dye film dosimeter to high-LET radiations. *Radiat. Res.* **97**, 1–15, 1984.

Horowitz, Y. S. The theoretical and microdosimetric basis of thermoluminescence and applications to dosimetry. *Phys. Med. Biol.* **26**, 765–824, 1981.

Horowitz, Y. S., D. Satinger, L. Oster, N. Issa, M. E. Brandan, O. Avila, M. Rodriguez-Villafuerte, I. Gamboa-deBuen, A. E. Buenfil, and C. Ruiz-Trejo. The extended track interaction model: supralinearity and saturation He-ion TL fuence response in sensitized TLD-100. *Radiat. Meas.* **33**, 459–473, 2001.

Hubbell, J. H., and S. M. Seltzer. Tables of X-ray mass attenuation coefficients and mass energy-absorption coefficients (version 1.4). Technical report, National Institute of Standards and Technology, Gaithersburg, MD, 2004.

Huston, A. L., B. L. Justus, P. L. Falkenstein, R. W. Miller, H. Ning, and R. Altemus. Remote optical fiber dosimetry. *Nucl. Instr. Meth. Phys. Res. B* **184**, 55–67, 2001.

IAEA. Atomic and molecular data for radiotherapy and radiation research. Technical Report TECDOC-799, International Atomic Energy Agency, Austria, 1995.

ICRP. 1990 Recommendations of the International Commission on Radiological Protection. Technical Report 60, International Commission on Radiological Protection, Oxford, UK, 1990.

ICRU. Linear energy transfer. Technical Report 16, International Commission on Radiation Units and Measurements, Washington, DC, 1970.

ICRU. Average energy required to produce an ion pair. Technical Report 31, International Commission on Radiation Units and Measurements, Washington, DC, 1979.

ICRU. Stopping powers and ranges for protons and alpha particles. Technical Report 49, International Commission on Radiation Units and Measurements, Washington, DC, 1993.

ICRU. Secondary electron spectra from charged particle interactions. Technical Report 55, International Commission on Radiation Units and Measurements, Bethesda, Maryland, 1995.

Iskef, H., J. W. Cunningham, and D. E. Watt. Projected ranges and effective stopping powers of electrons with energy between 20 eV and 10 keV. *Phys. Med. Biol.* **28**, 535–545, 1983.

Johns, H. E., and J. R. Cunningham. *The physics of radiology*. Charles C Thomas, Illinois, 4 edition, 1983.

Kalchgruber, R., and G. Wagner. Separate assessment of natural beta and gamma dose-rates with TL from α-Al_2O_3:C single-crystal chips. *Radiat. Meas.* **41**, 154–162, 2006.

Kalef-Ezra, J., and Y. S. Horowitz. Heavy charged particle thermoluminescence dosimetry: Track structure theory and experiment. *Int. J. Appl. Radiat. Isot.* **33**, 1085–1100, 1982.

Kanter, H., and E. J. Sternglass. Interpretation of range measurements for kilovolt electrons in solids. *Phys. Rev.* **126**, 620–626, 1962.

Katz, R., S. C. Sharma, and M. Homayoonfar. The structure of particle tracks. In Attix, F., and E. Tochilin, editors, *Topics in radiation dosimetry: Supplement 1*, pages 317–383. Academic Press, 1972.

Kiefer, J., and H. Straaten. A model of ion track structure base on classical collision dynamics. *Phys. Med. Biol.* **31**, 1201–1209, 1986.

Kobetich, E. J., and R. Katz. Energy deposition by electron beams and delta rays. *Phys. Rev.* **170**, 391–396, 1968.

Krämer, M. Calculation of heavy-ion track structure. *Nucl. Instr. Meth. Res. B* **11**, 14–20, 1995.

Lee, K. H., and J. H. Crawford. Luminescence of the F center in sapphire. *Phys. Rev. B* **19**, 3217–3221, 1979.

Maplesoft^{TM}. Maple 10. Waterloo Maple Inc., 2005.

Mark, S., Y. S. Horowitz, D. Satinger, Y. Haviv, and I. Orion. FLUKA Monte Carlo calculations of complete track helium ion and prton radial dose profiles in LiF. In *Proc. 15th International Conference on Solid State Dosimetry*, volume 1, page 280, Delft, The Netherlands, July 2007.

Markey, B. G., L. E. Colyott, and S. W. S. McKeever. Time-resolved optically stimulated luminescence from α-Al_2O_3:C. *Radiat. Meas.* **24**, 457–463, 1995.

Massillon-JL, G., I. Gamboa-deBuen, and M. E. Brandan. Observation of enhanced efficiency in the excitation of ion-induced LiF:Mg,Ti thermoluminescence peaks. *J. Appl. Phys.* **100**, 103521, 2006.

McKeever, S. W. S. New millenium frontiers of luminescence dosimetry. *Radiat. Prot. Dosim.* **100**, 27–32, 2002.

McKeever, S. W. S., and M. Akselrod. Radiation dosimetry using pulsed optically stimulated luminescence of Al_2O_3:C. *Radiat. Prot. Dosim.* **84**, 317–320, 1999.

McKeever, S. W. S., M. Akselrod, and B. Markey. Pulsed optically stimulated luminescence dosimetry using alpha-Al_2O_3:C. *Radiat. Prot. Dosim.* **65**, 267–272, 1996.

McKeever, S. W. S., E. R. Benton, R. Gaza, G. O. Sawakuchi, and E. G. Yukihara. Passive space radiation dosimetry using optically stimulated luminescence and plastic nuclear track detectors. *Radiat. Meas.* (to be submitted), 2007.

McKeever, S. W. S., and M. Moscovitch. On the advantages and disadvantages of optically stimulated luminescence dosimetry and thermoluminescence dosimetry. *Radiat. Prot. Dosim.* **104**, 263–270, 2003.

McKeever, S., M. Moscovitch, and P. Townsend. *Thermoluminescence dosimetry materials: properties and uses*. Nuclear Tecknology Publishing, England, 1995.

Mott, N. F. The scattering of fast electrons by atomic nuclei. *Proc. R. Soc. London A* **124**, 425–442, 1929.

NCRP. Operational radiation safety program for astronauts in low-Earth orbit: a basic framework: recommendations of the National Council on Radiation Protection and Measurements. Technical Report 142, National Council on Radiation Protection and Measurements, Bethesda, Maryland, 2002.

Nikjoo, H., S. Uehara, D. Emfietzoglou, and F. Cucinotta. Track-structure codes in radiation research. *Radiat. Meas.* **41**, 1052–1074, 2006.

Ohsawa, D., H. Kawauchi, M. Hirabayashi, Y. Okada, T. Honma, A. Higashi, S. Amano, Y. Hashimoto, F. Soga, and Y. Sato. An apparatus for measuring the energy and angular distribution of secondary electrons emitted from water vapor by fast heavy-ion impact. *Nucl. Instr. Meth. Res. B* **227**, 431–449, 2005a.

Ohsawa, D., Y. Sato, Y. Okada, V. P. Shevelko, and F. Soga. Unexpectedly large cross sections of high-energy electrons ejected from water vapor by 6.0-10.0 MeV/u He^{2+} ions. *Phys. Lett. A* **342**, 168–174, 2005b.

Olko, P. Microdosimetric modelling of physical and biological detectors. The Henryk Niewodniczański Institute of Nuclear Physics, Krakow, Poland, 2002. Habilitation Thesis.

Olko, P., P. Bilski, N. A. El-Faramawy, H. Y. Göksu, J. L. Kim, R. Kopec, and M. P. R. Waligórski. On the relationship between dose-, energy- and LET-response of thermoluminescence detectors. *Radiat. Prot. Dosim.* **119**, 15–22, 2006.

Oppenheimer, J. R., H. Snyder, and R. Serber. The production of soft secondaries by mesotrons. *Phys. Rev.* **57**, 75–81, 1940.

Pagonis, V., R. Chen, and J. Lawless. Nonmonotonic dose dependence of OSL intensity due to competition during irradiation and readout. *Radiat. Meas.* **41**, 903–909, 2006.

Polf, J. C., S. W. S. McKeever, M. S. Akselrod, and S. Holmstrom. A real-time, fibre optic dosimetry system using Al_2O_3 fibres. *Radiat. Prot. Dosim.* **100**, 301–304, 2002.

Ragu, M. R. *Heavy particle radiotherapy*. Academic Press, New York, 1980.

Rossi, B. *High-Energy Particles*. Prentice-Hall, Inc, New York, 1952.

Rossi, H. H., and M. Zaider. *Microdosimetry and its applications*. Springer-Verlag, Germany, 1996.

Rudd, M. E., Y. K. Kim, D. H. Madison, and T. J. Gay. Electron production in proton collisions with atoms and molecules: energy distributions. *Rev. Mod. Phys.* **64**, 441–478, 1992.

Sato, Y., D. Ohsawa, A. Higashi, H. Kawauchi, M. Hirabayashi, Y. Okada, S. Uehara, H. Nikjoo, and F. Soga. Secondary electrons from water vapor with the impact of 6.0 MeV/u He^{2+} ions: Atomic data and their application to biomedical investigations. *AIP Conf. Proc.* **771**, 128–137, 2005.

Sawakuchi, G. O., E. G. Yukihara, S. W. S. McKeever, and E. R. Benton. Optically stimulated luminescence fluence response of Al_2O_3:C dosimeters exposed to different types of radiation. *Radiat. Meas.* (doi:10.1016/j.radmeas.2007.08.003), 2007a.

Sawakuchi, G. O., E. G. Yukihara, S. W. S. McKeever, and E. R. Benton. Overlap of heavy charged particle tracks and the change in shape of optically stimulated luminescence decay curve of Al_2O_3:C. *Radiat. Meas.* (submitted), 2007b.

Sawakuchi, G. O., E. G. Yukihara, S. W. S. McKeever, E. R. Benton, Y. Uchihori, N. Yasuda, and H. Kitamura. Relative luminescence efficiencies from Al_2O_3:C irradiated with high-energy heavy charged particles. *J. Appl. Phys.* (to be submitted), 2007c.

Waligórski, M. P. R., R. N. Hamm, and R. Katz. The radial distribution of dose around the path of a heavy ion in liquid water. *Nucl. Tracks Radiat. Meas.* **11**, 309–319, 1986.

Waligórski, M. P. R., and R. Katz. Supralinearity of peak 5 and peak 6 in TLD-700. *Nucl. Instr. Meth.* **172**, 463–470, 1980.

Wingate, C. L., and J. W. Baum. Measured radial distributions of dose and LET for alpha and proton beams in hydrogen and tissue-equivalent gas. *Radiat. Res.* **65**, 1–19, 1976.

Yasuda, H., I. Kobayashi, and H. Morishima. Decaying patterns of optically stimulated luminescence from Al_2O_3:C for different quality radiations. *J. Nucl. Sci. Technol.* **39**, 211–213, 2002.

Yukihara, E. G., R. Gaza, S. W. S. McKeever, and C. G. Soares. Optically stimulated luminescence and thermoluminescence efficiencies for high-energy heavy charged particle irradiation in Al_2O_3: C. *Radiat. Meas.* **38**, 59–70, 2004a.

Yukihara, E. G., and S. W. S. McKeever. Ionisation density dependence of the optically and thermally stimulated luminescence from Al_2O_3:C. *Radiat. Prot. Dosim.* **119**, 206–217, 2006a.

Yukihara, E. G., and S. S. McKeever. Spectroscopy and optically stimulated luminescence of Al_2O_3:C using time-resolved measurements. *J. Appl. Phys.* **100**, 083512, 2006b.

Yukihara, E. G., G. O. Sawakuchi, S. Guduru, S. W. S. McKeever, R. Gaza, E. R. Benton, N. Yasuda, Y. Uchihori, and H. Kitamura. Application of the optically stimulated luminescence technique in space dosimetry. *Radiat. Meas.* **38**, 317–330, 2006.

Yukihara, E. G., V. H. Whitley, S. W. S. McKeever, A. E. Akselrod, and M. S. Akselrod. Effect of high-dose irradiation on the optically stimulated luminescence of Al_2O_3: C. *Radiat. Meas.* **38**, 317–330, 2004b.

Yukihara, E. G., V. H. Whitley, J. C. Polf, D. M. Klein, S. W. S. McKeever, A. E. Akselrd, and M. S. Akselrod. The effects of deep trap population on the thermoluminescence of Al_2O_3:C. *Radiat. Meas.* **37**, 627–638, 2003.

Yukihara, E. G., E. M. Yoshimura, T. D. Lindstrom, S. Ahmad, K. K. Taylor, and G. Mardirossian. High-precision dosimetry for radiotherapy using the optically stimulated luminescence technique and thin Al_2O_3:C dosimeters. *Phys. Med. Biol.* **50**, 5619–5628, 2005.

Zajic, V. Energy vs. LET vs. range calculator version 1.24. Brookhaven National Laboratory. Software.

Zhang, C. X., X. W. Liu, M. F. Li, and D. L. Luo. Numerical calculation of the radial distribution of dose around the path of a heavy ion. *Radiat. Prot. Dosim.* **52**, 93–96, 1994.

Zhou, D., E. Semones, R. Gaza, S. Johnson, N. Zapp, and M. Weyland. Radiation measured for ISS-Expedition 12 with different dosimeters. *Nucl. Instr. Meth. Phys. Res. A* (doi:10.1016/j.nima.2007.06.091), 2007.

Zhou, D., E. Semones, R. Gaza, and M. Weyland. Radiation measured with passive dosimeters in low Earth orbit. *Adv. Sp. Res.* (doi:10.1016/j.asr.2006.12.03), 2006.

APPENDIX A

RELATIVE LUMINESCENCE EFFICIENCY DATA

Figures A.1, A.2, and A.3 compare the relative luminescence efficiency data from Luxel^{TM} detectors and OSL and TL from Al_2O_3:C single crystal and TLD-100 detectors. Table A.1 presents the relative luminescence efficiency data of Luxel^{TM} detectors that was graphically represented in section 7.3. In this table we also include OSL and TL relative luminescence efficiency of Al_2O_3:C single crystal and TLD-100 detectors. Section 7.3 describes the methodology used to calculate the relative luminescence efficiencies, and chapter 6 presents details about the experimental setup and OSL and TLD readouts.

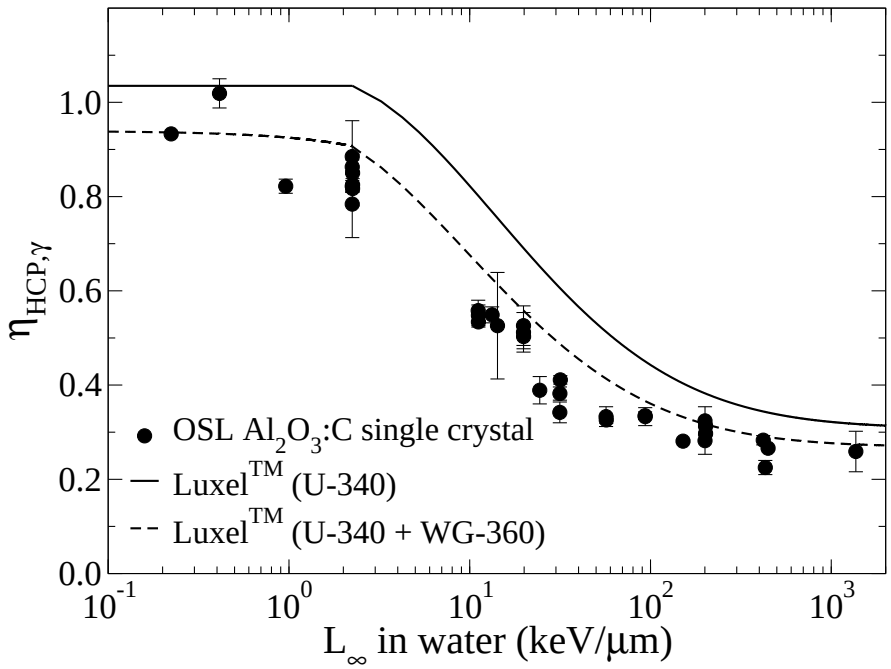

Figure A.1: $\eta_{HCP,\gamma}$ calculated in water of OSL from Al_2O_3:C single crystal detectors. We considered the OSL signal equal to the total area under the OSL curve. The OSL was measured with Hoya U-340 filter detecting both F-center and UV emission bands. For comparison we include the Luxel^{TM} data (full and dashed lines).

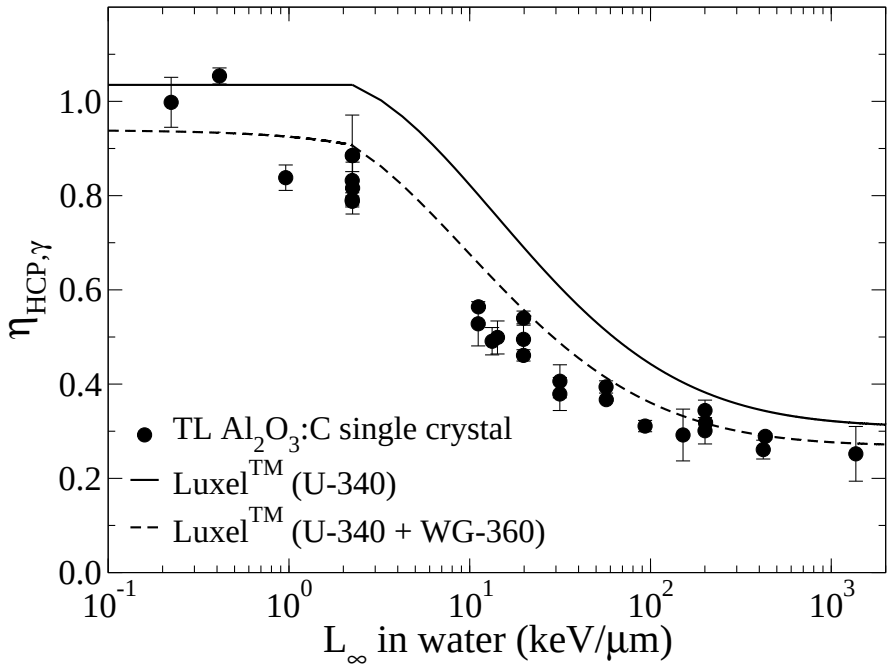

Figure A.2: $\eta_{HCP,\gamma}$ calculated in water of TL from Al_2O_3:C single crystal detectors. We considered the TL signal equal to the height of the dosimetric TL peak. The TL was measured with Corning 5-58 filter detecting both F-center emission band. For comparison we include the Luxel^{TM} data (full and dashed lines).

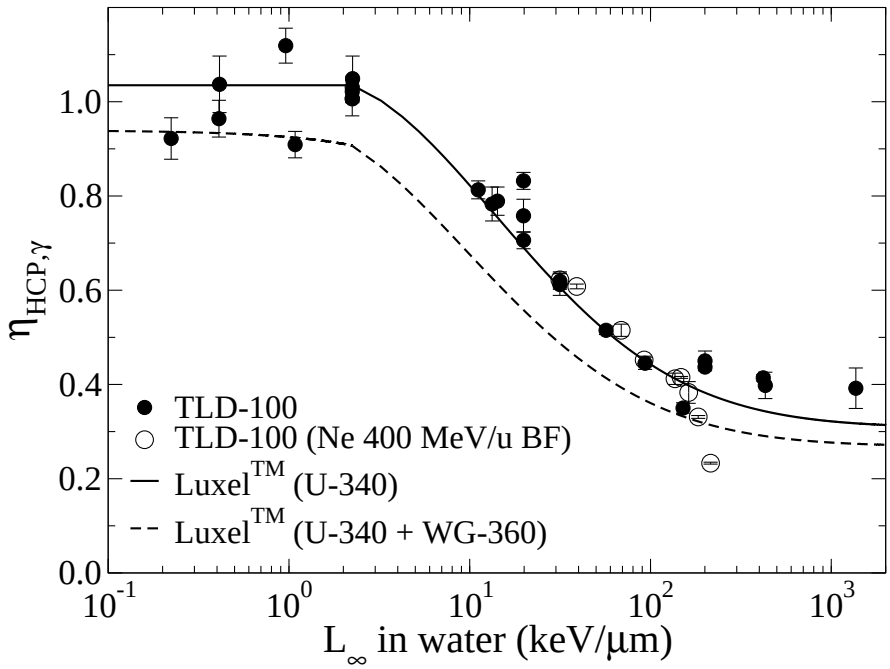

Figure A.3: $\eta_{HCP,\gamma}$ calculated in water of TL from TLD-100 detectors. We considered the TL signal equal to the height of the dosimetric TL peak. The TL was measured with Schott BG-39 filter. For comparison we include the Luxel^{TM} data (full and dashed lines).

Table A.1: Relative luminescence efficiency of HCP in respect to gamma radiation for 24 combinations of particles and energies. The relative luminescence efficiency was calculated in water. We considered the OSL signals from Luxel^{TM} and Al_2O_3:C single crystal detectors equal to the total area under the OSL curve, and the TL signals from Al_2O_3:C single crystal and TLD-100 detectors equal to the height of the dosimetric TL peaks. See section 6 for experimental details.

Beam	Energy (MeV/u)	$L_{\infty}^{H_2O}$ (keV/μm)	Al_2O_3:C single crystal TL (5-58 or BG-39) F-center	Al_2O_3:C single crystal OSL (U-340) F-center and UV emissions	Luxel^{TM} OSL (U-340) F-center and UV emissions	Luxel^{TM} OSL (WG-360 and U-340) F-center emission	TLD-100 TL (BG-39)
H 1000 MeV							
NSRL[1]-ICB[2] (2004)	1000	0.223	0.998 ± 0.053	0.933 ± 0.005	0.977 ± 0.005	0.908 ± 0.018	0.922 ± 0.044
NSRL-Eril[3] (2006)	1000	0.223			0.875 ± 0.017	0.850 ± 0.030	
NSRL-JSC[4] (2006)	1000	0.223				1.196 ± 0.011	
H 230 MeV							
LLUMC[5] (2004)	230	0.413	1.054 ± 0.017	1.019 ± 0.031	1.021 ± 0.003	0.951 ± 0.006	1.037 ± 0.060
H 70 MeV							
LLUMC (2004)	70	0.960	0.838 ± 0.027	0.822 ± 0.015	1.099 ± 0.010	0.928 ± 0.002	1.119 ± 0.037
H 40 MeV							
TAMU[6]-SRAG[7] (2006)	40	1.50			1.032 ± 0.060	0.848 ± 0.028	

[1]NASA Space Radiation Laboratory
[2]Irradiations performed as part of the ICCHIBAN project
[3]Irradiations performed by Eril Research Inc.
[4]Irradiations performed by Johnson Space Center
[5]Loma Linda University Medical Center
[6]Texas A & M University
[7]Irradiations performed by Space Radiation Analysis Group, NASA

H 30 MeV							
TAMU-SRAG (2006)	30	1.90			0.846 ± 0.022	0.721 ± 0.022	
He 150 MeV/u							
HIMAC-ICB2 (2002)	143.3	2.25	0.885 ± 0.006	0.825 ± 0.013	1.034 ± 0.007		
HIMAC-ICB4 (2003)	143.3	2.25		0.850 ± 0.040	1.040 ± 0.030		
HIMAC-OSU[8]1 (2004)	143.7	2.25			1.046 ± 0.006		
HIMAC-OSU2 (2004)	143.7	2.25	0.816 ± 0.055	0.817 ± 0.037	1.040 ± 0.023	0.916 ± 0.009	1.049 ± 0.048
HIMAC-OSU3 (2005)	144.2	2.24	0.788 ± 0.008	0.863 ± 0.015	1.018 ± 0.016	0.921 ± 0.006	1.031 ± 0.023
HIMAC-Eril (2005)	144.2	2.24	0.791 ± 0.015	0.784 ± 0.071	1.016 ± 0.024	0.915 ± 0.005	1.022 ± 0.023
HIMAC-ICB8 (2005)	144.2	2.24	0.832 ± 0.019	0.885 ± 0.076	1.019 ± 0.013	0.894 ± 0.025	1.006 ± 0.036
HIMAC-OSU4 (2006)	144.2	2.24	0.885 ± 0.086	0.822 ± 0.012	1.004 ± 0.014	0.893 ± 0.017	1.007 ± 0.009
H 24 MeV							
TAMU-SRAG (2006)	24	2.27			0.831 ± 0.026	0.710 ± 0.030	
H 20 MeV							
TAMU-SRAG (2006)	20	2.64			0.785 ± 0.013	0.666 ± 0.013	
H 17 MeV							
TAMU-SRAG (2006)	17	3.01			0.816 ± 0.019	0.675 ± 0.020	
H 14 MeV							
TAMU-SRAG (2006)	14	3.52			0.752 ± 0.017	0.622 ± 0.022	
C 400 MeV/u							
HIMAC-ICB2 (2002)	384.9	11.17	0.564 ± 0.003	0.534 ± 0.011	0.797 ± 0.007		
HIMAC-ICB4 (2003)	384.9	11.17		0.548 ± 0.022	0.833 ± 0.001		
HIMAC-OSU3 (2005)	386.9	11.14	0.528 ± 0.047	0.558 ± 0.022	0.819 ± 0.023	0.684 ± 0.007	0.813 ± 0.019
C 290 MeV/u							
HIMAC-OSU2 (2004)	277.2	13.30	0.491 ± 0.029	0.549 ± 0.017	0.782 ± 0.005	0.626 ± 0.008	0.783 ± 0.036
O 1000 MeV/u							
NSRL-ICB (2004)	1000	14.24	0.499 ± 0.035	0.526 ± 0.113	0.795 ± 0.004	0.625 ± 0.008	0.789 ± 0.030

[8]Irradiations performed by Oklahoma State University

O 400 MeV/u							
HIMAC-OSU2 (2004)	384.4	19.86	0.540 ± 0.015	0.503 ± 0.026	0.750 ± 0.032	0.597 ± 0.001	0.706 ± 0.018
HIMAC-Eril (2005)	385.5	19.84	0.495 ± 0.033	0.512 ± 0.042	0.769 ± 0.021	0.609 ± 0.013	0.832 ± 0.018
HIMAC-ICB8 (2005)	385.5	19.84	0.461 ± 0.012	0.526 ± 0.042	0.710 ± 0.023	0.555 ± 0.004	0.758 ± 0.035
C 135 MeV/u							
HIMAC-OSU1 (2004)	111.2	24.41			0.620 ± 0.005		
HIMAC-ICB6 (2004)	111.2	24.41		0.389 ± 0.029	0.626 ± 0.018	0.489 ± 0.015	
Ne 400 MeV/u							
HIMAC-ICB4 (2003)	368.5	31.70		0.411 ± 0.009	0.599 ± 0.002		
HIMAC-Eril (2005)	372.9	31.51	0.379 ± 0.035	0.342 ±0.022	0.560 ± 0.005	0.467 ± 0.016	0.612 ± 0.023
HIMAC-OSU4 (2006)	371.9	31.55	0.406 ± 0.035	0.382 ± 0.014	0.572 ± 0.004	0.474 ± 0.004	0.619 ± 0.017
Si 490 MeV/u							
HIMAC-ICB2 (2002)	442.5	56.93	0.367 ± 0.003	0.326 ± 0.007	0.485 ± 0.004		
HIMAC-OSU4 (2006)	444.8	56.80	0.394 ± 0.013	0.333 ± 0.021	0.469 ± 0.006	0.398 ± 0.009	0.515 ± 0.009
Ar 500 MeV/u							
HIMAC-ICB6 (2004)	448.6	93.54		0.333 ± 0.019	0.452 ± 0.004	0.359 ± 0.019	
HIMAC-ICB8 (2005)	450.7	93.34	0.311 ± 0.012	0.335 ± 0.008	0.441 ± 0.004	0.369 ± 0.007	0.445 ± 0.013
Ti 1000 MeV/u							
NSRL-OSU (2005)	977.6	108.2			0.436 ± 0.012	0.313 ± 0.013	
Fe 1000 MeV/u							
NSRL-ICB (2004)	968.0	151.4	0.292 ± 0.055	0.281 ± 0.004	0.358 ± 0.007	0.285 ± 0.014	0.350 ± 0.011
NSRL-Eril (2006)	967.0	151.4			0.373 ± 0.002	0.317 ± 0.007	
NSRL-JSC (2006)	967.0	151.4				0.343 ± 0.008	
Fe 500 MeV/u							
HIMAC-ICB2 (2002)	416.8	201.8	0.318 ± 0.005	0.297 ± 0.005	0.397 ± 0.003		
HIMAC-ICB4 (2003)	416.8	201.8		0.313 ± 0.006	0.423 ± 0.004		
HIMAC-OSU1 (2004)	416.8	201.8			0.394 ± 0.003		
HIMAC-Eril (2005)	423.7	200.3	0.301 ± 0.028	0.282 ± 0.029	0.374 ± 0.018	0.341 ± 0.020	0.450 ± 0.021
HIMAC-OSU4 (2006)	423.7	200.3	0.344 ± 0.022	0.324 ± 0.030	0.375 ± 0.006	0.324 ± 0.002	0.437 ± 0.006

Fe 200 MeV/u							
HIMAC-ICB8 (2005)	124.9	420.6	0.261 ± 0.020	0.283 ± 0.010	0.341 ± 0.009	0.285 ± 0.009	0.414 ± 0.007
HIMAC-OSU4 (2006)	120.4	431.8	0.289 ± 0.006	0.225 ± 0.015	0.312 ± 0.006	0.268 ± 0.004	0.398 ± 0.028
Kr 400 MeV/u							
HIMAC-ICB6 (2004)	313.1	447.2		0.266 ± 0.005	0.380 ± 0.005	0.316 ± 0.012	
Xe 290 MeV/u							
HIMAC-Eril (2005)	185.5	1368	0.252 ± 0.058	0.259 ± 0.043	0.344 ± 0.005	0.323 ± 0.011	0.392 ± 0.043

APPENDIX B

GEANT4 CODE FOR THE PHYSICS PROCESSES

B.1 ION PROCESSES

```
G4hLowEnergyIonisation* ionisation = new G4hLowEnergyIonisation();
ionisation −> SetElectronicStoppingPowerModel(particle,"ICRU_R49p");
ionisation −> SetNuclearStoppingPowerModel("ICRU_R49");
ionisation −> SetNuclearStoppingOn();
ionisation −> SetFluorescence(true);
ionisation −> ActivateAugerElectronProduction(true);
manager −> AddProcess(ionisation,-1,2,2);
manager −> AddProcess(new G4StepLimiter(),-1,-1,3);
```

B.2 ELECTRON PROCESSES

```
manager −> AddProcess(new G4MultipleScattering,-1,1,1);
manager −> AddProcess(new G4LowEnergyIonisation,-1,2,2);
G4LowEnergyBremsstrahlung* brem = new G4LowEnergyBremsstrahlung();
manager −> AddProcess(brem,-1,-1,3);
manager −> AddProcess(new G4StepLimiter(),-1,-1,3);
```

VITA

Gabriel Oliveira Sawakuchi

Candidate for the Degree of

Doctor of Philosophy

Dissertation: CHARACTERIZATION AND MODELING OF RELATIVE LUMINESCENCE EFFICIENCY OF OPTICALLY STIMULATED LUMINESCENCE DETECTORS EXPOSED TO HEAVY CHARGED PARTICLES

Major Field: Physics

Biographical:

Personal Data: Born in Barretos, SP, Brazil on December 05, 1979.

Education:

Received Bachelor of Science degree in Physics and Master of Science degree in Physics from University of Sao Paulo, Brazil, in July 2001 and in December 2003, respectively. Completed the requirements for the Doctor of Philosophy degree with major in Physics at Oklahoma State University in October 2007.

Experience:

Undergraduate research assistant in Physics at University of Sao Paulo, Brazil, 1998–2001. Graduate research assistant at University of Sao Paulo, Brazil, 2002–2003. Physics teaching assistant at University of Sao Paulo, Brazil, 2002. Physics teaching assistant at Oklahoma State University, 2004. Graduate research assistant at Oklahoma State University, 2004 to 2007.

Name: Gabriel Oliveira Sawakuchi Date of Degree: December, 2007

Institution: Oklahoma State University Location: Stillwater, Oklahoma

Title of Study: CHARACTERIZATION AND MODELING OF RELATIVE LUMINESCENCE EFFICIENCY OF OPTICALLY STIMULATED LUMINESCENCE DETECTORS EXPOSED TO HEAVY CHARGED PARTICLES

Pages in Study: 157 Candidate for the Degree of Doctor of Philosophy

Major Field: Physics

Scope and Method of Study: This work investigates the optically stimulated luminescence (OSL) response of carbon-doped aluminum oxide (Al_2O_3:C) detectors exposed to heavy charged particles (HCPs) with energies relevant to radiation protection in space, and cancer therapy. This investigation includes ground-based experiments in accelerators and theoretical studies of the detector's response. These theoretical studies are based on the track structure model (TSM) and require information of the spatial pattern of energy deposition around the HCP path – the radial dose distribution (RDD). Thus, RDDs were obtained using six analytical models, and Monte Carlo (MC) simulations with the code GEANT4. In addition, we propose a modified analytical model to improve the agreement between calculated and experimental efficiency values.

Findings and Conclusions: Dose response experiments showed that beta rays and H 1000 MeV radiations produced similar responses in the detectors and we concluded that the H 1000 MeV and beta radiations deposit energy similarly. We observed a common trend of decreasing the relative luminescence efficiency ($\eta_{HCP,\gamma}$) as increasing the unrestricted linear energy transfer in water ($L_{\infty}^{H_2O}$) for all the detectors. For Luxel™ detectors the $\eta_{HCP,\gamma}$ was close to unit for particles with $L_{\infty}^{H_2O}$ lower than 3 keV/μm. TSM using the RDD from Chatterjee and Schaefer, Butts and Katz, Waligórski *et al.*, Fageeha *et al.*, Kiefer and Straaten, and Geiß *et al.* models failed to predict the $\eta_{HCP,\gamma}$ values. We proposed a modified version of the RDD from Butts and Katz model, which agreed within 20 % with $\eta_{HCP,\gamma}$ experimental data. This was the first time that such agreement was achieved for a wide range of HCPs of different energies. MC simulations with GEANT4 agreed within 35 % with $\eta_{HCP,\gamma}$ experimental data. Finally, we suggested a correction method, based on the calculation of $\eta_{HCP,\gamma}$ using the TSM presented in this dissertation, to measure more reliable absorbed doses when using luminescence detectors in complex radiation fields.

ADVISOR'S APPROVAL: Eduardo G. Yukihara